Electrochemical CO_2 Reduction by Polymer-Encapsulated Cobalt Phthalocyanine: Controlling Coordination Environment to Modulate the Activity and Selectivity

by

Yingshuo Liu

A dissertation submitted in partial fulfillment
of the requirements for the degree of
Doctor of Philosophy
(Chemistry)
in the University of Michigan
2020

Doctoral Committee:

Assistant Professor Charles C. L. McCrory, Chair
Professor Suljo Linic
Professor Mark E Meyerhoff
Associate Professor Nathaniel K. Szymczak

Yingshuo Liu

yingshuo@umich.edu

ORCID iD: 0000-0003-4780-8384

Acknowledgements

First and foremost, I wish to thank my advisor, Professor Charles C. L. McCrory. He has been supportive since the days I began working on the project as a Rotator. I remember he used to say something to me like "I believe that you are an insightful and careful electrochemist, and if things not work, it's not because of you" to encourage me in the lab. Professor McCrory has supported me not only by providing a research assistantship, but also academically and emotionally through the rough road to finish this thesis. Thanks to him, I had the opportunity to start, design, and test my project independently. He helped me come up with the thesis topic and guided me over almost four years of development. And during the most difficult times when working on my projects, he gave me support and freedom I needed to move on.

My thesis committee guided me through all these years. I thank Professor Mark E Meyerhoff, Professor Nathaniel K. Szymczak, and Professor Suljo Linic for their guidance, advice, and inspiration in many ways. A part of my thesis work has been done in close collaboration with Professor James E. Penner-Hahn and Dr. Aniruddha Deb, I have benefited greatly from their perspectives on X-ray absorption spectroscopy technique and spectrum analysis. I thank my fellow labmates in McCrory Group: Weixuan Nie, Kwan Leung, Jeremy Kallick, Robert Bonsall, William Dean, Samuel Michaud, Taylor Soucy as well as previous lab members: Dr. Chia-Cheng Lin, Weijie Feng and Qi Wang, for the insightful discussions, for the projects we were working together, and for all the fun we have had in the last four years.

In addition, I would especially like to thank the Chemistry Department Staff at University of Michigan who have greatly supported my graduate study. I would like to thank Roy Wentz for

making and modifying my electrochemical cells efficiently and perfectly, which enabled me to finish my projects on time. I thank James Windak for training me on the instruments in the department, which is essential for me to become a successful chemist.

I would like to thank my friends at Ann Arbor for all the great times that we have shared. I am particularly thankful to Lu Zhang, a walking partner, a nice neighbor, and a good friend. Thank you for the company during those laughter and tears. I thank my previous labmate and my good friend, Qi Wang, for the unconditional support, and for all the fun we have had together.

I am deeply thankful to my family for their love, support, and sacrifices. Especially my mom and dad, without them, this thesis would never have been written. I dedicate this thesis to the memory of my grandfather Yonghe Liu, whose role in my life was, and remains, immense. This last word of acknowledgment I have saved for my beloved fiancé Yuda Chen, who has constantly encouraged me when the tasks seemed arduous and insurmountable. His infinite love and patience have supported me throughout this experience.

Table of Contents

List of Tables

List of Figures

Abstract

The discovery of systems that preferentially convert carbon dioxide to single products while suppressing competitive side reactions like hydrogen evolution is a critically important outstanding challenge in renewable energy storage and carbon dioxide remediation. The research approach examined in this thesis is to encapsulate molecular catalysts within hydrophobic coordinating polymers that influence the primary-, secondary-, and outer-coordination spheres of the catalytic active site and also control substrate delivery to promote selective CO_2 reduction (CO_2RR) and inhibit competitive side reactions. Toward this goal, cobalt phthalocyanine (CoPc) encapsulated in poly-4-vinylpyridine (P4VP) has been adsorbed to the carbon electrodes by physisorption to the carbon surface. The mechanism of CO_2RR by polymer-encapsulated CoPc has been investigated. Specifically, a series of electrochemical kinetic isotope effect (KIE) measurements and proton inventories on CoPc-P4VP and related systems were conducted to probe the mechanistic implications of primary-coordination and the proton involvement in the rate-determining step of the CO_2RR mechanism. These studies provide strong evidence that coordination of an axial ligand changes the rate-determining step of CO_2RR. Moreover, it has been confirmed that there exists proton relays in the CoPc-P4VP system. This work highlights the importance of both primary- and outer-coordination sphere effects in the rate and selectivity of CO_2RR by catalyst-polymer composite systems.

In collaboration with the Penner-Hahn group at the University of Michigan, *in situ* X-ray absorption near edge structure (XANES) was used to verify that Co is four-coordinate in CoPc, five-coordinate in axially coordinated CoPc(py), and mostly, but not completely, five-coordinate

in CoPc-P4VP. In addition, the coordination environment of CoPc-P4VP is pH-dependent, suggesting that the axial coordination of pyridyl groups in P4VP with CoPc is modulated by the protonation of the polymer membrane. Interestingly, different oxidation state changes for four- and five-coordinate CoPc upon reduction suggest that the reduced five-coordinate species have a HOMO with metal character which is different than the four-coordinate CoPc species and this may partially explain the increased activity for CO_2RR for the five-coordinate species.

Finally, in order to probe the effect of axial coordination on CoPc, a series of CoPc(L) complexes where the σ-donor strength of L is varied was examined. There is an increase in the observed overall electrochemical activity of the corresponding CoPc(L) as L moves from less to more electron donating strength as indicated by density functional theory (DFT) calculations. This result suggests that the increased CO_2RR activity observed upon axial coordination to CoPc is due to the increased energy of the dz^2 orbital, which is crucial for the development of new electrocatalysts for CO_2RR.

Chapter 1: Introduction

1.1 Preface

This chapter presents the challenge of electrochemical CO_2 reduction and how different approaches have been developed to address it, followed by the methodologies used in this work to investigate the electrocatalytic mechanism by polymer encapsulated molecular catalyst composite system for CO_2 reduction. This chapter of my dissertation is partially derived from the manuscript as originally published in *Comments on Inorganic Chemistry*,[1] and I was the primary author of the manuscript upon which this chapter is partially based, and I was responsible for writing and editing the third and fourth parts of the manuscript which are "Using overlayer films to control substrate transport and influence CO_2RR selectivity" and "Selective CO_2RR by polymer-catalyst composite films". Samuel E. Michaud was responsible for writing the second part of the manuscript which is "effect of local pH and local CO_2 concentration on CO_2RR selectivity at solid-state metal electrocatalysts". Kwan Yee Leung was responsible for literature searching and wring the comments on the effect of trace metal contaminations. Taylor L. Soucy was responsible for writing the mechanisms of electron and substrate transport in the polymer-coated or encapsulated system. Charles C. L. McCrory was responsible for wring the "Introduction" and "Conclusion", and editing the entire manuscript.

[1] From "Controlled Substrate Transport to Electrocatalyst Active Sites for Enhanced Selectivity in the Carbon Dioxide Reduction Reaction" by Yingshuo Liu, et al, 2019, *Comments on Inorganic Chemistry*, 39:5, 242-269. Copyright [2019] by Taylor & Francis. Reprinted with permission.

1.2 Abstract

The selective electrochemical reduction of CO_2 to value added products is a useful strategy for the local storage of intermittent energy sources as chemical fuels and the recycling of industrial CO_2 waste into industrial feedstocks. This chapter highlights some of the recent research focused specifically on modulating substrate delivery and local catalyst environment to enhance reaction and product selectivity in the CO_2 reduction reaction by both solid-state materials and discrete molecular systems. In this chapter, we discuss recent studies that focus on coating electrocatalysts with porous overlayers to directly control substrate delivery to the electrocatalyst surface, and using polymer encapsulation to modify the coordination environment surrounding molecular electrocatalysts to enhance activity and selectivity for CO_2 reduction. We believe that increased research in controlling substrate delivery to enhance reaction and product selectivity for the CO_2 reduction reaction is a promising strategy for designing new electrocatalytic systems for the selective and efficient conversion of CO_2 to value-added products.

1.3 Introduction to Electrochemical CO_2 Reduction: Challenge and Enzymatic System

The selective electrochemical conversion of CO_2 in the carbon dioxide reduction reaction (CO_2RR) offers an intriguing approach for the local storage of intermittent energy sources as chemical fuels (e.g. solar fuels) and for the recycling of industrial CO_2 waste into useful chemical feedstocks.[1-12] However, developing electrocatalytic systems that show promising reaction selectivity for the CO_2RR over competitive side reactions like the hydrogen evolution reaction (HER) and show promising product selectivity for the formation of single C-containing products remains a fundamental challenge in CO_2 conversion technology. State-of-the-art polycrystalline Cu electrocatalysts show high activity for the CO_2RR but tend to operate with low selectivity, generating up to 16 different C-based products as well as H_2.[13-17] Planar Au and Ag catalysts are more selective for CO_2 reduction to CO, but this increased selectivity is potential dependent and the systems still suffer from the competitive HER.[14, 18, 19] The desire for enhanced reaction and product selectivity for the CO_2RR has been the focus of intense research over the past few decades as has been summarized in several reviews.[2, 5-7, 14, 17, 19-49]

Enzymatic systems such as NiFe carbon monoxide dehydrogenase (CODH) provide fundamental insight for the design of electrocatalytic systems that operate with high activity and product selectivity.[6, 50] In these biological systems, fast catalytic activity and high product selectivity are achieved by carefully controlling the primary, secondary, and outer coordination spheres of the enzyme's active site. Of particular importance in enzymatic systems is the use of the outer-coordination sphere to exclude solvent (e.g. H_2O) from the active site, which is crucial for the stabilization of catalytic transition states[51, 52] and for the controlled delivery of substrate.[6] For example, in the case of NiFe CODH, coordination of CO_2 to the 2 e^- reduced NiFe active site

is thought to occur at the coordinatively-unsaturated Ni^{I} site, and the coordinated CO_2 is stabilized by H-bonding interactions with lysine and histidine moieties in the secondary coordination sphere (Figure 1.1).[6, 53, 54] Subsequent protonation and loss of water leads to the initial formation of a reduced CO_2 intermediate bridged by the Ni and Fe sites and the eventual cleavage of a C-O bond to form a $Ni^{II}CO$ species, which then releases CO.[6] Note that in this system, the active site resides in a hydrophobic core and H^+ delivery is carefully controlled through H^+ relays in the outer-coordination sphere. The control of primary, secondary, *and outer* coordination spheres in this system is essential for catalytic activity and selectivity.

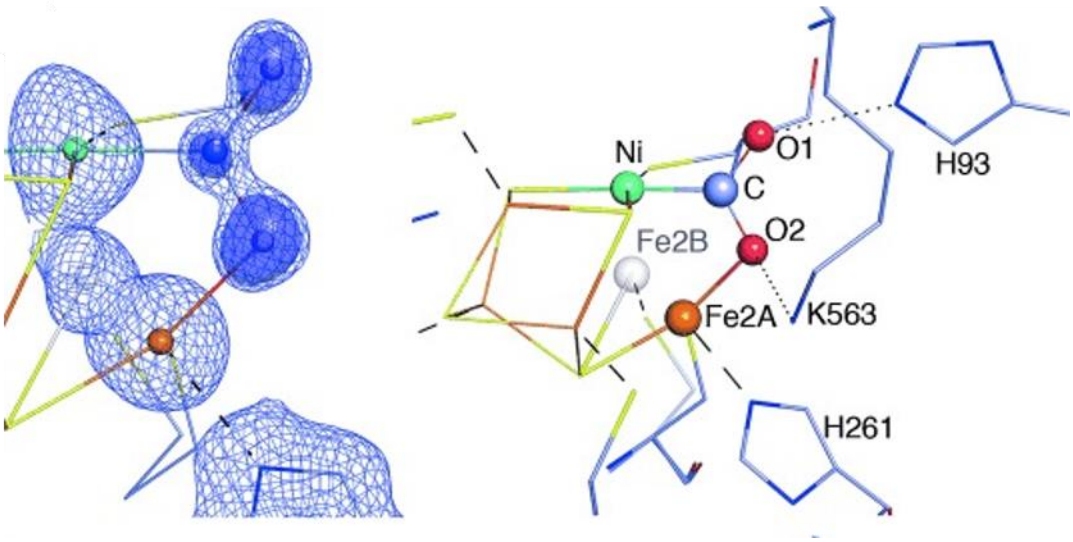

Figure 1.1 The proposed structure of coordinated CO_2 to the NiFe CODH active site. The CO_2 adduct is stabilized by H-bonding from histidine and lysine residues in the secondary coordination sphere. H^+ delivery to the active site is controlled through proton-relays in the protein structure. Adapted with permission from Ref. [54].

1.4 Using Overlayer Films to Control Substrate Transport and Influence CO_2RR Selectivity

One approach to controlling local pH and CO_2 concentration near catalyst active sites is to coat solid-state electrocatalyst surfaces with porous overlayers that directly control substrate transport to the catalyst surface (Figure 1.2). Overlayers have been used extensively to control stability and efficiency for the electrocatalytic oxygen reduction reaction (ORR)[55-57] and the HER,[58, 59] but are far less prevalent in the CO_2RR literature. However, overlayer-coated electrodes hold significance promise as electrocatalyst systems for enhanced CO_2RR reaction and product selectivity. For example, a recent DFT study on porous graphdiyne (GDY) coated Cu surface suggests that the GDY overlayer decreases reaction barriers and onset potential of CO_2RR intermediate steps, which enhances the performance of metal catalyst.[60] The GDY coating is thought to interact with CO_2 and increase local CO_2 concentration near the Cu surface. It may also stabilize *CO intermediates on the Cu surface favoring the subsequent reduction of *CO to CH_4.

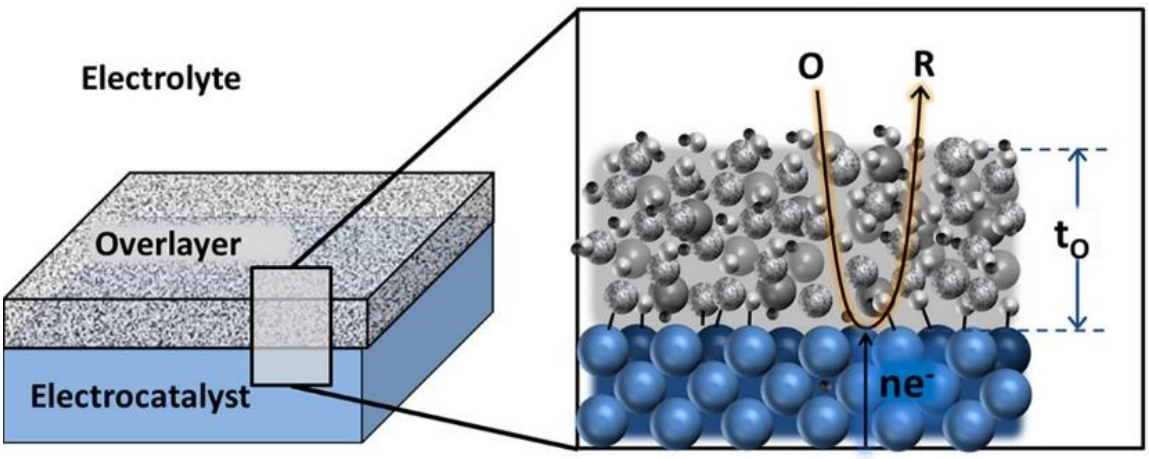

Figure 1.2 Illustration of an overlayer-coated electrode showing controlled substrate transport through the overlayer film to the electrocatalyst surface.[61] Adapted with permission from Esposito, D. V. *ACS Catal.* **2018**, *8*, 457-465. Copyright 2018 American Chemical Society

Polymer-coated catalysts are a specific subset of overlayer-coated electrodes which have been used to modulate the activity, product distribution, and stability of electrocatalysts for various electrocatalytic reactions including the CO_2RR.[62] The polymer films can impart significant benefits on the electrocatalysts by controlling substrate transport, stabilizing the reaction intermediate, and protecting against contaminants.[61, 62] When polymer-coated catalysts are used to enhance the CO_2RR, the hydrophobicity of polymer films can increase local CO_2 concentration near catalytic active sites and limit the transport of protons, thus enhancing the CO_2RR and suppressing the competitive HER.

For example, studies of CO_2RR by Cu surfaces coated with electropolymerized polypyrrole (PPy) films show a shift in the product distribution of CO_2RR towards more highly-reduced hydrocarbons while suppressing H_2 production.[63] The authors propose that the polypyrrole films decreases the concentration of H^+ and causes a change in the mechanism of the CO_2RR to a surface hydrogenation of CO_2 intermediates rather than sequential electron and proton transfer events.[63] Similar enhancement of the CO_2RR and suppression of the HER have been shown for MoS_x nanoparticle incorporated within polyethylenimine (PEI)-modified reduced graphene oxide films.[64] PEI is thought to suppress the HER by inhibiting H_2 formation,[64] and also to stabilize reaction intermediates through secondary-coordination sphere effects.[64, 65] In the case of the CO_2RR on poly-4-vinylpyrydine (P4VP) coated Cu electrodes, P4VP is postulated to coordinate with reduced Cu sites on the surfaces to form active Cu^{II}-P4VP complexes which strongly interact with CO_2. This polymer-coordination on the surface facilitates the formation of surface-CO_2 intermediates and limits the available sites for interactions with H^+, thus preferentially favoring the CO_2RR and suppressing the HER.[66]

Because of their hydrophobicity, polymer films can also increase local CO_2 concentration and stabilize reactive intermediates. For instance, it's thought that polymers such as P4VP and PEI might stabilize the formation of $CO_2^{\bullet -}$ radical anions either through direct electrostatic interactions between $CO_2^{\bullet -}$ and protonated sites on the polymer,[64, 65] or by forming a local non-aqueous environment which facilitates formation of the radical anion species.[66, 67] In addition, polymer films may increase the lifetime of desorbed intermediates. For example, Re surfaces coated with electropolymerized PPy films show increased activity for CO_2RR to CH_4 compared to bare Re.[68] It has been postulated that this increased activity for CH_4 production may be due to trapping of desorbed CO within the PPy matrix which increases the probability of CO re-adsorption and subsequent reduction to CH_4.[68]

Coating electrode surfaces with porous overlayers can also play an important role in decreasing transport of contaminants to the electrode surface and thus preventing electrode poisoning and deactivation.[59, 61, 69] This is particularly important for CO_2RR at Cu surfaces which are extremely susceptible to surface poisoning,[14, 70] especially by trace metal contaminants in the electrolyte solutions.[70-72] A recent study of CO_2RR by P4VP-coated Cu electrodes for the CO_2RR found that P4VP can act as a sink for heavy-metal contaminants in standard purity (99.7+ %) electrolytes, thereby decreasing the effect of the metal contaminants on the electrocatalytic activity and product distribution.[66]

1.5 Selective CO_2RR by Polymer-Catalyst Composite Films

In addition to serving as porous overlayers that control substrate transport to catalyst active sites, polymers can also be used to modulate the coordination environment of metal-macrocyclic complexes to increase their activity and selectivity for the CO_2RR. There are two common strategies for heterogenizing molecular catalysts within polymer films: 1) electropolymerization of metal complexes in which the molecular catalysts are directly incorporated into the polymer structure, and 2) polymer encapsulation in which the molecular catalyst is confined within a coordination polymer. The resulting polymer-catalyst composite films typically retain the main advantages of molecular electrocatalysts—including high selectivity for single products, single active sites, and tunable structures—while increasing effective charge transfer to the catalyst sites and increasing catalyst stability.

For electropolymerized catalyst-polymer composite films, 2-electron reduced products such as CO and HCOOH are the most common CO_2RR products in both aqueous and organic electrolyte solutions.[62, 73-78] More highly-reduced products (e.g. CH_4, CH_3OH, and C_2H_6) have been achieved by some polymeric structures,[79-82] especially systems with bimetallic or multimetallic active centers that can stabilize CO_2RR intermediates and/or facilitate C-C coupling.[79, 83, 84] However, proton-delivery can also play an important role in these systems. For instance, electropolymerized films of Co-polyvinylterpyridine complexes show selective CO_2RR towards the 2-electron production of HCOOH in non-aqueous solutions (DMF and acetonitrile),[78, 85] but these films reduce CO_2 by 4-electrons to formaldehyde in aqueous sodium perchlorate electrolytes.[86] It is postulated that the difference in the CO_2RR products in non-aqueous and aqueous electrolytes is due to proton-transport—when non-aqueous electrolytes are used, CO_2RR is limited by a lack of H^+ which results in release of HCOOH before it can be further reduced to

HCHO.[86] It's also worth noting that the electrocatalytic activity per active site decreases with increasing film thickness, presumably due to poor electron transport through the non-conducting polymer films.[86]

Polymer-encapsulation of molecular catalysts is another way to promote selective CO_2RR by composite catalyst-polymer films. In this case, the polymers can influence the activity of the molecular catalysts through numerous effects including primary coordination sphere effects such as axial-coordination to the metal active sites, secondary-coordination effects such as H-bonding interactions, and outer-coordination sphere effects such as controlled delivery of H^+ and CO_2 to the active sites.[87-92] A polymer-encapsulated system of particular interest to our group is cobalt phthalocyanine (CoPc) immobilized within poly-4-vinylpyridine (P4VP) films (Figure 1.3). CoPc-P4VP composite films have been shown to have enhanced CO_2RR activity and selectivity compared to the parent CoPc.[88-90] It was postulated that the enhancement in CO_2RR activity and selectivity was due to three synergistic effects imbued by the P4VP polymer. First, the pyridyl groups in P4VP can axially-coordinate to the Co metal center and facilitate CO_2 binding and reduction.[90] This is consistent with studies that show when σ-donating ligands such as pyridines or imidazoles are coordinated to metal porphyrin and phthalocyanine complexes, the resulting systems show an increase in catalytic activity for CO_2 reduction and O_2 reduction.[93-96] In addition, the polymer membrane can stabilize reduced CO_2 intermediates through H-bonding interactions with protonated pyridyl moieties. This proposed secondary-coordination sphere stabilization of reactive intermediates is analogous to that reported in several other studies of synthetic molecular catalysts.[97-101] Finally, the P4VP film can modulate H^+ transport to the active sites by using the pyridyl moieties as proton relays.

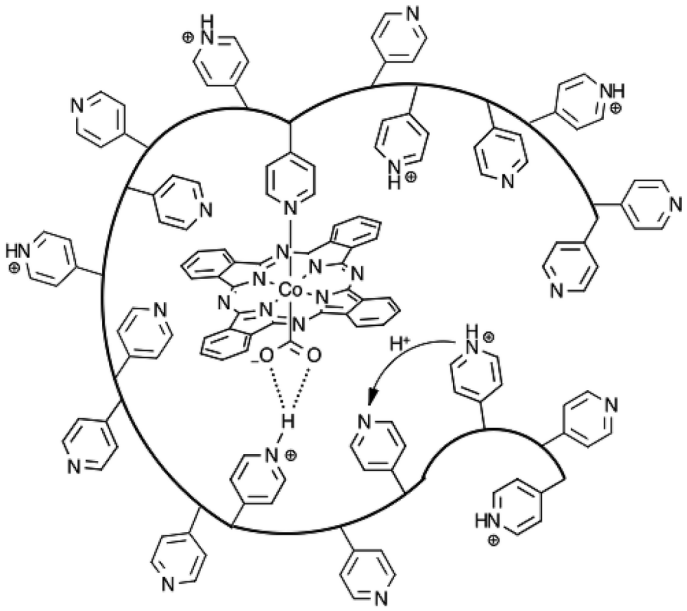

Figure 1.3 Cobalt phthalocyanine (CoPc) encapsulated within a poly-4-vinylpyridine (P4VP) film. The postulated primary coordination sphere effects (axial coordination of the pyridyl group to the CoPc), secondary coordination sphere effects (H-bonding stabilization of CO_2 intermediates), and outer coordination sphere effects (control of H^+-transport through a proton relay) are shown.[90] [W. W. Kramer and C. C. L. McCrory, Chem. Sci., 2016, 7, 2506] – Published by The Royal Society of Chemistry.

Our work has focused on distinguishing between the primary, secondary, and outer-coordination sphere effects in the polymer-encapsulated CoPc system and determining the extent to which each effect modulates the activity and selectivity for CO_2 reduction by CoPc. We systematically altered the polymer-encapsulated system to independently assess the role of each coordination sphere in the CO_2 reduction mechanism by the CoPc-P4VP system (Figure 1.4). In doing so, we determined the following effects: 1) axial coordination of pyridine to CoPc to form CoPc(py) leads to an increase in the CO_2 reduction activity and a moderate increase in selectivity; 2) immobilizing CoPc into poly-2-vinylpyridine (P2VP) to form CoPc-P2VP leads to an increase in the selectivity for CO production, but no change in the overall catalytic activity compared to the parent adsorbed CoPc. We propose that the steric congestion surrounding the P2VP pyridyl moieties prevents axial coordination to the Co metal center, and that inhibition of H_2 production in the CoPc-P2VP system is due to the limited transport of H^+ through the polymer film; and 3)

immobilizing CoPc(py) into P2VP to form the CoPc(py)-P2VP system leads to dramatically increased activity and selectivity for CO_2 reduction compared to the parent CoPc system. We hypothesize that the increase in selectivity is due to a combination of both axial-coordination effects and the outer-coordination sphere effects.[90] Note that rigorous studies on these types of polymers *have shown that* synergy between catalyst and polymer effects is required for increased activity and selectivity in polymer-encapsulated systems.[91]

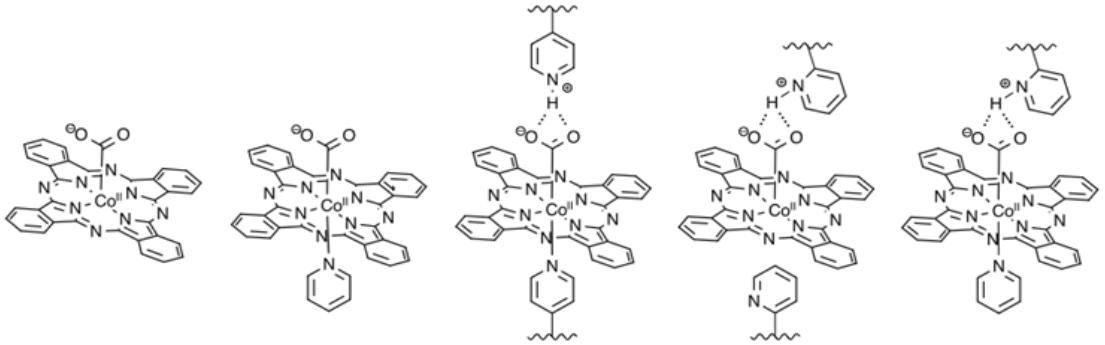

	CoPc	CoPc(py)	CoPc-P4VP	CoPc-P2VP	CoPc(py)-P2VP
ε_{CO}	36 ± 7%	68 ± 3%	89 ± 3%	73 ± 8%	83 ± 5%
TOF_{CO}	0.6 ± 0.3 s^{-1}	1.6 ± 1.0 s^{-1}	4.8 ± 0.6 s^{-1}	0.8 ± 0.2 s^{-1}	4.2 ± 0.7 s^{-1}

Figure 1.4 CO_2-reduction activity (TOF_{CO}) and Faradaic efficiency for CO production (ε_{CO}) by CoPc-P4VP and related systems. CoPc and CoPc(py) are complexes directly adsorbed to carbon electrodes with no polymer, whereas CoPc-P4VP, CoPc-P2VP, and CoPc(py)-P2VP are catalyst-polymer composites in which the catalyst is encapsulated within the P4VP or P2VP polymer.[90] Adapted with permission from: [W. W. Kramer and C. C. L. McCrory, Chem. Sci., 2016, 7, 2506] – Published by The Royal Society of Chemistry.

1.6 Methodology

1.6.1 Kinetic Isotope Effect

Kinetic Isotope Effect (KIE) measurements are used in Chapter 2 to probe the rate-determining step in the CO_2 reduction mechanism by CoPc. In general, a KIE is the change in the reaction rate of a chemical reaction when one of the atoms in the reactants is replaced by one of its isotopes. In our case, KIEs are measured as the ratio of rate constants or rate in H_2O and D_2O. Kinetic isotope effect reflects involvement of protons or deuterons in chemical reactions, and it occurs when H^+ directly participates in a rate-determining step in the reaction (e.g. a protonation or H+ transfer).[102] Consider an equilibrium process whose rate constants in H_2O and D_2O are κ_H and κ_D, respectively. The corresponding KIE is defined in Equation 1.1:

$$\text{KIE} = \frac{\kappa_H}{\kappa_D} \qquad (1.1)$$

Where κ_H and κ_D are the rate constants of reactions in H_2O and D_2O, respectively. KIEs larger than unity (faster rate in H_2O) are called normal isotope effects and those smaller than unity (faster rate in D_2O) are called inverse isotope effects.

KIE can be better understood using the transition state theory where there is an activated complex formed at the middle of the pathway from the reactant to the product. Using C-H and C-D bond as an example (Figure X), the two bonds have relatively the same electronic, translational and rotational properties, and the major factor contributing to KIEs is the vibrational frequencies which represented by the zero-point energies (C-H, C-D). The zero-point energy is the lowest possible energy of a system and equates to the ground state energy. Zero-point energy depends on the mass of the molecule, the heavier the molecule, the lower the frequency of vibration and the smaller the zero-point energy, as shown in the Figure 1.5, where deuterium is heavier than

hydrogen and therefore has the lower zero-point energy. The difference in zero-point energies result in different bond dissociation energies for C-H and C-D. The bond dissociation energy or the standard free energy of activation for C-D bond breaking $\Delta G^{\ddagger}_{C\text{-}D}$ is greater than that of C-H bond ($\Delta G^{\ddagger}_{C\text{-}H}$). This difference in activation energy due to isotopic replacement results in differing rates of reaction, which is measured by KIE. The rate for C-D bond dissociation is slower than the reaction rate for C-H bond dissociation. Note that isotope replacement does not change the electronic structure of the molecule, only the rate of the reaction is affected.

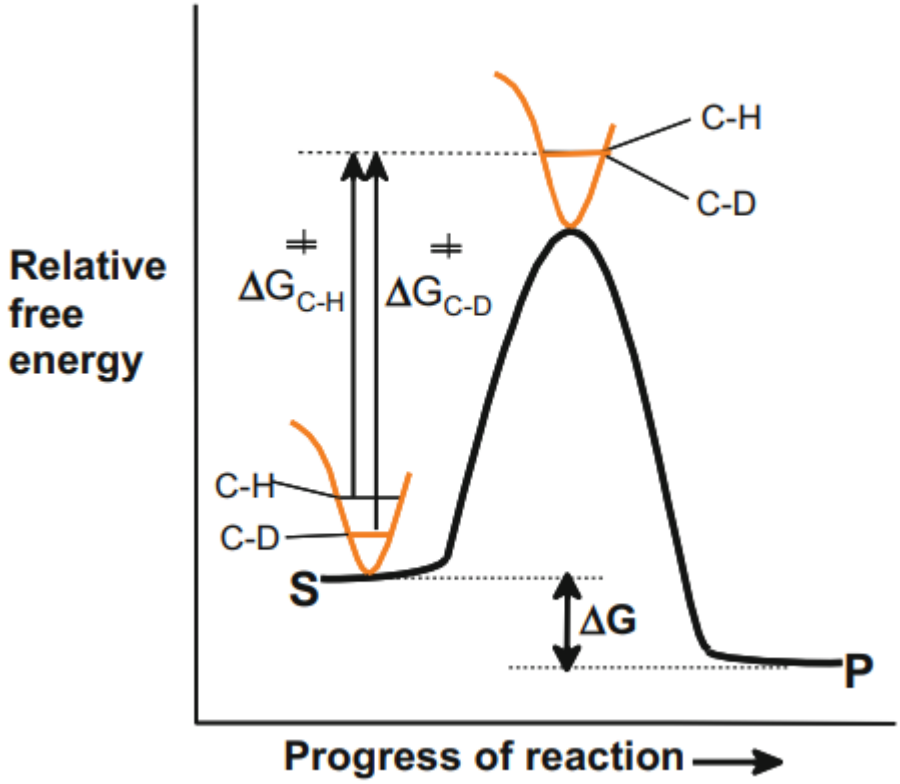

Figure 1.5 Reaction coordinate diagram for the C-H bond cleavage in an exergonic reaction. The transition state for both C-H and C-D bond cleavages are of similar energy. The zero-point energy mainly contributes to the difference between $\Delta G^{\ddagger}$ for C-H and C-D bonds. Reprint with permission from Ref.[103]

1.6.2 Proton Inventory

Proton inventory is used in Chapter 2 to determine the number of exchangeable protons in the structure of an enzyme or substrate that are active, and are involved in the catalytic mechanism. KIEs usually arise from differential isotopic fractionation at multiple exchangeable sites in the reactant and transition states. A proton inventory approach in which rate is measured in mixtures of the isotopic solvents H_2O and D_2O provides a tool for resolving contributions to the total isotope effect from multiple sites. Isotope effects in H_2O and D_2O mixtures can be described by the general form of the Gross-Butler equation (Equation 1.2), which represents the isotope effect arises from a combination of pronounced isotope effect at a few sites (i.e., these sites have ∅ values that are quite different than unity), and from a Z-effect (i.e. these sites have ∅ values that are very close to unity individually but has an aggregate isotope effect as a whole):[104]

$$k_n = k_0 \left[\frac{\prod_{i=1}^{x}(1-n+n\emptyset_{Ti})}{\prod_{i=1}^{x}(1-n+n\emptyset_{Ri})}\right] Z^n \qquad (1.2)$$

where k_0 is the kinetic rate constant in protic solution, k_n is the kinetic rate constant in a solution containing a mole fraction of D_2O of *n*, x is the number of hydrogenic sites in the reactant or transition state, $\emptyset_{Ti}$ and $\emptyset_{Ri}$ are the isotopic fractionation factors for hydrogenic site in the transition- and reactant-state, respectively. And *Z* is given by Equation 1.3:[105]

$$Z = \exp\left[-\gamma\left(1-\emptyset_{T,Z}\right)+\mu\left(1-\emptyset_{R,Z}\right)\right] \quad (1.3)$$

Z^n reflects the *Z*-effect, or the solvent isotope effect that arises from small contributions at a large number of identical hydrogenic sites. These large number of hydrogenic sites can occur either only in the transition-state ($\emptyset_{R,Z}=1, \emptyset_{T,Z}\neq 1$), the reactant-state ($\emptyset_{T,Z}=1, \emptyset_{,R,Z}\neq 1$), or from a combination in the reactant- and transition-states).[104] μ and γ are the number of hydrogenic sites in the reactant- and transition-state from *Z*-sites, respectively.[105] Note that when $Z = 1$ then

$\emptyset_{R,Z} = \emptyset_{T,Z} = 1$ and there are no *Z*-sites that contribute to the isotope effect. When $Z > 1$, then the Z-sites contribute an inverse isotope effect, and when $Z < 1$ then *Z*-sites contribute a normal isotope effect.[105]

In our case, the pronounced isotope effect occurs at a single hydrogenic site involved in step (iii) in Figure 2.3a in the main text, thus, Equation 1.2 reduces to:

$$k_n = k_0 \left(\frac{1-n+n\emptyset_T}{1-n+n\emptyset_R}\right) Z^n \qquad (1.4)$$

If we assume that the reactant-state fractionation factor $\emptyset_R$ for the hydrogen attached to the oxygen of CO_2 molecule is unity,[106] then Equation 1.4 becomes:

$$k_n = k_0 \, (1 - n + n\emptyset) Z^n \qquad (1.5)$$

Where $\emptyset$ is the isotopic fractionation factor for hydrogenic site involved in step (iii) in Fig. 3a (in main text) in the transition-state. Combining Equation 1.5 and equation ($\text{KIE} = \frac{k_\text{H}}{k_\text{D}} = \frac{j_\text{H}}{j_\text{D}}$) produce equation:

$$j_n = j_0 \, (1 - n + n\emptyset) Z^n \qquad (1.6)$$

In general, one can assess the number of protons involved in a reaction by the form/shape of a plot of k_n against n (Figure 1.6). For example, a dome-shaped curve derives from a combination of a primary kinetic isotope effect in the rate-determining step with aggregate inverse KIE arises from a series of hydrogenic sites (Z sites) where each individual KIE is very small. A linear shaped curve usually generated by systems involving one hydrogenic site.[104]

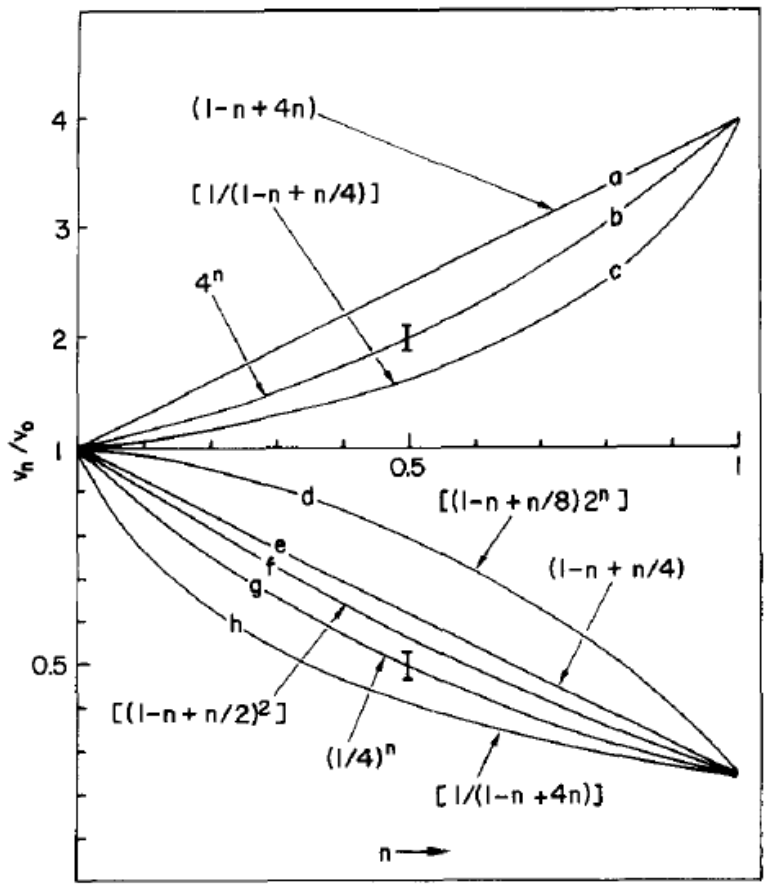

Figure 1.6 Some typical shapes of proton inventory curves. Reprint with permission from Ref.[106]

1.6.3 *In situ* XAS

In order to understand the structure and coordination environment of electrocatalysts, and particularly how they change during electrochemical reaction processes, *in situ* characterizations are necessary to capture the real structures of catalysts that only exist in intermediate reaction states to elucidate the reaction mechanism. *In situ* electorchemical X-ray absorption spectroscopy (XAS) has been developed to investigate electronic structure, oxidation states, local coordination environment under electrochemical reaction conditions.

XAS is an element-specific technique, and the XAS spectra of the element of interest is characterized by an abrupt increase in absorption at a specific X-ray photon energy which is related to the binding energy of the absorbing element.[107, 108] The sharp increases in absorption are called absorption edges, and correspond to the energy required to eject a core electron into the LUMO or to the continuum thus producing a photoelectron. The absorption discontinuity is known as the K-edge, when the photoelectron originates from a 1s core level, and an L-edge when the ionization is from a 2s or 2p electron. The edge regions in the XAS spectra are found to a wealth of information as shown in Figure 1.7a. When the X-ray photon energy is not very strong, it leads to a flat region or background, and some unfavored transitions such as 1s-3d transition will appear as a pre-edge peak. Once the X-ray photon energies are strong enough to eject a core electron into the LUMO (Figure 1.7b), this specific X-ray energy is strongly absorbed by the element, resulting a sudden discontinuous increase in absorption, which is referred to as X-ray absorption near edge structure (XANES) (Figure 1.7a).[108, 109] The XANES spectra provide detailed information about the oxidation state and coordination environment of the metal atoms.[110] With the further increase in X-ray energies, the core electrons are ejected into the continuum state (Figure 1.7b), forming the outgoing and scattering wave interference with neighboring atoms (Figure 1.7c). The constructive and deconstructive interferences caused by those waves form the oscillation above the edge, which are often referred to as extended X-ray absorption fine structure (EXAFS) (Figure 1.7a). The EXAFS region is sensitive to the radial distribution of electron density around the absorbing element and is used for determining local atomic structure such as bond length and coordination number.[107, 109] In this thesis, XANES is used in Chapter 3 to determine the coordination environment and oxidation states change of the catalysts, and the relatively low concentration of Co in the samples precluded measurement of EXAFS spectra.

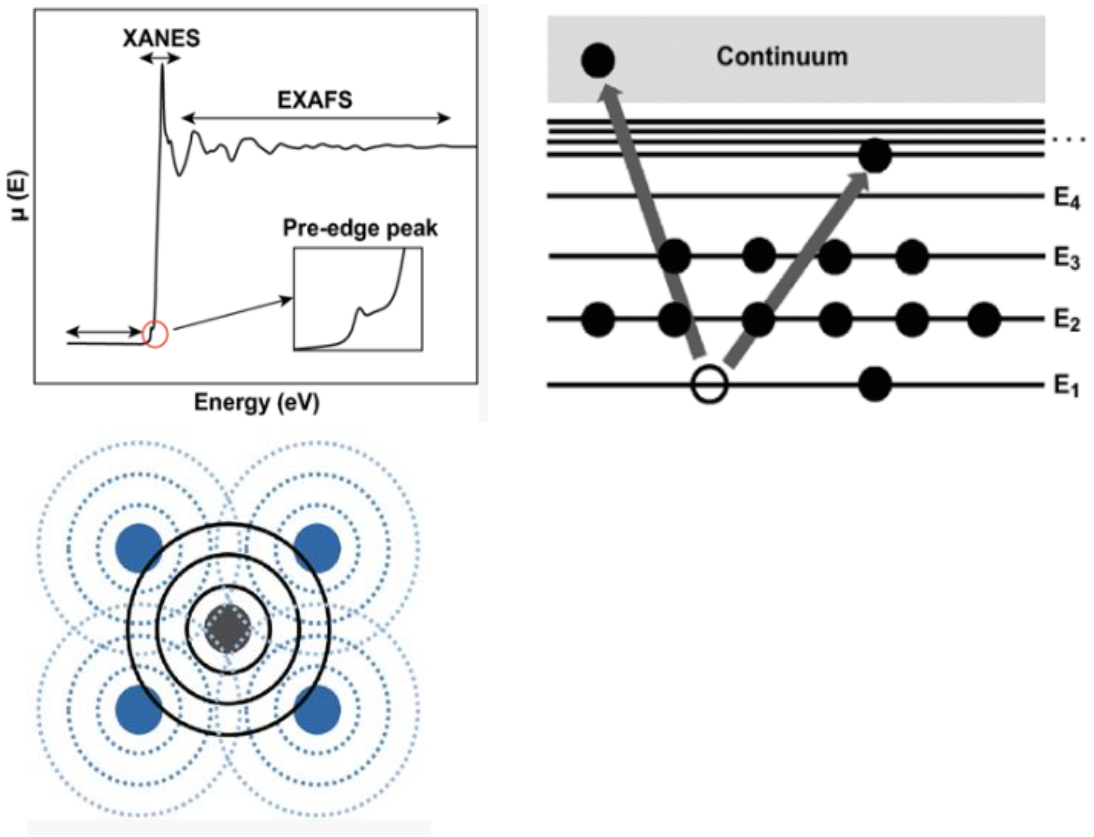

Figure 1.7 a, Schematic of XAS spectrum including pre-edge, XANES, and EXAFS regions. **b,** Schematic of the X-ray absorption process and electron excited process, the black circle is electrons. **c,** Schematic of interference pattern creating by the outgoing (solid black lines) and reflected (dashed blue lines) photoelectron waves between absorbing atom (gray) and its nearest atoms (purple). Adapted with permission from Ref.[109]

In research described in Chapter 3, the fluorescence mode is used for XAS signal collection, which measures the emitted X-ray fluorescence. The intensity of the fluorescence is proportional to the absorption of the X-ray by the element. Fluorescence mode can be used to measure dilute, non-homogeneous samples.[109] In a custom-designed *in situ* electrochemical cell setup (Figure 1.8),[111] the cell holds three electrodes (CE: counter electrode, RE: reference electrode, WE: working electrode) in the electrolyte solution. It also has gas inlet and outlet for sparking the gas reactants such as CO2 and O2. The catalysts are coated on carbon paper, and emerged in the electrolyte solution. The front window is glued by Kapton film to prevent any

leakage of electrolyte.[111] The thickness of the cell where X-ray passes is usually designed to be very thin to prevent the attenuation of the X-ray by the electrolyte.

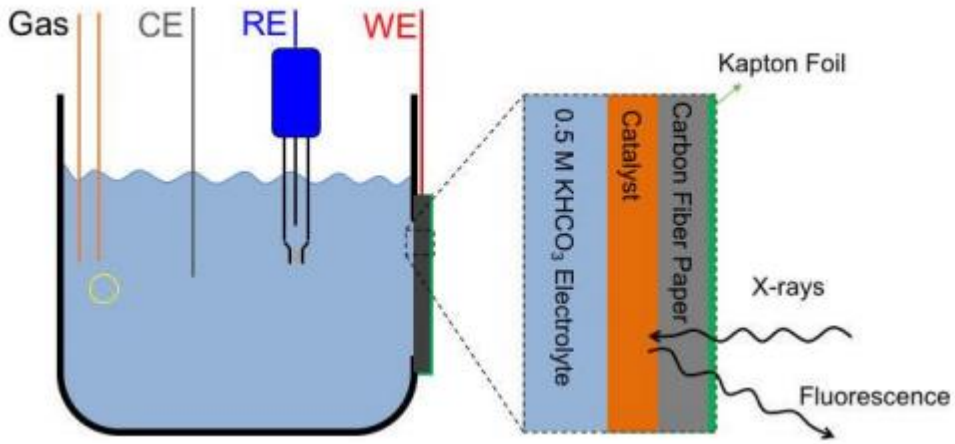

Figure 1.8 Schematic structure of the electrochemical cell used for *in situ* XAS experiments. Adapted with permission from Ref.[111]

1.7 References

1. N. S. Lewis, G. Crabtree, A. J. Nozik, M. R. Wasielewski and A. P. Alivisatos, *Basic Research Needs for Solar Energy Utilization*, Department of Energy, 2005.
2. E. E. Benson, C. P. Kubiak, A. J. Sathrum and J. M. Smieja, *Chem. Soc. Rev.*, 2009, **38**, 89-99.
3. D. T. Whipple and P. J. A. Kenis, *The Journal of Physical Chemistry Letters*, 2010, **1**, 3451-3458.
4. C. M. Friend, M. S. Sanford and H. D. Abruña, *Catalytic Chemistry Workshop on Defining Critical Directions for the Future*, National Science Foundation, 2011.
5. J. L. Inglis, B. J. MacLean, M. T. Pryce and J. G. Vos, *Coord. Chem. Rev.*, 2012, **256**, 2571-2600.
6. A. M. Appel, J. E. Bercaw, A. B. Bocarsly, H. Dobbek, D. L. DuBois, M. Dupuis, J. G. Ferry, E. Fujita, R. Hille, P. J. A. Kenis, C. A. Kerfeld, R. H. Morris, C. H. F. Peden, A. R. Portis, S. W. Ragsdale, T. B. Rauchfuss, J. N. H. Reek, L. C. Seefeldt, R. K. Thauer and G. L. Waldrop, *Chem. Rev.*, 2013, **113**, 6621-6658.
7. J. Qiao, Y. Liu, F. Hong and J. Zhang, *Chem. Soc. Rev.*, 2014, **43**, 631-675.
8. S. Berardi, S. Drouet, L. Francas, C. Gimbert-Surinach, M. Guttentag, C. Richmond, T. Stoll and A. Llobet, *Chem. Soc. Rev.*, 2014, **43**, 7501-7519.
9. D. G. Nocera, *Acc. Chem. Res.*, 2017, **50**, 616-619.
10. T. P. Senftle and E. A. Carter, *Acc. Chem. Res.*, 2017, **50**, 472-475.
11. A. J. Martín, G. O. Larrazábal and J. Pérez-Ramírez, *Green Chemistry*, 2015, **17**, 5114-5130.
12. D. Pletcher, *Electrochem. Commun.*, 2015, **61**, 97-101.
13. K. P. Kuhl, E. R. Cave, D. N. Abram and T. F. Jaramillo, *Energy Environ. Sci.*, 2012, **5**, 7050-7059.
14. Y. Hori, in *Modern Aspects of Electrochemistry*, ed. C. G. Vayemas, Springer, New York, 2008, vol. 42, pp. 89-189.
15. C. W. Li and M. W. Kanan, *J. Am. Chem. Soc.*, 2012, **134**, 7231-7234.
16. K. J. P. Schouten, E. Pérez Gallent and M. T. M. Koper, *J. Electroanal. Chem.*, 2014, **716**, 53-57.
17. M. Gattrell, N. Gupta and A. Co, *J. Electroanal. Chem.*, 2006, **594**, 1-19.
18. T. Hatsukade, K. P. Kuhl, E. R. Cave, D. N. Abram and T. F. Jaramillo, *Phys. Chem. Chem. Phys.*, 2014, **16**, 13814-13819.
19. Y. Hori, K. Kikuchi and S. Suzuki, *Chem. Lett.*, 1985, **14**, 1695-1698.
20. F. R. Keene, C. Creutz and N. Sutin, *Coord. Chem. Rev.*, 1985, **64**, 247-260.
21. I. Taniguchi, in *Modern Aspects of Electrochemistry No. 20*, eds. J. O. M. Bockris, R. E. White and B. E. Conway, Springer US, Boston, MA, 1989, DOI: 10.1007/978-1-4684-8762-6_5, pp. 327-400.
22. J. P. Collin and J. P. Sauvage, *Coord. Chem. Rev.*, 1989, **93**, 245-268.
23. J. Costamagna, G. Ferraudi, J. Canales and J. Vargas, *Coord. Chem. Rev.*, 1996, **148**, 221-248.
24. M. Jitaru, D. A. Lowy, M. Toma, B. C. Toma and L. Oniciu, *J. Appl. Electrochem.*, 1997, **27**, 875-889.
25. T. Sakakura, J.-C. Choi and H. Yasuda, *Chem. Rev.*, 2007, **107**, 2365-2387.
26. Y. Hori, in *Handbook of Fuel Cells*, John Wiley & Sons, Ltd, 2010, DOI: 10.1002/9780470974001.f207055.
27. C. D. Windle and R. N. Perutz, *Coord. Chem. Rev.*, 2012, **256**, 2562-2570.
28. C. Finn, S. Schnittger, L. J. Yellowlees and J. B. Love, *Chem. Commun.*, 2012, **48**, 1392-1399.

29. C. Costentin, M. Robert and J.-M. Saveant, *Chem. Soc. Rev.*, 2013, **42**, 2423-2436.
30. Y. Oh and X. Hu, *Chem. Soc. Rev.*, 2013, **42**, 2253-2261.
31. K. A. Grice and C. P. Kubiak, in *Adv. Inorg. Chem.*, eds. M. Aresta and R. van Eldik, Academic Press, 2014, vol. 66, pp. 163-188.
32. X. Lu, D. Y. C. Leung, H. Wang, M. K. H. Leung and J. Xuan, *ChemElectroChem*, 2014, **1**, 836-849.
33. R. J. Lim, M. Xie, M. A. Sk, J.-M. Lee, A. Fisher, X. Wang and K. H. Lim, *Catal. Today*, 2014, **233**, 169-180.
34. A. Goeppert, M. Czaun, J.-P. Jones, G. K. Surya Prakash and G. A. Olah, *Chem. Soc. Rev.*, 2014, DOI: 10.1039/c4cs00122b.
35. K. Kobayashi and K. Tanaka, *Phys. Chem. Chem. Phys.*, 2014, **16**, 2240-2250.
36. P. Kang, Z. Chen, M. Brookhart and T. J. Meyer, *Top. Catal.*, 2015, **58**, 30-45.
37. R. Kortlever, J. Shen, K. J. P. Schouten, F. Calle-Vallejo and M. T. M. Koper, *The Journal of Physical Chemistry Letters*, 2015, **6**, 4073-4082.
38. B. Kumar, J. P. Brian, V. Atla, S. Kumari, K. A. Bertram, R. T. White and J. M. Spurgeon, *Catal. Today*, 2016, **270**, 19-30.
39. N. Elgrishi, M. B. Chambers, X. Wang and M. Fontecave, *Chem. Soc. Rev.*, 2017, **46**, 761-796.
40. J. Bonin, A. Maurin and M. Robert, *Coord. Chem. Rev.*, 2017, **334**, 184-198.
41. J.-W. Wang, W.-J. Liu, D.-C. Zhong and T.-B. Lu, *Coord. Chem. Rev.*, 2019, **378**, 237-261.
42. A. Taheri and L. A. Berben, *Chem. Commun.*, 2016, **52**, 1768-1777.
43. S. Lee and J. Lee, *ChemSusChem*, 2016, **9**, 333-344.
44. Q. Lu and F. Jiao, *Nano Energy*, 2016, **29**, 439-456.
45. N. Yang, S. R. Waldvogel and X. Jiang, *ACS Appl. Mater. Interfaces*, 2016, **8**, 28357-28371.
46. G. Zhao, X. Huang, X. Wang and X. Wang, *J. Mater. Chem. A*, 2017, **5**, 21625-21649.
47. F. N. Al-Rowaili, A. Jamal, M. S. Ba Shammakh and A. Rana, *ACS Sustain. Chem. Eng.*, 2018, **6**, 15895-15914.
48. W. Yang, K. Dastafkan, C. Jia and C. Zhao, *Advanced Materials Technologies*, 2018, **3**, 1700377.
49. J. Wu, T. Sharifi, Y. Gao, T. Zhang and P. M. Ajayan, *Adv. Mater.*, 2019, **31**, 1804257.
50. A. Parkin, J. Seravalli, K. A. Vincent, S. W. Ragsdale and F. A. Armstrong, *J. Am. Chem. Soc.*, 2007, **129**, 10328-10329.
51. M. J. Dewar and D. M. Storch, *Proc. Natl. Acad. Sci. U.S.A.*, 1985, **82**, 2225-2229.
52. A. Warshel, P. K. Sharma, M. Kato, Y. Xiang, H. Liu and M. H. M. Olsson, *Chem. Rev.*, 2006, **106**, 3210-3235.
53. J. H. Jeoung and H. Dobbek, *Science*, 2007, **318**, 1461-1464.
54. J. Fesseler, J.-H. Jeoung and H. Dobbek, *Angew. Chem. Int. Ed.*, 2015, **54**, 8560-8564.
55. S. Takenaka, H. Miyamoto, Y. Utsunomiya, H. Matsune and M. Kishida, *J. Phys. Chem. C*, 2014, **118**, 774-783.
56. S. Takenaka, N. Susuki, H. Miyamoto, E. Tanabe, H. Matsune and M. Kishida, *J. Catal.*, 2011, **279**, 381-388.
57. S. Takenaka and M. Kishida, *Catalysis Surveys from Asia*, 2013, **17**, 71-84.
58. N. H. Khdary and M. A. Ghanem, *RSC Adv.*, 2014, **4**, 50114-50122.
59. N. Y. Labrador, E. L. Songcuan, C. De Silva, H. Chen, S. J. Kurdziel, R. K. Ramachandran, C. Detavernier and D. V. Esposito, *ACS Catalysis*, 2018, **8**, 1767-1778.
60. X. Chen, Z.-Z. Lin, M. Ju and L.-X. Guo, *Appl. Surf. Sci.*, 2019, **479**, 685-692.

61. D. V. Esposito, *ACS Catalysis*, 2018, **8**, 457-465.
62. S. Ponnurangam, I. V. Chernyshova and P. Somasundaran, *Adv. Colloid Interface Sci.*, 2017, **244**, 184-198.
63. R. Aydın, H. Ö. Doğan and F. Köleli, *Applied Catalysis B: Environmental*, 2013, **140-141**, 478-482.
64. F. Li, S.-F. Zhao, L. Chen, A. Khan, D. R. MacFarlane and J. Zhang, *Energy & Environmental Science*, 2016, **9**, 216-223.
65. S. Zhang, P. Kang, S. Ubnoske, M. K. Brennaman, N. Song, R. L. House, J. T. Glass and T. J. Meyer, *J. Am. Chem. Soc.*, 2014, **136**, 7845-7848.
66. S. Ponnurangam, C. M. Yun and I. V. Chernyshova, *ChemElectroChem*, 2016, **3**, 74-82.
67. E. Szaniawska, I. A. Rutkowska, M. Frik, A. Wadas, E. Seta, A. Krogul-Sobczak, K. Rajeshwar and P. J. Kulesza, *Electrochim. Acta*, 2018, **265**, 400-410.
68. R. Schrebler, P. Cury, C. Suárez, E. Muñoz, H. Gómez and R. Córdova, *J. Electroanal. Chem.*, 2002, **533**, 167-175.
69. A. A. Oughli, A. Ruff, N. P. Boralugodage, P. Rodríguez-Maciá, N. Plumeré, W. Lubitz, W. J. Shaw, W. Schuhmann and O. Rüdiger, *Nat. Commun.*, 2018, **9**, 864.
70. E. L. Clark, J. Resasco, A. Landers, J. Lin, L.-T. Chung, A. Walton, C. Hahn, T. F. Jaramillo and A. T. Bell, *ACS Catal.*, 2018, **8**, 6560-6570.
71. Y. Hori, H. Konishi, T. Futamura, A. Murata, O. Koga, H. Sakurai and K. Oguma, *Electrochim. Acta*, 2005, **50**, 5354-5369.
72. A. Wuttig and Y. Surendranath, *ACS Catalysis*, 2015, **5**, 4479-4484.
73. N. Han, Y. Wang, L. Ma, J. Wen, J. Li, H. Zheng, K. Nie, X. Wang, F. Zhao, Y. Li, J. Fan, J. Zhong, T. Wu, D. J. Miller, J. Lu, S.-T. Lee and Y. Li, *Chem*, 2017, **3**, 652-664.
74. D. Quezada, J. Honores, M. García, F. Armijo and M. Isaacs, *New J. Chem.*, 2014, **38**, 3606-3612.
75. J. Honores, M. J. Aguirre and M. Isaacs, *J. Coord. Chem.*, 2014, **67**, 4090-4100.
76. A. Deronzier, in *Conducting Polymers and Polymer Electrolytes*, American Chemical Society, 2002, vol. 832, ch. 11, pp. 141-153.
77. S. Sato, T. Arai and T. Morikawa, *Nanotechnology*, 2017, **29**, 034001.
78. H. C. Hurrell, A. L. Mogstad, D. A. Usifer, K. T. Potts and H. D. Abruna, *Inorg. Chem.*, 1989, **28**, 1080-1084.
79. M. García, M. J. Aguirre, G. Canzi, C. P. Kubiak, M. Ohlbaum and M. Isaacs, *Electrochim. Acta*, 2014, **115**, 146-154.
80. P. Dreyse, J. Honores, D. Quezada and M. Isaacs, *ChemSusChem*, 2015, **8**, 3897-3904.
81. M. Bakir, B. P. Sullivan, S. G. MacKay, R. W. Linton and T. J. Meyer, *Chem. Mater.*, 1996, **8**, 2461-2467.
82. S. Zhang, P. Kang, M. Bakir, A. M. Lapides, C. J. Dares and T. J. Meyer, *Proc. Natl. Acad. Sci. U.S.A*, 2015, **112**, 15809.
83. M. D. Porosoff and J. G. Chen, *J. Catal.*, 2013, **301**, 30-37.
84. A. A. Peterson and J. K. Nørskov, *The Journal of Physical Chemistry Letters*, 2012, **3**, 251-258.
85. C. Arana, M. Keshavarz, K. T. Potts and H. D. Abruña, *Inorg. Chim. Acta*, 1994, **225**, 285-295.
86. J. A. Ramos Sende, C. R. Arana, L. Hernandez, K. T. Potts, M. Keshevarz-K and H. D. Abruna, *Inorg. Chem.*, 1995, **34**, 3339-3348.

87. T. Yoshida, T. Iida, T. Shirasagi, R.-J. Lin and M. Kaneko, *J. Electroanal. Chem.*, 1993, **344**, 355-362.
88. T. Yoshida, K. Kamato, M. Tsukamoto, T. Iida, D. Schlettwein, D. Wöhrle and M. Kaneko, *J. Electroanal. Chem.*, 1995, **385**, 209-225.
89. T. Abe, T. Yoshida, S. Tokita, F. Taguchi, H. Imaya and M. Kaneko, *J. Electroanal. Chem.*, 1996, **412**, 125-132.
90. W. W. Kramer and C. C. L. McCrory, *Chem. Sci.*, 2016, **7**, 2506-2515.
91. Y. Y. Birdja, R. E. Vos, T. A. Wezendonk, L. Jiang, F. Kapteijn and M. T. M. Koper, *ACS Catal.*, 2018, **8**, 4420-4428.
92. Y. Liu and C. C. L. McCrory, *Nat. Commun.*, 2019, **10**, 1683.
93. S. Samanta, P. K. Das, S. Chatterjee and A. Dey, *J. Porphyrins Phthalocyanines*, 2015, **19**, 92-108.
94. R. Cao, R. Thapa, H. Kim, X. Xu, M. Gyu Kim, Q. Li, N. Park, M. Liu and J. Cho, *Nat. Commun.*, 2013, **4**, 2076.
95. T. Atoguchi, A. Aramata, A. Kazusaka and M. Enyo, *J. Electroanal. Chem. Interfacial Electrochem.*, 1991, **318**, 309-320.
96. H. Aga, A. Aramata and Y. Hisaeda, *J. Electroanal. Chem.*, 1997, **437**, 111-118.
97. R. L. Shook and A. S. Borovik, *Inorg. Chem.*, 2010, **49**, 3646-3660.
98. S. A. Cook and A. S. Borovik, *Acc. Chem. Res.*, 2015, **48**, 2407-2414.
99. C.-Y. Yeh, C. J. Chang and D. G. Nocera, *J. Am. Chem. Soc.*, 2001, **123**, 1513-1514.
100. C. K. Chang, Y. Liang, G. Aviles and S.-M. Peng, *J. Am. Chem. Soc.*, 1995, **117**, 4191-4192.
101. C. M. Moore and N. K. Szymczak, *Chem. Sci.*, 2015, **6**, 3373-3377.
102. T. E. DeCoursey and V. V. Cherny, *The Journal of General Physiology*, 1997, **109**, 415.
103. N. S. Punekar, in *ENZYMES: Catalysis, Kinetics and Mechanisms*, ed. N. S. Punekar, Springer Singapore, Singapore, 2018, DOI: 10.1007/978-981-13-0785-0_27, pp. 287-299.
104. A. Kohen and H. H. Limbach, *Isotope effects in chemistry and biology*, cRc Press, Boca Raton, 2005.
105. R. L. Schowen, *J. Labelled Compd. Radiopharm.*, 2007, **50**, 1052-1062.
106. K. Venkatasubban and R. L. Schowen, *Crit. Rev. Biochem.*, 1984, **17**, 1-44.
107. J. E. Penner-Hahn, in *eLS*, 2005, DOI: 10.1038/npg.els.0002984.
108. J. Yano and V. K. Yachandra, *Photosynth. Res.*, 2009, **102**, 241.
109. M. Wang, L. Árnadóttir, Z. J. Xu and Z. Feng, *Nano-Micro Letters*, 2019, **11**, 47.
110. D. C. Koningsberger, *X-ray absorption: principles, applications, techniques of EXAFS, SEXAFS, and XANES*, John Wiley and Sons, United States, 1988.
111. Z. Weng, Y. Wu, M. Wang, J. Jiang, K. Yang, S. Huo, X.-F. Wang, Q. Ma, G. W. Brudvig, V. S. Batista, Y. Liang, Z. Feng and H. Wang, *Nat. Commun.*, 2018, **9**, 415.

Chapter 2: Modulating the Mechanism of Electrocatalytic CO_2 Reduction by Cobalt Phthalocyanine through Polymer Coordination and Encapsulation

2.1 Preface

This chapter presents the study of electrocatalytic CO_2 reduction by polymer encapsulated molecular cobalt complex, and is an expansion of previous work.[1-3] In this study, a strategy has been developed to examine mechanistic implications of primary- and outer-coordination sphere effects on the CO_2 reduction activity by polymer encapsulated cobalt complex composites. This chapter of my dissertation is derived from manuscript as originally published in *Nature Communications*.[1] I was the primary author on the manuscript upon which this chapter is based, and I was responsible for all electrochemical sample preparations, measurements, and analysis as well as the writing and preparation of the manuscript. Dr. Charles McCrory provided significant insight and expertise in electroanalytical techniques and analysis, and reviewed and revised the manuscript.

[1] From "Modulating the mechanism of electrocatalytic CO_2 reduction by cobalt phthalocyanine through polymer coordination and encapsulation" by Yingshuo Liu, et al, 2019, *Nature Communications*, 10, 1683. Copyright [2019] by Springer Nature. Reprinted with permission.

2.2 Abstract

The selective and efficient electrochemical reduction of CO_2 to single products is crucial for solar fuels development. Encapsulating molecular catalysts such as cobalt phthalocyanine within coordination polymers such as poly-4-vinylpyridine leads to dramatically increased activity and selectivity for CO_2 reduction. In this study, we use a combination of kinetic isotope effect and proton inventory studies to explain the observed increase in activity and selectivity upon polymer encapsulation. We provide evidence that axial-coordination from the pyridyl moieties in poly-4-vinylpyridine to the cobalt phthalocyanine complex changes the rate-determining step in the CO_2 reduction mechanism accounting for the increased activity in catalyst-polymer composite. Moreover, we show that proton delivery to the cobalt center within the polymer is controlled by a proton relay mechanism that inhibits competitive hydrogen evolution. These mechanistic findings provide design strategies for selective CO_2 reduction electrocatalysts and serve as a model for understanding the catalytic mechanism of related heterogeneous systems.

2.3 Introduction

The selective electrochemical conversion of CO_2 to value-added products in the CO_2 reduction reaction (CO_2RR) offers a promising approach for the recycling of CO_2 into value-added products and the storage of intermittent energy sources as chemical fuels.[4-7] State-of-the-art polycrystalline Cu catalysts produce useful products such as methanol, but do so non-selectively and form a variety of other gaseous and liquid products including H_2 from competitive H^+ or water reduction.[8-11] Materials such as planar polycrystalline Au[12] and Ag foils[13] and some metal-doped nitrogenated carbon materials (MNCs) with M-N_4 porphyrin-like active sites[14-17] are more selective for CO_2 reduction to single C-containing products, primarily CO, but these systems still suffer from competitive H_2 evolution reaction (HER). For instance, planar polycrystalline Ag catalysts selectively reduce CO_2 to CO with > 90% Faradaic efficiency at -1.1 V vs RHE, but that selectivity drops to 60% Faradaic efficiency due to competitive H_2 evolution when the potential changes by 0.2 V in either direction.[13] Similar potential-dependence on product distribution is seen for various MNC materials.[15, 17, 18] Therefore, the discovery of systems that preferentially promote selective CO_2 reduction to single products with high activity while suppressing (HER) is critically important for the realization of selective electrochemical CO_2 reduction.

Our research approach is to encapsulate molecular catalysts within coordinating polymers to promote selective CO_2 reduction. By encapsulating the molecular catalysts within the coordinating polymers, we are able to not only control H^+ and CO_2 delivery to the catalyst centers, but also tune catalytic activity through primary-, secondary-, and outer-coordination sphere effects. These polymer-catalyst composite systems are inspired by enzymatic systems such as NiFe carbon monoxide dehydrogenase and FeFe hydrogenase where fast catalytic activity and high product

selectivity are achieved by carefully controlling the primary-, secondary-, and outer-coordination spheres of the enzyme's active site.[19-21]

Our initial studies focused on encapsulating cobalt phthalocyanine (CoPc) within the coordinating polymer poly-4-vinylpyridine (P4VP).[1] When adsorbed onto graphite electrodes without a polymer binder, CoPc by itself is a non-selective CO_2RR catalyst that shows only modest activity for CO_2 reduction to CO in aqueous citrate and phosphate solutions accompanied by significant co-generation of H_2 from the competitive HER.[1-3, 22] Previous studies have also shown that incorporation of CoPc within P4VP adsorbed onto graphite electrodes results in increased activity and selectivity for CO_2 reduction over competitive HER compared to the parent CoPc complex.[1-3] It has been postulated that the enhanced activity and selectivity is due to three synergistic effects: 1) axial-coordination of pyridyl to the Co center in the primary-coordination sphere increasing the catalyst's nucleophilicity for CO_2 binding, 2) H-bonding interactions in the secondary-coordination sphere that stabilize reactive CO_2 intermediates, and 3) control of proton delivery through the use of the pyridyl residues within the polymer as proton relays in the outer-coordination sphere (Figure 2.1).[1, 3] We propose that axial coordination of pyridyl facilitates CO_2 coordination and thus changes the rate-determining step of CO_2RR by five-coordinate CoPc-P4VP systems to a step subsequent to CO_2 coordination. In addition, the increase in selectivity for CO_2RR over HER could be due to a weak acid effect from the protonated pyridyl residues on the proton relays. The protonated pyridyl residues in the polymer may be acidic enough to act as a proton relay and donor to the activated CO_2 intermediate, but proton transport through the polymer may be sluggish enough to suppress HER activity. Other recent studies have supported the assertion that synergy between catalyst and polymer effects is required for increased activity and selectivity in polymer-encapsulated systems.[23-31]

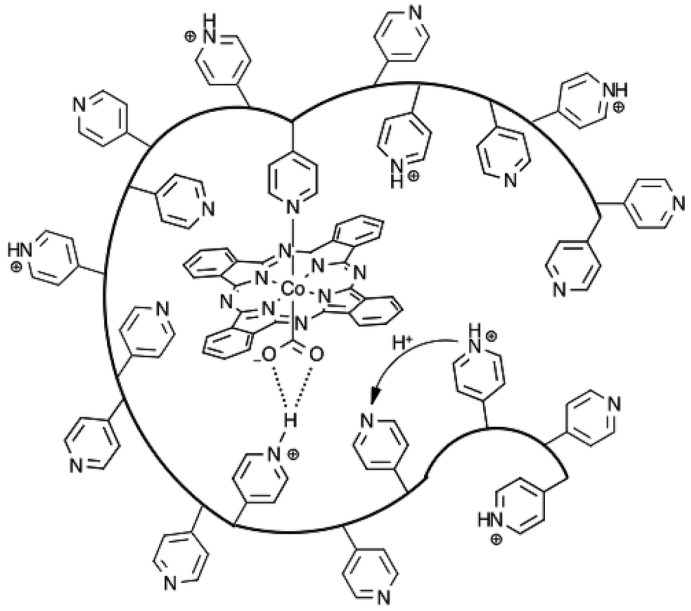

Figure 2.1 An illustration of a cobalt phthalocyanine (CoPc) encapsulated within a hydrophobic poly-4-vinylpyridine (P4VP) membrane highlighting the postulated primary-, secondary-, and outer-coordination sphere effects.[1] [W. W. Kramer and C. C. L. McCrory, *Chem. Sci.*, 2016, **7**, 2506] – Published by the Royal Society of Chemistry.

In this work, we expand upon our previous studies of the CoPc-polymer systems to explicitly investigate the mechanistic implications of primary- and outer-coordination sphere effects on the CO_2 reduction activity by catalyst-polymer composites. To do this, we use a combination of kinetic isotope effect (KIE) measurements and proton inventory studies to determine both the involvement of protons in the rate-determining step of the catalytic mechanism and the mechanism of H^+ transport through the polymer chain as we systematically alter the nature of the CoPc-polymer interactions. We observe a difference in the measured KIE for the four-coordinate CoPc systems (such as CoPc and CoPc-P2VP) compared to the five-coordinate systems (such as CoPc(py) and CoPc-P4VP) that is consistent with a change in the rate-determining step of the mechanism from CO_2 binding step to a subsequent protonation of the coordinated CO_2 intermediate. In addition, using proton inventory studies—a technique that is used in enzymology to study the kinetics of proton delivery to enzymatic active centers based on the attenuation of

kinetic rates as a function of fractional solvent deuteration[32-35]—we show that proton-transport to the Co active site in CoPc-P4VP and related systems is controlled by proton relays in the polymer rather than diffusion through the film. Thus, we provide direct experimental evidence that proton relays in the outer-coordination sphere of the catalyst for the CoPc-P4VP play an important role in promoting selective catalytic activity as has been suggested for other synthetic molecular and enzymatic systems.[36, 37] We believe this work is among the first examples of extending proton inventory studies from traditional enzymological systems to electrocatalytic studies in synthetic molecular-based assemblies.[38] Our studies help us to better understand the CO_2 reduction mechanism of polymer-encapsulated catalysts for comparison to related MNC and planar metal catalyst systems and more generally provides a strategy to probe fundamental catalytic mechanism of CO_2 reduction by molecular assemblies using KIE and proton inventory measurements.

2.4 Results

2.4.1 Surface Immobilized Catalysts and Catalyst-Polymer Systems

To determine both the involvement of protons in the rate-determining step of the catalytic mechanism and the mechanism of H^+ transport through the polymer chain, we use a combination of kinetic isotope effect (KIE) measurements and proton inventory studies on different catalytic systems as we systematically alter the nature of the CoPc-polymer interactions (Figure 2.2). All catalysts and catalyst-polymer composite systems studied were surface-immobilized by drop-casting a catalyst film directly onto edge-plane graphite (EPG) disk electrodes and drying at 70 ºC as described in the Supplementary Methods section in the Appendix chapter. For each system, plots of peak area as a function of scan rate for the non-catalytic $[CoPc]^+/[CoPc]$ peak are linear (Figure A.1–Figure A.14) which is consistent with a surface-immobilized species. The Co loading of each system was calculated to be 2.19×10^{-9} mol cm^{-2} based on the deposition procedures and this was confirmed by dissolving the catalyst film from the surface into 1 M HNO_3 aqueous solution and then measuring the concentration in the resulting solution with ICP-MS (Table A.1).

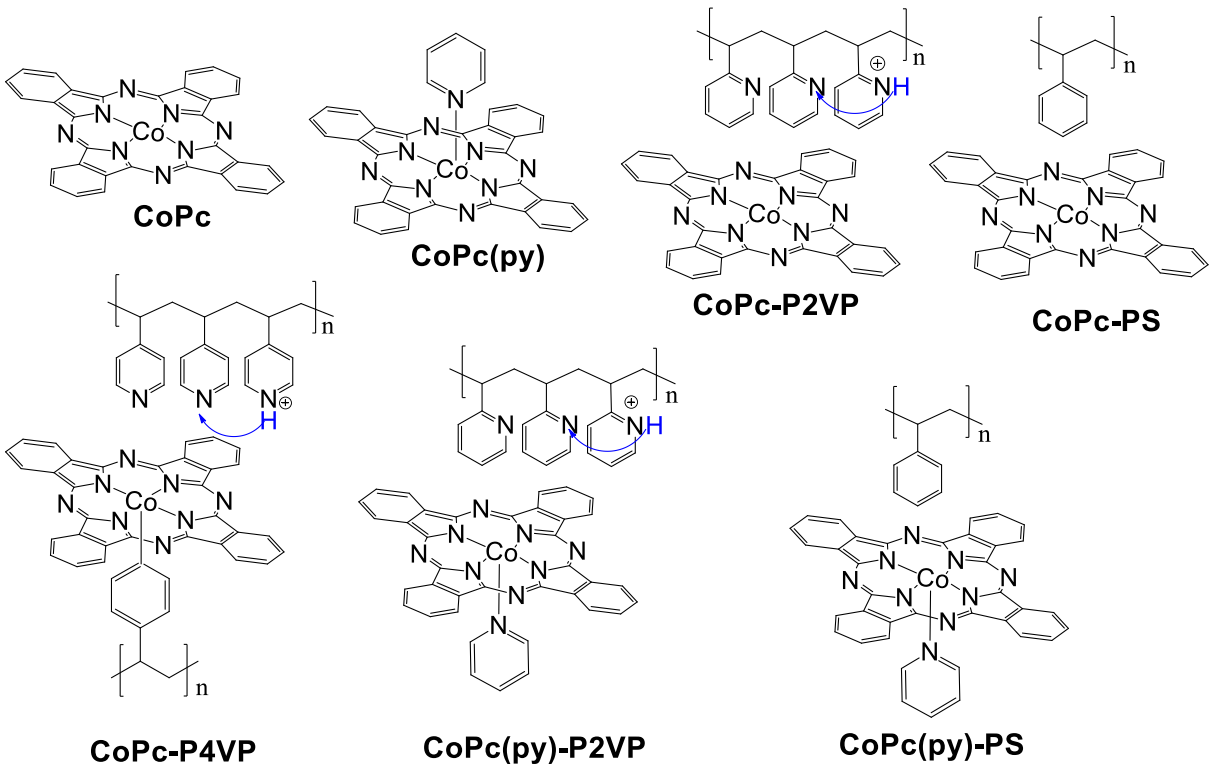

Figure 2.2 Catalyst and polymer-catalyst composite systems investigated in this work along with their postulated coordination environment and proton relays.

2.4.2 Proposed CO_2RR Mechanisms by CoPc

The exact mechanism for electrocatalytic CO_2 reduction by CoPc remains a point of discussion within the community. Based on previously reported experimental evidence, a proposed mechanism for CO_2 reduction by CoPc with the competitive HER pathway is shown in Figure 2.3a.[2, 3] In the proposed mechanism, CoPc is first reduced to $[CoPc]^-$ followed by protonation of the complex (presumably on the Pc ring) to form [CoPcH] and a second reduction to produce $[CoPcH]^-$. Here, there is a branch in the mechanism where $[CoPcH]^-$ can either react with H^+ to evolve H_2 and regenerate the CoPc starting material in step (iv), or $[CoPcH]^-$ can react with CO_2 to form a CO_2 adduct in step (i) that, upon subsequent protonation in step (iii), generates CO.[2, 3] This mechanism is consistent with previous results for CoPc and CoPc-P4VP in phosphate

solutions which show the onset of catalytic activity occurs at the second reduction event in the voltammogram.[1, 2] However, our recent electrochemical study of CoPc in DMSO solutions suggest that under conditions of low H^+ activity, a third reduction event is required for catalytic turnover of CO_2RR (see Figure A.15). This is consistent with a previous spectroelectrochemical studies in organic systems under CO_2, which suggests that further reduction of the [CoPc-CO] adduct is required to release CO and re-enter the catalytic cycle at $[CoPc]^-$ (Figure 2.3b).[3] Alternatively, recent reports of CO_2 reduction by adsorbed CoPc in bicarbonate solutions have suggested that CO_2 coordination may occur at the 1 e^- reduced species,[39] and this pathway has been further supported by a recent Tafel analysis and DFT studies (Figure 2.3c).[40] Although we cannot distinguish between the three mechanisms, all support our postulate that promotion of CO_2 reduction over competitive H_2 evolution can be achieved by either a) facilitating CO_2-coordination or b) controlling H^+ delivery to the active site to inhibit the competitive H_2 evolution pathway. In addition, all three pathways are consistent with our KIE and proton inventory studies discussed below. The mechanistic discussions in the manuscript will focus on the mechanism shown in Figure 2.3a because it is the mechanism that has been proposed to operate under our reaction conditions.

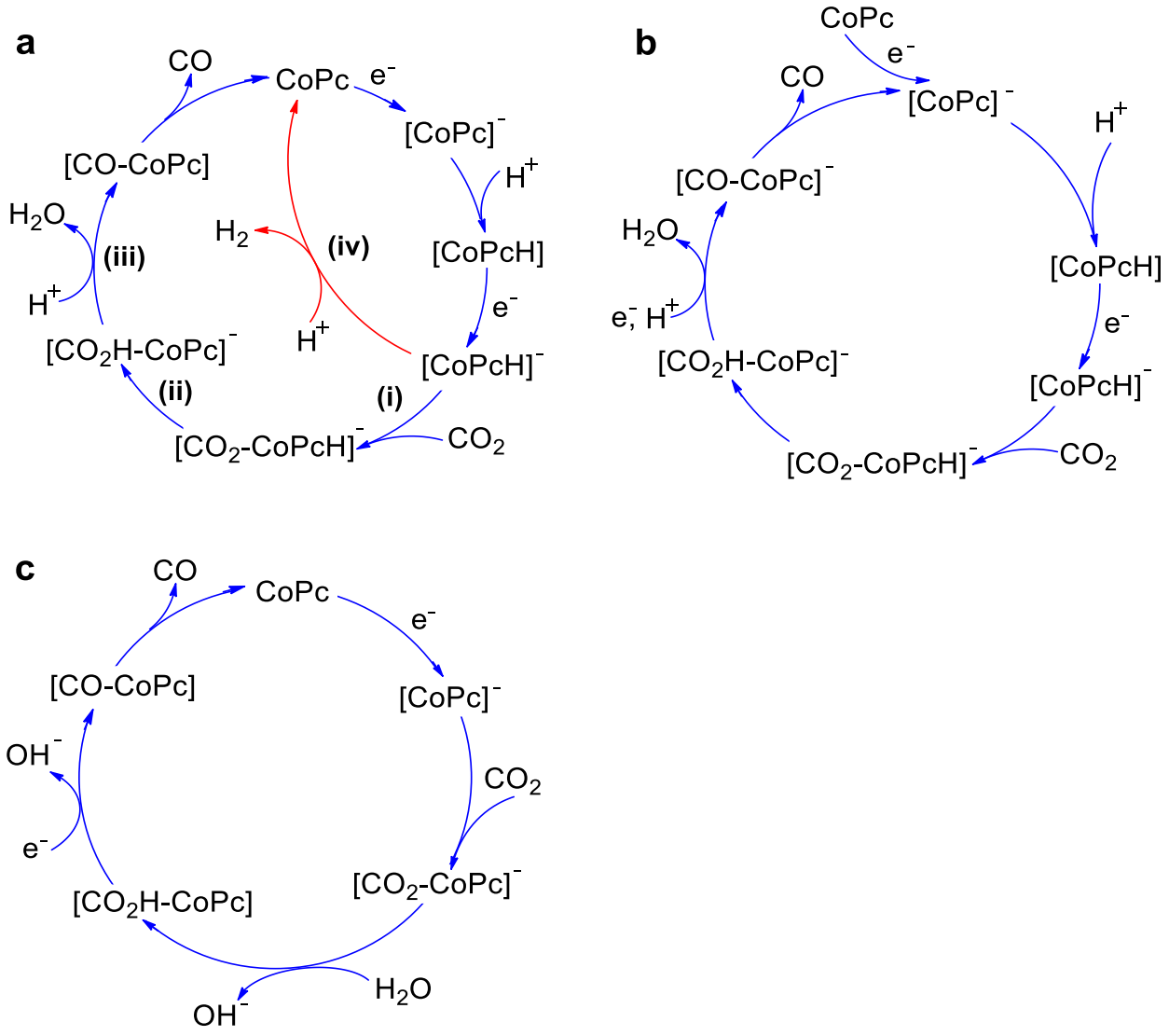

Figure 2.3 Proposed CO_2 reduction mechanisms of CoPc in this work and other proposed mechanisms. a, A proposed mechanism for CO_2 reduction by CoPc showing pathway for competitive H_2 generation.[2, 3, 22] Note that we do not assign individual oxidation states to the Co center and instead refer to the overall charge on the entire complex. Reported molecular orbital calculations of CoPc suggest that the first reduction may be a metal-centered reduction of $Co^{II}Pc$ to $Co^{I}Pc$ followed by a second ligand-based reduction.[41] Other proposed CO_2 reduction by CoPc in **b,** organic solutions[3] and **c,** low concentration bicarbonate buffer in aqueous solution.[39, 40]

2.4.3 Kinetic Isotope Effect Studies

Kinetic isotope effect (KIE) studies were conducted to investigate the influence of axial ligand coordination to CoPc on the CO_2RR mechanism. The magnitude of kinetic isotope effect is

given by Equation 2.1, where j_H is the electrocatalytic current density measured in the protic solution and j_D is the electrocatalytic current density measured in the deuterated solution:

$$\mathbf{KIE} = \frac{\boldsymbol{j_H}}{\boldsymbol{j_D}} \qquad (2.1)$$

Note that Equation 2.1 assumes that the electrochemical reaction rate is directly proportional to the measured current density which is generally expected for a reaction occurring at a surface-immobilized species.[42-44] However, Equation 2.1 is valid for determining KIE only for systems in which the Faradaic efficiency, ε, is the same for an electrocatalytic reaction conducted in protic and deuterated solvent. To confirm that the Faradaic efficiency for CO production does not change as the electrolyte is changed from a protic solution to a deuterated solution, we conducted 2-h controlled potential electrolyses (CPE) measurements in sealed electrochemical cell and measured the Faradaic efficiencies for CO and H_2/D_2 (Figure 2.4a, Table A.2) for each system. In general, the Faradaic efficiencies for a given system do not change as we change from a protic electrolyte to a deuterated electrolyte, validating our use of Equation 2.1 for determining the KIE. Note that longer-term 8-h CPE measurements show equivalent Faradaic efficiency and minimal loss of activity suggesting the catalyst systems investigated in this study are relatively stable under the reaction conditions (see Table A.3 and Figure A.16).

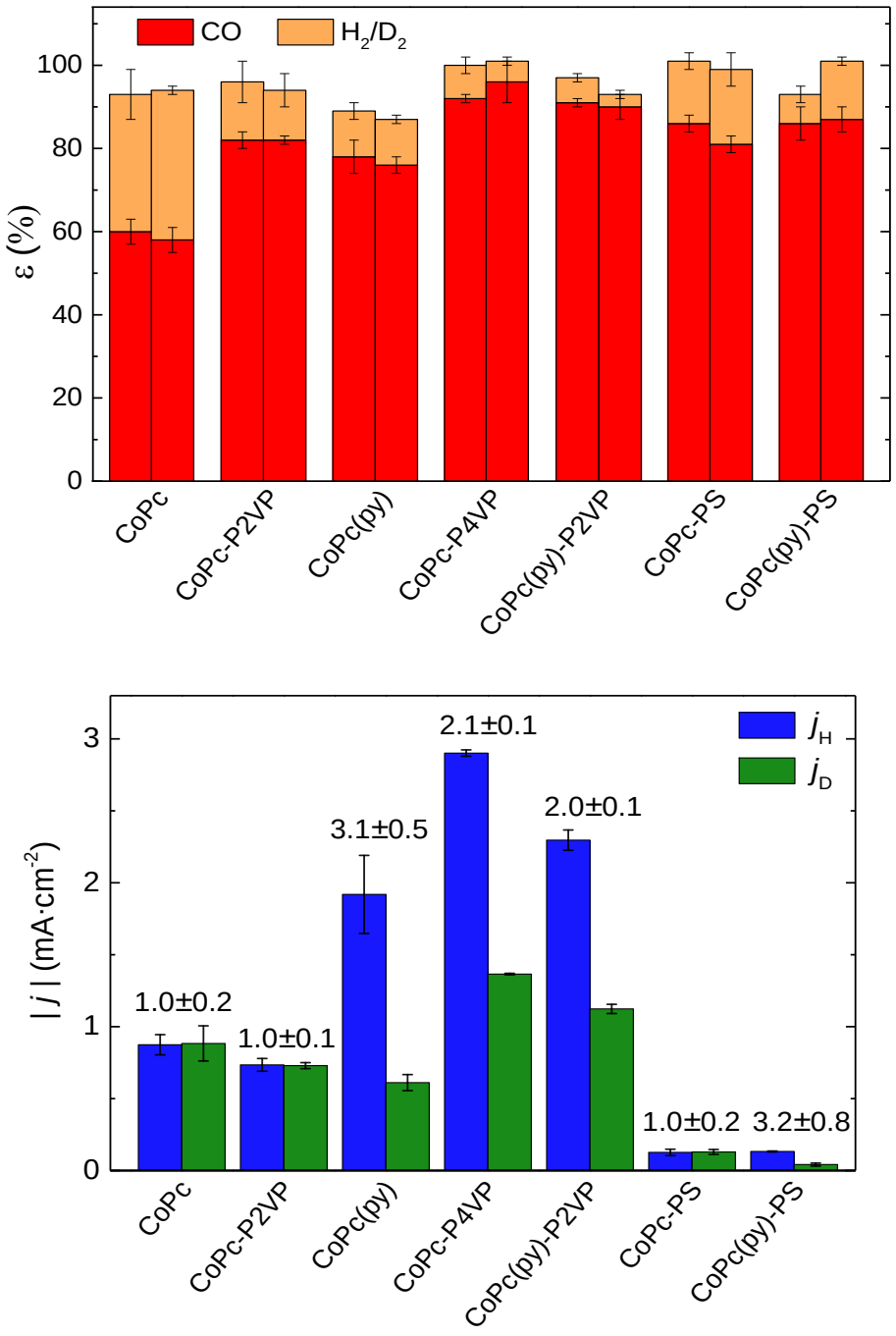

Figure 2.4 CO_2 reduction performance in protic and deuterated solutions. a, Faradaic efficiencies (ε) of 2-h controlled potential electrolyses at -1.25 V vs. SCE for H_2/D_2 (orange) and CO (red) in protic electrolyte (left bar), and in deuterated electrolyte (right bar). **b,** Measured current densities at -1.25 V vs. SCE in protic electrolyte (blue bar) and deuterated electrolyte (green bar) for each of the systems shown in Fig. 2. Kinetic isotope effect values are listed above the bars and also summarized in Table 1. All reported values are averages from 3 or more independent measurements, and all errors are given as standard deviations.

In general, a KIE > 1 suggests that a proton transfer event is present in the rate-determining step of the mechanism, whereas a KIE $\approx$ 1 suggests no involvement of a formal proton-transfer event in the rate-determining step.[32, 45-47] Thus, evaluation of the KIE for the adsorbed CoPc parent complex and our modified CoPc systems can provide information regarding the rate-determining step in the proposed electrocatalytic CO_2RR mechanism shown in Figure 2.3a. To determine the KIE for our systems, we measured the electrocatalytic current for CO_2RR both in pH 5 phosphate solution and in pD 5 deuterated phosphate solution using 2-min rotating disk chronoamperometric (CA) step measurements at -1.25 V vs. SCE and a rotation rate of 1600 rpm (representative CA measurements for each system investigated are shown in Figure A.17–Figure A.27). The measured current densities and KIE values are reported in Figure 2.4b, and all the KIE study results for CO_2RR are summarized in Table 1. Note that ICP-MS measurements show no difference in Co loading on samples measured pre-CA measurements and identically-prepared samples measured post-CA measurements (Table A.1). This suggests there is no loss of Co during the electrolyses.

Table 2.1 Activity and Faradaic Efficiency (ε) Measurements for Catalysts in Protic and Deuterated Solutions, and Determined Kinetic Isotope Effects

Catalyst	$j_{H,D}$ ($mA \cdot cm^{-2}$)	$TOF_{CO\ H,D}$ [d] (s^{-1})	$\varepsilon_{CO,H}$ (%)	$\varepsilon_{CO,D}$ (%)	KIE	Proton Inventory Parameters	
						ϕ	Z
CoPc	(H)[b] -0.87 ± 0.07 (D)[c] -0.88 ± 0.12	(H) 1.24 ± 0.12 (D) 1.21 ± 0.18	60 ± 3	58 ± 3	1.0 ± 0.2	—[e]	—[e]
CoPc-P2VP[a]	(H) -0.73 ± 0.04 (D) -0.73 ± 0.02	(H) 1.42 ± 0.09 (D) 1.41 ± 0.04	82 ± 2	82 ± 1	1.0 ± 0.1	—[e]	—[e]
CoPc(py)	(H) -1.92 ± 0.27 (D) -0.61 ± 0.06	(H) 3.54 ± 0.53 (D) 1.10 ± 0.11	78 ± 4	76 ± 2	3.1 ± 0.5	0.30 ± 0.01	1.02 ± 0.02
CoPc-P4VP[a]	(H) -2.90 ± 0.02 (D) -1.37 ± 0.01	(H) 6.31 ± 0.08 (D) 3.10 ± 0.16	92 ± 1	96 ± 5	2.1 ± 0.1	0.29 ± 0.01	1.65 ± 0.03
CoPc(py)-P2VP[a]	(H) -2.30 ± 0.07 (D) -1.12 ± 0.03	(H) 4.94 ± 0.16 (D) 2.39 ± 0.10	91 ± 1	90 ± 3	2.0 ± 0.1	0.30 ± 0.01	1.60 ± 0.03
CoPc-PS[a]	(H) -0.13 ± 0.02 (D) -0.13 ± 0.02	(H) 0.26 ± 0.04 (D) 0.25 ± 0.03	86 ± 2	81 ± 2	1.0 ± 0.2	—[e]	—[e]
CoPc(py)-PS[a]	(H) -0.13 ± 0.00 (D) -0.04 ± 0.01	(H) 0.27 ± 0.01 (D) 0.09 ± 0.02	86 ± 4	87 ± 3	3.2 ± 0.8	0.29 ± 0.02	1.06 ± 0.04

All measurements conducted at -1.25 V vs. SCE. All reported values are averages from 3 or more independent measurements, and all errors are given as standard deviations. [a] Polymer-catalyst composite films were drop-cast from deposition solutions containing 1 % w/v polymer. [b] Under protic condition. [c] Under deuterated condition. [d] Turnover frequencies for CO (TOF_{CO}) is calculated from both the overall activity measured in rotating disk chronoamperometric (CA) steps at -1.25 V vs. SCE and the faradaic efficiencies measured in 2-h controlled potential electrolyses (CPE) (see A.1.3 for detailed explanation). [e] Not measured.

The parent four-coordinate CoPc system shows no kinetic isotope effect in our studies which is consistent with a rate-determining CO_2-coordination step (Figure 2.3a, step (i)). In the case of CoPc-P2VP, the CoPc complex is immobilized within a non-coordinating P2VP polymer

and again, there is no observed KIE. In contrast, the five-coordinate CoPc(py) system shows a KIE = 3.1, suggesting a rate-determining proton transfer step in the mechanism (Figure 2.3a, step (iii)). When the five-coordinate CoPc(py) is immobilized within P2VP to form CoPc(py)-P2VP, we observe a smaller KIE = 2.0 compared to the CoPc(py). Likewise, when CoPc is immobilized within the coordinating polymer P4VP to form CoPc-P4VP, the observed KIE = 2.1. The results with CoPc-P4VP and CoPc(py)-P2VP suggest that the polyvinylpyridine polymers are moderating the extent of KIE for the five-coordinate CoPc systems with axially-ligated pyridyls. To confirm that this moderation of the KIE is specifically due to the polyvinylpyridine and not a general effect with any polymer, we measured the KIE of CoPc and CoPc(py) immobilized within polystyrene (PS) where we expect no primary-, secondary-, or outer-coordination sphere effects within the polymer. In this case, CoPc-PS shows no kinetic isotope effect, and CoPc(py)-PS has KIE = 3.2, which is nearly identical to that of CoPc(py) without an encapsulating polymer. Based on the larger KIE for CoPc(py) compared to that of CoPc-P4VP and CoPc(py)-P2VP, we hypothesize that the pyridyls in the polymer act as a proton relay controlling proton delivery to the CoPc active sites, and these sites have a weak inverse isotope effect (KIE < 1) that, in aggregate, moderates the overall KIE for CoPc-P4VP and CoPc(py)-P2VP compared to CoPc(py). Note that additional KIE measurements for HER for the catalysts studied in this work were also measured, and these results are summarized in Table A.4.

To confirm the 5-coordinate nature of the CoPc in CoPc(py), CoPc-P4VP, CoPc(py)-P2VP, CoPc(py)-PS, and CoPc(py)-P2VP, we conducted UV-Vis spectroscopy studies of drop-cast films to characterize the coordination environment (see A.1.3 for more details). As shown in Figure A.28, the Q band of CoPc in PS and P2VP near 669 nm is red shifted to 674 nm in UV-vis absorption spectrum of CoPc in P4VP, and CoPc(py) in PS and P2VP films. Similarly, red shifted

Q band is also exhibited in the UV-vis spectrum of CoPc(py) as prepared and CoPc(py) as synthesized solutions by about 5 nm compared to that of CoPc (Figure A.29). These red shifts are consistent with that the Q band of metalloporphyrin-like complexes will red shift when there is an electron-donating ligand coordinated axially with the central metal ions,[48, 49] which is attributed to the π to π^* transition of the ligands, leading to the more negative electron density of the central metal ions.[50] Thus, the UV-vis spectrum suggests the formation of the axial coordination of CoPc in CoPc-P4VP, CoPc(py)-PS, CoPc(py)-P2VP samples, and CoPc(py) solutions.

Recent studies have suggested that CoPc aggregation occurs when adsorbed to carbon surfaces at high loadings[39, 51, 52] and that this aggregation limits the number of exposed active sites and, therefore, the measured per-CoPc TOFs.[39] To explore whether aggregation influences the results of our mechanistic studies, we explored the loading dependence of CoPc both physisorbed onto EPG and within the P4VP films over 4 orders of magnitude between 2.19×10^{-11} mol cm^{-2} to 2.19×10^{-7} mol cm^{-2} (results are summarized in Figure A.30–Figure A.32). We observe a decrease in TOF for CO_2RR with increasing CoPc loading consistent with previous aggregation studies.[39] However, importantly the KIE results are statistically equivalent at every loading suggesting that aggregation does not change the rate-determining step in the catalytic mechanism (see Table A.5).

To confirm that the observed increased activity for CoPc(py) and CoPc-P4VP compared to the parent CoPc system is not due to electrocatalytic CO_2 reduction by free pyridine in solution or the polymer pyridyl group, we conducted several control experiments. We have previously conducted CPE experiments with CoPc-modified carbon electrodes in CO_2-saturated pH 5 phosphate solutions containing 0.05 mM dissolved pyridine and saw no significant change in the CO_2RR activity and Faradaic efficiency compared to analogous studies with no dissolved pyridine present.[1] In addition, we have previously shown that CPE experiments conducted with EPG

electrodes coated with P4VP (with no CoPc) showed negligible CO_2RR activity.[1] In this work we have conducted additional CPE experiments with bare EPG electrodes in CO_2-saturated pH 5 phosphate solutions containing 0.05 mM dissolved pyridine and see negligible activity for CO_2RR (Table A.6). Based on the results of these control experiments, we conclude that the enhanced current we observe in the CoPc(py) and CoPc-P4VP systems is not due to direct electrocatalytic CO_2 reduction by free pyridine and/or the pyridyl moieties in the P4VP polymer.

2.4.4 Proton Inventory Studies

Although we invoke the existence of proton relays to help explain trends in catalyst selectivity and activity in the CoPc-P4VP and related systems, traditional KIE measurements are not sufficient to definitively argue for their existence. To provide further support for the existence of proton relays within our catalyst-polymer systems we have conducted electrochemical proton inventory studies. The proton inventory method is a technique that is used in enzymology to study the kinetics of proton delivery to enzymatic active centers in which the attenuation of a kinetic rate is measured as a function of the fractional concentration of D_2O in a mixed D_2O-H_2O solvent.[32-35] The method is particularly useful for resolving the number of exchangeable hydrogenic sites that contribute to the catalytic rate within a system.[53-55] The dependence of the rate attenuation on fractional deuteration of the electrolyte can be expressed with a modified Gross-Butler equation (Equation 2.2).

$$j_n = j_0(1 - n + n\phi)Z^n \qquad (2.2)$$

$$n = \frac{[D_2O]}{[D_2O]+[H_2O]} \qquad (2.3)$$

Here, the measured current density at a given fractional deuteration concentration *n* (Equation 2.3), j_0 is the measured current density in solutions with only protic electrolyte present, ϕ is the isotopic fractionation parameter which is related to the propensity for a hydrogenic site in the rate-determining step of the reaction to interact with D^+ compared to water, and *Z* is a parameter related to the aggregate isotope effect from multiple equivalent hydrogenic sites, called *Z*-sites, with individual weak isotope effects (see A.1.3 for an explanation of Equation 2.2).[33, 44, 53]

For all the systems investigated, the electrocatalytic current for CO_2RR was measured in partially deuterated phosphate solutions at pH/pD = 5 using 2-min rotating disk CA measurements at -1.25 V vs. SCE and a rotation rate of 1600 rpm. Partially deuterated phosphate solutions were prepared by mixing appropriate amounts of the pH 5 phosphate solution and pD 5 deuterated phosphate solution. In a plot of j_n/j_0 as a function of *n*, the shape of the resulting curve is dependent on the relative sizes of ϕ and *Z*. $Z > 1$ suggests there is an aggregate inverse isotope effect at the *Z*-sites, and $Z \approx 1$ suggests there are no *Z*-sites contributing to the observed kinetics (see section A.1.3 for further discussion of the *Z* parameter).[33, 44] A plot of j_n/j_0 as a function of *n* for CoPc-P4VP results in a non-linear dome-shaped response as shown in Figure 2.5a, and a fit of this curve to equation (2) results in $\phi \approx 0.3$ and $Z > 1$. Note that ϕ represents the isotopic fractionation factor of the hydrogenic site involved in step (iii) in Fig. 3a, and $\phi \approx 0.3$ is a typical fractionation factor for transition-state hydrogen bridges corresponding to hydrogen transfer reactions of small molecules.[53] These results are consistent with a normal isotope effect at a single hydrogenic site in the rate-determining step at the active site coupled with an aggregate inverse-isotope effect from the *Z*-sites (pyridyl sites on the polymer). Note that a weak inverse-isotope effect is a somewhat common phenomena for H^+ exchange reactions at weak bases such as pyridine.[53] The results of the CoPc-P4VP proton inventory studies support our hypothesis that

proton delivery to the active site is controlled by a polymer-based proton relay mechanism. Note that in our analysis we do not take into account contributions to the overall isotope effect from the expected H-bonding interactions between the P4VP polymer and reactive CO_2 intermediates (i.e. secondary-coordination sphere effects). This is because weak H-bonds tend to have negligible isotope effects with $\phi \sim 1$ and therefore do not typically contribute significantly to the overall isotope effect.[47]

In contrast to CoPc-P4VP, the activity of CoPc(py) shows a linear attenuation with increasing *n* confirming that without the encapsulating polymer only one hydrogenic site (the hydrogenic site involved in step (iii) in Figure 2.3a) is involved in the rate-determining step of the catalytic mechanism and there is no *Z*-effect (i.e. $Z \approx 1$). This is also consistent with the larger observed KIE = 3.1 for CoPc(py) compared to KIE = 2.1 for CoPc-P4VP, where the overall KIE is modulated by the inverse-isotope effects of the *Z*-sites. Note that CoPc(py)-P2VP with axially-coordinated pyridyls (Figure 2.5a) shows a response nearly identical to that of CoPc-P4VP with identical values of ϕ and *Z* (Table 2.1). Both the parent CoPc system (Figure 2.5a) and the CoPc-P2VP system (Figure 2.5a) show no attenuation of activity in the proton inventory studies as expected from our KIE measurements and consistent with a rate-limiting step (i) (Figure 2.3a) in the catalytic cycle for the parent system.

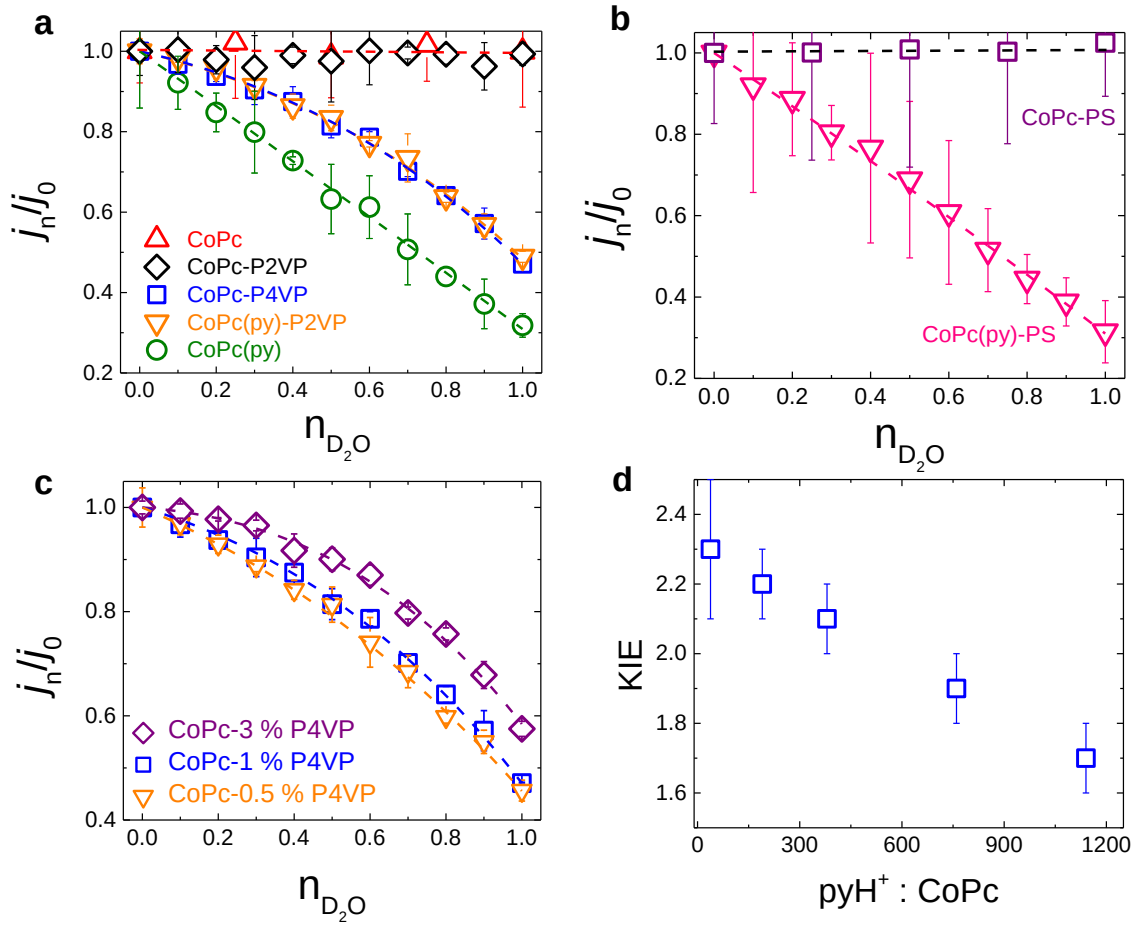

Figure 2.5 Proton Inventory Studies of CoPc and Related systems. a, Proton inventory studies of CO_2 reduction by CoPc (red triangles), CoPc-P2VP (black diamonds), CoPc-P4VP (blue squares), CoPc(py)-P2VP (orange triangles) and CoPc(py) (green circles). The red dashed line is the guide to the eye for CoPc and CoPc-P2VP (j_n = j_0 at every n measured), and the blue, orange and green dashed lines are fits to the data using Equation 2.2. The resulting values for ϕ and Z are shown in Table 2.1. Note that KIE =j_H/j_D. **b,** Proton inventory studies of CO_2 reduction by CoPc-PS (purple squares) and CoPc(py)-PS (pink triangles). The purple dashed line is the guide to the eye for CoPc-PS case (j_n = j_0 at every n measured), and the pink dashed line is a fit to the data using Equation 2.2. The resulting values for ϕ and Z are shown in Table 2.1 Note that KIE =j_H/j_D. **c,** Proton inventory studies of CO_2 reduction by CoPc-P4VP drop-cast from deposition solutions with different P4VP loadings: 0.5 % w/v (orange triangles), 1 % w/v (blue squares), and 3 % w/v (purple diamonds). The dashed lines are fits to the data by Equation 2.2 and the resulting values for ϕ and Z are shown in Table 2. **d,** KIE value decreases with increasing the pyH^+ : CoPc ratio in the polymer. All reported values are averages from 3 or more independent measurements, and all errors are given as standard deviations.

In order to confirm that the kinetic isotope effect originates from the proton channel along the partially protonated pyridyl residues rather the mass transport of protons through the polymer

membrane, proton inventory studies for CoPc and CoPc(py) encapsulated in PS were performed. CoPc-PS (Figure 2.5b) shows identical behavior to that of CoPc (Figure 2.5a), and CoPc(py)-PS (Fig. 5b) shows identical behavior to that of CoPc(py) (Figure 2.5a) for proton inventory studies. This suggests that the dome-shaped responses of CoPc-P4VP and CoPc(py)-P2VP are due to a specific proton relay effect imbued by the pyridyl moieties and not a general behavior of polymers without proton relays. Note that similar proton inventory behavior is shown in the catalytic systems in this study at other potentials investigated (see Figure A.33–Figure A.39).

2.4.5 Polymer Loading Dependence on KIE and *Z*

Our KIE and proton inventory studies provide strong evidence that pyridyls within the polyvinylpyridine polymers act as proton relays to control proton delivery to the CoPc active sites, and the weak-inverse isotope effect from the pyridyl moieties moderates the KIE for CoPc- P4VP compared to CoPc(py). Based on these observations, we postulate that increasing the ratio of pyridyl to CoPc within the polymer-composite film should lead to an increase in the number of *Z*-sites in the film, which in turn will decrease the overall observed KIE. To test this, we investigated the proton inventory behavior and KIE for CO_2RR by CoPc-P4VP prepared from deposition solutions with different polymer loadings and the results are summarized in Table 2.2. Proton inventory measurements of CoPc-P4VP (Figure 2.5c, Table 2.2) show an increase in the *Z*-value as the polymer loading (and py-to-Co ratio) increase as expected, and the measured KIE values decrease as the polymer loading increases (Figure 2.5d). These results are consistent with our previous observations regarding the existence of pyridyl-based proton relays with weak inverse isotope effects in the polyvinylpyridine polymers. Note that the CO_2RR activity slightly increases

with increasing P4VP loading. We postulate that this may be due to increased CO_2 partitioning within largely-hydrophobic polymer layer which may lead to higher overall catalytic activity.[2, 3]

Table 2.2 Results of Kinetic Isotope Effects and Proton Inventory Measurements for CoPc-P4VP with different P4VP loadings

P4VP (%)	py:CoPc[a]	pyH^+:CoPc[b]	$j_{H, D}$ ($mA \cdot cm^{-2}$)	$TOF_{CO\ H,D}$[e] (s^{-1})	KIE	Proton Inventory Parameters	
						ϕ	Z
0.1	190	38	(H)[c] -2.09 ± 0.06 (D)[d] -0.92 ± 0.06	(H) 4.39 ± 0.16 (D) 1.96 ± 0.13	2.3 ± 0.2	—[f]	—[f]
0.5	950	190	(H) -2.67 ± 0.10 (D) -1.22 ± 0.05	(H) 5.81 ± 0.29 (D) 2.59 ± 0.18	2.2 ± 0.1	0.31 ± 0.01	1.45 ± 0.03
1	1900	380	(H) -2.90 ± 0.02 (D) -1.37 ± 0.01	(H) 6.31 ± 0.08 (D) 3.10 ± 0.16	2.1 ± 0.1	0.29 ± 0.01	1.65 ± 0.03
2	3800	760	(H) -3.03 ± 0.09 (D) -1.60 ± 0.06	(H) 6.73 ± 0.29 (D) 3.36 ± 0.17	1.9 ± 0.1	—[f]	—[f]
3	5700	1140	(H) -3.17 ± 0.04 (D) -1.82 ± 0.05	(H) 6.96 ± 0.17 (D) 3.91 ± 0.13	1.7 ± 0.1	0.31 ± 0.01	1.89 ± 0.03

All measurements conducted at -1.25 V vs. SCE. All reported values are averages from 3 or more independent measurements, and all errors are given as standard deviations. aRatio of py to CoPc as determined by calculating the relative amount of P4VP and CoPc drop-cast on the EPG surface. bRatio of protonated pyH+ to CoPc assuming 20% of the pyridyl residues are protonated within the polymer at pH 5. cUnder protic condition. dUnder deuterated condition. eTurnover frequencies for CO (TOFCO) is calculated from both the overall activity measured in rotating disk chronoamperometric (CA) steps at -1.25 V vs. SCE and the faradaic efficiencies measured in 2-h controlled potential electrolyses (CPE) (see section A.1.3 for detailed explanation). fNot measured.

2.5 Discussion

We believe the experimental techniques applied in and the mechanistic insights derived from this work can serve as a model for understanding the catalytic mechanisms of related heterogeneous electrocatalysts. For example, previous studies of CO_2 reduction with CoPc adsorbed onto graphitic carbon show non-selective CO_2 reduction to CO with ε_{CO} ranging from ~ 40% to ~ 60% with appreciable competitive H_2 evolution,[1, 2, 22, 56] which is consistent with this study. However, recent reports show that CoPc adsorbed onto highly-oxygenated carbon nanotubes (CNTs) synthesized from high-temperature calcination of carbon-precursors in air selectively reduces CO_2 with ε_{CO} ~ 80−90 % at optimized potential, pH, and loading conditions.[40, 56, 57] It has been postulated that the π-π interactions between the CNTs and the macrocyclic CoPc complexes may explain the increased activity of CoPc and related systems when absorbed onto CNTs.[40, 56, 57] We propose that an additional reason for the increased activity of CoPc adsorbed onto CNTs may be axial-coordination of impurities in the CNTs structure, such as oxide- and hydroxyl-defect sites, with the adsorbed CoPc. These proposed axial interactions in the CoPc-CNT system are analogous to the axial-coordination of pyridine and P4VP to CoPc in our studies. Note that similar increases in activity for O_2 reduction by macrocyclic Co and Fe complexes adsorbed onto defect-rich carbon supports has been previously observed,[58-62] and was largely attributed to axial-coordination of the metal complexes to organic functional groups on the carbon surfaces.[59-62] While directly probing the nature of the CoPc-CNTs interactions is beyond the scope of our current study, we suggest that similar electrochemical KIE measurements to those conducted here can be used as a tool to determine the nature of the rate-determining step of CO_2 reduction by CoPc adsorbed onto CNTs and thereby determine the nature of the CoPc-CNTs interactions.

Perhaps one of the most-promising CO_2RR materials mechanistically related to the CoPc and CoPc-P4VP systems is MNC materials—extended graphitic structures with discrete M-N_4 porphyrin-like active sites.[17] Studies exploring the mechanism of low-overpotential CO_2 reduction at M-N_4 active sites suggest that rate-determining step is a decoupled proton-electron transfer event forming an M-CO_2H adduct via a process similar to step (i) and subsequent intramolecular H^+ transfer in step (ii) shown in Figure 2.3a.[15, 18] In addition, CO production has been shown to be pH independent at the M-N_4 site,[18] which is consistent with our observation that CoPc and CoPc-P2VP operate with the same TOF_{CO} despite the increase in local pH near the Co active site in CoPc-P2VP as evidenced by the decrease in competitive H_2 evolution for CoPc-P2VP compared to CoPc. The correlation between the mechanistic insights provided in previous studies for the MNC materials and our mechanistic observations for CoPc-P4VP and related systems suggest that the polymer-encapsulated CoPc materials may be a useful and easily-tunable model system that, in future studies, can be leveraged to provide further insight into the activity, selectivity and mechanism of CO_2 reduction by heterogeneous MNC materials.

2.6 Experimental

2.6.1 Electrolyte Solution Preparation and pH Measurements

All pH measurements were conducted with a Fisher Scientific Accumet AB200 pH meter with an Accumet pH/ATC Epoxy Body Combination Electrode calibrated with a three-point calibration curve at pH = 4.01, 7.00, and 10.01. For estimating pD, measurements were conducted in deuterated solvents using the pH meter and the pD was calculated by the following equation: $pD = pH_{meter\ reading} + 0.40$.[63, 64] pH 5 phosphate solutions were prepared from 0.1 M NaH_2PO_4 solutions adjusted to pH 5 by the addition of aqueous 1 M NaOH. pD 5 deuterated phosphate solutions were prepared by titrating 1.189 g D_3PO_4 (85 wt % solution) with 1.025 g NaOD (40 wt % solution) in ~ 100 mL D_2O to produce a 0.1 M NaD_2PO4 solution in D_2O, and then titrated with 1 M NaOD D_2O solution. Partially deuterated phosphate solutions were prepared by mixing appropriate amounts of the pH 5 phosphate solution and pD 5 deuterated phosphate solution.

2.6.2 Preparation of Modified Electrodes

All deposition solutions were prepared from DMF solutions containing 0.05 mM CoPc. The deposition solutions for polymer-encapsulated CoPc were prepared by dissolving the desired amount of polymer in the 0.05 mM CoPc/DMF solution. For the deposition of CoPc-P4VP films, the deposition solution contained 0.1-3 % w/v of P4VP in DMF solution (detailed preparation conditions are provided in A.1.3). In the case of CoPc-P4VP films, the py:Co ratio was determined by calculating the relative amount of pyridyl groups in P4VP and CoPc drop-cast on the EPG surface.

For the deposition solution of CoPc(py), a mixture of pyridine and DMF solution (19:1 DMF/pyridine) was used as the solvent in place of DMF. To confirm that the deposited film from

the above method was indeed CoPc(py), we also independently synthesized 5-coordinate CoPc(py) and confirmed it using elemental analysis (Table A.7). Drop-cast films prepared using our traditional method and the synthesized CoPc(py) showed analogous KIE and proton inventory results (see Figure A.40 and Table A.8), suggesting the prepared films are identical.

Prior to modification, 5 mm diameter edge plane graphite (EPG) disk electrodes (3.81 mm EPG disk encapsulated in epoxy, 0.114 cm^2 effective surface area, Pine Research Instrumentation) were manually polished with 600 grit SiC grinding paper (Buehler CarbiMet) followed by sonication in ultrapure water for ~ 1 min. Modified working electrodes were prepared by first drop-casting 5 μL deposition solution onto EPG electrode. The disks electrodes were then placed in a drying oven at ~ 70 °C for ~ 15 minutes to allow the solvent to evaporate.

2.6.3 Electrochemical Measurements

Electrochemical measurements were conducted using a Bio-Logic SP200 potentiostat/galvanostat, and data were recorded using the Bio-Logic EC-Lab software package. Reference electrodes were commercial saturated calomel electrodes (SCE, CH-Instruments) externally referenced to ferrocenecarboxylic acid in 0.2 M phosphate buffer at pH 7 (0.284 V vs. SCE),[65] and auxiliary electrodes were carbon rods (99.999 %, Strem Chemicals Inc.). Working electrodes were the modified EPG electrodes described previously. In all cases, the working electrode was separated from the auxiliary electrode by a Nafion membrane. Unless otherwise noted, all electrochemical measurements were conducted at least three times with independently prepared electrodes, all values reported are the averages of these repetitions, and all reported errors are standard deviations.

For rotating disk CA step measurements, the modified EPG working electrodes were mounted in a Pine Research Instrumentation E6-series Change Disk rotating disk electrode (RDE) assembly attached to an MSR rotator. CA measurements were conducted at 1600 rpm with 2-min potential steps from -1.00 V to -1.25 V vs. SCE at 0.05 V increments. The 1600 rpm rotation rate was meant to ensure steady-state delivery of substrate to our surface to allow for accurate comparisons of catalytic rates. Note that 1600 rpm does not imply kinetically-limiting conditions—mass transport to catalyst sites in non-uniform catalyst-polymer composite films is not governed by simple Koutecký-Levich kinetics.[66-68] Rotating disk CA measurements were conducted in a custom two-compartment glass cell (Figure A.41). The first compartment held the rotating disk working electrode and reference electrode in ~ 30 mL solution, and the second compartment held the auxiliary electrode in ~ 15 mL solution. The two compartments were separated by a Nafion cation exchange membrane. Both compartments were sparged with CO_2 for ~30 min prior to each set of measurements, and the headspace was blanketed with CO_2 during the measurements. The CO_2 used was first saturated with electrolyte solution by bubbling through a gas washing bottle filled with the same electrolyte solution used in the cell to minimize electrolyte evaporation in the cell during the course of the measurements. IR drop was compensated at 85 % through positive feedback using the Bio-Logic EC-Lab software. In general, our electrochemical cell for CA measurement had Ru = ∼100 Ω in pH 5 or pD 5 phosphate solution.

Controlled potential electrolyses (CPE) were conducted at room temperature in two custom, gas-tight, two-chamber U-cells (Figure A.42). The modified working electrode was held in a RDE internal hardware kit (Pine Research Instrumentation) and mounted into a custom PEEK sleeve. For the electrolysis measurements, the main chamber held the working electrode and an SCE reference electrode in ~ 25 mL of electrolyte, and the total headspace in the main chamber

was measured individually after each experiment, approximately 25 mL, by measuring the amount of water needed to refill the main chamber. The auxiliary chamber held the auxiliary carbon rod electrode in 15 mL electrolyte. The two chambers were separated with a Nafion cation exchange membrane. Prior to each experiment, both chambers were sparged with CO_2 for ~ 30 min and then the main chamber was sealed under CO_2 atmosphere**.** The uncompensated resistance of the cell was measured with a single-point high-frequency impedance measurement. In general, our electrochemical cell for CPE had Ru = ∼200 Ω in pH 5 or pD 5 phosphate solution.

2.6.4 Product Detection and Quantification

After CPE, gaseous and liquid samples were collected and analyzed using gas chromatography (GC) and high-performance liquid chromatography (HPLC), respectively. For gaseous samples, analysis was conducted using a Thermo Scientific Trace 1310 GC system with two analyzer channels for the detection of H_2 and C1-C2 products. A Pressure-Lok gas-tight syringe (10 mL, Valco VICI Precision Sampling, Inc.) was used to collect 5 mL aliquots from the main-chamber headspace of the cell, and each aliquot was injected directly into the 3 mL sample loop. Using a custom valve system, column configuration, and method provided by Thermo Scientific, gases were separated such that H_2 was detected on the first channel using an Ar carrier gas and thermal conductivity detector (TCD), and all other gases were detected on the second channel using a He carrier gas and a TCD. The GC system was calibrated using calibration gas mixtures (SCOTTY Specialty Gas) at H_2 = 0.02, 0.05, 0.5, and 1 % v/v, and CO = 0.02, 0.05, 0.5, 1, and 7 % v/v. An example chromatograph of a calibration mixture containing 0.05 % H_2, 0.05 % CO, and 99.9 % N_2, is shown in Figure A.43. Chromatographs were analyzed using the Chromeleon Console WorkStation software.

For liquid samples, 1 mL aliquots of post-electrolysis solutions were analyzed for liquid products such as formic acid using a Thermo Scientific UltiMate 3000 high-performance liquid chromatography (HPLC) system equipped with a refractive index detector (RFD), a 5 cm Thermo Scientific™ HyperREZ™ XP Carbohydrate H^+ LC guard column and a 30 cm Thermo Scientific™ HyperREZ™ XP Carbohydrate H^+ LC analytical column in series using a 5 mM H_2SO_4 aqueous mobile phase at a constant temperature of 50 °C. The detection limit of the HPLC for formic acid was determined to be 0.1 mM. In general, no formic acid was observed in the electrolyte solution after the electrolyses.

Faradaic efficiencies (ε) were determined by dividing the moles of each product detected by the total moles of electrons calculated from the amount of charge passed during the CPE as described in Equation 2.4:

$$\varepsilon = \frac{\frac{V_{HS}}{V} \times C \times 2F}{Q} \qquad (2.4)$$

Here, V_{HS} is the volume of the headspace in the main chamber of the cell (mL), V is the molar volume of gas at 25 °C and 1.0 atm (24.5 L mol^{-1}), C is the volume percent of product detected by GC (%), F is the Faraday constant (C mol^{-1}), and Q is the charge passed during the CPE measurement (C).

2.7 Conclusions

We have investigated the electrochemical CO_2RR mechanism for CoPc encapsulated in a coordinating polymer using a combination of kinetic isotope effect measurements and proton inventory studies. Specifically, KIE studies suggest that axial-coordination of pyridyl/pyridine to CoPc to form a putative five-coordinate species changes the rate-determining step of the catalytic mechanism from a CO_2-binding step (step (i), Figure 2.3a) in the case of CoPc to a subsequent protonation step (step (iii), Figure 2.3a) in the case of the five-coordinate species. The axially-coordinated pyridine/pyridyl can be either a discrete ligand (CoPc(py), CoPc(py)-P2VP, CoPc(py)-PS) or be attached to an encapsulating polymer (CoPc-P4VP). Moreover, our proton inventory studies strongly suggest that proton delivery to the CoPc active sites in the polyvinylpyridine-encapsulated systems is controlled by a polymer-based proton relay mechanism involving the pyridyl moieties. Our work here provides a strategy to modulate the catalytic activity of this class of catalyst-polymer composite systems by 1) controlling the extent of axial-coordination to the catalyst center and 2) controlling the fractional protonation of the polymer to modulate the nature and extent of the proton relays in the encapsulating polymer. The mechanistic insights for the CoPc-P4VP and related systems introduced in this work reinforce the findings of previous studies of catalytic mechanism at M-N_4 active sites in heterogeneous MNC materials. The systems and experimental techniques developed in this work will serve as a useful model for further probing catalytic activity and mechanisms in future MNCs and polymer-encapsulated catalyst materials which will facilitate the development of new, more-active electrocatalytic systems for selective CO_2 reduction.

2.8 References

1. W. W. Kramer and C. C. L. McCrory, *Chem. Sci.*, 2016, **7**, 2506-2515.
2. T. Yoshida, K. Kamato, M. Tsukamoto, T. Iida, D. Schlettwein, D. Wöhrle and M. Kaneko, *J. Electroanal. Chem.*, 1995, **385**, 209-225.
3. T. Abe, T. Yoshida, S. Tokita, F. Taguchi, H. Imaya and M. Kaneko, *J. Electroanal. Chem.*, 1996, **412**, 125-132.
4. E. E. Benson, C. P. Kubiak, A. J. Sathrum and J. M. Smieja, *Chem. Soc. Rev.*, 2009, **38**, 89-99.
5. J. L. Inglis, B. J. MacLean, M. T. Pryce and J. G. Vos, *Coord. Chem. Rev.*, 2012, **256**, 2571-2600.
6. D. G. Nocera, *Acc. Chem. Res.*, 2017, **50**, 616-619.
7. T. P. Senftle and E. A. Carter, *Acc. Chem. Res.*, 2017, **50**, 472-475.
8. K. P. Kuhl, E. R. Cave, D. N. Abram and T. F. Jaramillo, *Energy Environ. Sci.*, 2012, **5**, 7050-7059.
9. Y. Hori, in *Modern Aspects of Electrochemistry*, ed. C. G. Vayemas, Springer, New York, 2008, vol. 42, pp. 89-189.
10. M. Gattrell, N. Gupta and A. Co, *J. Electroanal. Chem.*, 2006, **594**, 1-19.
11. H. Ooka, M. C. Figueiredo and M. T. M. Koper, *Langmuir*, 2017, **33**, 9307-9313.
12. H. Yoshio, K. Katsuhei and S. Shin, *Chem. Lett.*, 1985, **14**, 1695-1698.
13. T. Hatsukade, K. P. Kuhl, E. R. Cave, D. N. Abram and T. F. Jaramillo, *Phys. Chem. Chem. Phys.*, 2014, **16**, 13814-13819.
14. A. S. Varela, N. Ranjbar Sahraie, J. Steinberg, W. Ju, H.-S. Oh and P. Strasser, *Angew. Chem. Int. Ed.*, 2015, **54**, 10758-10762.
15. W. Ju, A. Bagger, G.-P. Hao, A. S. Varela, I. Sinev, V. Bon, B. Roldan Cuenya, S. Kaskel, J. Rossmeisl and P. Strasser, *Nat. Commun.*, 2017, **8**, 944.
16. P. Su, K. Iwase, S. Nakanishi, K. Hashimoto and K. Kamiya, *Small*, 2016, **12**, 6083-6089.
17. A. S. Varela, W. Ju and P. Strasser, *Adv. Energy Mater.*, 2018, **8**, 1703614.
18. A. S. Varela, M. Kroschel, N. D. Leonard, W. Ju, J. Steinberg, A. Bagger, J. Rossmeisl and P. Strasser, *ACS Energy Lett.*, 2018, **3**, 812-817.
19. A. M. Appel, J. E. Bercaw, A. B. Bocarsly, H. Dobbek, D. L. DuBois, M. Dupuis, J. G. Ferry, E. Fujita, R. Hille, P. J. A. Kenis, C. A. Kerfeld, R. H. Morris, C. H. F. Peden, A. R. Portis, S. W. Ragsdale, T. B. Rauchfuss, J. N. H. Reek, L. C. Seefeldt, R. K. Thauer and G. L. Waldrop, *Chem. Rev.*, 2013, **113**, 6621-6658.
20. A. Parkin, J. Seravalli, K. A. Vincent, S. W. Ragsdale and F. A. Armstrong, *J. Am. Chem. Soc.*, 2007, **129**, 10328-10329.
21. J. Fesseler, J.-H. Jeoung and H. Dobbek, *Angew. Chem. Int. Ed.*, 2015, **54**, 8560-8564.
22. C. M. Lieber and N. S. Lewis, *J. Am. Chem. Soc.*, 1984, **106**, 5033-5034.
23. Y. Y. Birdja, R. E. Vos, T. A. Wezendonk, L. Jiang, F. Kapteijn and M. T. M. Koper, *ACS Catal.*, 2018, **8**, 4420-4428.
24. S. Ponnurangam, I. V. Chernyshova and P. Somasundaran, *Adv. Colloid Interface Sci.*, 2017, **244**, 184-198.
25. B. L. Wadsworth, D. Khusnutdinova and G. F. Moore, *J. Mater. Chem. A*, 2018, **6**, 21654-21665.
26. A. Krawicz, J. Yang, E. Anzenberg, J. Yano, I. D. Sharp and G. F. Moore, *J. Am. Chem. Soc.*, 2013, **135**, 11861-11868.
27. H. Jeong, M. J. Kang, H. Jung and Y. S. Kang, *Faraday Discuss.*, 2017, **198**, 409-418.

28. Z. Kap, E. Ülker, S. V. K. Nune and F. Karadas, *J. Appl. Electrochem.*, 2018, **48**, 201-209.
29. J. Mahmood, S.-M. Jung, S.-J. Kim, J. Park, J.-W. Yoo and J.-B. Baek, *Chem. Mater.*, 2015, **27**, 4860-4864.
30. H. Fang, J. Chen, M.-S. Balogun, Y.-X. Tong and J. Zhang, *ACS Appl. Nano Mater.*, 2018, **1**, 6477-6482.
31. F. Zhao, J. Zhang, T. Abe, D. Wöhrle and M. Kaneko, *J. Mol. Catal. A: Chem.*, 1999, **145**, 245-256.
32. K. B. Schowen and R. L. Schowen, in *Methods Enzymol.*, Academic Press, 1982, vol. 87, pp. 551-606.
33. R. L. Schowen, *J. Labelled Compd. Radiopharm.*, 2007, **50**, 1052-1062.
34. I. Efimov, S. K. Badyal, C. L. Metcalfe, I. Macdonald, A. Gumiero, E. L. Raven and P. C. E. Moody, *J. Am. Chem. Soc.*, 2011, **133**, 15376-15383.
35. K. L. Pankhurst, C. G. Mowat, E. L. Rothery, J. M. Hudson, A. K. Jones, C. S. Miles, M. D. Walkinshaw, F. A. Armstrong, G. A. Reid and S. K. Chapman, *J. Biol. Chem.*, 2006, **281**, 20589-20597.
36. A. D. Wilson, R. H. Newell, M. J. McNevin, J. T. Muckerman, M. Rakowski DuBois and D. L. DuBois, *J. Am. Chem. Soc.*, 2006, **128**, 358-366.
37. A. Heine, G. DeSantis, J. G. Luz, M. Mitchell, C.-H. Wong and I. A. Wilson, *Science*, 2001, **294**, 369.
38. A. Z. Haddad, S. P. Cronin, M. S. Mashuta, R. M. Buchanan and C. A. Grapperhaus, *Inorg. Chem.*, 2017, **56**, 11254-11265.
39. M. Zhu, R. Ye, K. Jin, N. Lazouski and K. Manthiram, *ACS Energy Lett.*, 2018, **3**, 1381-1386.
40. N. Han, Y. Wang, L. Ma, J. Wen, J. Li, H. Zheng, K. Nie, X. Wang, F. Zhao, Y. Li, J. Fan, J. Zhong, T. Wu, D. J. Miller, J. Lu, S.-T. Lee and Y. Li, *Chem*, 2017, **3**, 652-664.
41. M.-S. Liao and S. Scheiner, *J. Chem. Phys.*, 2001, **114**, 9780-9791.
42. J. Hirst, B. A. C. Ackrell and F. A. Armstrong, *J. Am. Chem. Soc.*, 1997, **119**, 7434-7439.
43. N. Khadka, R. D. Milton, S. Shaw, D. Lukoyanov, D. R. Dean, S. D. Minteer, S. Raugei, B. M. Hoffman and L. C. Seefeldt, *J. Am. Chem. Soc.*, 2017, **139**, 13518-13524.
44. A. Kohen and H. H. Limbach, *Isotope effects in chemistry and biology*, cRc Press, Boca Raton, 2005.
45. D. B. Northrop, *Biochemistry*, 1975, **14**, 2644-2651.
46. S. Sawata, M. Komiyama and K. Taira, *J. Am. Chem. Soc.*, 1995, **117**, 2357-2358.
47. R. Schowen, *Isot. Eff. Chem. Biol.*, 2006, 765-789.
48. T. Nyokong, *Polyhedron*, 1995, **14**, 2325-2329.
49. B. Ramdhanie, L. N. Zakharov, A. L. Rheingold and D. P. Goldberg, *Inorg. Chem.*, 2002, **41**, 4105-4107.
50. N. Li, Y. Wang, C. Wu, W. Lu, K. Pei and W. Chen, *Appl. Surf. Sci.*, 2018, **434**, 1112-1121.
51. I. S. Hosu, Q. Wang, A. Vasilescu, S. F. Peteu, V. Raditoiu, S. Railian, V. Zaitsev, K. Turcheniuk, Q. Wang, M. Li, R. Boukherroub and S. Szunerits, *RSC Adv.*, 2015, **5**, 1474-1484.
52. C. A. Caro, F. Bedioui and J. H. Zagal, *Electrochim. Acta*, 2002, **47**, 1489-1494.
53. K. S. Venkatasubban and R. L. Schowen, *Crit. Rev. Biochem.*, 1984, **17**, 1-44.
54. S.-i. Nakano and P. C. Bevilacqua, *J. Am. Chem. Soc.*, 2001, **123**, 11333-11334.
55. M. S. Matta and V. Diep Thi, *J. Am. Chem. Soc.*, 1986, **108**, 5316-5318.
56. X. Zhang, Z. Wu, X. Zhang, L. Li, Y. Li, H. Xu, X. Li, X. Yu, Z. Zhang, Y. Liang and H. Wang, *Nat. Commun.*, 2017, **8**, 14675.
57. H. Zhao, Y. Zhang, B. Zhao, Y. Chang and Z. Li, *Environ. Sci. Technol.*, 2012, **46**, 5198-5204.

58. J. E. Hutchison, T. A. Postlethwaite, C.-h. Chen, K. W. Hathcock, R. S. Ingram, W. Ou, R. W. Linton, R. W. Murray, D. A. Tyvoll, L. L. Chng and J. P. Collman, *Langmuir*, 1997, **13**, 2143-2148.
59. A. Bettelheim, R. J. H. Chan and T. Kuwana, *J. Electroanal. Chem.*, 1980, **110**, 93-102.
60. C. L. Ni and F. C. Anson, *Inorg. Chem.*, 1985, **24**, 4754-4756.
61. C. Shi and F. C. Anson, *Inorg. Chem.*, 1990, **29**, 4298-4305.
62. I. Bhugun and F. C. Anson, *Inorg. Chem.*, 1996, **35**, 7253-7259.
63. P. K. Glasoe and F. A. Long, *J. Phys. Chem.*, 1960, **64**, 188-190.
64. A. K. Covington, M. Paabo, R. A. Robinson and R. G. Bates, *Anal. Chem.*, 1968, **40**, 700-706.
65. E. Liaudet, F. Battaglini and E. J. Calvo, *J. Electroanal. Chem. Interfacial Electrochem.*, 1990, **293**, 55-68.
66. N. Oyama and F. C. Anson, *Anal. Chem.*, 1980, **52**, 1192-1198.
67. J. Leddy and A. J. Bard, *J. Electroanal. Chem. Interfacial Electrochem.*, 1983, **153**, 223-242.
68. R. G. Compton, M. E. Laing, A. Ledwith and I. I. Abu-Abdoun, *J. Appl. Electrochem.*, 1988, **18**, 431-440.

Chapter 3: Determining the Coordination Environment and Electronic Structure of Polymer-Encapsulated Cobalt Phthalocyanine under Electrocatalytic CO_2 Reduction Conditions

3.1 Preface

In this chapter, *in situ* electrochemical X-ray absorption spectroscopy (XAS) studies were conducted to confirm the postulated primary coordination of CoPc in P4VP, and to gain further understanding of this system regarding the CoPc geometry and the localization of electrons during the course of CO_2RR. This work was in collaboration with the Penner-Hahn laboratory at University of Michigan. This chapter of my dissertation is derived from manuscript as originally published in journal *Dalton Transactions*.[1] I am the first author on the manuscript, the other authors are Aniruddha Deb, Kwan Yee Leung, Weixuan Nie, James E. Penner-Hahn, and Charles C. L. McCrory. I was responsible for all sample preparation, electrochemical measurements and analysis as well as the writing and preparation of the manuscript. The design of the XAS cell and the collection of all the XAS spectra were conducted in collaboration with Aniruddha Deb, who's also responsible for the XAS spectra interpretation and analysis. Kwan Yee Leung and Weixuan Nie were involved in electrolyte preparation and XAS data collection. Dr. Charles C. L. McCrory provided significant insights in electrochemical measurement and manuscript reviewing and

[1] From "Determining the coordination environment and electronic structure of polymer-encapsulated cobalt phthalocyanine under electrocatalytic CO_2 reduction conditions using *in situ* X-Ray absorption spectroscopy" by Yingshuo Liu, et al, 2020, *Dalton Transactions*, Advance Article. Copyright [2020] by ROYAL SOCIETY OF CHEMISTRY.

revision. Dr. James E. Penner-Hahn provided significant insights in XAS spectra interpretation and analysis, and manuscript reviewing and revision.

3.2 Abstract

Encapsulating cobalt phthalocyanine (CoPc) within the coordinating polymer poly-4-vinylpyridine (P4VP) results in a catalyst-polymer composite (CoPc-P4VP) that selectively reduces CO_2 to CO at fast rates with a low overpotential. In previous studies, we postulated that the enhanced selectively for CO over H_2 production within CoPc-P4VP compared to the parent CoPc complex is due to a combination of primary, secondary, and outer-coordination sphere effects imbued by the encapsulating polymer. In this work, we perform *in situ* electrochemical X-ray absorption spectroscopy measurements to study the oxidation state and coordination environment of Co as a function of applied potential for CoPc, CoPc-P4VP, and CoPc with and without an axially-coordinated py, CoPc(py). Using *in situ* X-ray absorption near edge structure (XANES) we provide experimental support for our previous hypothesis that Co changes from a 4-coordinate square-planar geometry in CoPc to a mostly 5-coordinate species in CoPc(py) and CoPc-P4VP. The coordination environment of CoPc-P4VP is potential-independent but pH-dependent, suggesting that the axial coordination of pyridyl groups in P4VP to CoPc is modulated by the protonation of the polymer. Finally, we show that, upon reduction, the oxidation state of Co in the 4-coordinate CoPc is different from that in the 5-coordinate CoPc(py), suggesting that the primary coordination sphere modulates the resting oxidation state under catalytically-relevant conditions.

3.3 Introduction

The efficient and selective electrochemical conversion of CO_2 to single products in the CO_2 reduction reaction (CO_2RR) has provoked intense scientific interest, both as a means of storing energy from intermittent energy sources such as solar and wind in the form of chemical fuels[1-6] and of recycling CO_2 in industrial waste streams into useful industrially-relevant chemical feedstocks.[5-8] In particular, there has been significant recent research exploring the activity of cobalt phthalocyanine (CoPc) and related complexes for the CO_2RR in aqueous solutions.[9-22] In general, many of these systems show high activity and selectivity for CO_2 reduction to CO,[9-13, 16-22] and in some cases under optimized conditions and very negative potentials, the sequential reduction of CO_2 to CO to methanol.[14, 15] However, many of these systems cast the CoPc materials onto high-surface area carbon supports such as oxidized carbon paper,[11, 20] conductive carbon black,[10, 12] or multi-walled carbon nanotubes,[14, 15, 17, 23] each of which have surface functional groups that may coordinate to CoPc and influence its electronic structure and activity for the CO_2RR.[14, 24] Moreover, many of the reported CoPc-based electrocatalyst systems use Nafion as a polymer binder,[10-12, 14, 15, 17, 18, 20, 23] but, in general, the influence of the polymer on the coordination environment and mechanism of CoPc for the CO_2RR is not fully understood.

Our research has focused on understanding the role of encapsulating polymers on the coordination environment of CoPc, and in turn how changes in the coordination environment influence catalytic activity and reaction selectivity for the CO_2RR over competitive HER. In particular, previous investigations have shown that immobilizing cobalt phthalocyanine (CoPc), an active but non-selective catalyst for the CO_2RR in aqueous phosphate electrolyte,[9, 25, 26] within a poly-4-vinylpyridine (P4VP) polymer on a graphite electrode dramatically increases the complex's catalytic activity and selectivity for the CO_2RR.[9, 26, 27] We have shown that the resulting

CoPc-P4VP system is a highly active and selective electrocatalytic system for the reduction of CO_2 to CO.[9] The increased activity and selectivity of CoPc-P4VP has been attributed to three effects of P4VP on the coordination environment of the CoPc complex as shown in Figure 3.1.[9, 27] First, in the catalyst's primary coordination sphere, axial coordination of pyridyl groups in P4VP to the Co-center of CoPc increases the catalyst's nucleophilicity and promotes CO_2 binding. Second, in the catalyst's secondary coordination sphere, protonated pyridyl groups in P4VP stabilize coordinated CO_2RR intermediates via H-bonding interactions. Third, in the catalyst's outer coordination sphere, H^+ transport to the catalyst active site occurs via a proton relay mechanism involving pyridyl groups in P4VP.

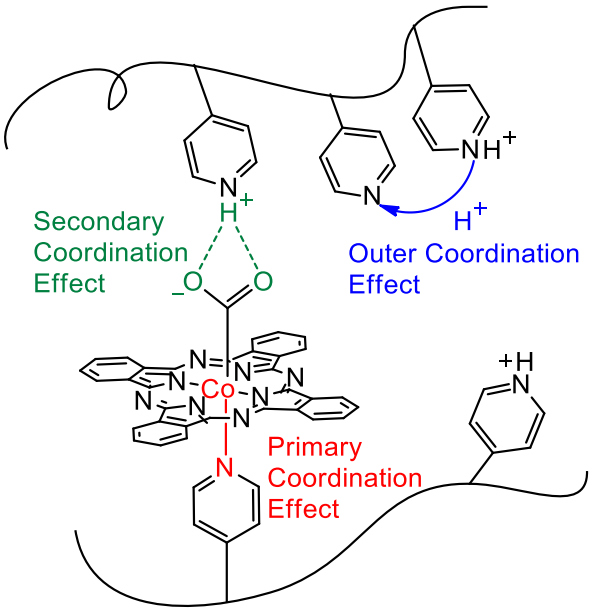

Figure 3.1 An illustration of CoPc encapsulated in P4VP highlighting the primary, secondary, and outer coordination sphere effects.

The effect of the coordination environment on the enhanced activity and selectivity of CoPc-P4VP for the CO_2RR has been supported by recent electrochemical mechanistic and kinetic studies.[9, 19] In particular, the axial ligation of the pyridyl groups in the P4VP polymer to CoPc play a crucial role in the catalytic mechanism for the CO_2RR. CoPc-P4VP reduces CO_2 with 3-4

times the activity of the parent CoPc complex[25,26] due to a shift in the rate determining step of the catalytic mechanism from an initial CO_2 binding step to a subsequent protonation event upon axial coordination of the pyridyl groups to CoPc.[26] In contrast, in CoPc-P2VP, CoPc is immobilized in a P2VP polymer such that axial coordination of the polymer pyridyl groups to CoPc is sterically hindered (see Scheme 3.1). The CoPc-P2VP system reduces CO_2 with no enhancement of activity relative to the parent CoPc complex due to the lack of axial coordination from the P2VP pyridyl groups to the CoPc.[25,26] An implicit assumption in our previous studies is that CoPc-P4VP exists primarily as a 5-coordinate complex under our catalytic conditions, whereas CoPc-P2VP exists primarily as a 4-coordinate complex under identical conditions. Moreover, we assumed that the coordination environment of the CoPc does not change under electrocatalytic CO_2 reduction conditions. The work presented here provides direct evidence supporting for these previous assumptions.

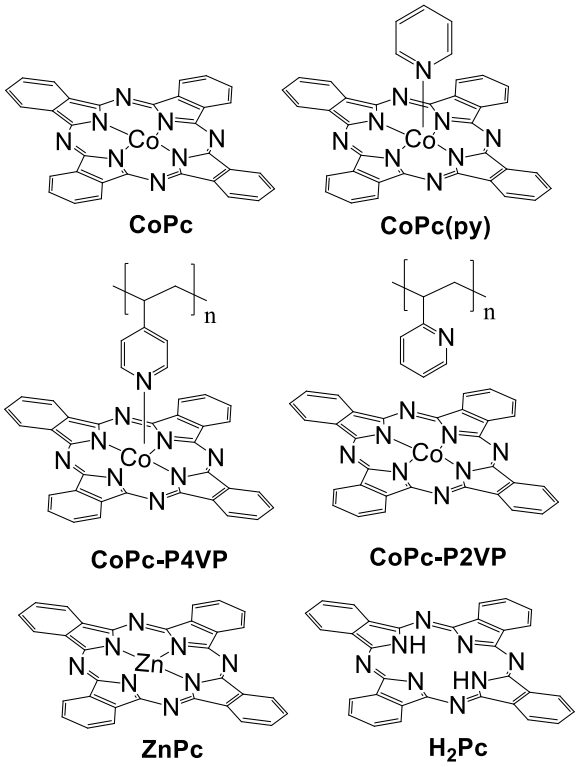

Scheme 3.1 Catalyst and polymer-catalyst composite systems investigated in this work along with their postulated axial coordination.

In this study, we measure the coordination environment of CoPc-P4VP both as deposited and under electrocatalytic CO_2 reduction conditions using *in situ* X-ray absorption spectroscopy (XAS). In particular, we use X-ray absorption near edge structure (XANES) measurements to characterize the coordination geometry and oxidation state of the Co center in CoPc-P4VP and related systems (Scheme 3.1) adsorbed onto carbon supports and under applied electrochemical potential both in the presence and absence of CO_2. We show that the parent CoPc complex and the composite CoPc-P2VP film show an intense pre-edge feature in the Co K-edge XANES spectra associated with a 1s-4p pre-edge peak characteristic of square-planar macrocyclic Co complexes as expected for these systems. However, for CoPc(py) and CoPc-P4VP, where we expect a 5-coordinate square pyramidal structure, we observe a dramatic decrease in the 1s-4p pre-edge peak intensity consistent with conversion from square-planar geometry to a 5-coordinate square-

pyramidal complex. The steady-state coordination geometry of the CoPc-P4VP remains constant regardless of applied potential and even in the presence of CO_2 under electrocatalytic conditions.

In addition, we have measured the oxidation state of the Co in CoPc, CoPc-P4VP and related systems as a function of applied potential. Specifically, we show that the first oxidation and first reduction of the adsorbed 5-coordinate CoPc(py) species have metal-based character, which are consistent with the findings of previous theoretical studies[10, 28] and previously proposed catalytic mechanisms for the CO_2RR by CoPc that assert an initial Co-based reduction.[11, 26, 27, 29-32] However, in the case of 4-coordinate CoPc, we find that the energy of the Co K-edge does not change as a function of applied potential, suggesting that redox events in CoPc are ligand-based under our conditions. This is an interesting result that differs from the findings of previous reports for CoPc,[10, 11, 26-32] but is not entirely unknown for cobalt complexes with redox-active ligands.[33-35] We discuss the implications of the XAS results on the catalytic mechanism for the CO_2RR by CoPc and conduct additional experiments to assess the importance of the Co center on the CO_2RR in the CoPc system.

3.4 Results and Discussion

Our lab[9, 19, 36] and others[26, 27] have shown that encapsulating CoPc within a coordinating polymer such as P4VP results in a dramatic increase in activity and selectivity for the CO_2RR over competitive hydrogen evolution. This difference in CO_2RR activity and selectivity for the CoPc-P4VP catalyst-polymer composite compared to the parent CoPc complex has been attributed to changes in the coordination environment surrounding the CoPc complex in the polymer.[9, 19, 26, 27, 36] In particular, we have previously proposed that axial coordination of pyridyl groups from the P4VP to the Co center in CoPc is partially responsible for the increased activity and selectivity of

CoPc-P4VP compared to CoPc.[9, 19] In this work, we use *in situ* electrochemical XAS measurements to experimentally verify the coordination environment of Co in CoPc-P4VP and related systems under electrocatalytically-relevant conditions and potentials.

Normalized XANES measurements were compared under different conditions over the range of 7705–7755 eV. Information about the electronic structure and Co-coordination environment of each sample was determined by comparing to standard compounds of CoPc and CoPc(py). For each set of measurements, the electrochemical XAS cell was assembled with freshly prepared electrodes. Note that it has been previously reported that CoPc undergoes significant aggregation when adsorbed onto carbon surfaces at high loadings which influences the observed activity per Co site,[11] but does not influence the catalytic mechanism.[19] In our system, CoPc,[19] CoPc-P4VP,[19] and CoPc(py) (Figure A.45) all show similar extents of aggregation at our Co loadings, suggesting that any observed differences in the measured XANES spectra for these three systems cannot be explained by differences in extent of aggregation.

The XANES spectra can be characterized by two peaks, a weaker 1s-3d pre-edge peak at ~7710 eV and a stronger 1s-4p pre-edge peak at ~7716 eV. The former is found to increase in intensity as a metal site distorts from centrosymmetric to non-centrosymmetric coordination environment; this is interpreted as resulting from an increase in 3d+4p mixing in the non-centrosymmetric environment. The 1s-4p peak is characteristic of square-planar complexes[37] and has been interpreted as either 1s-4p+shakedown[38, 39] or a direct 1s-4p transition.[40] Regardless of the assignment, it is well-established that this peak is characteristic of Co in square-planar environments,[10, 39] with significantly decreasing intensity when complexes go from square-planar to square-pyramidal and finally to octahedral geometries (this peak is also weak for tetrahedral complexes,[37] but those are not considered further here, given the rigidity of the phthalocyanine

ring). The XANES spectra of CoPc and CoPc(py) standards are shown in Figure 3.2. The XANES of the CoPc standard shows the typical 4-coordinate strong pre-edge (1s-4p) peak at ~7716 eV, while coordination in the CoPc(py) standard shows a weak pre-edge peak at ~7716 eV, which is consistent with a conversion from a square-planar Co geometry to a 5-coordinate square-pyramidal CoPc(py) complex.[11, 19]

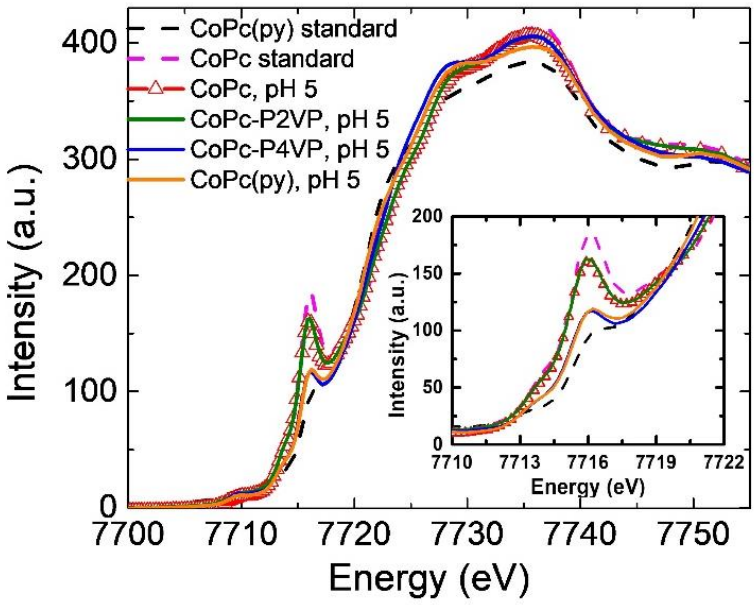

Figure 3.2 *XANES* spectra of CoPc/CP, CoPc-P2VP/CP, CoPc-P4VP/CP, and CoPc(py)/CP immersed in pH 5 phosphate electrolyte solution. XANES measurements of independently synthesized 4-coordinate CoPc and pure 5-coordinate CoPc(py) dry powders are included as standards. The inset is a zoom-in of the 1s-4p peak at 7716 eV. An strong peak at 7716 eV is characteristic of Co in a square planar geometry as observed for CoPc/CP and CoPc-P2VP/CP, whereas a weak peak is associated with Co in a non-square planar geometry as observed for CoPc(py)/CP and CoPc-P4VP/CP. In the case of CoPc(py)/CP and CoPc-P4VP/CP, we attribute this non-square planar geometry to formation of a 5-coordinate Co species upon axial ligation to pyridine or polymer-pyridyl groups, respectively.

3.4.1 Coordination Environment of Polymer-Encapsulated CoPc Complexes

In previous studies, the catalytic activity of CoPc as a catalyst for CO_2 reduction was investigated primarily in aqueous solution, with or without polymer encapsulation.[9, 19, 26, 27] For

this reason, we examined the coordination environment of the parent CoPc, CoPc(py) with an axially-coordinated pyridine, CoPc-P4VP encapsulated in a coordinating P4VP polymer, and CoPc-P2VP encapsulated in a non-coordinating P2VP polymer. In all 4 cases, the sample was absorbed on a carbon paper (CP) support and exposed to pH 5 phosphate solution. The coordination environment was characterized by the relative intensity of the 1s-4p peak. The XANES spectra for these samples, along with those for the CoPc and CoPc(py) standards are shown in Figure 3.2. CoPc/CP shows an strong 1s-4p peak at 7716 eV consistent with a 4-coordination Co center, whereas CoPc(py)/CP and CoPc-P4VP/CP have nearly identical spectra with a weak peak indicating primarily 5-coordinate cobalt in these systems. The spectrum for CoPc-P2VP/CP is nearly identical to that for CoPc/CP, suggesting that the cobalt remains 4-coordinate in the non-coordinating P2VP polymer. These XANES results experimentally verify our previous hypothesis that Co exists as a 4-coordinate species in CoPc and CoPc-P2VP, and a 5-coordinate species in CoPc-P4VP and when CoPc(py) is deposited directly onto graphite surfaces.[9, 19] The small differences between the spectra for the surface adsorbed samples and the reference CoPc and CoPc(py) dry standards may indicate either an equilibrium between 4- and 5-coordinate species in the coated samples or alternatively may simply reflect the sensitivity of XANES to longer distance interactions which vary between the microcrystalline reference standard compounds and the coated samples. Note that CoPc has been reported to axially-coordinate to activated carbon supports such as carbon nanotubes as evidenced by a decrease in the intensity of the 1s-4p_z peak in the Co K-edge spectra.[14] Our data demonstrates that the majority of the Co is 4-coordinate in CoPc/CP and not axially-coordinated to the carbon surface. However, we cannot exclude the possibility that a small fraction of the CoPc coordinates to an oxide species on the carbon paper forming an active species for CO_2RR.

3.4.2 Coordination Environment of CoPc/CP and Related Systems as a Function of pH

As solution pH changes, there will be corresponding change in fractional protonation of pyridyl groups in P4VP.[27] This, in turn, may modulate the extent of pyridyl groups to CoPc in CoPc-P4VP—in more acidic solutions, fewer unprotonated pyridyl groups may be available to coordinate Co in CoPc-P4VP. To investigate how the coordination environment of CoPc in P4VP and in CoPc(py) is modulated by pH, Co K-edge XANES were measured for CoPc(py)/CP and CoPc-P4VP/CP as a function of pH at open circuit potential under N_2. In the CoPc(py)/CP sample exposed to phosphate solutions (Figure 3.3a), there is a stronger 1s-4p peak at every pH compared to the dry CoPc(py) standard. This increased intensity of the 1s-4p peak for CoPc(py)/CP exposed to phosphate solution suggests that any exposure to electrolyte results in loss of some fraction of the coordinated pyridines. When CoPc(py)/CP is exposed to pH 3, the intensity of the 1s-4p peak is greatest, and thus pyridine loss is largest. We postulate that at pH 3, the protonation of pyridine ($pK_a = 5.2$)[41] is favored which facilitates pyridine dissociation from CoPc(py). At pH $\geq$ 5, we expect the pyridine groups in CoPc(py) should remain largely deprotonated and thus we expect a larger fraction of the CoPc(py) will remain 5-coordinate. This postulate is supported by the XANES measurements which show a decreased intensity of the 1s-4p peak for CoPc(py) exposed pH $\geq$ 5 solutions consistent with increased 5-coordinate character compared to that of CoPc(py) exposed to pH 3 solution.

In contrast, the CoPc-P4VP/CP sample does not exhibit the same extent of pH-dependent change in coordination environment as does CoPc(py). In particular, the CoPc encapsulated in P4VP shows only a slight decrease in 5-coordinate species with decreasing pH (Figure 3.3b), which we attribute to the influence of the polymer conformation on the effective pK_a of the Co-bound pyridine groups. In order to confirm that the axial ligation in CoPc-P4VP comes from the

backbone pyridine, a control experiment was conducted with CoPc encapsulated in P2VP. The Co XANES of CoPc-P2VP/CP under different pH conditions as shown in Figure 3.3c. Here the shapes and the positions of the pre-edge is preserved, indicating that CoPc remains 4-coordinate throughout the pH range of 9 to 3, is consistent with the conclusion that P2VP does not coordinate with CoPc because of the steric hindrance.

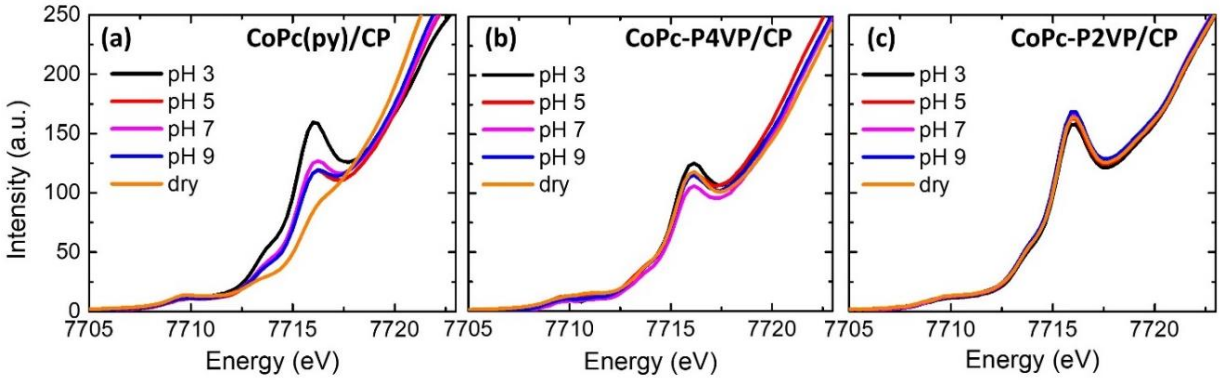

Figure 3.3 Pre-edge spectra near 7716 eV of **(a)** CoPc(py)/CP, **(b)** CoPc-P4VP/CP, and **(c)** CoPc-P2VP/CP exposed to phosphate solutions at different pH under N_2 atmosphere at open circuit potential.

3.4.3 Coordination Environment and Oxidation State of CoPc/CP and Related Systems as a Function of Applied Potential

To determine whether the CoPc remains 5-coordinate in P4VP polymer and in CoPc(py) during the course of reduction as we previously proposed,[9] we measured XANES for CoPc/CP, CoPc(py)/CP, and CoPc-P4VP/CP exposed to pH 5 phosphate electrolyte solution as a function of applied potential. The electrochemical redox potentials of CoPc immobilized on an edge plane graphite electrode (CoPc/EPG) in pH 5 phosphate electrolyte solution were evaluated using Cyclic Voltammetry (CV) as shown in Figure 3.4. The observed CV is consistent with those previously reported or this system.[9] The broad quasi-reversible peaks at 0.50 V and -0.34 V vs. SCE are assigned to the oxidation and first reduction of CoPc, respectively. The second reduction at ~ -1.1

V is the onset potential for HER and/or CO_2RR under both N_2 or CO_2. Note that CoPc-P4VP and CoPc(py) immobilized on EPG exposed to pH 5 phosphate electrolyte show similar CV features as CoPc, as shown in Figure A.46-A.47. Sequential *in situ* Co K-edge XANES measurements were made while holding the CoPc/CP and related modified electrodes at 1.2 V (oxidized complex), 0 V (neutral complex), -0.5 V (singly-reduced complex), and -1.25 V (doubly-reduced complex) vs. SCE as shown in Figure 3.5. The corresponding chronoamperometry data are shown in Figure A.48-A.53.

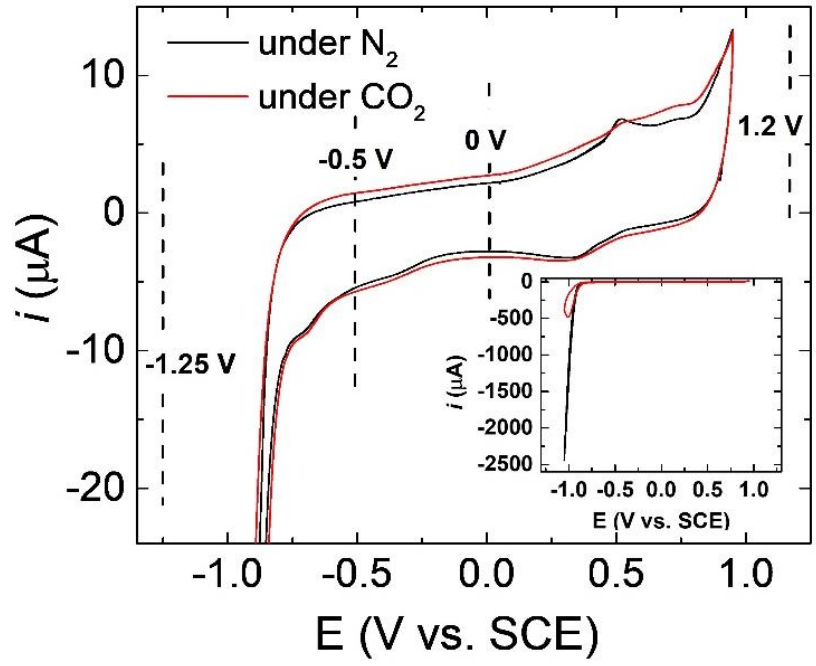

Figure 3.4 Cyclic voltammogram (CV) of CoPc/EPG electrode in pH 5 phosphate electrolyte under both N_2 and CO_2 atmospheres. The main figure shows the main electrochemical features preceding catalysis, and the inset shows the catalytic features as well.

The XANES spectra for the CoPc/CP system (Figure 3.5a-b) show an strong 1s-4p peak at 7716 eV suggesting the steady-state coordination environment surrounding Co remains primarily 4-coordinate at all applied potentials under both N_2 and CO_2. In comparison, the CoPc(py)/CP system (Figure 3.5c-d) and the CoPc-P4VP/CP system (Figure 3.5e-f) both show a much weaker

1s-4p peak suggesting that the steady-state coordination environment surrounding Co remains primarily 5-coordinate in these systems at all potentials in both N_2 and CO_2. These studies show that the steady-state coordination environment is largely potential-independent, and is dictated by the coordination of pyridine ligand or pyridyl groups in P4VP, and not transiently-associating ligands like CO_2 under electrocatalytic conditions.

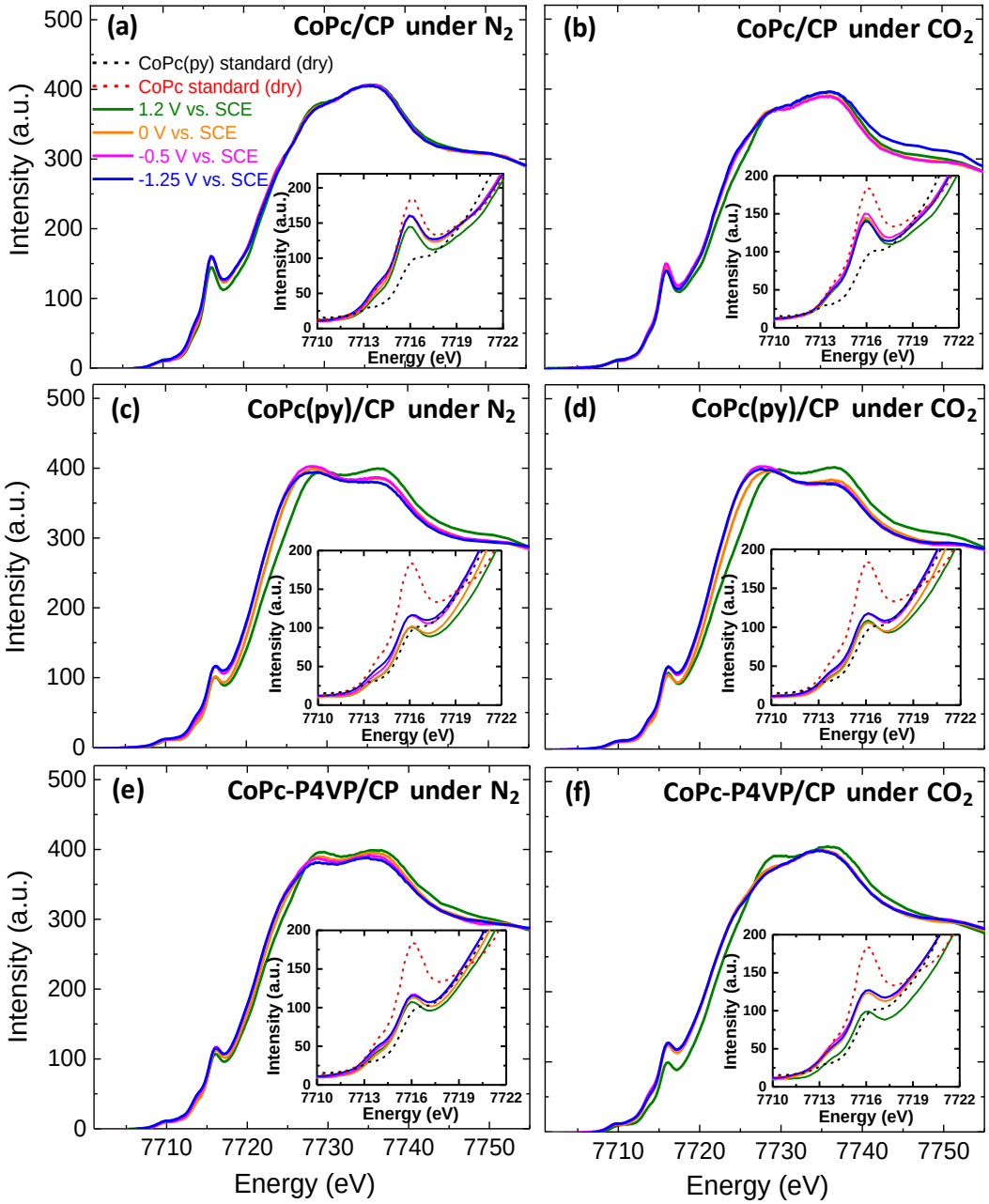

Figure 3.5 *In situ* XANES spectra of CoPc-based systems absorbed onto carbon paper electrodes and exposed to pH 5 phosphate electrolyte solution at four different potentials: **(a)** CoPc/CP under N_2, **(b)** CoPc/CP under CO_2, **(c)** CoPc(py)/CP under N_2, **(d)** CoPc(py)/CP under CO_2, (e) CoPc-P4VP/CP under N_2, (f) CoPc-P4VP/CP under CO_2. The inset in each panel is the zoomed-in region showing the 1s-4p features near 7716 eV.

In addition, in the case of CoPc/CP, the energy and shape of the Co K-edge does not change appreciably as a function of applied potential under either N_2 or CO_2 (Figure 3.5a-b), suggesting the oxidation and reduction events at CoPc are primarily ligand based under these conditions and

do not involve a formal change in the oxidation state of the Co center as illustrated in Scheme 3.2 [i], except for a small increase in oxidation state upon oxidation under CO_2. For comparison, the energy of the edge for CoPc(py)/CP shifts as a function of applied potential under both N_2 and CO_2 (Figure 3.5c-d). In particular, starting at the neutral complex at 0 V vs SCE, as we apply a more positive potential of 1.2 V vs SCE there is an edge shift to higher energy, indicative of an increase in the average Co oxidation state. Likewise, when we apply a more negative potential of −0.5 V vs SCE, we observe an edge shift to lower energy indicative of a decrease in the average Co oxidation state. However, there is no additional change in edge position when applying an even more negative potential of −1.25 V vs SCE. These results suggest that the oxidation and first reduction of the CoPc(py)/CP system involve changes in the Co oxidation state, but the second reduction is largely ligand-based as illustrated in Scheme 3.2 [ii]. Previous studies have used the energy of the 1s-3d peak to determine oxidation state of Co complexes, particularly in tetrahedral complexes where there is a more intense 1s-3d transition, with a shift of ~ 0.4 eV per unit change in oxidation state. [42, 43] We do not see any resolvable shift in 1s-3d energy; this is not surprising given the weak, broad nature of the 1s-3d transitions in our samples.

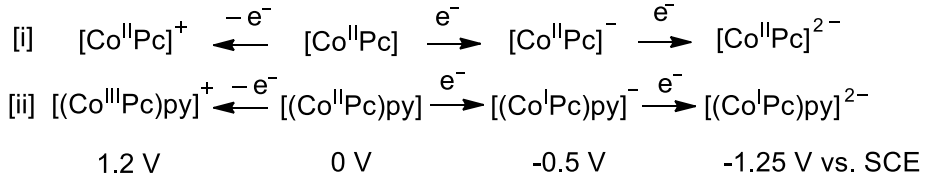

Scheme 3.2 Proposed electrochemical mechanism for 4-coordinate [i] and 5-coordiante [ii] CoPc at different applied potentials with individual oxidation states on the Co center.

Previously proposed mechanisms for CoPc-catalyzed CO_2 reduction suggest that the first two electrochemical processes are Co-based ($Co^{III/II}$ and $Co^{II/I}$), whereas the third is ligand-based, analogous to the process shown in Scheme 3.2 [ii].[26, 29-31] This is qualitatively consistent with our experimental findings for CoPc(py)/CP. In contrast, CoPc/CP show no evidence of change in the

Co oxidation state upon either reduction or oxidation under N_2, and a small change on oxidation under CO_2, suggesting that the redox events are primarily ligand-based for this 4-coordinate Co species. Previous studies conducted with structurally similar metal porphyrins have reported that axial ligation to the metal center modifies the electronic structure of the metal porphyrin complexes that can alter the redox center of the complexes.[44, 45] We hypothesize that difference in the redox mechanisms for the surface immobilized CoPc/CP and CoPc(py)/CP is due to the fact that axial pyridine ligand interacts with Co orbitals to introduce more Co-character into the HOMO, and this increased Co-mixing in the HOMO lead to increased extent of Co-character in the redox events for the CoPc(py)/CP system. This hypothesis is supported by DFT studies of Co complexes with axial ligands CO (π-accepting) and HCN (σ-donating).[28, 46]

In the case of CoPc-P4VP/CP under N_2, the energy and shape of the XANES edge shows shifts upon oxidation and reduction that are qualitatively similar to those observed for CoPc(py)/CP, but the magnitude of these shifts is smaller (Figure 3.5e). Specifically, starting at the neutral complex at 0 V vs SCE, as we apply a more positive potential of 1.2 V vs SCE, there is an edge shift to slightly higher energy and when we apply a more negative potential of −0.5 V vs SCE, there is an edge shift to lower energy. There is no additional change in edge position when applying an even more negative potential of −1.25 V vs SCE. The magnitude of the edge shifts at 1.2 V vs SCE and −0.5 V vs SCE under N_2 are detectable but smaller in magnitude than those observed for CoPc(py)/CP, suggesting that the oxidation and the first reduction in CoPc-P4VP/CP has some Co-character but is not exclusively metal-centered. These decreased magnitude of the edge-shift in CoPc-P4VP/CP compared to CoPc(py)/CP could be due to the pyridyl groups in P4VP having less ability to donate electron density to the Co center in CoPc-P4VP compared to the free pyridine ligands in CoPc(py). This hypothesis is supported by the lower pK_a of pyridyl

groups in P4VP compared to free pyridine.[47] The less electron-donating pyridyls in the polymer may result in weaker axial ligation of the pyridyl groups to the Co center in CoPc-P4VP/CP, leading to decreased Co-mixing in the HOMO and thus less extent of Co-character in the redox events for CoPc-P4VP/CP compared to CoPc(py)/CP. Under CO_2, CoPc-P4VP/CP still shows an edge-shift upon oxidation similar to that observed under N_2. However, under CO_2, there is no change in edge energy upon reduction even at the most negative applied potentials (Figure 3.5f).

3.4.4 The Role of Co Center in CoPc for CO_2RR

Our *in situ* electrochemical XANES experimental results suggest that reductions of the parent 4-coordinate CoPc do not involve Co-based oxidation state changes, whereas the 5-coordinate CoPc(py) does change oxidation state upon the first reduction event, which is not consistent with the previously reported mechanistic hypothesis and DFT computation results for CoPc.[10, 11, 26-32] In the case of CoPc, the lack of redox activity at the Co center might suggest that the Co could be replaced with a redox-inactive metal, or even completely removed from the Pc ligand, and the system might still retain activity for CO_2RR. Although we find this argument somewhat unlikely, to test if Co center is necessary for CO_2RR we measured the electrocatalytic CO_2RR activities and product distributions of ZnPc and the metal-free H_2Pc immobilized onto EPG electrodes and compared them to those measured for CoPc/EPG in previously reported studies.[19] The results are summarized in Figure 3.6.

From our CPE studies, we found that ZnPc/EPG exposed to pH 5 phosphate electrolyte exhibits lower activity and less selectivity for CO_2RR compared to CoPc/EPG under identical conditions. The metal-free H_2Pc/EPG exhibits negligible CO_2RR activity and mostly HER activity, as has been previously reported.[48] These results suggest that the Co center plays an

important role in CO_2RR in CoPc even though it is not redox active according to the *in situ* XANES data. To further probe the role of metal center, additional CVs for ZnPc and CoPc complexes dissolved in homogenous DMSO solutions were measured as shown in Figure A.54. The shifts of redox couples of CoPc compared to ZnPc suggests that the Co center in CoPc influences the energy of molecular orbitals of the metal phthalocyanine complex even if the Co center itself does not show a change in oxidation state upon oxidation or reduction.

Note that when ZnPc is immobilized in P4VP, the resulting ZnPc-P4VP has similar TOF for CO_2RR compared to that of ZnPc, but the overall activity is dramatically suppressed due to limited substrate transport. The overall activity and TOF for CO_2RR for ZnPc-P4VP/EPG is significantly lower than that of CoPc-P4VP/EPG. This results suggests that pyridyl moieties in P4VP either do not axially coordinate with ZnPc, or any axial coordination does not result in enhanced catalytic activity.

The fact that the ZnPc/EPG has only 3× less activity than CoPc/EPG, as compared to the ~25× lower activity for ZnPc-P4VP/EPG compared to CoPc-P4VP/EPG, is consistent with our proposal that the redox-activity in the 4-coordinate CoPc systems are primarily ligand based (Scheme 3.2[i]), whereas the redox-activity in the 5-coordinate CoPc-P4VP systems has more metal-character (Scheme 3.2[ii]). Because Zn is not expected to show metal-based redox activity under these conditions, the fact that ZnPc/EPG shows activity in the same order of magnitude as CoPc-EPG is consistent with the metal center in both cases being necessary for CO_2 coordination/reduction, but not necessarily the site of primary redox activity. For comparison, the fact that CoPc-P4VP/EPG has dramatically-enhanced (~25× higher) activity compared to Zn-P4VP/EPG is consistent with our assertion that the two metal centers have dramatically-different roles in these two systems. One explanation for such a dramatic difference is that the axial-

coordination of the pyridyl groups to the Co center in the CoPc-P4VP/EPG system results in a 5-coordinate Co center with a greater degree of redox activity, whereas the redox-activity is still likely ligand-based in the ZnPc-P4VP/EPG system regardless of whether the Zn is axially-coordinated to a pyridyl group. Thus, these activity results are qualitatively consistent with the assertions regarding the center of redox activity from our XANES experiments.

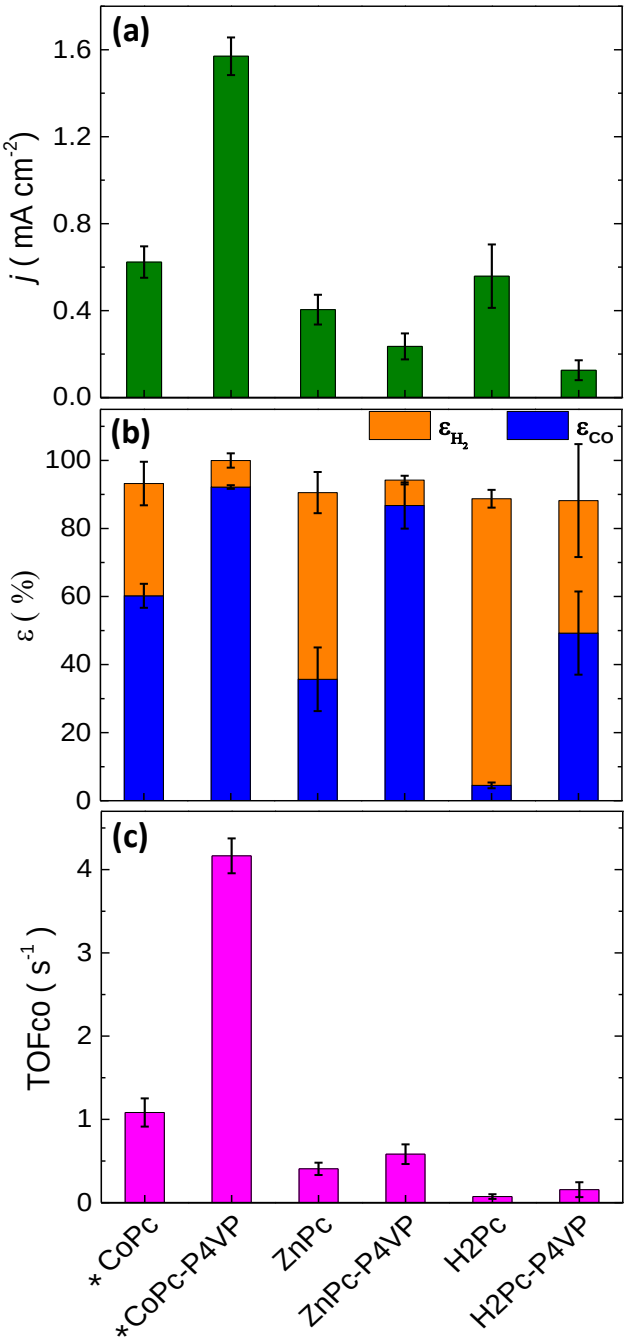

Figure 3.6 CPE results for CoPc, ZnPc, H_2Pc and related systems. **(a)** overall current density; **(b)** Faradaic efficiencies for H_2 (orange bar) and CO (blue bar); and **(c)** turnover frequency for CO production. All measurements conducted in pH 5 phosphate solutions under CO_2 atmosphere at -1.25 V vs. SCE. All reported values are averages from 3 or more independent measurements, and the errors are given as standard deviations. *CoPc and *CoPc-P4VP data is from reference.[19]

3.5 Experimental

3.5.1 Materials and Chemicals

All purchased chemicals were used as received unless otherwise specified. Cobalt phthalocyanine (CoPc, 97%), poly-4-vinylpyridine (P4VP, average Mw ~ 160,000), poly-2-vinylpyridine (P2VP, average Mw ~ 159,000), N,N-dimethylformamide (DMF, ACS grade), pyridine (ACS grade, ≥ 99%), dimethyl sulfoxide (DMSO, ACS grade, ≥ 99.9%), Zinc phthalocyanine (ZnPc, 97%), H_2-phthalocyanine (H_2Pc, 98%), ferrocenecarboxylic acid (97%), sodium phosphate monobasic (NaH_2PO_4, BioXtra, > 99%), sodium hydroxide (NaOH, BioXtra, ≥ 98%), phosphoric acid (H_3PO_4, ≥ 85 wt. % in H_2O, ≥ 99.999% trace metals basis), boron nitride, and Nafion-117 cation exchange membrane (Nafion) were purchased from Sigma Aldrich. Tetrabutylammonium hexaflurophosphate (nBu_4NPF_6, > 98.0%) was purchased from TCI America and recrystallized from Methonal/H_2O (v/v = 8/1). Edge plane graphite disk electrodes (EPG, 5 mm diameter, effective electrode surface area: 0.114 cm^2) were purchased from Pine Research Instrumentation. Carbon paper (AvCarb P50) was purchased from the Fuel Cell Store. Carbon rods were purchased from Strem Chemicals, Inc. Pt wire (99.99%, 0.02" diameter) was purchased from Surepure Chemetals L.L.C. Compressed CO_2 gas (99.8%) was purchased from Cryogenic Gases. All water used in this study was ultrapure water (18.2 MΩ·cm resistivity) purified with a Thermo Scientific GenPure UV-TOC/UF xCAD-plus water purification system.

3.5.2 Preparation of CoPc and CoPc(py) Standard Complexes

The 4-coordinate CoPc complex was purified using a previously reported preparation by heating the as-purchased complex at ~210 °C under vacuum for 24 h.[49] The 5-coordinate CoPc(py)

complex was synthesized using a previously reported preparation by first heating CoPc in pure pyridine under reflux until the CoPc solid was fully dissolved, then cooling the system to 100 °C to obtain a precipitate that was filtered and dried under vacuum.[50] Both the 4-coordinate CoPc and 5-coordinate CoPc(py) standard complexes were characterized by elemental analysis conducted by Midwest Microlab, Inc. Anal. Calcd (found) for CoPc, ($C_{32}H_{16}CoN_8$): %C 67.25 (66.97), %H 2.82 (2.96), %N 19.61 (19.45). Anal. Calcd (found) for CoPc(py), ($C_{37}H_{21}CoN_9$): %C 68.30 (67.98), % H 3.25 (3.26), % N 19.38 (19.21).

3.5.3 Preparation of Modified Carbon Paper Electrodes

CoPc: The CoPc/DMF deposition solution was prepared by dissolving 3 mg of CoPc in 100 mL DMF. The resulting solution was sonicated for 30 min to fully disperse the CoPc. CoPc coated carbon paper electrode were prepared by drop-casting a total volume of 2.5 mL of the CoPc/DMF deposition solution to form a 3 cm diameter circular coating on a carbon paper disk of 6.5 cm diameter. The DMF solvent was evaporated by flowing N_2 gas over the sample at room temperature for ~4.5 h. The resulting Co loading was ~ 1.9×10^{-8} mol cm^{-2}. The CoPc coated carbon paper electrodes are designated CoPc/CP

CoPc(py): The CoPc(py) deposition solution was prepared by dissolving 3 mg of CoPc in 5 mL of pyridine. The resulting solution was sonicated for 30 min to fully disperse the CoPc. CoPc(py) coated carbon paper electrodes were prepared by drop-casting a total volume of 0.125 mL of the CoPc(py) deposition solution to form a 3 cm diameter circular coating on a carbon paper disk of 4 cm diameter. The extra pyridine solvent was evaporated by flowing N_2 gas over the sample at room temperature for ~4.5 h. The resulting Co loading was ~ 1.9×10^{-8} mol cm^{-2}. The CoPc(py) coated carbon paper electrodes are designated CoPc(py)/CP.

CoPc-P4VP (P2VP): The CoPc-P4VP (1% w/v) and CoPc-P2VP (1% w/v) deposition solutions were prepared by dissolving 0.025 g of P4VP (or P2VP) in 2.5 mL of the CoPc/DMF solution. The resulting solution was sonicated for 20 mins to fully dissolve the P4VP (or P2VP) and disperse the CoPc. CoPc-P4VP (or CoPc-P2VP) coated carbon paper electrodes were prepared by drop-casting a total volume of 2.5 mL of the CoPc-P4VP/DMF (or CoPc-P2VP/DMF) deposition solution to form a 3 cm diameter circular coating on a carbon paper disk of 4 cm diameter. The DMF solvent was evaporated over N_2 gas at room temperature for ~4.5 h. The resulting Co loading was ~ 1.9×10^{-8} mol cm^{-2}. The CoPc-P4VP and CoPc-P2VP coated carbon paper electrodes are designated CoPc-P4VP/CP and CoPc-P2VP/CP, respectively.

3.5.4 Electrolyte Solution Preparation

All electrolyte solutions were prepared using ultrapure water. The pH 3 phosphate solutions were prepared from a 0.1 M NaH_2PO_4 solution adjusted to pH 3 by the addition of 1 M H_3PO_4 solution. The pH 5, 7, and 9 phosphate solutions were prepared from a 0.1 M NaH_2PO_4 solution adjusted to the appropriate pH by the addition of 1 M NaOH solution. All solution pH were measured using a Thermo Scientific™ Orion™ 2 STAR pH meter with a Triode™ pH/ATC electrode (9157BNMD) calibrated with a three-point calibration curve at pH = 4.01, 7.00, and 10.01.

3.5.5 X-ray Absorption Spectroscopy

X-ray absorption spectra were measured at SSRL beamline 7-3, with a Rh coated Si harmonic rejection mirror set to E_c = 12 keV, and a fully-tuned Si[220] double-crystal monochromator. The incident intensity was monitored using a N_2 filled ion chamber, and the

energy was calibrated by simultaneous measurement of the absorption spectrum of a Co foil inserted downstream of the sample. X-ray absorption for the electrochemical samples was measured as fluorescence excitation spectra using a solid-state energy-resolving 30-element Ge detector. In addition, transmission mode measurements were made on solid samples of CoPc and CoPc(py), prepared by grinding to a fine powder in BN. X-ray absorbance for all samples was measured by scanning in steps of: 10 eV over the pre-edge (7479-7689 eV), 0.25 eV over the edge (7689-7739 eV) and steps of 1.0 above the edge. The relatively low concentration of Co on the electrodes precluded measurement of EXAFS spectra.

All of the fluorescence channels of each spectrum were analyzed to ensure the absence of artifacts and then averaged. The XANES spectra were then normalized using to the tabulated Co-K absorption cross-sections below (7490-7690 eV) and well above (7790-8200 eV) the edge-region[51] using a single cubic polynomial which is interpolated through the XANES region and scaled using a single scale factor with the M-BACK program.[52]

3.5.6 *In Situ* Electrochemical XAS Measurements

The *in situ* electrochemical XAS measurements were performed using a custom-made XAS cell (Figure A.44) using a Bio-Logic SP200 potentiostat, and electrochemical data was recorded using the Bio-Logic EC-Lab v10.44 software package. The XAS cell chamber held ~40 ml of solution, and the X-ray path length in the cell was ~1 mm to minimize the attenuation of the incident beam. Measurements were performed using an aqueous electrolyte of pH 5 phosphate solution unless otherwise indicated. CoPc, CoPc(py), CoPc-P2VP, and CoPc-P4VP were dropcast onto carbon paper as described above. Note that CoPc is essentially insoluble in water[53, 54] so no

aqueous solution phase measurements were attempted—the CoPc and related systems were always deposited onto a high-surface area carbon support for the aqueous measurements.

The *in situ* electrochemical XAS measurements consisted of a series of controlled-potential electrolysis experiments between 1.2 V and −1.25 V vs SCE. Unless otherwise noted, the working electrode was the catalyst-modified carbon paper, the reference electrode was a commercial saturated calomel electrode (SCE, CH-Instruments) externally referenced to ferrocenecarboxylic acid in 0.2 M phosphate buffer at pH 7 (0.284 V vs. SCE),[55] and the auxiliary electrode was a carbon rod (99.999%, Strem Chemicals Inc.). Prior to each controlled potential electrolysis (CPE) experiment, the cell was flushed with CO_2 or N_2 for ~40 min and then the headspace was blanketed with a flow of CO_2 or N_2 during the measurements. The CO_2 or N_2 used was saturated with electrolyte solution by bubbling through a gas washing bottle filled with the same electrolyte solution used in the XAS cell to minimize electrolyte evaporation in the cell during the course of the measurements. When saturated with CO_2, the pH 5 electrolyte solution had a measured pH = 4.7. The uncompensated resistance of the cell was measured with a single-point high-frequency impedance measurement, and all electrochemical CPE measurements were automatically *i*R-compensated at 85% through positive feedback using the Bio-Logic EC-Lab software. In general, our XAS electrochemical cell had an uncompensated resistance R_u = ∼10 Ω in pH 5 phosphate electrolyte solution. The solutions were not stirred during the CPE experiments, and after each potential change the system was allowed to equilibrate for 15 min before collecting XAS data.

3.5.7 Cyclic Voltammetry (CV) of Modified EPG Electrodes

Cyclic Voltammetry (CV) experiments of modified EPG electrodes were conducted in a glass two-chamber cell under N_2 or CO_2. The working electrodes were catalyst-modified EPG

electrodes, the reference electrode was a commercial SCE, and the auxiliary electrode was a carbon rod separated from the working and reference electrodes by a Nafion membrane. The scan rate was 0.2 V/s, and the CVs were *i*R compensated at 85% through positive feedback using the EC-Lab software.

Prior to modification, 5 mm diameter EPG disk electrodes were manually polished on 600 grit SiC grinding paper (Buehler, Carbimet Plain) followed by sonication in ultrapure water for ~1 min. The same CoPc, CoPc-P4VP, and CoPc(py) deposition solutions used for the preparation of the catalyst-modified carbon paper electrodes were used for the preparation of the catalyst-modified EPG electrodes. Catalyst-modified EPG electrodes were prepared by drop-casting 5 μL of the appropriate deposition solutions onto the EPG electrodes. The disk electrodes were then placed in an oven at ~70 °C for ~15 minutes to allow the solvent to evaporate.

3.5.8 Sealed-Cell Controlled Potential Electrolyses of Modified EPG Electrodes with ZnPc and H_2Pc

Prior to modification, 5 mm diameter EPG disk electrodes were manually polished on 600 grit SiC grinding paper (Buehler CarbiMet) followed by sonication in ultrapure water for ~ 1 min. Modified working electrodes were prepared by first drop-casting 5 μL 0.05 mM ZnPc or 0.05mM H_2Pc deposition solution onto EPG electrode. The disks electrodes were then placed in an oven at ~70 °C for ~15 minutes to allow the solvent to evaporate.

The deposition solutions for P4VP-encapsulated ZnPc or H_2Pc were prepared by dissolving 0.025 g of P4VP in 2.5 mL of either 0.05 mM ZnPc/DMF or 0.05 mM H_2Pc/DMF solution. Modified working electrodes for polymer encapsulated catalysts were prepared by drop-casting 5 μL ZnPc-P4VP/DMF or H_2Pc-P4VP/DMF deposition solution onto EPG electrode, followed by

heating in the oven at ~70 °C for ~15 minutes to allow the solvent to evaporate. Controlled potential electrolysis (CPE) was conducted at room temperature in a custom, gas-tight, two-chamber U-cell as previously described.[19] The main chamber held the modified working electrode and an SCE reference electrode. The auxiliary chamber held the auxiliary carbon rod electrode. The two chambers were separated with a Nafion cation exchange membrane. Prior to each experiment, the electrolyte in both chambers were sparged with CO_2 for ~30 min and then the main chamber was sealed under CO_2 atmosphere. The CPE experiments were conducted with no *i*R compensation for solution resistance, and the reported electrolysis potentials are the actual applied potentials. The uncompensated resistance of the cell was measured with a single-point high-frequency impedance measurement. In general, our electrochemical cell for CPE had an uncompensated resistance R_u = ~200 Ω in pH 5 phosphate electrolyte solution. The product detection and quantification were conducted as previously described.[19] All experiments were performed at least three times with independently prepared electrodes, all reported values are the averages of these repetitions, and uncertainties are reported as standard deviations.

3.6 Conclusion

In this work, we used *in situ* electrochemical XAS to study the oxidation state and coordination environment of Co as a function of applied potential for CoPc, CoPc-P4VP, and CoPc(py) adsorbed onto carbon paper electrodes. We show that the coordination environment of Co changes from 4-coordinate in CoPc/CP to 5-coordinate in CoPc(py)/CP, and that CoPc-P4VP/CP exists mostly, although perhaps not completely, as a 5-coordinate Co complex. The coordination environment of CoPc(py)/CP is pH-dependent, suggesting that the axial coordination of pyridine group to CoPc is modulated by the pH of the electrolyte. The Co coordination environment of CoPc is not influenced by solution pH or applied potential. However, the apparent Co oxidation state, as judged by the edge energy, is largely independent of applied potential for 4-coordinate CoPc but shows a potential-dependent shift for 5-coordinate CoPc-P4VP and CoPc(py), suggesting that the primary-coordination sphere effects may have an important role in modulating the steady-state oxidation state of Co under catalytic turnover conditions. These findings corroborate our previous hypotheses regarding coordination environment of CoPc and related systems under applied potential, and provide new important mechanistic insights regarding the electronic structure of CoPc under CO_2RR conditions.

3.7 References

1. E. E. Benson, C. P. Kubiak, A. J. Sathrum and J. M. Smieja, *Chem. Soc. Rev.*, 2009, **38**, 89-99.
2. J. L. Inglis, B. J. MacLean, M. T. Pryce and J. G. Vos, *Coord. Chem. Rev.*, 2012, **256**, 2571-2600.
3. A. M. Appel, J. E. Bercaw, A. B. Bocarsly, H. Dobbek, D. L. DuBois, M. Dupuis, J. G. Ferry, E. Fujita, R. Hille, P. J. A. Kenis, C. A. Kerfeld, R. H. Morris, C. H. F. Peden, A. R. Portis, S. W. Ragsdale, T. B. Rauchfuss, J. N. H. Reek, L. C. Seefeldt, R. K. Thauer and G. L. Waldrop, *Chem. Rev.*, 2013, **113**, 6621-6658.
4. J. Qiao, Y. Liu, F. Hong and J. Zhang, *Chem. Soc. Rev.*, 2014, **43**, 631-675.
5. A. J. Martín, G. O. Larrazábal and J. Pérez-Ramírez, *Green Chemistry*, 2015, **17**, 5114-5130.
6. T. P. Senftle and E. A. Carter, *Acc. Chem. Res.*, 2017, **50**, 472-475.
7. D. T. Whipple and P. J. A. Kenis, *The Journal of Physical Chemistry Letters*, 2010, **1**, 3451-3458.
8. P. De Luna, C. Hahn, D. Higgins, S. A. Jaffer, T. F. Jaramillo and E. H. Sargent, *Science*, 2019, **364**, eaav3506.
9. W. W. Kramer and C. C. L. McCrory, *Chem. Sci.*, 2016, **7**, 2506-2515.
10. N. Han, Y. Wang, L. Ma, J. Wen, J. Li, H. Zheng, K. Nie, X. Wang, F. Zhao, Y. Li, J. Fan, J. Zhong, T. Wu, D. J. Miller, J. Lu, S.-T. Lee and Y. Li, *Chem*, 2017, **3**, 652-664.
11. M. Zhu, R. Ye, K. Jin, N. Lazouski and K. Manthiram, *ACS Energy Lett.*, 2018, **3**, 1381-1386.
12. H. Wu, M. Zeng, X. Zhu, C. Tian, B. Mei, Y. Song, X.-L. Du, Z. Jiang, L. He, C. Xia and S. Dai, *ChemElectroChem*, 2018, **5**, 2717-2721.
13. Y. Cheng, J.-P. Veder, L. Thomsen, S. Zhao, M. Saunders, R. Demichelis, C. Liu, R. De Marco and S. P. Jiang, *J. Mater. Chem. A*, 2018, **6**, 1370-1375.
14. E. Boutin, M. Wang, J. C. Lin, M. Mesnage, D. Mendoza, B. Lassalle-Kaiser, C. Hahn, T. F. Jaramillo and M. Robert, *Angew. Chem. Int. Ed.*, 2019, **58**, 16172-16176.
15. Y. Wu, Z. Jiang, X. Lu, Y. Liang and H. Wang, *Nature*, 2019, **575**, 639-642.
16. J. Choi, P. Wagner, S. Gambhir, R. Jalili, D. R. MacFarlane, G. G. Wallace and D. L. Officer, *ACS Energy Lett.*, 2019, **4**, 666-672.
17. M. Wang, K. Torbensen, D. Salvatore, S. Ren, D. Joulié, F. Dumoulin, D. Mendoza, B. Lassalle-Kaiser, U. Işci, C. P. Berlinguette and M. Robert, *Nat. Commun.*, 2019, **10**, 3602.
18. M. Zhu, J. Chen, R. Guo, J. Xu, X. Fang and Y.-F. Han, *Applied Catalysis B: Environmental*, 2019, **251**, 112-118.
19. Y. Liu and C. C. L. McCrory, *Nat. Commun.*, 2019, **10**, 1683.
20. J. S. Zeng, N. Corbin, K. Williams and K. Manthiram, *ACS Catal.*, 2020, **10**, 4326-4336.
21. A. De Riccardis, M. Lee, R. V. Kazantsev, A. J. Garza, G. Zeng, D. M. Larson, E. L. Clark, P. Lobaccaro, P. W. W. Burroughs, E. Bloise, J. W. Ager, A. T. Bell, M. Head-Gordon, G. Mele and F. M. Toma, *ACS Applied Materials & Interfaces*, 2020, **12**, 5251-5258.
22. Z. Yang, X. Zhang, C. Long, S. Yan, Y. Shi, J. Han, J. Zhang, P. An, L. Chang and Z. Tang, *CrystEngComm*, 2020, **22**, 1619-1624.
23. X. Zhang, Z. Wu, X. Zhang, L. Li, Y. Li, H. Xu, X. Li, X. Yu, Z. Zhang, Y. Liang and H. Wang, *Nat. Commun.*, 2017, **8**, 14675.
24. J. Wang, X. Huang, S. Xi, J.-M. Lee, C. Wang, Y. Du and X. Wang, *Angew. Chem. Int. Ed.*, 2019, **58**, 13532-13539.
25. C. M. Lieber and N. S. Lewis, *J. Am. Chem. Soc.*, 1984, **106**, 5033-5034.

26. T. Yoshida, K. Kamato, M. Tsukamoto, T. Iida, D. Schlettwein, D. Wöhrle and M. Kaneko, *J. Electroanal. Chem.*, 1995, **385**, 209-225.
27. T. Abe, T. Yoshida, S. Tokita, F. Taguchi, H. Imaya and M. Kaneko, *J. Electroanal. Chem.*, 1996, **412**, 125-132.
28. M.-S. Liao and S. Scheiner, *J. Chem. Phys.*, 2001, **114**, 9780-9791.
29. B. R. Kozub and R. G. Compton, *Sensors and Actuators B: Chemical*, 2010, **147**, 350-358.
30. F. Bedioui, E. De Boysson, J. Devynck and K. J. Balkus, *J. Electroanal. Chem. Interfacial Electrochem.*, 1991, **315**, 313-318.
31. H. A. Dinçer, A. Koca, A. Gül and M. B. Koçak, *Dyes and Pigments*, 2008, **76**, 825-831.
32. D. Kulaç, M. Bulut, A. Altındal, A. R. Özkaya, B. Salih and Ö. Bekaroğlu, *Polyhedron*, 2007, **26**, 5432-5440.
33. W. I. Dzik, J. I. van der Vlugt, J. N. H. Reek and B. de Bruin, *Angew. Chem. Int. Ed.*, 2011, **50**, 3356-3358.
34. A. L. Smith, K. I. Hardcastle and J. D. Soper, *J. Am. Chem. Soc.*, 2010, **132**, 14358-14360.
35. A. L. Smith, L. A. Clapp, K. I. Hardcastle and J. D. Soper, *Polyhedron*, 2010, **29**, 164-169.
36. Y. Liu, K. Y. Leung, S. E. Michaud, T. L. Soucy and C. C. L. McCrory, *Comments Inorg. Chem.*, 2019, **39**, 242-269.
37. L. S. Kau, D. J. Spira-Solomon, J. E. Penner-Hahn, K. O. Hodgson and E. I. Solomon, *Journal of the American Chemical Society*, 1987, **109**, 6433-6442.
38. S. E. Shadle, J. E. Penner-Hahn, H. J. Schugar, B. Hedman, K. O. Hodgson and E. I. Solomon, *Journal of the American Chemical Society*, 1993, **115**, 767-776.
39. J.-P. Dodelet, in *N4-Macrocyclic Metal Complexes*, eds. J. H. Zagal, F. Bedioui and J.-P. Dodelet, Springer New York, New York, NY, 2006, DOI: 10.1007/978-0-387-28430-9_3, pp. 83-147.
40. N. C. Tomson, K. D. Williams, X. Dai, S. Sproules, S. DeBeer, T. H. Warren and K. Wieghardt, *Chemical Science*, 2015, **6**, 2474-2487.
41. H. C. Brown and X. R. Mihm, *J. Am. Chem. Soc.*, 1955, **77**, 1723-1726.
42. J. P. Krogman, J. R. Gallagher, G. Zhang, A. S. Hock, J. T. Miller and C. M. Thomas, *Dalton Trans.*, 2014, **43**, 13852-13857.
43. B. Hu, A. "Bean" Getsoian, N. M. Schweitzer, U. Das, H. Kim, J. Niklas, O. Poluektov, L. A. Curtiss, P. C. Stair, J. T. Miller and A. S. Hock, *J. Catal.*, 2015, **322**, 24-37.
44. P. Cocolios and K. M. Kadish, *Isr. J. Chem.*, 1985, **25**, 138-147.
45. A. B. P. Lever and J. P. Wilshire, *Can. J. Chem.*, 1976, **54**, 2514-2516.
46. M.-S. Liao and S. Scheiner, *J. Chem. Phys.*, 2002, **117**, 205-219.
47. Y. E. Kirsh and O. P. Komarova, *Polymer Science U.S.S.R.*, 1976, **18**, 223-228.
48. N. Furuya and K. Matsui, *J. Electroanal. Chem. Interfacial Electrochem.*, 1989, **271**, 181-191.
49. J. Janczak and R. Kubiak, *Inorg. Chim. Acta*, 2003, **342**, 64-76.
50. F. Cariati, D. Galizzioli, F. Morazzoni and C. Busetto, *J. Chem. Soc., Dalton Trans.*, 1975, DOI: 10.1039/DT9750000556, 556-561.
51. W. McMaster, N. Del Grande, J. Mallett and J. Hubbell, *Compliation of x-ray cross-sections*, Lawrence Livermore National Laboratory: Livermore, CA, 1969.
52. T.-C. Weng, G. S. Waldo and J. E. Penner-Hahn, *Journal of Synchrotron Radiation*, 2005, **12**, 506-510.
53. A. R. Harutyunyan, A. A. Kuznetsov, O. A. Kuznetsov and O. L. Kaliya, *J. Magn. Magn. Mater.*, 1999, **194**, 16-21.

54. W. Shi-Kang, Z. Hou-Chen, C. Guo-Zhu, X. Da-Nian and X. Hui-Jun, *Acta Chimica Sinica English Edition*, 1985, **3**, 21-25.
55. E. Liaudet, F. Battaglini and E. J. Calvo, *J. Electroanal. Chem. Interfacial Electrochem.*, 1990, **293**, 55-68.

Chapter 4: The Effect of σ-donor Strength of Axially-Coordinating Ligands on the CO_2 Reduction Activity of CoPc

4.1 Preface

This work presents a study of the effect of axial coordinating ligand on a cobalt complex for electrochemical CO_2 reduction (CO_2RR). We show that the increased CO_2RR activity observed upon axial coordination to CoPc is due to the increased σ-donor strength of the axial ligand on CoPc. In addition, carbon black powders were used as electron shuttles within the catalyst-polymer composite system to increase the electron transport in the polymer thus increase the overall catalytic activity of the catalyst. These findings are crucial for the development of new electrocatalysts for CO_2RR.

This chapter of my dissertation is derived from a manuscript that is currently in preparation. I am the first author on this manuscript and was responsible for all the electrochemical measurements and analysis as well as the writing and preparation of the manuscript. The other authors are Weijie Feng, Kevin E. Rivera-Cruz, and Charles C. L. McCrory. Weijie Feng and Enrique Rivera Cruz are responsible for calculating energies of molecular orbitals using DFT analysis. Charles C. L. McCrory provided significant insight and expertise in electroanalytical techniques and analysis.

4.2 Abstract

In the previous studies, it was shown that axial coordination of a pyridyl moieties to CoPc (either exogenous or within poly-4-vinylpyridine polymer) dramatically increases the complex's activity for CO_2RR. We hypothesize that axial coordination to the Co active site leads to an increase in the Co dz^2 orbital, which increases the complex's nucleophilicity and facilitates CO_2 coordination compared to the parent CoPc. The magnitude of the energy increase in the Co dz^2 orbital should depend on the σ-donor strength of the axial ligand—a stronger σ-donating ligand (L) will increase the overall CO_2RR activity of axially coordinated CoPc(L) and vice versa. To test this, we have studied a series of CoPc(L) complexes where the σ-donor strength of L is varied. We show an increase in the observed overall electrochemical activity of the corresponding CoPc(L) as L moves from less to more σ-donating ligand strength. This observation of the trend of the electrochemical activity as a function of σ-donor strength supports our hypothesis that the increased CO_2RR activity observed upon axial coordination to CoPc is due to the increased energy of the dz^2 orbital, which is crucial for the development of new electrocatalyst for CO_2RR.

4.3 Introduction

The electrochemical conversion of CO_2 into energy-rich fuels and chemicals has gained significant interest as a potential strategy for simultaneously mitigating global CO_2 concentration and effectively storing intermittent renewable energy from sources such as solar and wind.[1-12] At the same time, intermittent electricity generation can be stored in an energy-dense, portable form in chemical bonds. However, poor product selectivity due to the competitive hydrogen evolution reaction (HER) is still a major obstacle to the development of CO_2 reduction (CO_2RR).[13-19]

Our recent studies have shown that encapsulating molecular catalysts within polymers that specifically modulate the coordination environment surrounding the metal active sites leads to the increased CO_2RR selectivity and activity.[20, 21] We have demonstrated that embedding cobalt phthalocyanine (CoPc) into poly-4-vinylpyridine (P4VP) polymers dramatically increases the complex's activity and selectivity for the electrochemical reduction of CO_2 to CO. It has been hypothesized that this increase in activity and selectivity was due to three effects: i) axial-coordination of pyridyl in P4VP to the Co center increases the catalyst's nucleophilicity for CO_2 binding, ii) H-bonding interactions that stabilize reactive CO_2 intermediates, and iii) control of H^+ delivery through use of the partially protonated pyridyl residues within the polymer as proton relays.[20, 21] In particular, the axial coordination of pyridyl groups to CoPc plays an important role in the catalytic mechanism for CO_2RR. We hypothesize that the axial coordination increases the energy of the Co dz^2 orbital which binds and activates the CO_2, thus promoting CO_2RR.

To test this, we have modulated the σ-donor strength of the axial ligand on CoPc for CO_2 reduction. We show that increasing the σ-donor strength of the axial ligand increases the energy of Co dz^2 orbital, as evidenced by Density Functional Theory (DFT) calculations and UV-vis studies. The increase σ-donor strength of the axial ligand also leads to an increase in the overall

catalytic activity of CoPc complex for CO_2 reduction, providing experimental evidence that the dz^2 energy and catalytic activity are likely correlated.

In addition, we selected the most active axial ligand that we tested on CoPc and immobilized the complex into the poly-2-vinylpyridine (P2VP) matrix on a carbon black support where synergistic primary-, secondary- and outer-coordination sphere effects are present and the rate of electron transport is increased. The composite system with added carbon black achieved high activity (~ 8 mA cm^{-2}, TOF = 12 s^{-1}) and selectivity (~ 87 % Faradaic efficiency) for the CO_2RR to CO. We anticipate this work provides crucial insights into the design of highly-active electrocatalytic CO_2RR systems for selective CO_2 conversion.

4.4 Results and Discussion

In this chapter, the effects of σ-donor strength of the axial ligand (Figure 4.1) on CoPc has been investigated using a combined experimental and theoretical approach. We have modulated the σ-donor strength of the axial ligand through systematic modification of the coordinating pyridine: i) through para-substitution of the pyridine with electron donating substituents, ii) by adding N groups into the conjugated pyridine ring, and iii) by modifying σ-donating imidazole and pyrazole rings. The ligands for each series are shown in Figure 4.1 in the order of increasing σ-donor ability from left to right by measuring the coupling constant between the donor group and the methylmercury (II) cation which is an ideal ion for investigating the donor properties of unidentate ligands.[22-26]

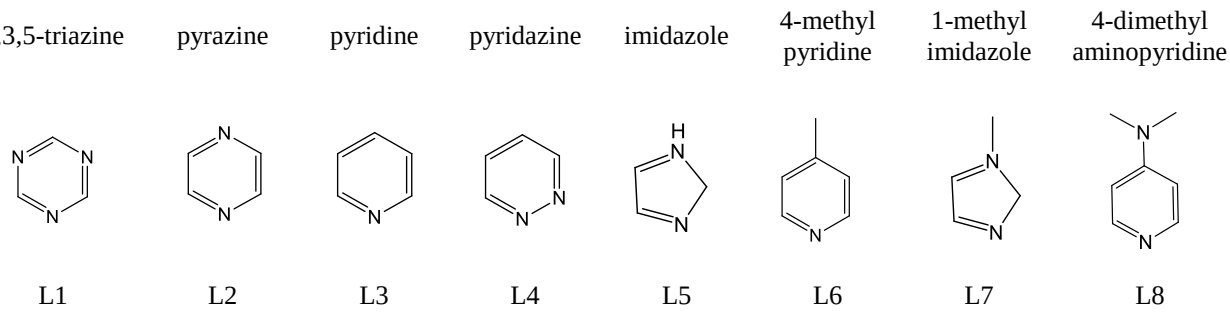

Figure 4.1 Axial ligand (L) on CoPc investigated in this work

4.4.1 UV-Vis Study

To quantify the σ-donating nature of the axial ligands in CoPc(L) catalysts, we conducted UV-Vis spectroscopy studies of CoPc(L) deposition solutions (see Experimental section for more details). As shown in Figure A.55, the Q band of CoPc near 660 nm is red-shifted to 670 nm in UV-vis absorption spectrum of CoPc(L) solutions. These are consistent with that the Q bands of metalloporphyrin-like complexes will red shift when there is an electron-donating ligand

coordinated axially with the central metal ions,[27, 28] leading to the more negative electron density of the central metal ions.[29] Moreover, a more red-shift indicates a more electron-donating ability of the ligand.[29] Hence, the red-shifts presented in the UV-vis spectra of CoPc and CoPc(L) can be used to identify the formation and the extent of the coordination bonding between axial ligands and CoPc.

The magnitude of Q band red-shifts in the UV-vis spectra of CoPc(L) solutions compared to that of CoPc are plotted in Figure 4.2b as function of σ-donor strength. The magnitude of the Q band red-shift increases with increasing axial ligand σ-donor strength. The Q band shift data is consistent with the ordering of the σ-donating abilities of axial ligand L.

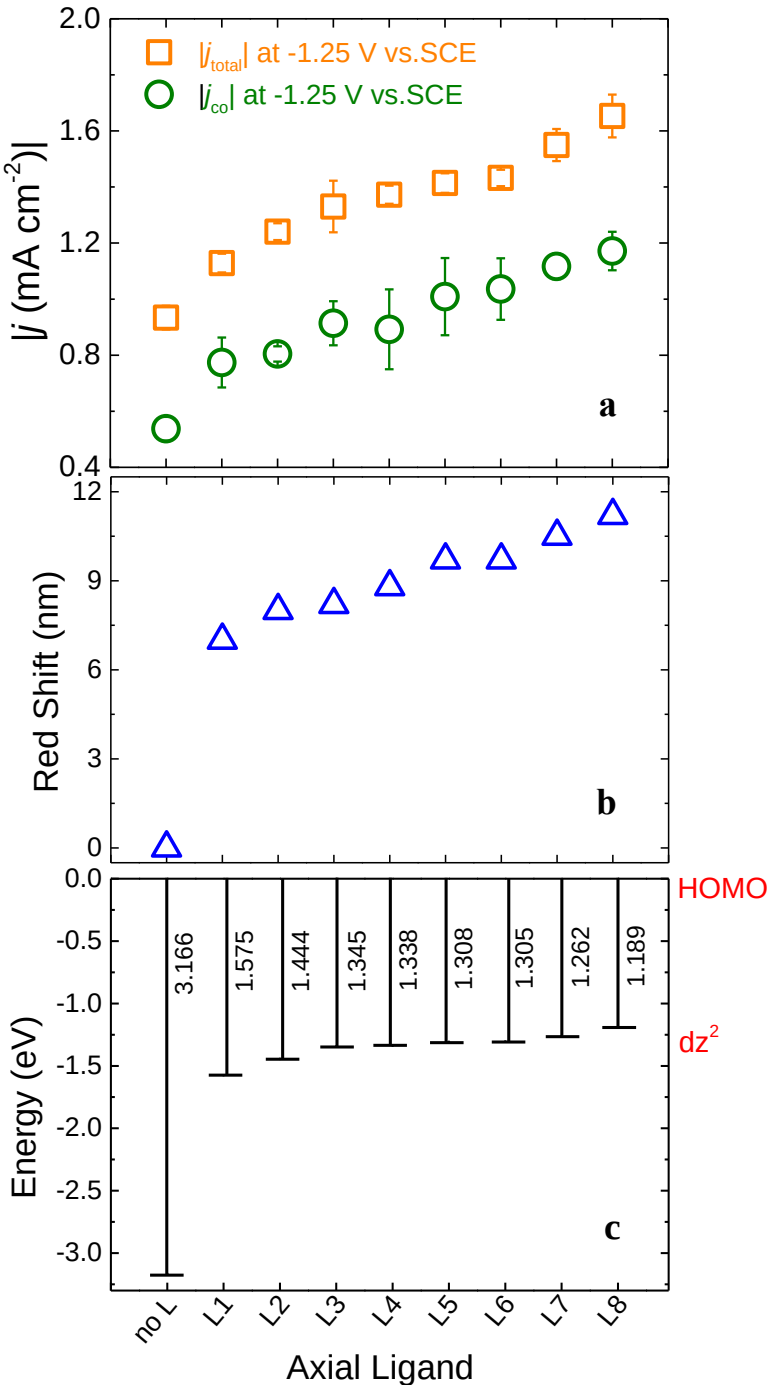

Figure 4.2 a, Measured electrochemical CO_2RR activity; **b,** Measured Q band red-shifts in the UV-vis spectra; **c,** Calculated HOMO-dz^2 energy difference and of CoPc(L). Note that the j_{CO} was calculated by multiplying the total *j* measured under RDE CA by the ε_{CO} measured under 2 h CPE.

4.4.2 Density Functional Theory (DFT) Calculations

To understand how does the axial coordination of ligands L1-L8 influence the CoPc electron structure, the energies of the HOMO and dz^2 orbitals in CoPc and CoPc(L) were simulated by density functional theory (DFT) calculations with B3LYP functional using the Gaussian 09 package. Our calculations show that the highest occupied molecular orbital (HOMO) of all the catalyst complexes investigated are ligand-based (Figure 4.3). Moreover, the energy of Co dz^2 orbital in CoPc(L) dramatically increases upon axial coordination compared to the parent CoPc complex. Figure 4.2c presents the magnitude of the energy increase of Co dz^2 orbital with respect to HOMO in each CoPc(L) complex. The DFT calculated the increase of dz^2 orbital for CoPc(L) complexes are consistent with the Q band data (Figure 4.2 b, c), strongly supporting our hypothesis that the axial coordination to CoPc increases the energy of the Co dz^2 orbital, which is dependent on the σ-donor strength of the axial ligand.

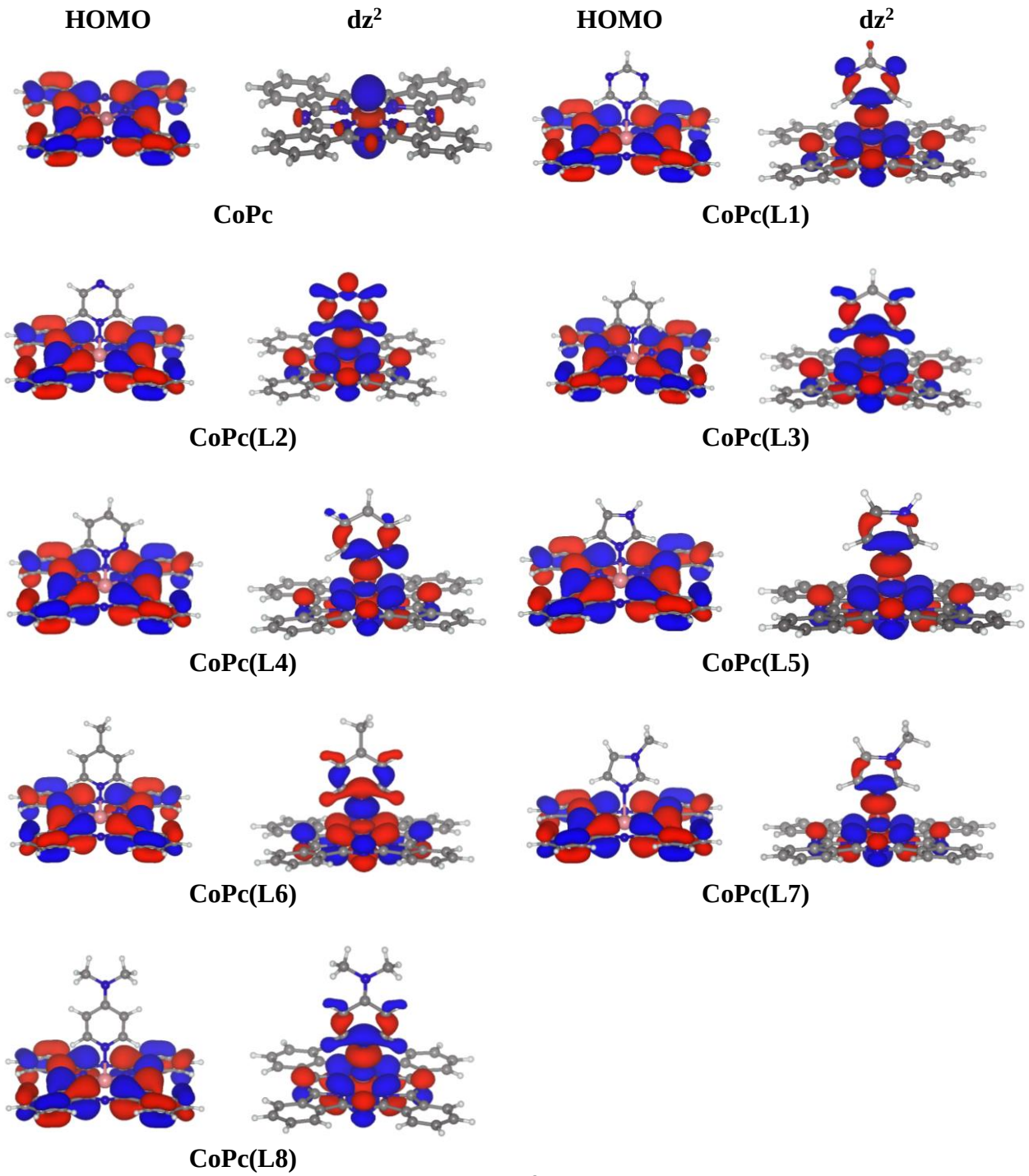

Figure 4.3 Schematic presentation of the HOMO (left) and dz^2 orbitals (right) CoPc and CoPc(L) molecules with the calculated charge distributions (red and blue) based on DFT calculations (red ball = Co, blue ball = N, grey ball = C, white ball = H).

4.4.3 Electrochemical Measurements

To investigate the influence of σ-donor strength of the axial coordination on CO_2RR activity of CoPc in the absence of the polymer film, edge plane graphite (EPG) electrodes modified with the axially coordinated catalysts, CoPc(L1-L8), were prepared using a deposition solution of CoPc in DMF solution containing the axial ligands L1-L8, respectively. A large excess of the axial ligand (1,000 times) was employed in the deposition solutions to ensure the equilibrium would favor the axially coordinated species.[27] The electrochemical performance of each CoPc(L) catalyst was investigated using a three-electrode electrochemical cell in a rotating disk electrode configuration. The CO_2RR activity was evaluated by rotating disk electrode voltammetry (RDEV) at 1 mV s^{-1} scan rate and 1600 rpm rotation rate from –0.9 to –1.4 V vs. SCE. This scan rate is slow enough to ensure steady-state behavior at the electrode surface, and the rotation rate is sufficient fast to aid in product removal and limit bubble formation from evolved CO and H_2 at the electrode surface. RDEVs of all the catalysts studied are shown in Figure 4.4. Under a CO_2 atmosphere, the plateau of the catalytic wave at approximately –1.25 V vs. SCE for all the modified electrodes was attributed to catalytic CO_2 reduction. In addition, each catalyst was investigated by a series of controlled-potential chronoamperometric (CA) steps. In such experiments, the potential is held constant for 2 min, and the resulting current-time should decay to a steady-state value at time > 2s.[30, 31] Representative steady-state currents determined from CA step measurements for each catalyst are shown as red open squares in Figure 4.4, and show good agreement when overlaid with the RDEV measurements, which indicates steady-state conditions.

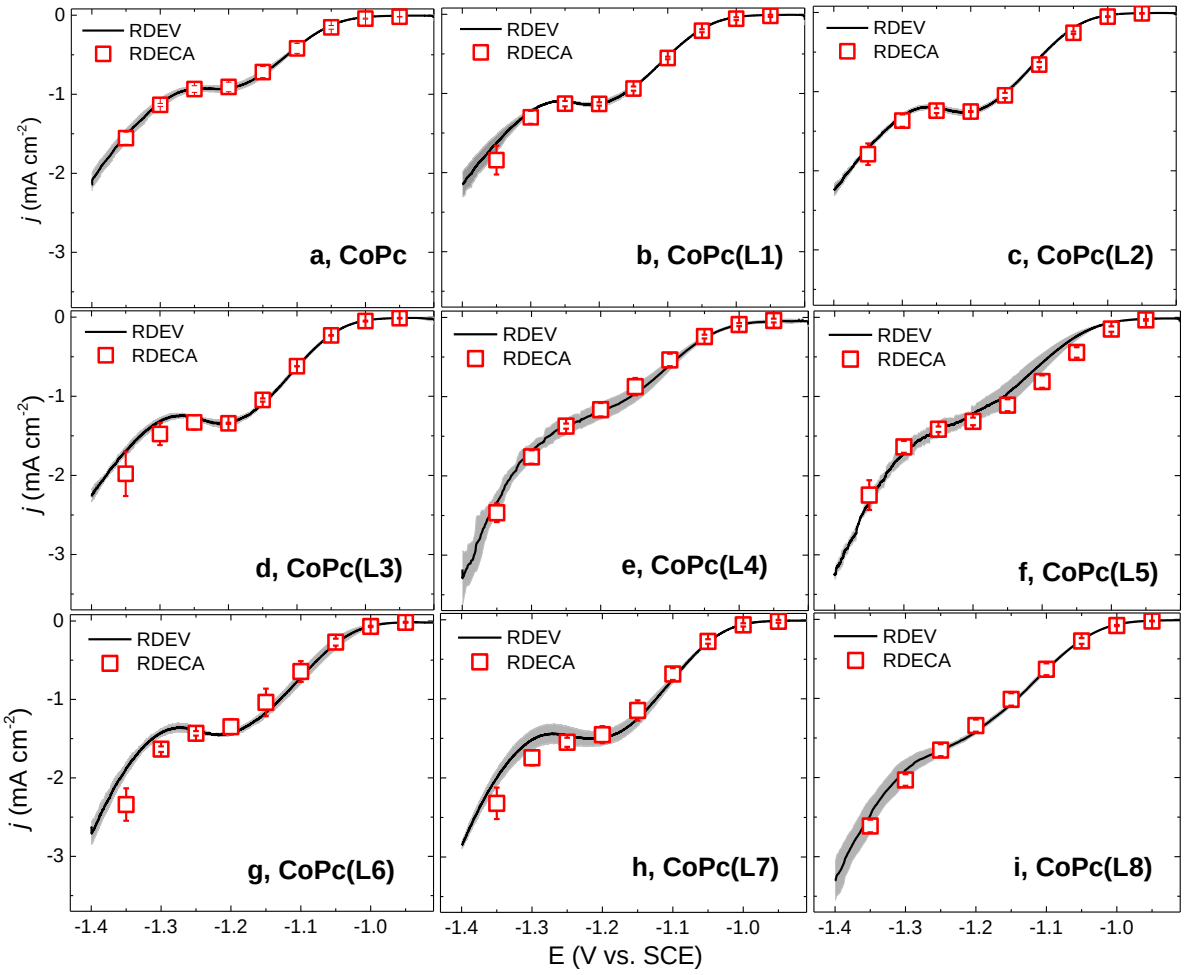

Figure 4.4 Rotating disk electrode voltammogram (RDEV) of the CO2RR by CoPc(L) catalysts at 1 mV s^{-1} scan rate and 1600 rpm in CO_2 saturated pH 5 phosphate solution. The results of 2 min rotating disk electrode chronoamperometric (CA) steps (red open square) are shown for comparison, and the close overlay of the data suggests good approximation of steady-state conditions.

The results of 2 min rotating disk electrode CA steps (red open square) in Figure 4.4 at –1.25 V vs. SCE are used primarily for comparison of CO_2RR activities between axial ligand (L) investigated in this study, and the results are plotted in Figure 4.2a. We show an increase in the CO_2 reduction activity of the corresponding CoPc(L) as the σ-donor ability of L is increased. We believe that the enhanced activity of CoPc(L) compared to parent complex shows that the coordinating ligand effects is responsible for the observed increases in the rate of the CO_2RR. We hypothesize that the axial coordination raises the energy of the cobalt dz^2 orbital. When the metal

center is reduced to Co(I), filling the dz^2 orbital (Figure 4.5), the metal becomes a stronger nucleophile, and it better able to bind and activate the Lewis acidic carbon of CO_2.[20] Therefore, the observation of the change of the CO_2 reduction activity as function of σ-donor strength supports our hypothesis that the increased CO_2 reduction activity observed upon axial coordination to CoPc is correlated with the increased energy of the dz^2 orbital.

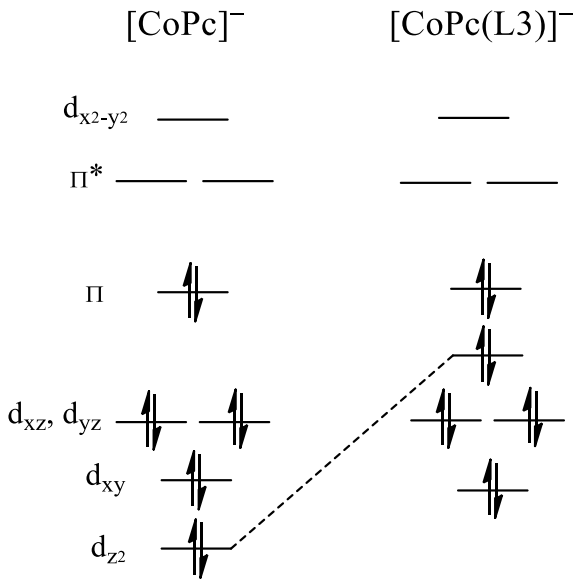

Figure 4.5 Relative energies of the cobalt d-orbitals and relevant ligand π orbitals in the 1 e^- reduced form of CoPc and CoPc(L3). Axial coordination increases the energy of the dz^2 orbital, increasing nucleophilicity for CO_2 binding.

Controlled potential electrolysis (CPE) were performed at –1.25 V vs. SCE to assess Faradaic efficiencies for CO_2 reduction by CoPc and CoPc(L) modified electrodes. Electrolyses were conducted for 2 h under a CO_2 atmosphere in a constantly stirred, CO_2 saturated, pH 5 phosphate electrolyte in a gas-tight, two-compartment electrolysis cell as previously described in Chapter 2.[21] The product detection and quantification were conducted as previously described in Chapter 2.[21] All experiments were performed at least three times with independently prepared electrodes. The results of these experiments are summarized in Figure 4.6 and Table A.9, all reported values are the averages of these repetitions, and uncertainties are reported as standard

deviations. As shown in Figure 4.6, the only products observed for CoPc and CoPc(L) catalysts were CO and H_2, no liquid products were detected within our detection limits (~ 100 μM). Faradaic efficiencies (ε) for CO are ~ 60 % for CoPc and ~ 70 % for CoPc(L) catalysts. The observed higher activity and ε_{CO} for CoPc(L) is consistent with our previous findings that the coordinating ligand effect is responsible for the enhanced CO_2 reduction, and the formation of axial coordination shifted the rate-determining step from a CO_2 binding step to a subsequent protonation step.[21] The ε_{CO} for all the axially-coordinated CoPc(L) studied are relatively the same, which suggests that the effect of σ-donating strength of the axial ligand does not change the rate-determining step of CO_2 reduction in CoPc(L). In addition, the activity for CO_2 reduction under CPE increases as a function of σ-donating strength of the axial ligand is consistent with the measurements under RDE CA measurements.

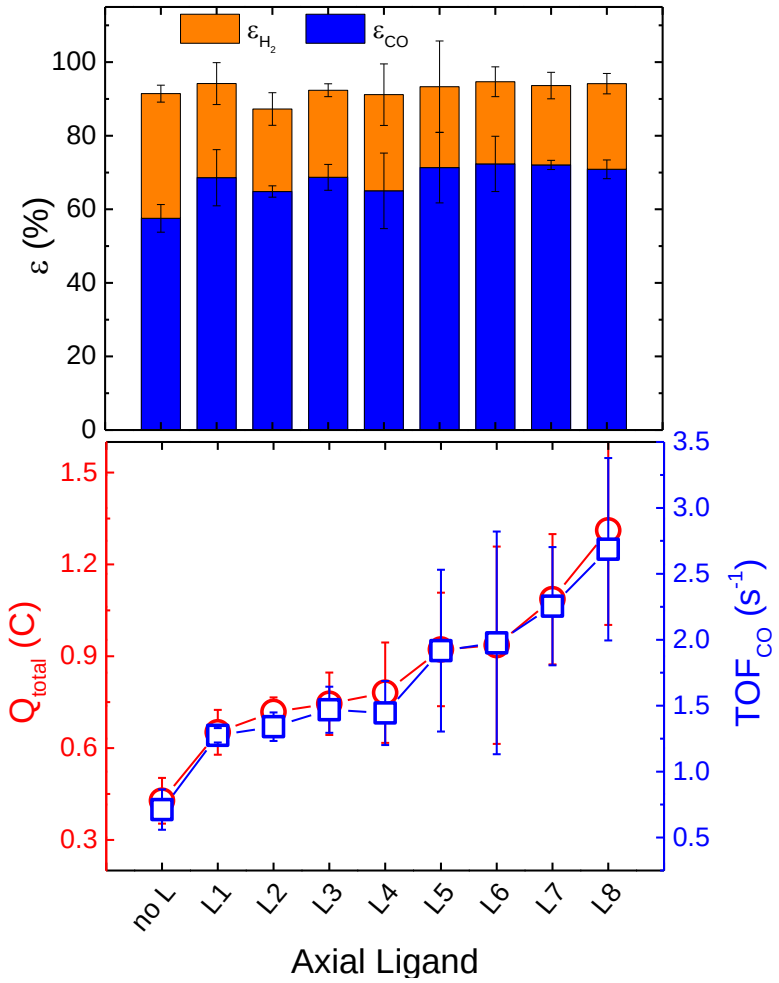

Figure 4.6 CO_2RR performance of CoPc and CoPc(L) modified electrodes **a,** Faradaic efficiencies (ε), and **b,** Total activity (Q_{total}) (red open circle) and turnover frequencies for CO (TOF_{CO}) (blue open square) obtained from 2 h CPE at –1.25 V vs. SCE in CO_2 saturated pH 5 phosphate electrolyte under CO_2 atmosphere. All reported values are averages from 3 independent measurements, and all errors are given as standard deviations.

4.4.4 Dependence of CO_2RR Performance on Catalyst Loading on Carbon Black

The most active complex, CoPc(L8) complex was immobilized into the P2VP matrix (denoted as CoPc(L8)-P2VP) to examine the effect of axial coordination on the CO_2RR in the presence of the synergistic secondary- and outer-coordination sphere effects. Previous experiments have shown that increasing CoPc-P4VP film thickness while keeping the CoPc-to-P4VP ratio constant results in a corresponding decrease in catalytic activity.[21] We hypothesize that there is a limiting film thickness after which additional CoPc is no longer electronically accessible due to inefficient charge transport through the non-conducting P4VP polymer. In order to increase the activity of the composite for CO_2RR, carbon black (CB) which can increase the conductivity of the polymer matrix[32] was incorporated into the CoPc(L8)-P2VP composite to facilitate electron transport to the embedded catalyst sites.

When we prepared sufficient amount of carbon black (1 % w/v) with different CoPc(L8)-P2VP catalyst loadings ranging from 6.37×10^{-9} to 1.02×10^{-7} mol cm^{-2} CoPc(L8), as shown in Figure 4.7, we see an initial increase in activity with increasing film thickness up to 9 mA cm^{-2}. However, further increase of catalyst up to 1.02×10^{-7} mol cm^{-2} CoPc(L8) decreased the CO_2RR activity, probably due to the CO_2 transport limitations resulting from the thick catalyst layer. Therefore, the above result indicates an optimum catalytic activity of 9 mA cm^{-2} for CoPc(L8)-P2VP/CB composite system for CO_2RR.

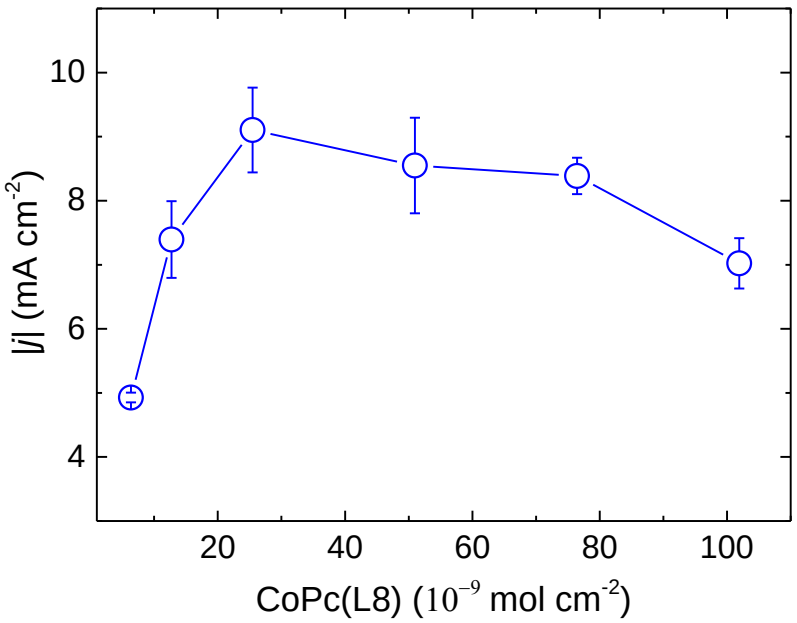

Figure 4.7 CO_2 reduction activity as a function of the polymer and catalyst loading with carbon black (CB) incorporated. Here, CoPc loading is used as a proxy for polymer film thickness.

2 h CPE experiments were performed at –1.25 V vs. SCE to assess product distributions for CO_2RR by CoPc(L8)-P2VP/CB composite. Electrolyses were conducted at the same conditions described previously, and the results are summarized in Table A.9. The only products observed were CO and H_2, no liquid products were detected. ε_{CO} for CoPc(L8)-P2VP/CB is ~ 85 %, much higher than CoPc(L8), which is attributed to the secondary- and outer-coordination sphere effects that arise from the partially protonated pyridyl groups throughout P2VP. This result indicates that carbon black greatly improves the electron transport in the catalyst-polymer without decreasing the selectivity for CO_2RR. The slightly higher ε_{H2} is attributed to the background HER from carbon black support.

The integration of molecular species onto electrodes for electrochemical CO_2RR gives an enhancement of the catalytic activity[20, 33-35] and overcomes limitations from diffusion-controlled

electrocatalysis with catalysts in the bulk solution.[36-39] In this case, carbon black serves as a platform for the immobilization of molecular electrocatalysts. Their high surface area and excellent conductivity allow grafting of large amounts of electrocatalytically active species while retaining good electron transfer properties. The CoPc(L8)-P2VP/CB composite catalyst shows much stronger CO_2RR activity compared to the previously reported CoPc(py)-P2VP system immobilized on EPG electrode,[21] which suggests that the carbon black support plays an important role on the catalytic activity towards CO_2RR. We hypothesize that the increased catalytic activity is attributed to the large surface area and high electron conductivity of carbon black as well as the π-π interaction between the polymer and the carbon black surface.

4.5 Experimental

4.5.1 Materials and Chemicals

All purchased chemicals were used as received unless otherwise specified. Cobalt phthalocyanine (CoPc, 97%), poly-2-vinylpyridine (P2VP, average Mw ~ 159,000), N,N-Dimethylformamide (DMF, ACS grade), 1,3,5-triazine (97%), pyrazine (> 99%), pyridine (ACS grade, ≥ 99%), pyridazine (98%), imidazole (99%), 4-methyl pyridine (99%), 1-methyl imidazole (≥ 99%), 4-dimethyl aminopyridine (≥ 99%), sodium phosphate monobasic (BioXtra, > 99.0%), graphite power (< 20 μm, synthetic), and Nafion-117 cation exchange membrane (Nafion) were purchased from Sigma Aldrich. Nitric acid (TraceMetal grade, 67-70 %) were purchased from Fisher Scientific. Cobalt ICP standard (1000 ppm Co in 3 % HNO_3) was purchased from Ricca Chemical Company. Diamond polishing slurries were purchased from Struers. Edge-plane graphite disk electrodes (5 mm diameter, effective electrode area: 0.114 cm^2) were purchased from Pine Research Instrumentation. Glassy carbon disk electrodes (5 mm in diameter, effective electrode area 0.196 cm^2 were purchased from HTW Germany. Compressed CO_2 gas (99.8 %) was purchased from Cryogenic Gases. All water used in this study was ultrapure water (18.2 MΩ·cm resistivity) purified with a Thermo Scientific GenPure UV-TOC/UF xCAD-plus water purification system.

4.5.2 Preparation of Deposition Solutions and Modified Edge Plane Graphite (EPG) Electrodes

All deposition solutions were prepared from DMF solutions containing 0.05 mM CoPc. The deposition solutions for axial coordinated CoPc were prepared by dissolving the 0.05 M of axial ligad (L) in the 0.05 mM CoPc/DMF solution. Prior to modification, 5 mm diameter edge

plane graphite (EPG) disk electrodes (3.81 mm EPG disk encapsulated in epoxy, 0.114 cm^2 effective surface area, Pine Research Instrumentation) were manually polished with 600 grit SiC grinding paper (Buehler CarbiMet) followed by sonication in ultrapure water for ~ 1 min. Modified working electrodes were prepared by first drop-casting 5 μL deposition solution onto EPG electrode. The disks electrodes were then placed in a drying oven at ~ 70 °C for ~ 15 minutes to allow the solvent to evaporate.

4.5.3 Preparation of Modified Electrodes with Carbon Black Support

The deposition solutions were prepared from DMF solutions containing 0.05 mM CoPc, CoPc molecules were dispersed in DMF via sonication for 30 minutes, followed by the addition of 3% w/v P2VP and allowed to disperse via 30-minute sonication. 1% w/v carbon black (CB) was added to the solution, followed by sonication for 30 minutes. The mixture was stirred for 12 h, which was then centrifuged at 14000 rpm for 30 minutes at –11 ºC. The supernatant was decanted, and 1 mL of fresh DMF was added. The resulting deposition suspension was vortexed for 30 sec at 3000 rpm, and sonicated for 30 sec.

For the CoPc(L8)-P2VP composite with different CoPc(L8) concentrations ranging from 0.125 mM to 0.2 mM CoPc in the deposition solution, films were prepared by first mixing different concentrations of CoPc(L8) and 3 % w/v P2VP in DMF solution followed by addition of ~20 μm CB particles (1% w/v) to adsorb the catalyst-polymer composite before finally depositing the resulting suspension onto the glassy carbon electrode surfaces. This film preparation strategy allows for independent control of catalyst, polymer, and CB loading.

Prior to modification, 5 mm diameter glassy carbon (GC) disk electrodes were polished on a Struers LaboPol-5 Polisher. The GC electrodes were loaded into a brass electrode holder with

polishing side on a Struers MD-Floc cloth polishing pad. The electrodes were polished under 2 unit pressure with sequential diamond polishing slurry of the following sizes: 9 µm, 6 µm, 3 µm, and 1 µm, each for 1 minute at 200 rpm rotation rate. The electrodes were sonicated in isopropanol for 1 min followed by 1 min of sonication in ultrapure water between each polishing.

The modified GC electrodes were prepared by drop-casting 5 µL of the deposition suspension, allowing the surface to dry in an oven at 60 ºC for 15 minutes, and was repeated by a second coating of 5 µL of the deposition suspension.

4.5.4 Electrochemical Measurements

Electrochemical measurements were conducted using a Bio-Logic SP200 potentiostat, and data were recorded using the Bio-Logic EC-Lab software package. Reference electrodes were commercial saturated calomel electrodes (SCE, CH-Instruments) externally referenced to ferrocenecarboxylic acid in 0.2 M phosphate buffer at pH 7 (0.284 V vs. SCE),[40] and auxiliary electrodes were carbon rods (99.999 %, Strem Chemicals Inc.). Working electrodes were the modified EPG electrodes described previously. In all cases, the working electrode was separated from the auxiliary electrode by a Nafion membrane. Unless otherwise noted, all electrochemical measurements were conducted at least three times with independently prepared electrodes, all values reported are the averages of these repetitions, and all reported errors are standard deviations.

For rotating disk CA step measurements, the modified EPG working electrodes were mounted in a Pine Research Instrumentation E6-series Change Disk rotating disk electrode (RDE) assembly attached to an MSR rotator. CA measurements were conducted at 1600 rpm with 2-min potential steps from -0.95 V to -1.35 V vs. SCE at 0.05 V increments. The 1600 rpm rotation rate was meant to ensure steady-state delivery of substrate to our surface to allow for accurate

comparisons of catalytic rates. Note that 1600 rpm does not imply kinetically-limiting conditions—mass transport to catalyst sites in non-uniform catalyst-polymer composite films is not governed by simple Koutecký-Levich kinetics.[41-43] Rotating disk CA measurements were conducted in a custom two-compartment glass cell as previously used.[21] The first compartment held the rotating disk working electrode and reference electrode in ~ 30 mL solution, and the second compartment held the auxiliary electrode in ~ 15 mL solution. The two compartments were separated by a Nafion cation exchange membrane. Both compartments were sparged with CO_2 for ~30 min prior to each set of measurements, and the headspace was blanketed with CO_2 during the measurements. The CO_2 used was first saturated with electrolyte solution by bubbling through a gas washing bottle filled with the same electrolyte solution used in the cell to minimize electrolyte evaporation in the cell during the course of the measurements. IR drop was compensated at 85 % through positive feedback using the Bio-Logic EC-Lab software. In general, our electrochemical cell for CA measurement had Ru = ~100 Ω in pH 5 phosphate solution.

Controlled potential electrolyses (CPE) were conducted at room temperature in two custom, gas-tight, two-chamber U-cells as previously described.[21] The modified working electrode was held in a RDE internal hardware kit (Pine Research Instrumentation) and mounted into a custom PEEK sleeve. For the electrolysis measurements, the main chamber held the working electrode and an SCE reference electrode in ~ 25 mL of electrolyte, and the total headspace in the main chamber was measured individually after each experiment by measuring the amount of water needed to refill the main chamber. The auxiliary chamber held the auxiliary carbon rod electrode in 15 mL electrolyte. The two chambers were separated with a Nafion cation exchange membrane. Prior to each experiment, both chambers were sparged with CO_2 for ~ 30 min and then the main chamber was sealed under CO_2 atmosphere**.** The uncompensated resistance of the cell was

measured with a single-point high-frequency impedance measurement. In general, our electrochemical cell for CPE had Ru = ~200 Ω in pH 5 phosphate solution. The product detection and quantification were conducted as previously described.[21] All experiments were performed at least three times with independently prepared electrodes, all reported values are the averages of these repetitions, and uncertainties are reported as standard deviations.

4.5.5 UV-Vis Spectroscopy Study

Liquid CoPc(L)/DMF samples were analyzed using PerkinElmer Lambda 265 UV-Vis Spectrophotometer with fast mode and baseline correction. 0.01 mM CoPc/DMF solution and 0.01 mM CoPc(L) solutions are prepared by diluting the corresponding deposition solution by 5 times (see Preparation of Deposition Solutions).

4.5.6 Density Functional Theory (DFT) Calculation Methods

The energies of the HOMO and dz^2 orbitals in CoPc and CoPc(L) were simulated by density functional theory (DFT) calculations with B3LYP functional using the Gaussian 09 package. The 6-311+g(d,p) basis set was used for light atoms (C, H, O, N) and the triple-ζ tzvp basis set with pseudopotential was used for heavy atoms (Co). All species were calculated with the ½ spin multiplicities, neutral charge. The geometries optimizations and energy of the orbitals in CoPc and CoPc(L) were simulated by DFT calculations adopting B3LYP functional in the Gaussian 09 package (detailed calculation information is shown in Supplemental Information for Chapter 4 in the Appendix Chapter).

4.6 Conclusion

We have investigated the effect of the axial coordination to metal center in CoPc for CO_2RR by a series of axially-coordinated CoPc complexes, and demonstrated the correlation between σ-donor strength of the axial ligand and catalytic activity of the complexes. First, we demonstrated that increasing the σ-donor strength of the axial ligand increases the energy of Co dz^2 orbital, and thus increases the overall catalytic activity of CoPc complex for CO_2 reduction using Density Functional Theory (DFT) calculations and UV-vis studies. Then, we showed that these systems with σ-donor show higher CO_2RR activity. Additionally, we immobilized the most active complex, CoPc(L8), into P2VP matrix to examine the axial coordination effect in the presence of the synergistic secondary- and outer-coordination sphere effects. Carbon black support was embedded into the catalyst composite to increase the electron transport in the catalyst-polymer film and thus increase the activity for the CO_2RR. At optimum catalyst and polymer loadings, enhanced CO_2RR activity (~ 9 mA cm^{-2} at -1.25 V vs. SCE) is achieved. These studies provide important design considerations by introducing axial coordination and carbon black support for future CO_2RR catalysts.

4.7 References

1. N. S. Lewis, G. Crabtree, A. J. Nozik, M. R. Wasielewski and A. P. Alivisatos, *Basic Research Needs for Solar Energy Utilization*, Department of Energy, 2005.
2. E. E. Benson, C. P. Kubiak, A. J. Sathrum and J. M. Smieja, *Chem. Soc. Rev.*, 2009, **38**, 89-99.
3. D. T. Whipple and P. J. A. Kenis, *The Journal of Physical Chemistry Letters*, 2010, **1**, 3451-3458.
4. C. M. Friend, M. S. Sanford and H. D. Abruña, *Catalytic Chemistry Workshop on Defining Critical Directions for the Future*, National Science Foundation, 2011.
5. J. L. Inglis, B. J. MacLean, M. T. Pryce and J. G. Vos, *Coord. Chem. Rev.*, 2012, **256**, 2571-2600.
6. A. M. Appel, J. E. Bercaw, A. B. Bocarsly, H. Dobbek, D. L. DuBois, M. Dupuis, J. G. Ferry, E. Fujita, R. Hille, P. J. A. Kenis, C. A. Kerfeld, R. H. Morris, C. H. F. Peden, A. R. Portis, S. W. Ragsdale, T. B. Rauchfuss, J. N. H. Reek, L. C. Seefeldt, R. K. Thauer and G. L. Waldrop, *Chem. Rev.*, 2013, **113**, 6621-6658.
7. J. Qiao, Y. Liu, F. Hong and J. Zhang, *Chem. Soc. Rev.*, 2014, **43**, 631-675.
8. S. Berardi, S. Drouet, L. Francas, C. Gimbert-Surinach, M. Guttentag, C. Richmond, T. Stoll and A. Llobet, *Chem. Soc. Rev.*, 2014, **43**, 7501-7519.
9. D. G. Nocera, *Acc. Chem. Res.*, 2017, **50**, 616-619.
10. T. P. Senftle and E. A. Carter, *Acc. Chem. Res.*, 2017, **50**, 472-475.
11. A. J. Martín, G. O. Larrazábal and J. Pérez-Ramírez, *Green Chemistry*, 2015, **17**, 5114-5130.
12. D. Pletcher, *Electrochem. Commun.*, 2015, **61**, 97-101.
13. C. M. Lieber and N. S. Lewis, *J. Am. Chem. Soc.*, 1984, **106**, 5033-5034.
14. K. P. Kuhl, E. R. Cave, D. N. Abram and T. F. Jaramillo, *Energy Environ. Sci.*, 2012, **5**, 7050-7059.
15. Y. Hori, in *Modern Aspects of Electrochemistry*, ed. C. G. Vayemas, Springer, New York, 2008, vol. 42, pp. 89-189.
16. M. Gattrell, N. Gupta and A. Co, *J. Electroanal. Chem.*, 2006, **594**, 1-19.
17. H. Ooka, M. C. Figueiredo and M. T. M. Koper, *Langmuir*, 2017, **33**, 9307-9313.
18. H. Yoshio, K. Katsuhei and S. Shin, *Chem. Lett.*, 1985, **14**, 1695-1698.
19. A. S. Varela, M. Kroschel, N. D. Leonard, W. Ju, J. Steinberg, A. Bagger, J. Rossmeisl and P. Strasser, *ACS Energy Lett.*, 2018, **3**, 812-817.
20. W. W. Kramer and C. C. L. McCrory, *Chem. Sci.*, 2016, **7**, 2506-2515.
21. Y. Liu and C. C. L. McCrory, *Nat. Commun.*, 2019, **10**, 1683.
22. A. J. Canty, P. Barron and P. C. Healy, *J. Organomet. Chem.*, 1979, **179**, 447-458.
23. A. J. Canty, N. Chaichit, B. M. Gatehouse, E. E. George and G. Hayhurst, *Inorg. Chem.*, 1981, **20**, 2414-2422.
24. A. J. Canty and C. V. Lee, *Organometallics*, 1982, **1**, 1063-1066.
25. A. J. Canty and C. V. Lee, *Inorg. Chim. Acta*, 1981, **54**, L205-L206.
26. D. L. Rabenstein, *Acc. Chem. Res.*, 1978, **11**, 100-107.
27. T. Nyokong, *Polyhedron*, 1995, **14**, 2325-2329.
28. B. Ramdhanie, L. N. Zakharov, A. L. Rheingold and D. P. Goldberg, *Inorg. Chem.*, 2002, **41**, 4105-4107.
29. N. Li, Y. Wang, C. Wu, W. Lu, K. Pei and W. Chen, *Appl. Surf. Sci.*, 2018, **434**, 1112-1121.
30. A. J. Bard and L. R. Faulkner, in *Electrochemical Methods: Fundamentals and applications*, John Wiley & Sons, Inc., Hoboken, NJ, 2nd edn., 2001, pp. 353-354.

31. K. B. Prater and A. J. Bard, *J. Electrochem. Soc.*, 1970, **117**, 207.
32. J.-C. Huang, *Adv. Polym. Tech.*, 2002, **21**, 299-313.
33. T. E. Rosser, C. D. Windle and E. Reisner, *Angew. Chem. Int. Ed.*, 2016, **55**, 7388-7392.
34. N. Elgrishi, S. Griveau, M. B. Chambers, F. Bedioui and M. Fontecave, *Chem. Commun.*, 2015, **51**, 2995-2998.
35. G. Neri, J. J. Walsh, C. Wilson, A. Reynal, J. Y. C. Lim, X. Li, A. J. P. White, N. J. Long, J. R. Durrant and A. J. Cowan, *PCCP*, 2015, **17**, 1562-1566.
36. S. Lin, C. S. Diercks, Y.-B. Zhang, N. Kornienko, E. M. Nichols, Y. Zhao, A. R. Paris, D. Kim, P. Yang, O. M. Yaghi and C. J. Chang, *Science*, 2015, **349**, 1208.
37. A. Maurin and M. Robert, *Chem. Commun.*, 2016, **52**, 12084-12087.
38. J. J. Walsh, G. Neri, C. L. Smith and A. J. Cowan, *Chem. Commun.*, 2014, **50**, 12698-12701.
39. R. M. Bullock, A. K. Das and A. M. Appel, *Chemistry – A European Journal*, 2017, **23**, 7626-7641.
40. E. Liaudet, F. Battaglini and E. J. Calvo, *J. Electroanal. Chem. Interfacial Electrochem.*, 1990, **293**, 55-68.
41. N. Oyama and F. C. Anson, *Anal. Chem.*, 1980, **52**, 1192-1198.
42. J. Leddy and A. J. Bard, *J. Electroanal. Chem. Interfacial Electrochem.*, 1983, **153**, 223-242.
43. R. G. Compton, M. E. Laing, A. Ledwith and I. I. Abu-Abdoun, *J. Appl. Electrochem.*, 1988, **18**, 431-440.

Chapter 5: Conclusions, Recommendations, and Future Research

5.1 Conclusions

In this dissertation, studies were presented on encapsulating transition metal catalysts within coordinating polymers that control the coordination environment of the catalysts to promote selective and active CO_2 reduction (CO_2RR). Studies of polymer-encapsulated catalysts for the CO_2RR have focused on cobalt phthalocyanine (CoPc) encapsulated within poly-4-vinylpyridine (P4VP) forming CoPc-P4VP composite films.

In initial work, a strategy was developed to determine the mechanistic implications of primary- and outer-coordination sphere effects on the CO_2 reduction activity by P4VP encapsulated CoPc composites. First, using electrochemical kinetic isotope effect (KIE) measurements, it was shown that axial-coordination to the CoPc changes the rate determining step from a CO_2 coordination step in the case of four-coordinate CoPc to a subsequent protonation event in the case of five-coordinate CoPc(py) or CoPc-P4VP. Additionally, using proton inventory studies—a technique used in enzymology to study the kinetics of proton delivery to enzymatic active sites—to the our electrocatalytic system, it was confirmed that proton delivery to the Co active site in CoPc-P4VP is controlled by a proton-relay mechanism rather than proton diffusion through the film. This is one of the first examples of experimental verification of a multi-site relay-based proton delivery mechanism in a synthetic electrocatalytic system.

Follow-up studies involves using *in situ* X-ray Absorption Spectroscopy (XAS) to experimentally confirm the postulated coordination environments that Co exists as a four-

coordinate species in CoPc and a five-coordinate species in CoPc(py) and CoPc-P4VP when these materials are adsorbed onto graphite surfaces, and that this coordination is retained upon reduction in our initial studies. In particular, *in situ* X-ray absorption near edge structure (XANES) was used to verify that Co is four-coordinate in CoPc, five-coordinate in CoPc(py), and mostly, but not completely, five-coordinate in CoPc-P4VP. In addition, it was shown that the coordination environment of CoPc-P4VP is potential-independent but pH-dependent, suggesting that the axial coordination of pyridyl groups in P4VP with CoPc is modulated by the protonation of the polymer membrane. Finally, it was shown that electrochemical reduction of CoPc does not result in an oxidation state change—the reduction is ligand-based. However, CoPc(py) and CoPc-P4VP show an oxidation-state change upon reduction. This suggests that the reduced five-coordinate species have a HOMO with metal character which is different than the four-coordinate CoPc species and may partially explain the increased activity for CO_2RR for the five-coordinate species.

In preliminary studies, it has been shown that the σ-donor ability of the axial coordination ligand to CoPc influences the complex's activity for electrochemical CO_2 reduction. A series of CoPc(L) complexes was studied where the σ-donor strength of L varies. The σ-donor strength of the axial ligands were evaluated by the energy difference between the Co dz^2 orbital and the complex's HOMO calculated by density functional theory (DFT) for each CoPc(L) system and the red-shift of the Q band in each UV-vis spectrum of CoPc(L). It was found that a decrease in the observed overall electrochemical activity of the corresponding CoPc(L) as L moves from more to less donating strength as indicated by the HOMO-dz^2 energy difference. This observation of the trend of the electrochemical activity as a function of σ-donor strength supports the hypothesis that the increased CO_2RR activity observed upon axial coordination to CoPc is due to the increased energy of the dz^2 orbital, which is crucial for the development of new electrocatalyst for CO_2RR.

Advances in experimental techniques have revealed a wealth of mechanistic information in recent years, yet detailed thermodynamics and kinetic studies of the metal complex would help to understand the mechanisms for CO_2 reduction. Ground-breaking research has to be continued to produce renewable fuels (e.g. CO, methanol, ethanol) via low-energy pathways using selective earth-abundant catalysts.

5.2 Recommendations and Future Research

5.2.1 Controlling Charge and Substrate Transport in Polymer-Catalyst Composites

Although the catalyst-polymer systems can promote selective and active CO_2 reduction, preliminary experiments show that increasing CoPc-P4VP film thickness while keeping the CoPc-to-P4VP ratio constant results in a corresponding decrease in catalytic activity (Figure 5.1). This decrease is attributed to the sum of two distinct effects: i) there is a limiting film thickness after which additional CoPc is no longer electronically accessible due to inefficient charge transport through the non-conducting P4VP polymer; and ii) as the film thickness increases, the transport of CO_2 to the interior sites (which are still electronically accessible) decreases leading to an overall decrease in catalytic current and turnover frequency. Therefore, it is worth studying this decrease in activity with increasing film thickness to determine the relationship between charge and CO_2 transport within the film and overall catalytic activity. Based on these findings, we can develop new polymer-catalyst composite systems specifically tailored to increase the rate of charge transport and/or the rate of CO_2 transport.

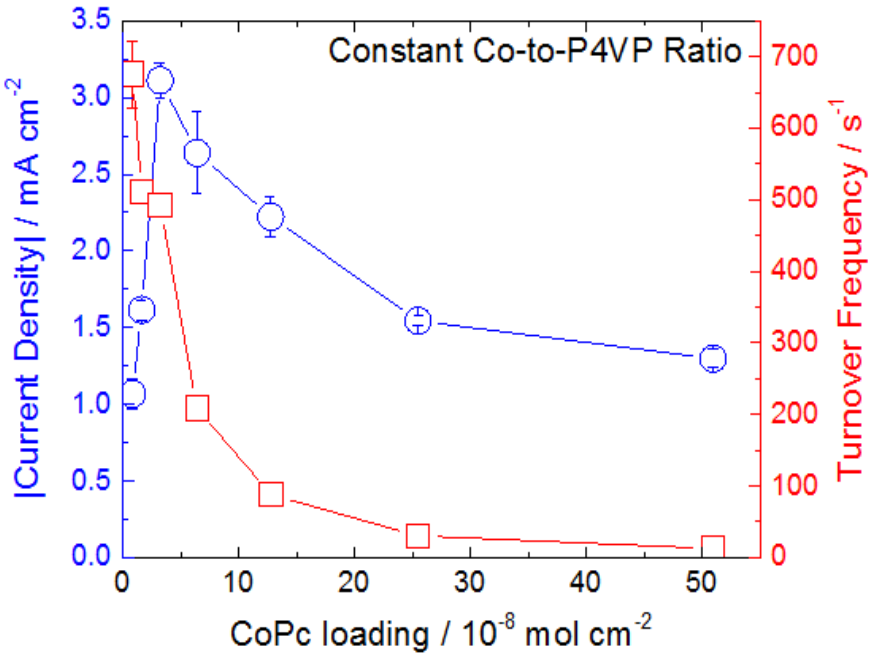

Figure 5.1 CO_2 reduction activity decreases as the polymer and catalyst loading increases on a planar glassy carbon electrode. Here, CoPc loading is used as a proxy for film thickness.

It is expected that the use of a suitable redox mediator, which is mobile or has high charge self-exchange property, within the polymer membrane to carry electrons might greatly increase the reactivity of CoPc and therefore the number of catalysts within the film that are available for CO_2 reduction. Another approach might be incorporating carbon–based electron shuttles such as carbon black (CB) into the CoPc-P4VP composite to facilitate electron transport to the embedded catalyst sites. We expect that as we increase the fraction of CB in the films, we will observe a corresponding increase in activity to some limiting current at which activity is limited by inefficient CO_2-transport. Films will be prepared by first fully mixing CoPc and P4VP in nonaqueous solution followed by addition of ~20 μm CB particles to adsorb the catalyst-polymer composite before finally depositing the resulting suspension onto the electrode surfaces using previously reported procedures. This film preparation strategy allows for independent control of CoPc, CB, and P4VP loading. Previously we had shown that when the CoPc-P4VP film thickness

increases while keeping the CoPc-to-P4VP ratio constant there is a corresponding decrease in catalytic activity (Figure 5.1). When we conduct the same experiments with sufficient loadings of carbon black (Figure 5.2), we see an initial increase in activity with increasing film thickness until reaching a plateau of ~10 mA cm^{-2} with high (> 0.51 mg cm^{-2}) CB loading. This preliminary data suggests that increasing charge transport does increase overall activity, but at sufficiently fast charge transport we become limited by another factor such as substrate transport.

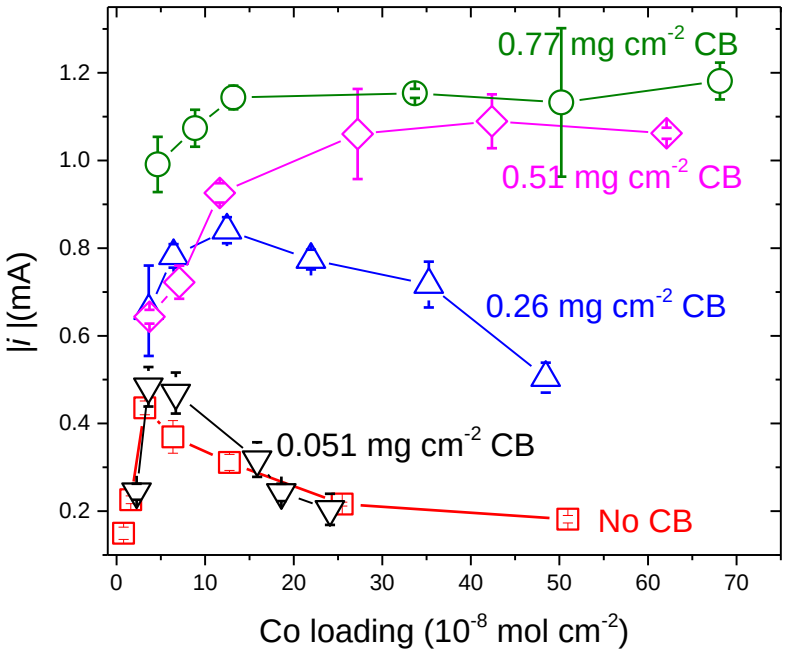

Figure 5.2 CO_2 reduction activity as a function of the polymer and catalyst loading with different amounts of carbon black (CB) incorporated. Here, CoPc loading is used as a proxy for polymer film thickness.

One possible approach to investigate CO_2 transport within the polymer could be using different types of polymers with different CO_2 solubility, and using copolymers and blend polymers with different CO_2 transport capabilities. For controlling the H^+ transport, because relative concentration of H^+ in film depends on the buffering equilibrium of the polymer, we can control H^+ transport by controlling relative pKa of polymer film. To do this, we can modulate the

pKa of the protonated polymer through systematic modification of the pendant moieties within the polymer chain.

5.2.2 pH Effects on the Proton Delivery within the CoPc-P4VP Catalyst System

In preliminary studies, it was shown that the outer-coordination sphere plays an important role in the inhibition of competitive H_2 generation when performing electrocatalytic CO_2 reduction with CoPc-P4VP and CoPc-P2VP. The hypothesis was that the pendant pyridine moieties in the polymer create proton relays that control proton transport throughout the polymer film. The thought is that both protonated and deprotonated sites within the P4VP polymer are necessary for proton-relays to exist, and that these proton relays control H^+ delivery to the metal active site in CoPc-P4VP and thus control the system's preference for CO_2 reduction over competitive H_2 evolution. One possible approach to test this hypothesis is to study the effect of changing the pH on the Faradaic efficiency for CO production, the kinetic isotope effect, and the overall CO_2 reduction activity. By controlling the pH in the electrolyte solution, it is possible to directly control the fraction of pyridine sites that are protonated within the P4VP polymer.

5.2.3 Effect of Electronic Structure of Metal Complex on Axial Coordination Promotion of CO_2 Reduction

Additional preliminary results have shown that the axial coordination to the CoPc catalyst can affect the energies of the molecular orbitals of CoPc. In particular, there is experimental evidence strongly suggests that axial coordination to CoPc can increase the energy of the dz^2 orbital, which is crucial for the enhanced CO_2RR activity. In addition, our *in situ* XAS results indicate the electrons are delocalized on Pc ligand during electrochemical reactions. These

experimental findings suggest that electronic structures of the metal complexes may change the performance of CO_2RR by these catalysts. To test this, it should be possible to modulate the electronic structures of metal complexes within the polymer by i) changing the metal center in MPc, and ii) modifying the ligand structure of CoPc. These experiments will specifically help in understanding the effect of electronic structure of a metal catalyst when designing new catalyst-polymer composite systems.

5.2.4 Determine the Coordination of CoPc with Underlying Substrate and the Effect of Different Substrates for CO_2RR

High CO_2RR activity and CO selectivity can be achieved by CoPc deposited on carbon nanotubes (CNTs) and oxygen-functionalized carbon paper (O_xC), similar increases in activity are reported for O_2 reduction by Co and Fe complexes adsorbed onto defect-rich carbon supports.[1-5] The increased activity of CoPc adsorbed onto CNTs and O_xC may be due to axial-coordination of impurities in the CNTs structure (such as oxide- and hydroxyl-defect sites) or the oxygen in O_xC with the adsorbed CoPc. To test this, it should be possible to use a proton inventory technique to confirm the postulated axial coordination of CoPc with the underlying substrates (such as CNTs and O_xC). In addition, by studying the KIE values on each substrate, it should be possible to figure out the percentage of CoPc molecules that forms axial coordination with each substrates. This will provide mechanistic insights on electrocatalytic reactions by molecular complexes on defect-rich carbon substrates.

5.3 References

1. J. E. Hutchison, T. A. Postlethwaite, C.-h. Chen, K. W. Hathcock, R. S. Ingram, W. Ou, R. W. Linton, R. W. Murray, D. A. Tyvoll, L. L. Chng and J. P. Collman, *Langmuir*, 1997, **13**, 2143-2148.
2. A. Bettelheim, R. J. H. Chan and T. Kuwana, *J. Electroanal. Chem.*, 1980, **110**, 93-102.
3. C. L. Ni and F. C. Anson, *Inorg. Chem.*, 1985, **24**, 4754-4756.
4. C. Shi and F. C. Anson, *Inorg. Chem.*, 1990, **29**, 4298-4305.
5. I. Bhugun and F. C. Anson, *Inorg. Chem.*, 1996, **35**, 7253-7259.

Appendix A: Supplementary Information

A.1 Supplementary Information for Chapter 2

A.1.1 Supplementary Figures

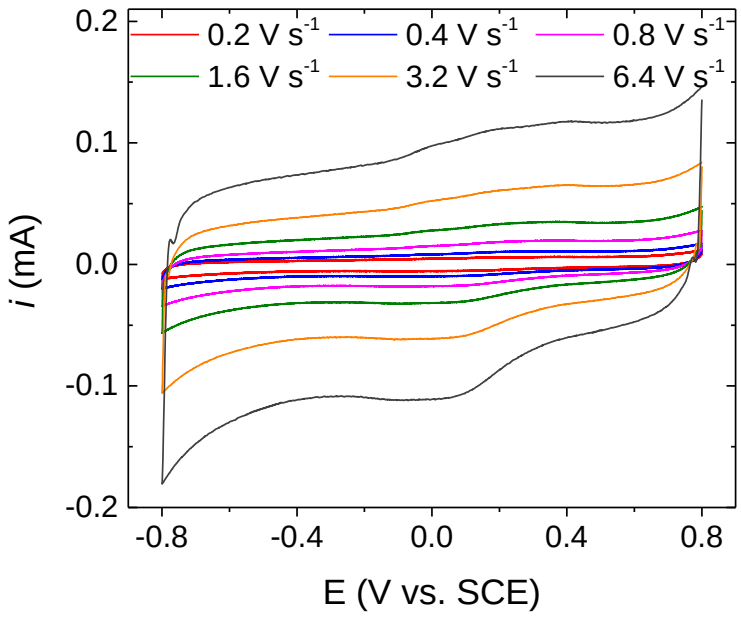

Figure A.1 Cyclic voltammograms of CoPc on EPG in pH 5 phosphate solution recorded at potentials positive of the catalytic current at different scan rates under N_2 atmosphere. The redox couple at $E_{1/2}$ = 0.18 V is assigned to the $[CoPc]^+/[CoPc]$ couple. The broad peaks are consistent with π-π stacking and aggregation of the CoPc molecules.

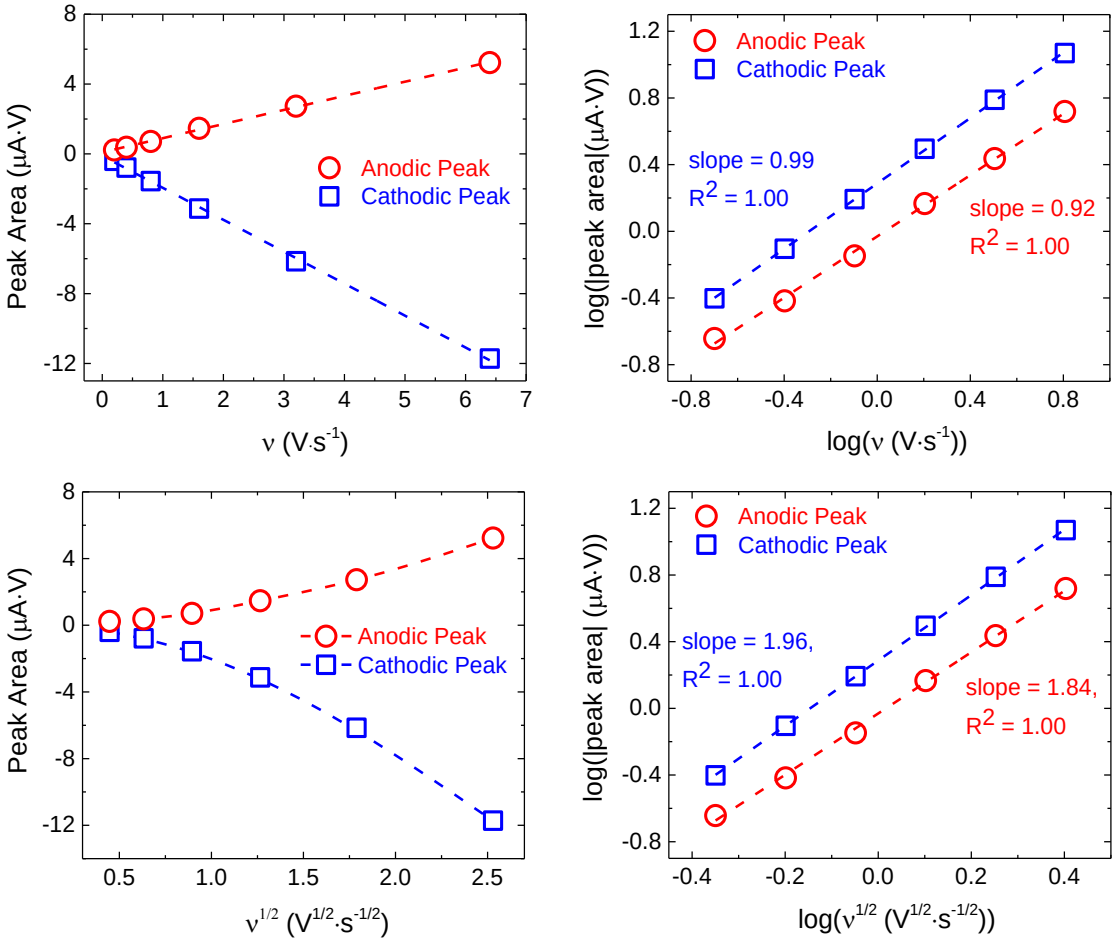

Figure A.2 Scan Rate Dependence Study of CoPc on EPG
a, Plots of peak area vs. scan rate for the $[CoPc]^+/[CoPc]$ peaks in CoPc are linear, which is consistent with electron transfer to a surface-immobilized species.
b, Plots of log(|peak area|) vs. log(scan rate) for the $[CoPc]^+/[CoPc]$ peaks in CoPc have slopes ~ 1, which is consistent with a 1st order dependence on scan rate as expected for a surface-immobilized species.
c, Plots of peak area vs. $(\text{scan rate})^{1/2}$ for the $[CoPc]^+/[CoPc]$ peaks in CoPc are non-linear which is not consistent with electron transfer to a diffusing species in solution.
d, Plots of log(|peak area|) vs. $\log((\text{scan rate})^{1/2})$ for the $[CoPc]^+/[CoPc]$ peaks in CoPc have slopes ~ 2, which is inconsistent with electron transfer to a diffusing species in solution and instead is consistent with a surface-immobilized species.

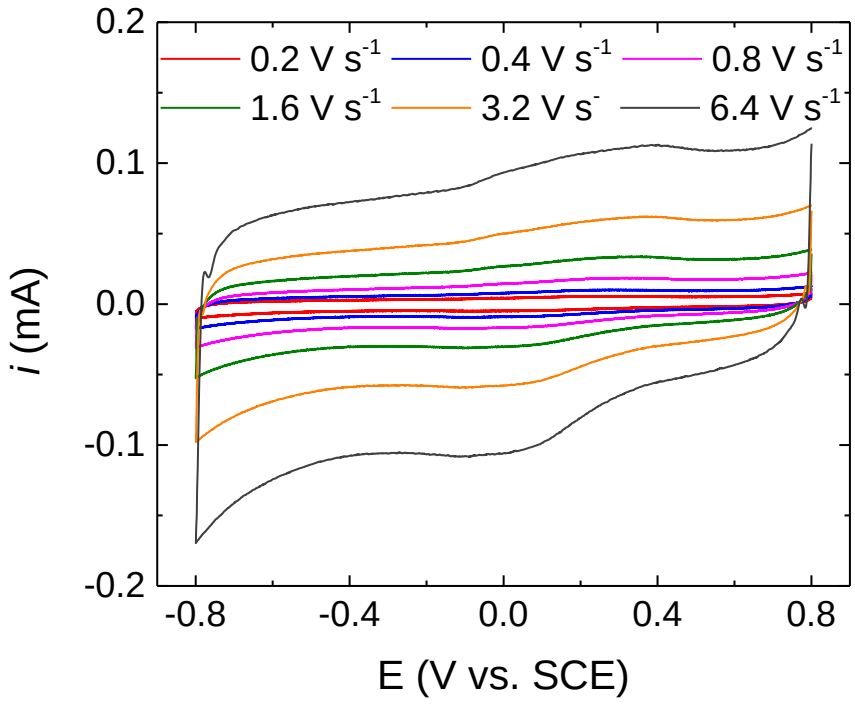

Figure A.3 Cyclic voltammograms of CoPc(py) on EPG in pH 5 phosphate solution recorded at potentials positive of the catalytic current at different scan rates under N_2 atmosphere. The redox couple at $E_{1/2}$ = 0.18 V is assigned to the $[CoPc]^+/[CoPc]$ couple. The broad peaks are consistent with π-π stacking and aggregation of the CoPc molecules.

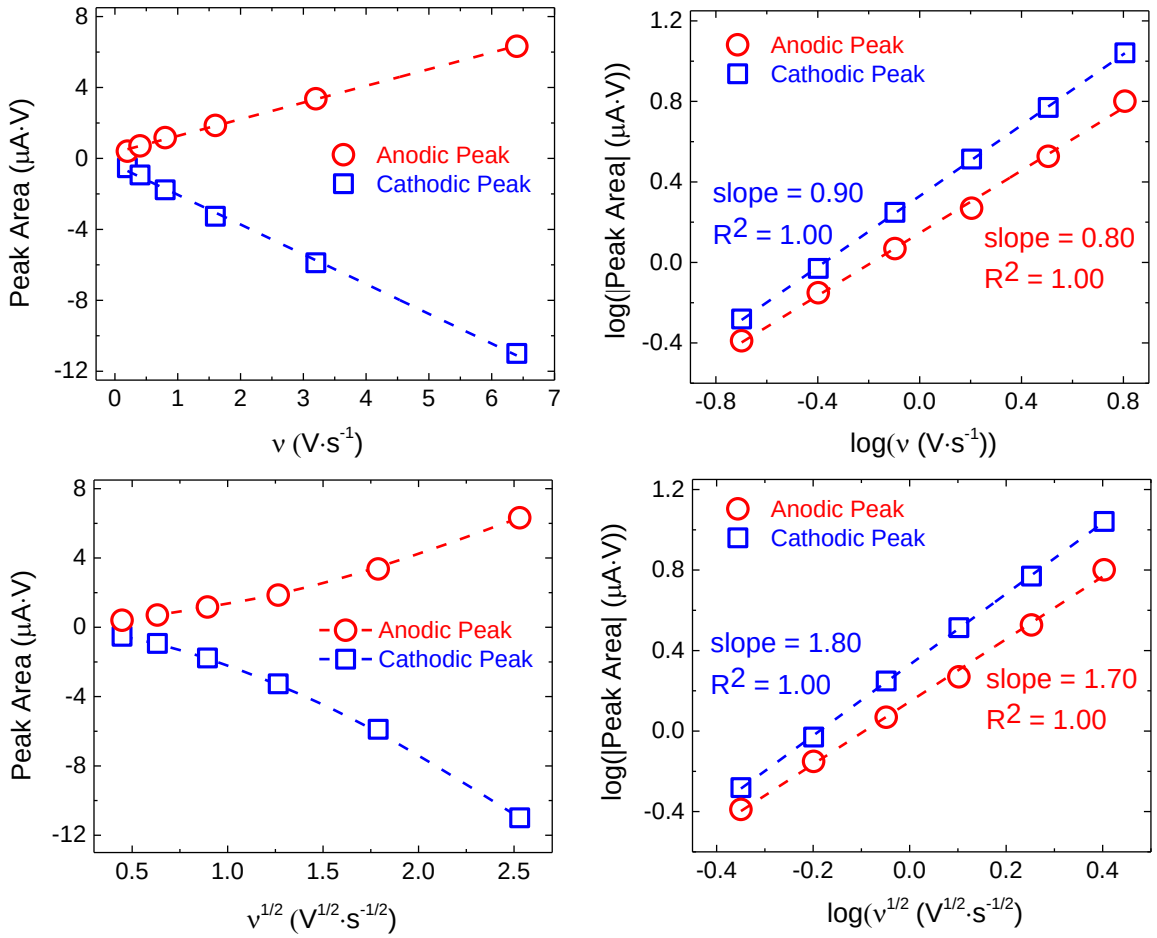

Figure A.4 Scan Rate Dependence Study of CoPc(py) on EPG
a, Plots of peak area vs. scan rate for the $[CoPc]^+/[CoPc]$ peaks in CoPc(py) are linear, which is consistent with electron transfer to a surface-immobilized species.
b, Plots of log(|peak area|) vs. log(scan rate) for the $[CoPc]^+/[CoPc]$ peaks in CoPc(py) have slopes ~ 1, which is consistent with a 1st order dependence on scan rate as expected for a surface-immobilized species.
c, Plots of peak area vs. $(\text{scan rate})^{1/2}$ for the $[CoPc]^+/[CoPc]$ peaks in CoPc(py) are non-linear which is not consistent with electron transfer to a diffusing species in solution.
d, Plots of log(|peak area|) vs. $\log((\text{scan rate})^{1/2})$ for the $[CoPc]^+/[CoPc]$ peaks in CoPc(py) have slopes ~ 2, which is inconsistent with electron transfer to a diffusing species in solution and instead is consistent with a surface-immobilized species.

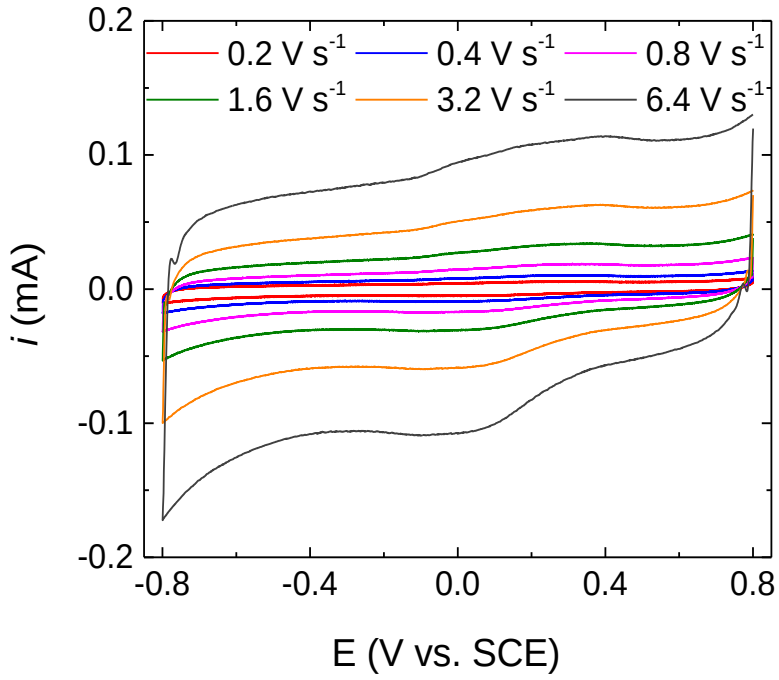

Figure A.5 Cyclic voltammograms of CoPc-P4VP on EPG in pH 5 phosphate solution recorded at potentials positive of the catalytic current at different scan rates under N_2 atmosphere. The redox couple at $E_{1/2}$ = 0.18 V is assigned to the $[CoPc]^+/[CoPc]$ couple. The broad peaks are consistent with π-π stacking and aggregation of the CoPc molecules.

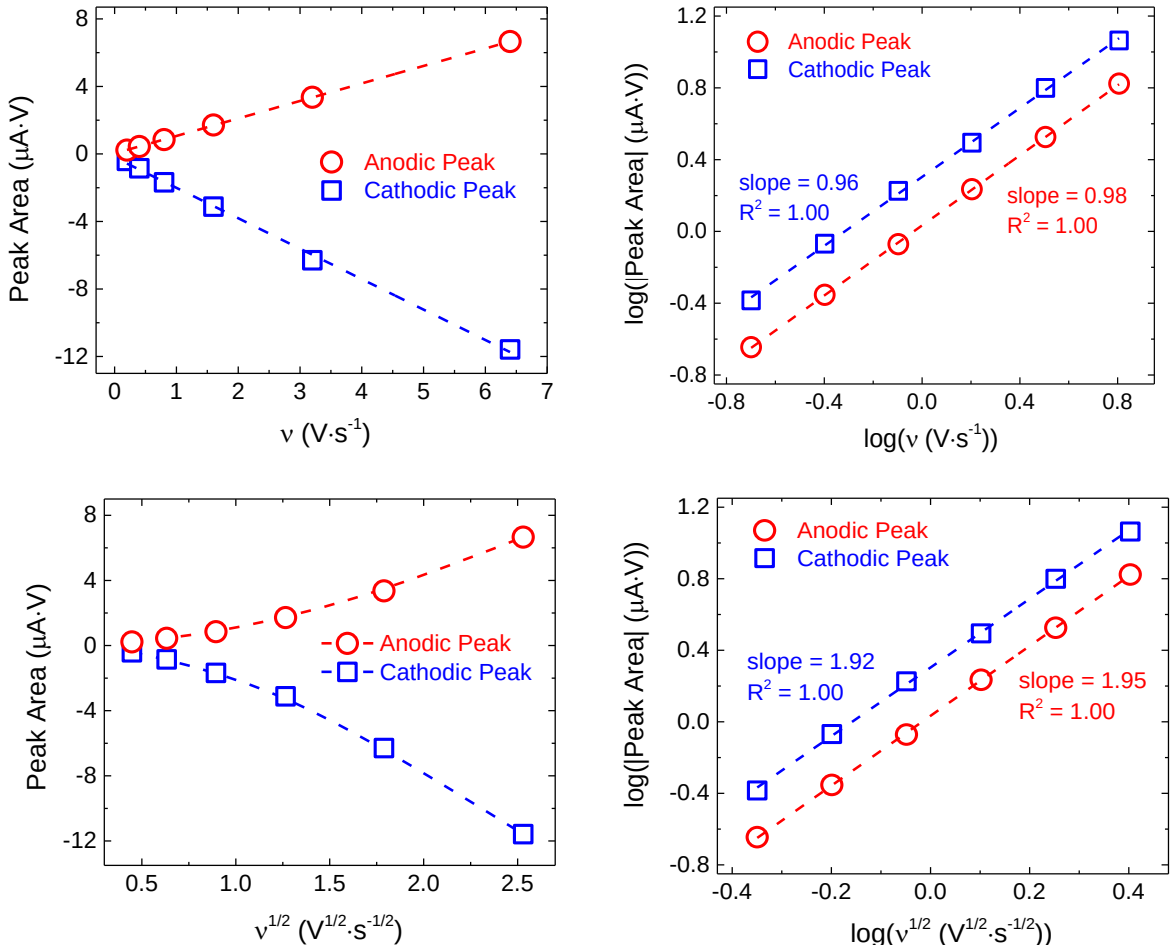

Figure A.6 Scan Rate Dependence Study of CoPc-P4VP on EPG
a, Plots of peak area vs. scan rate for the $[CoPc]^+/[CoPc]$ peaks in CoPc-P4VP are linear, which is consistent with electron transfer to a surface-immobilized species.
b, Plots of log(|peak area|) vs. log(scan rate) for the $[CoPc]^+/[CoPc]$ peaks in CoPc-P4VP have slopes ~ 1, which is consistent with a 1st order dependence on scan rate as expected for a surface-immobilized species.
c, Plots of peak area vs. $(\text{scan rate})^{1/2}$ for the $[CoPc]^+/[CoPc]$ peaks in CoPc-P4VP are non-linear which is not consistent with electron transfer to a diffusing species in solution.
d, Plots of log(|peak area|) vs. $\log((\text{scan rate})^{1/2})$ for the $[CoPc]^+/[CoPc]$ peaks in CoPc-P4VP have slopes ~ 2, which is inconsistent with electron transfer to a diffusing species in solution and instead is consistent with a surface-immobilized species.

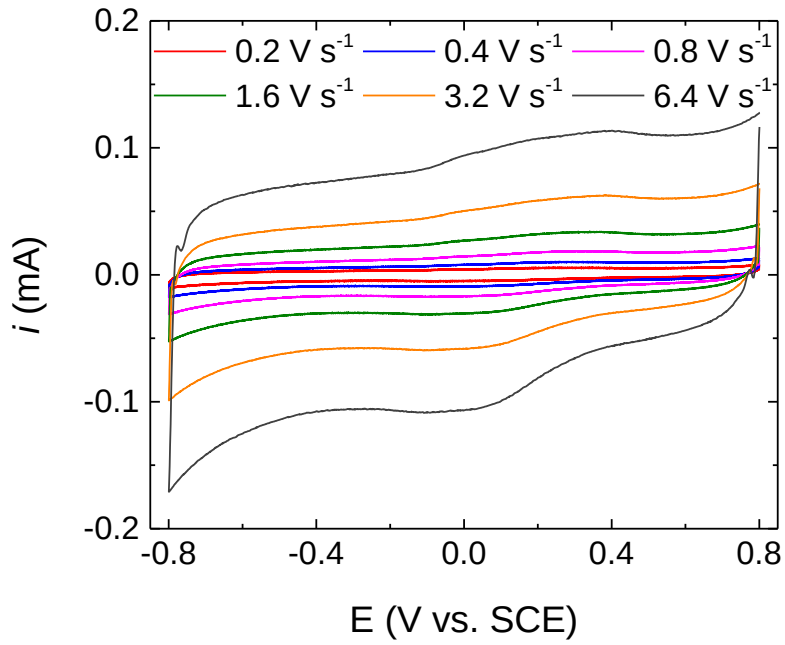

Figure A.7 Cyclic voltammograms of CoPc-P2VP on EPG in pH 5 phosphate solution recorded at potentials positive of the catalytic current at different scan rates under N_2 atmosphere. The redox couple at $E_{1/2}$ = 0.18 V is assigned to the $[CoPc]^+/[CoPc]$ couple. The broad peaks are consistent with π-π stacking and aggregation of the CoPc molecules.

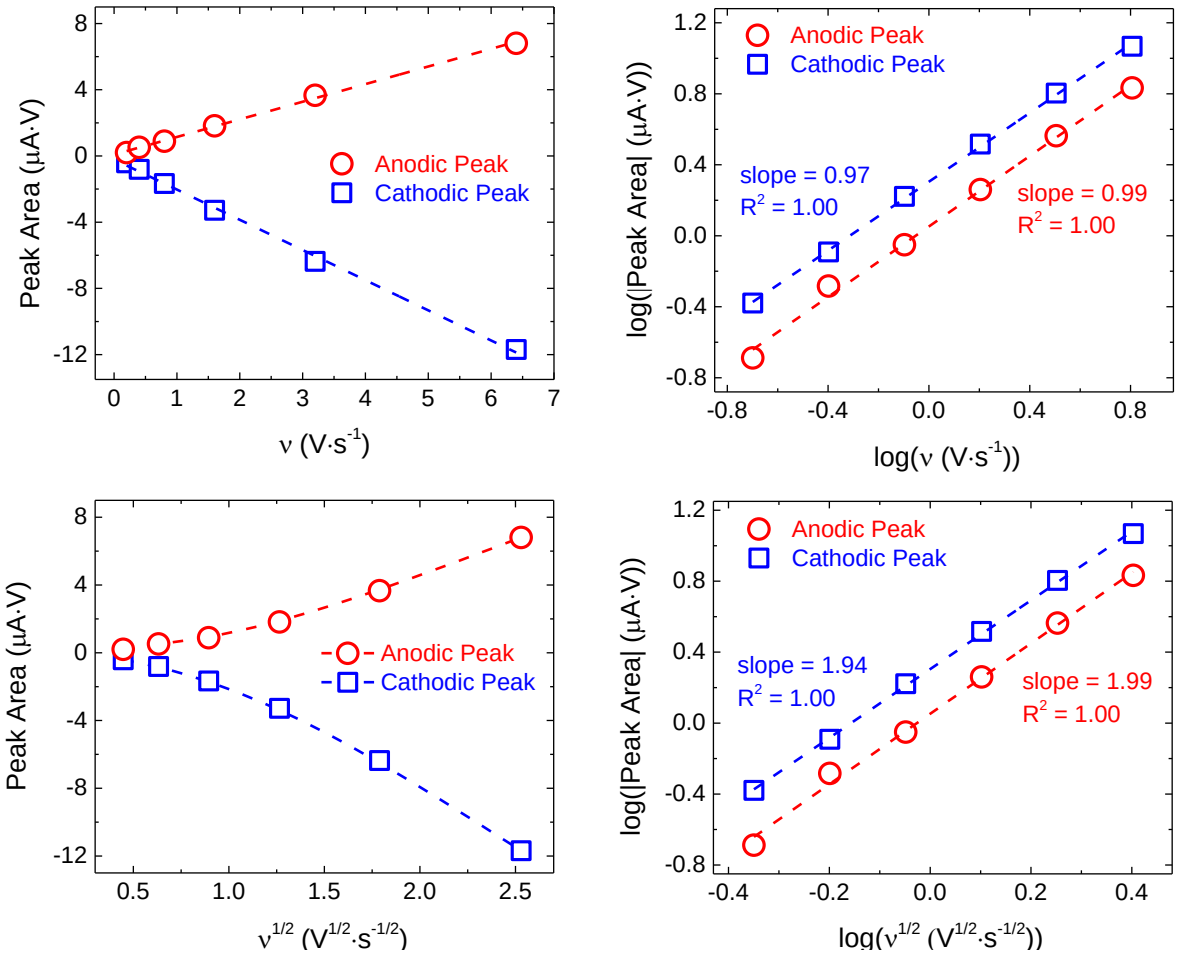

Figure A.8 Scan Rate Dependence Study of CoPc-P2VP on EPG
a, Plots of peak area vs. scan rate for the $[CoPc]^+/[CoPc]$ peaks in CoPc-P2VP are linear, which is consistent with electron transfer to a surface-immobilized species.
b, Plots of log(|peak area|) vs. log(scan rate) for the $[CoPc]^+/[CoPc]$ peaks in CoPc-P2VP have slopes ~ 1, which is consistent with a 1st order dependence on scan rate as expected for a surface-immobilized species.
c, Plots of peak area vs. $(\text{scan rate})^{1/2}$ for the $[CoPc]^+/[CoPc]$ peaks in CoPc-P2VP are non-linear which is not consistent with electron transfer to a diffusing species in solution.
d, Plots of log(|peak area|) vs. $\log((\text{scan rate})^{1/2})$ for the $[CoPc]^+/[CoPc]$ peaks in CoPc-P2VP have slopes ~ 2, which is inconsistent with electron transfer to a diffusing species in solution and instead is consistent with a surface-immobilized species.

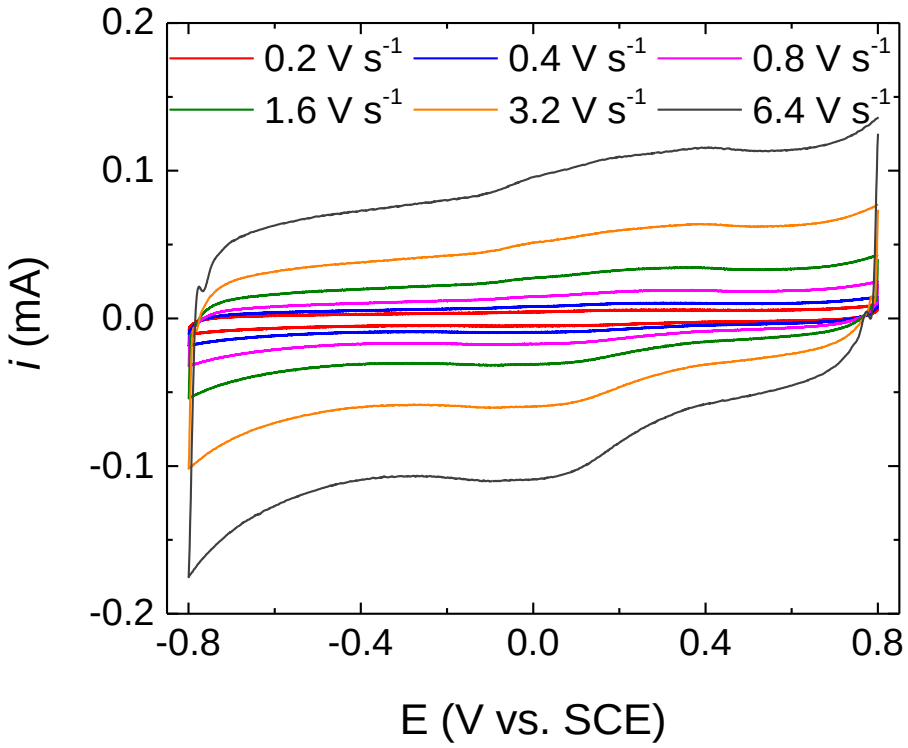

Figure A.9 Cyclic voltammograms of CoPc(py)-P2VP on EPG in pH 5 phosphate solution recorded at potentials positive of the catalytic current at different scan rates under N_2 atmosphere. The redox couple at $E_{1/2}$ = 0.18 V is assigned to the $[CoPc]^+/[CoPc]$ couple. The broad peaks are consistent with π-π stacking and aggregation of the CoPc molecules.

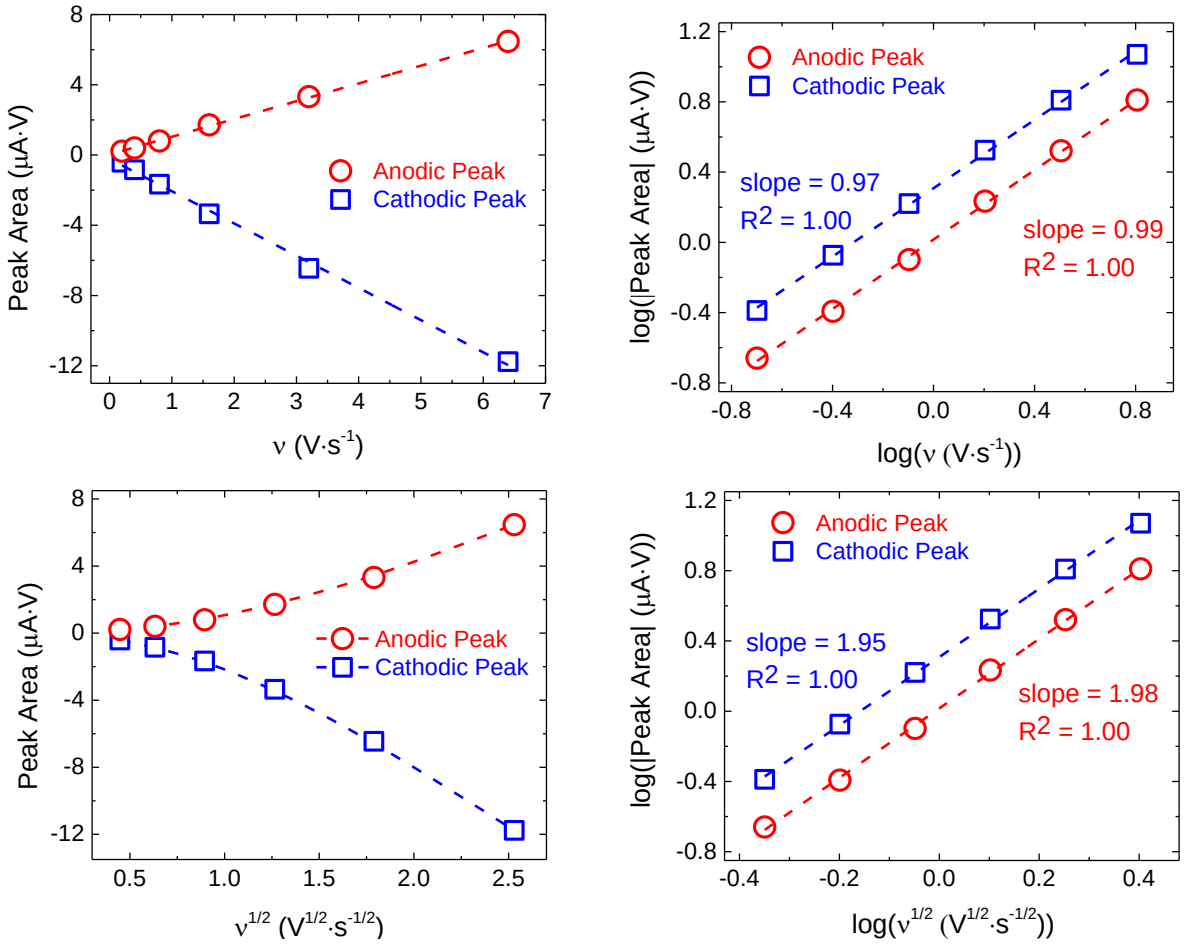

Figure A.10 Scan Rate Dependence Study of CoPc(py)-P2VP on EPG
a, Plots of peak area vs. scan rate for the $[CoPc]^+/[CoPc]$ peaks in CoPc(py)-P2VP are linear, which is consistent with electron transfer to a surface-immobilized species.
b, Plots of log(|peak area|) vs. log(scan rate) for the $[CoPc]^+/[CoPc]$ peaks in CoPc(py)-P2VP have slopes ~ 1, which is consistent with a 1st order dependence on scan rate as expected for a surface-immobilized species.
c, Plots of peak area vs. $(\text{scan rate})^{1/2}$ for the $[CoPc]^+/[CoPc]$ peaks in CoPc(py)-P2VP are non-linear which is not consistent with electron transfer to a diffusing species in solution.
d, Plots of log(|peak area|) vs. $\log((\text{scan rate})^{1/2})$ for the $[CoPc]^+/[CoPc]$ peaks in CoPc(py)-P2VP have slopes ~ 2, which is inconsistent with electron transfer to a diffusing species in solution and instead is consistent with a surface-immobilized species.

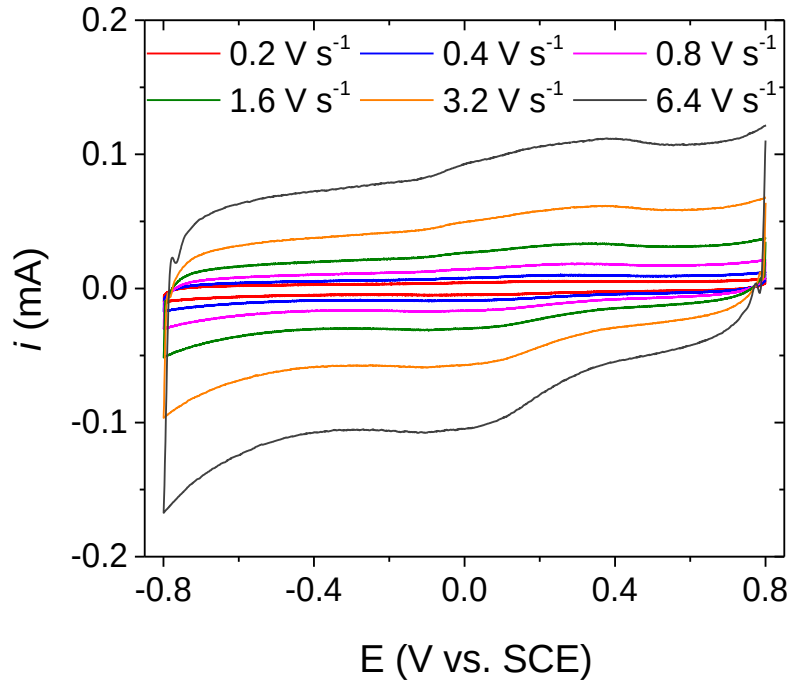

Figure A.11 Cyclic voltammograms of CoPc-PS on EPG in pH 5 phosphate solution recorded at potentials positive of the catalytic current at different scan rates under N_2 atmosphere. The redox couple at $E_{1/2} = 0.18$ V is assigned to the $[CoPc]^+/[CoPc]$ couple. The broad peaks are consistent with π-π stacking and aggregation of the CoPc molecules.

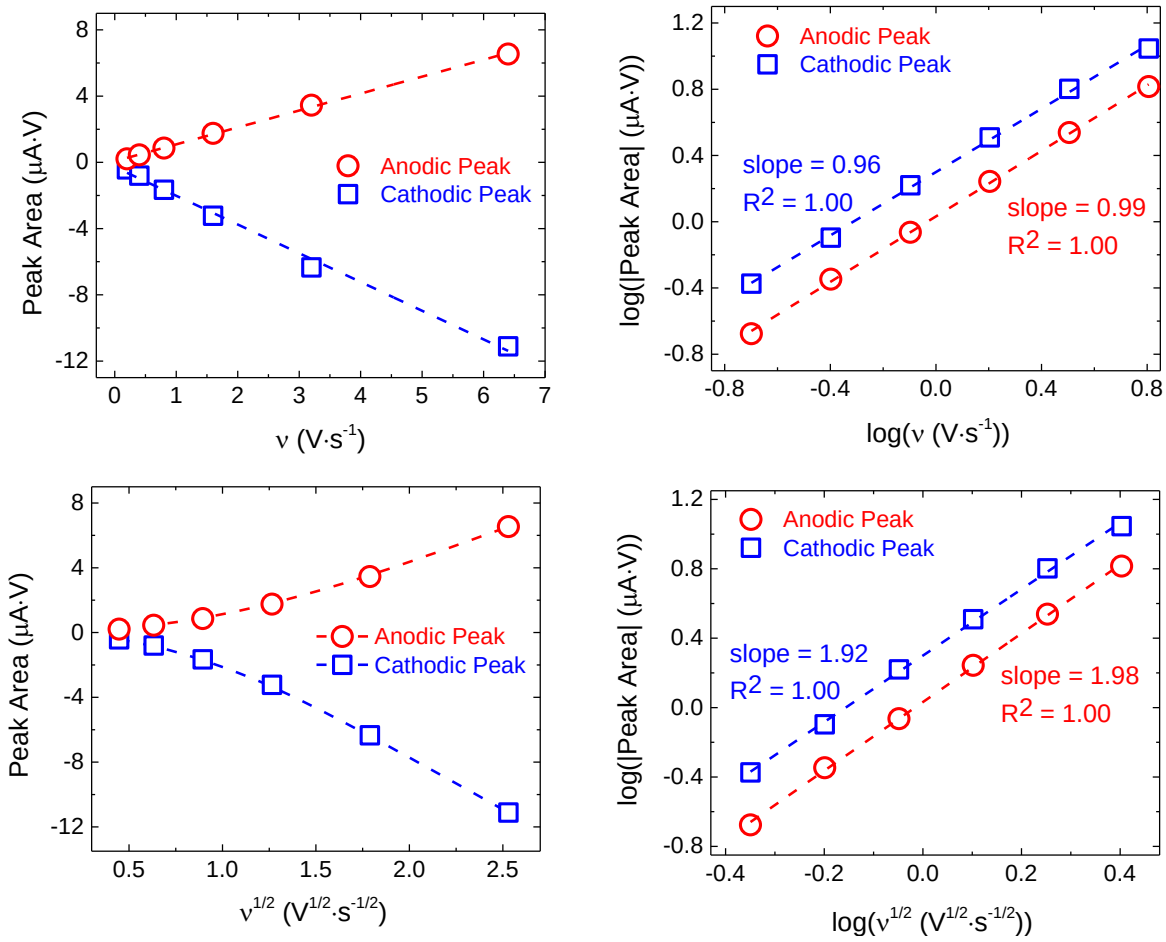

Figure A.12 Scan Rate Dependence Study of CoPc-PS on EPG
a, Plots of peak area vs. scan rate for the $[CoPc]^+/[CoPc]$ peaks in CoPc-PS are linear, which is consistent with electron transfer to a surface-immobilized species.
b, Plots of log(|peak area|) vs. log(scan rate) for the $[CoPc]^+/[CoPc]$ peaks in CoPc-PS have slopes ~ 1, which is consistent with a 1st order dependence on scan rate as expected for a surface-immobilized species.
c, Plots of peak area vs. $(\text{scan rate})^{1/2}$ for the $[CoPc]^+/[CoPc]$ peaks in CoPc-PS are non-linear which is not consistent with electron transfer to a diffusing species in solution.
d, Plots of log(|peak area|) vs. $\log((\text{scan rate})^{1/2})$ for the $[CoPc]^+/[CoPc]$ peaks in CoPc-PS have slopes ~ 2, which is inconsistent with electron transfer to a diffusing species in solution and instead is consistent with a surface-immobilized species.

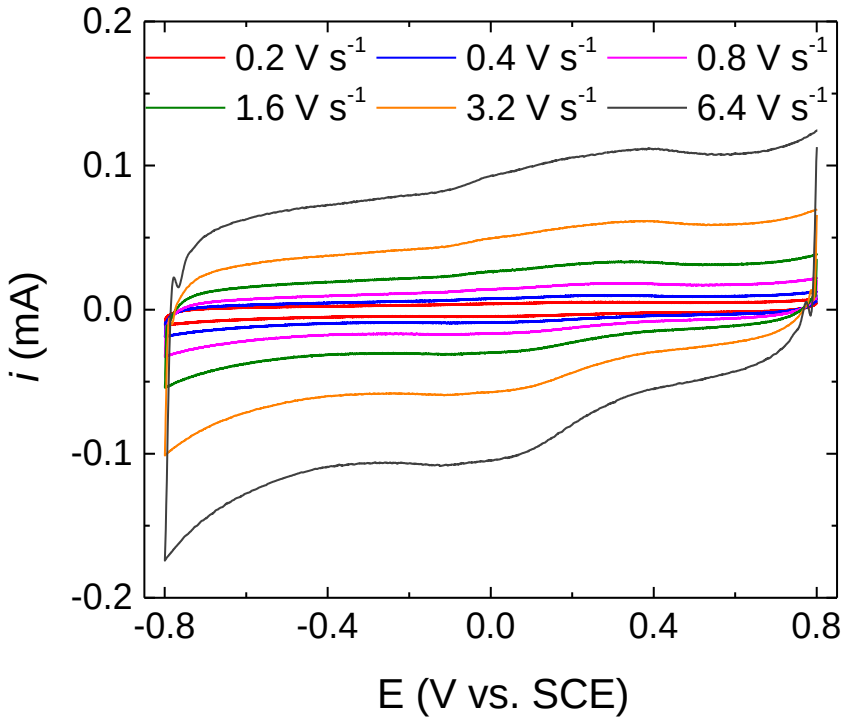

Figure A.13 Cyclic voltammograms of CoPc(py)-PS on EPG in pH 5 phosphate solution recorded at potentials positive of the catalytic current at different scan rates under N_2 atmosphere. The redox couple at $E_{1/2}$ = 0.18 V is assigned to the $[CoPc]^+/[CoPc]$ couple. The broad peaks are consistent with π-π stacking and aggregation of the CoPc molecules.

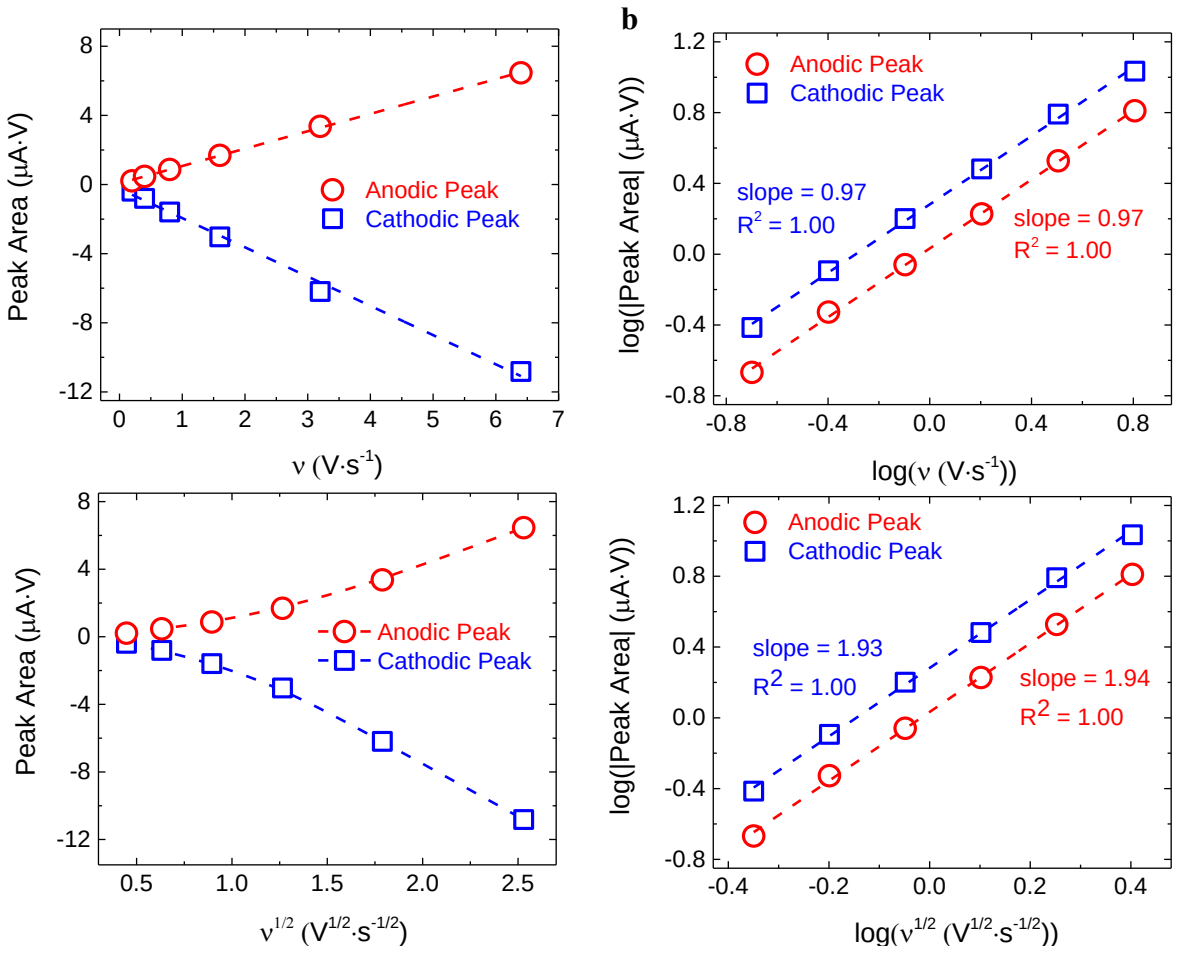

Figure A.14 Scan Rate Dependence Study of CoPc(py)-PS on EPG
a, Plots of peak area vs. scan rate for the $[CoPc]^+/[CoPc]$ peaks in CoPc(py)-PS are linear, which is consistent with electron transfer to a surface-immobilized species.
b, Plots of log(|peak area|) vs. log(scan rate) for the $[CoPc]^+/[CoPc]$ peaks in CoPc(py)-PS have slopes ~ 1, which is consistent with a 1st order dependence on scan rate as expected for a surface-immobilized species.
c, Plots of peak area vs. $(\text{scan rate})^{1/2}$ for the $[CoPc]^+/[CoPc]$ peaks in CoPc(py)-PS are non-linear which is not consistent with electron transfer to a diffusing species in solution.
d, Plots of log(|peak area|) vs. $\log((\text{scan rate})^{1/2})$ for the $[CoPc]^+/[CoPc]$ peaks in CoPc(py)-PS have slopes ~ 2, which is inconsistent with electron transfer to a diffusing species in solution and instead is consistent with a surface-immobilized species.

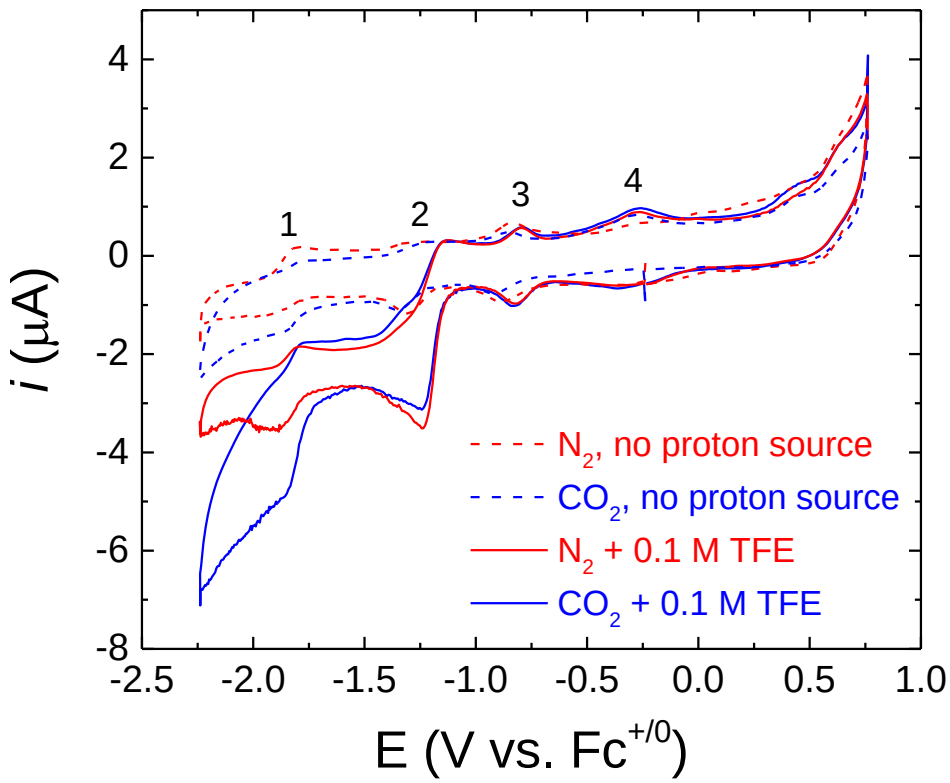

Figure A.15 Cyclic voltammogram (CV) of 0.2 mM CoPc in DMSO with 0.1 M nBu_4NPF_6 under N_2 and CO_2 without any proton source added, and in the presence of 0.1 M TFE. Conditions: scan rate: 50 mV/s; working electrode: glassy carbon working electrode; reference electrode: $Ag/AgNO_3$ (1 mM); counter electrode: Pt wire. Note that all CVs have been IR compensated. In the absence of CO_2 and proton source, four reversible peaks (labeled 1-4) are observed at $E_{1/2}$ = -1.80 V, -1.22 V, -0.75 V, and -0.25 V vs. $Fc^{+/0}$, respectively. We tentatively assign these peaks to the following redox couples: 1) $[Co^{I}Pc]^{2-}/[Co^{I}Pc]^{3-}$, 2) $[Co^{I}Pc]^{-}/[Co^{I}Pc]^{2-}$, 3) $[Co^{II}Pc]^{0}/[Co^{I}Pc]^{-}$ and 4) $[Co^{III}Pc]^{+}/[Co^{II}Pc]^{0}$, which is consistent with previously reported electrochemical studies of CoPc in organic solutions.[1-3] The onset potential of the electrocatalytic HER occurs near peak 2 at ~ -1.1 V vs. $Fc^{+/0}$, and the onset potential of the electrocatalytic CO_2 reduction occurs near peak 1 at ~ -1.75 V vs. $Fc^{+/0}$.

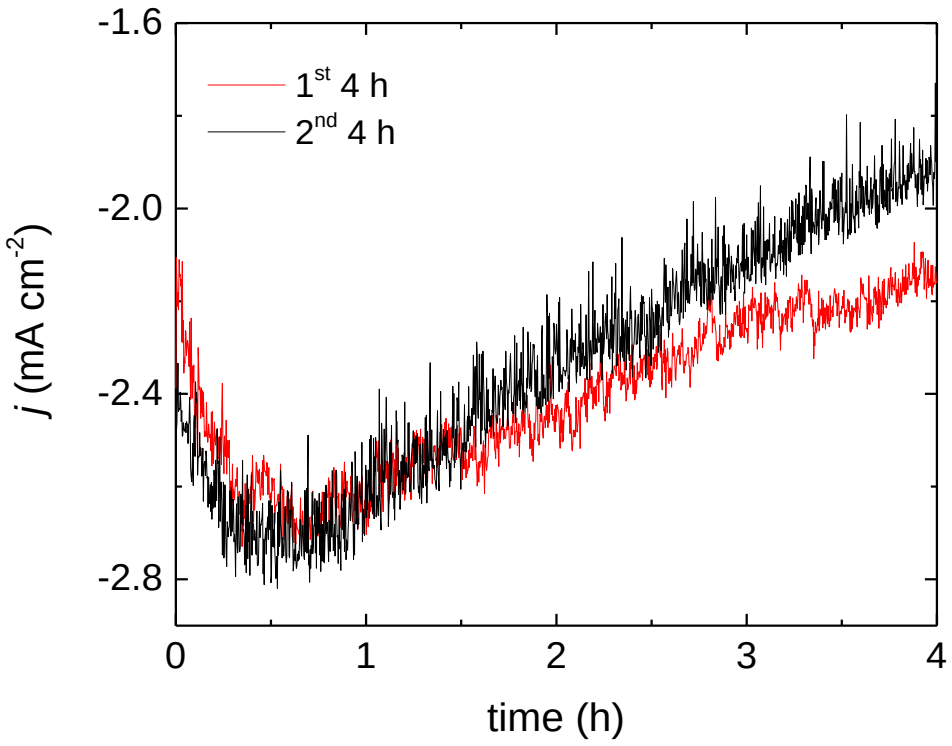

Figure A.16 Representative 4-h controlled potential electrolyses (CPE) for CoPc-P4VP at -1.25 V vs. SCE, the 2nd 4 h CPE is conducted after re-saturate the same electrolyte with CO_2 with the same catalyst. See Table A.3 for the results from CPE.

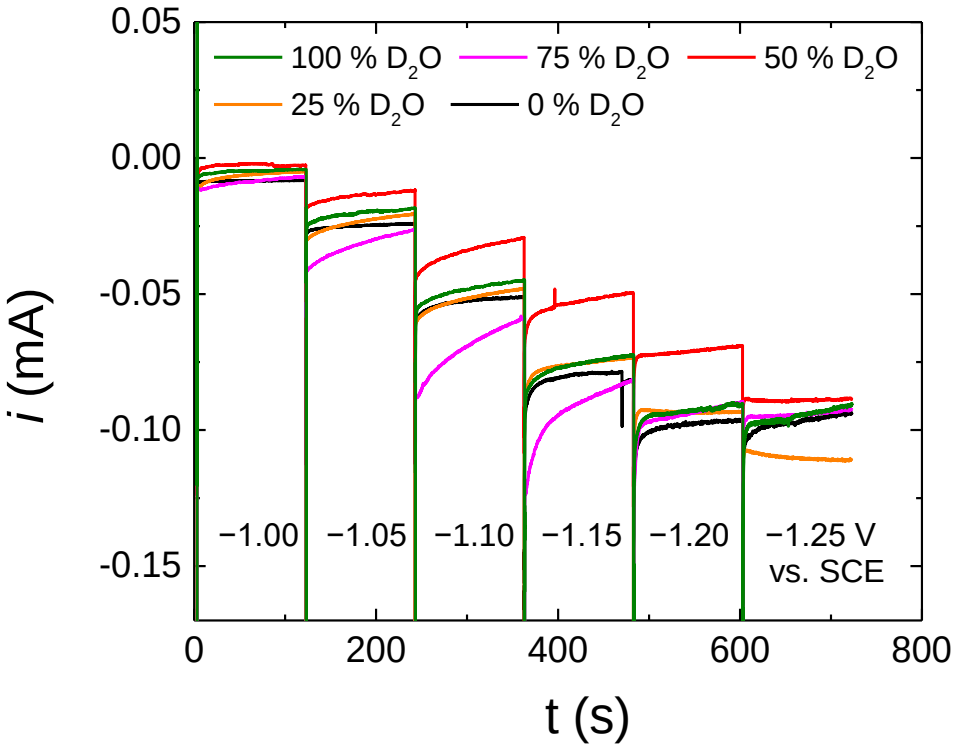

Figure A.17 Representative rotating disk chronoamperometric (CA) step measurements conducted at 1600 rpm with 2-min potential steps from -1.00 V to -1.25 V vs. SCE at 0.05 V increments for CoPc.

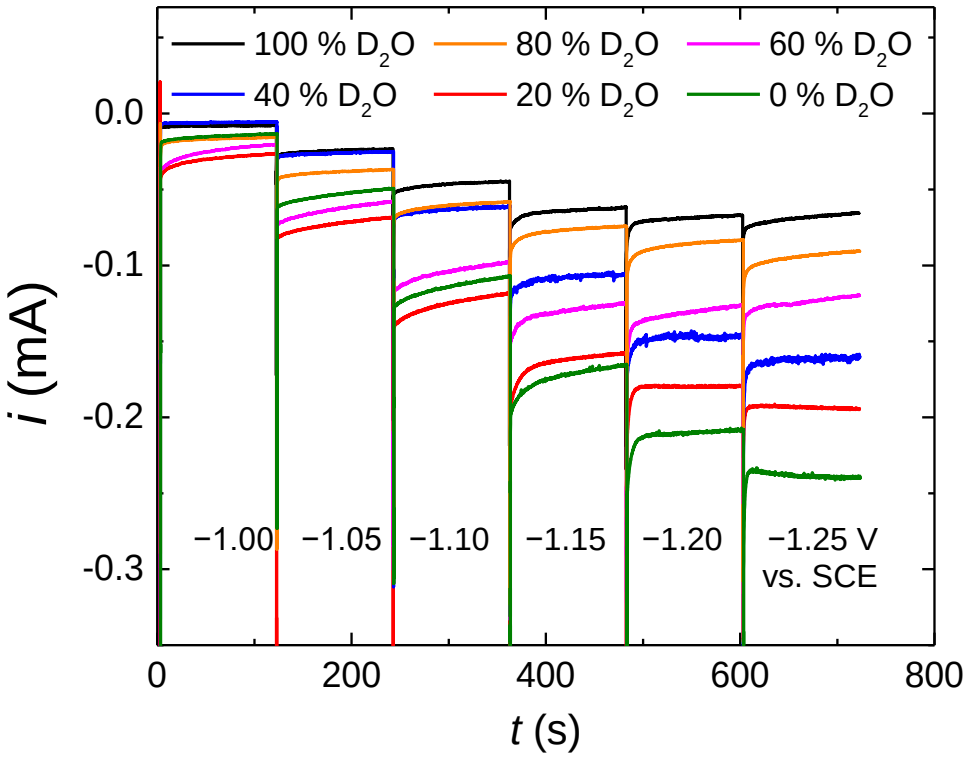

Figure A.18 Representative rotating disk chronoamperometric (CA) step measurements conducted at 1600 rpm with 2-min potential steps from -1.00 V to -1.25 V vs. SCE at 0.05 V increments for CoPc(py).

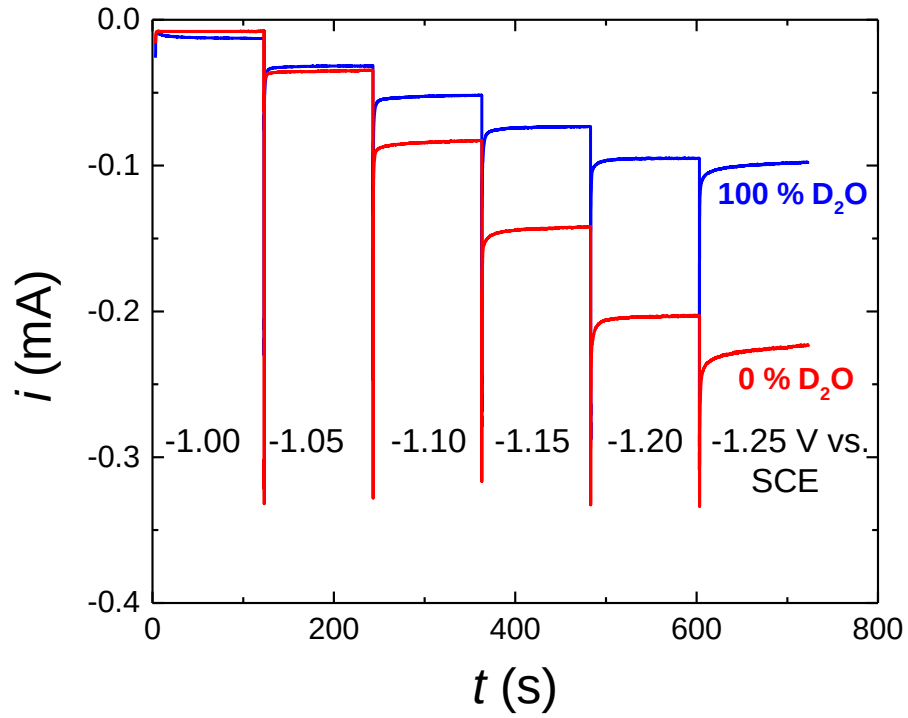

Figure A.19 Representative rotating disk chronoamperometric (CA) step measurements conducted at 1600 rpm with 2-min potential steps from -1.00 V to -1.25 V vs. SCE at 0.05 V increments for CoPc-0.1 %P4VP.

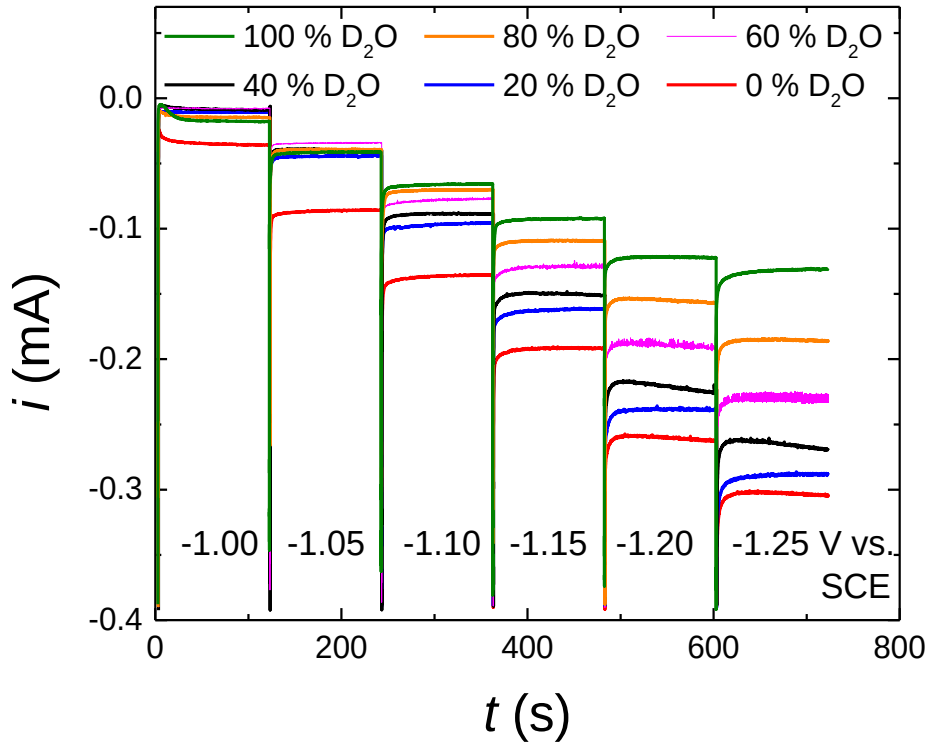

Figure A.20 Representative rotating disk chronoamperometric (CA) step measurements conducted at 1600 rpm with 2-min potential steps from -1.00 V to -1.25 V vs. SCE at 0.05 V increments for CoPc-0.5 %P4VP.

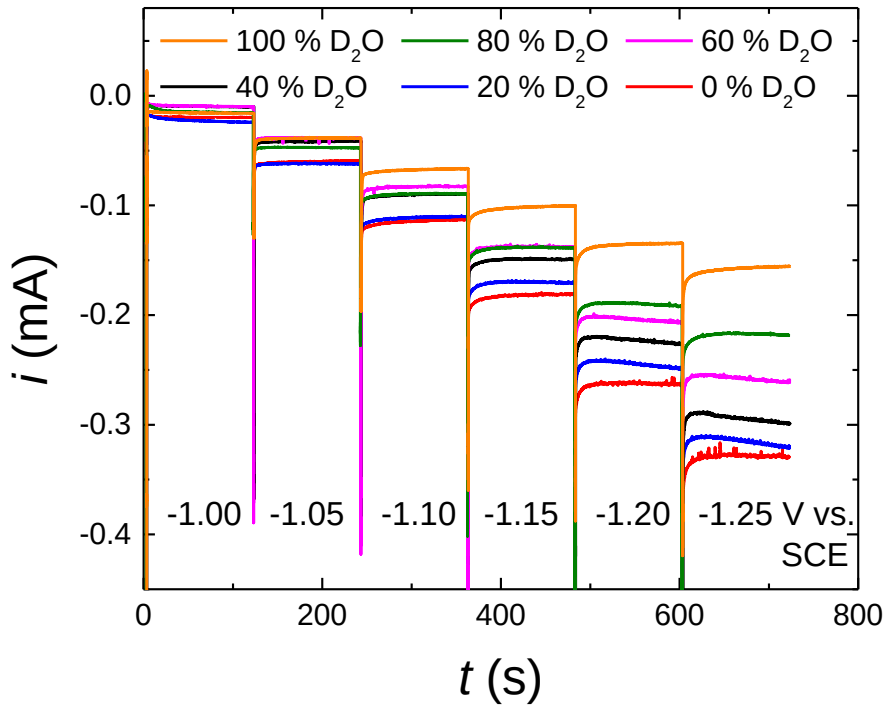

Figure A.21 Representative rotating disk chronoamperometric (CA) step measurements conducted at 1600 rpm with 2-min potential steps from -1.00 V to -1.25 V vs. SCE at 0.05 V increments for CoPc-1 %P4VP.

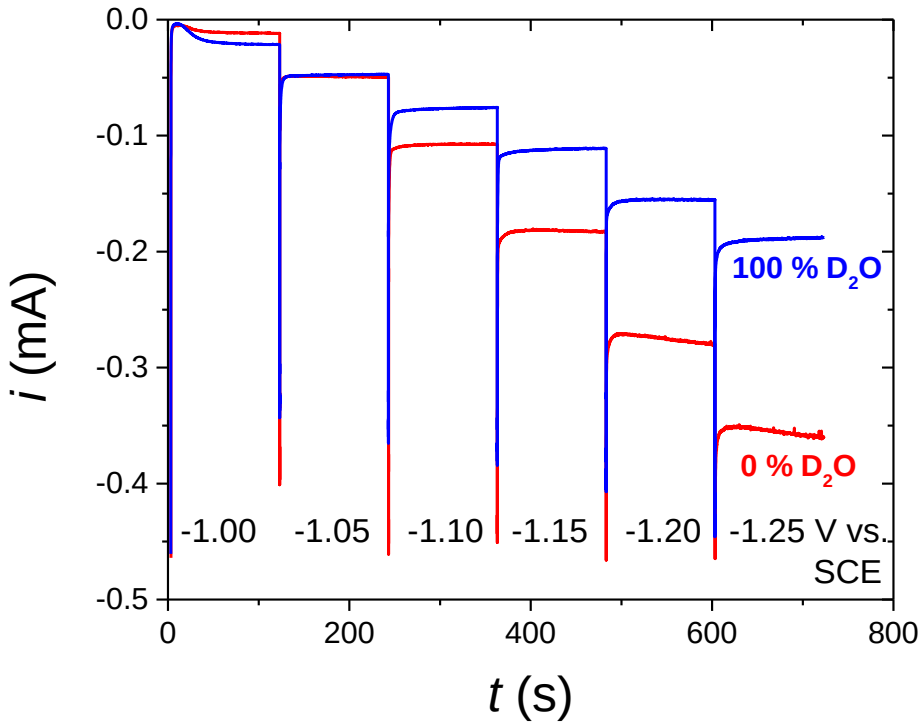

Figure A.22 Representative rotating disk chronoamperometric (CA) step measurements conducted at 1600 rpm with 2-min potential steps from -1.00 V to -1.25 V vs. SCE at 0.05 V increments for CoPc-2 %P4VP.

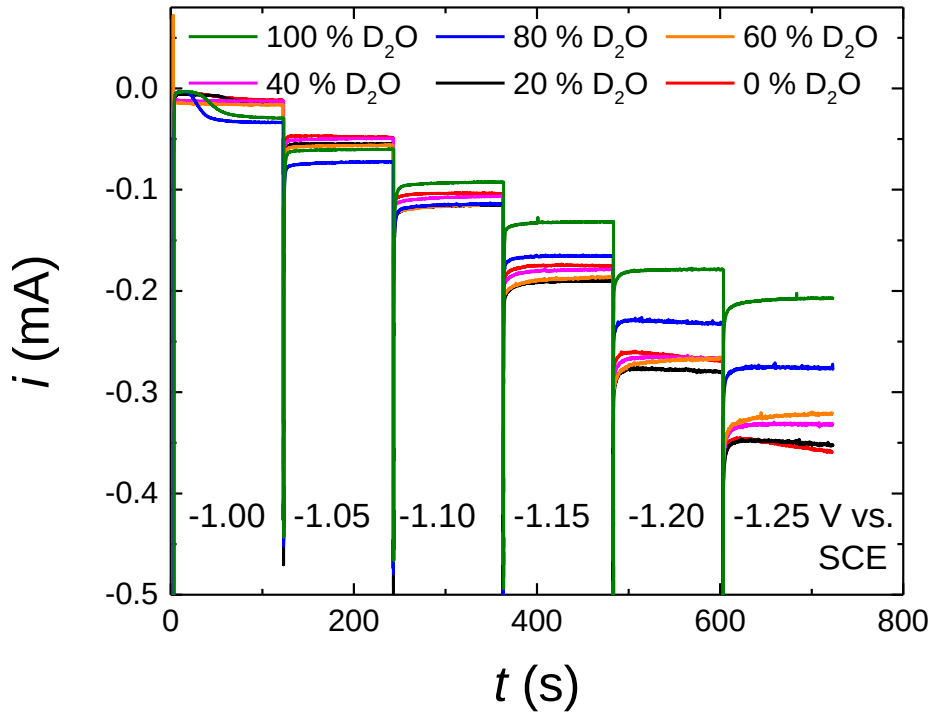

Figure A.23 Representative rotating disk chronoamperometric (CA) step measurements conducted at 1600 rpm with 2-min potential steps from -1.00 V to -1.25 V vs. SCE at 0.05 V increments for CoPc-3 %P4VP.

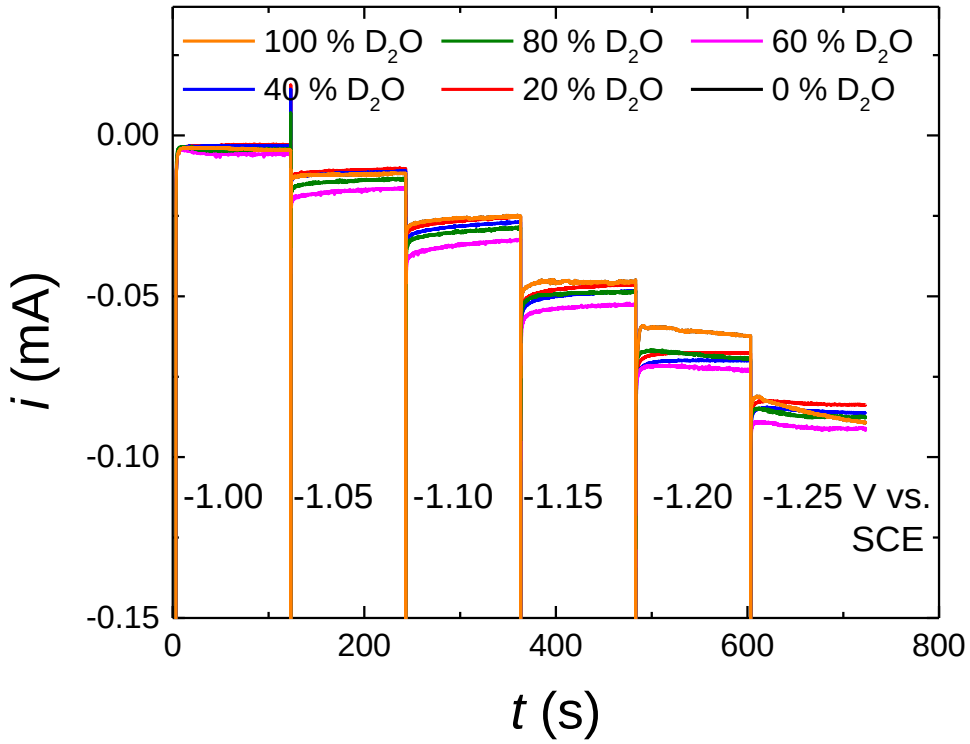

Figure A.24 Representative rotating disk chronoamperometric (CA) step measurements conducted at 1600 rpm with 2-min potential steps from -1.00 V to -1.25 V vs. SCE at 0.05 V increments for CoPc-P2VP.

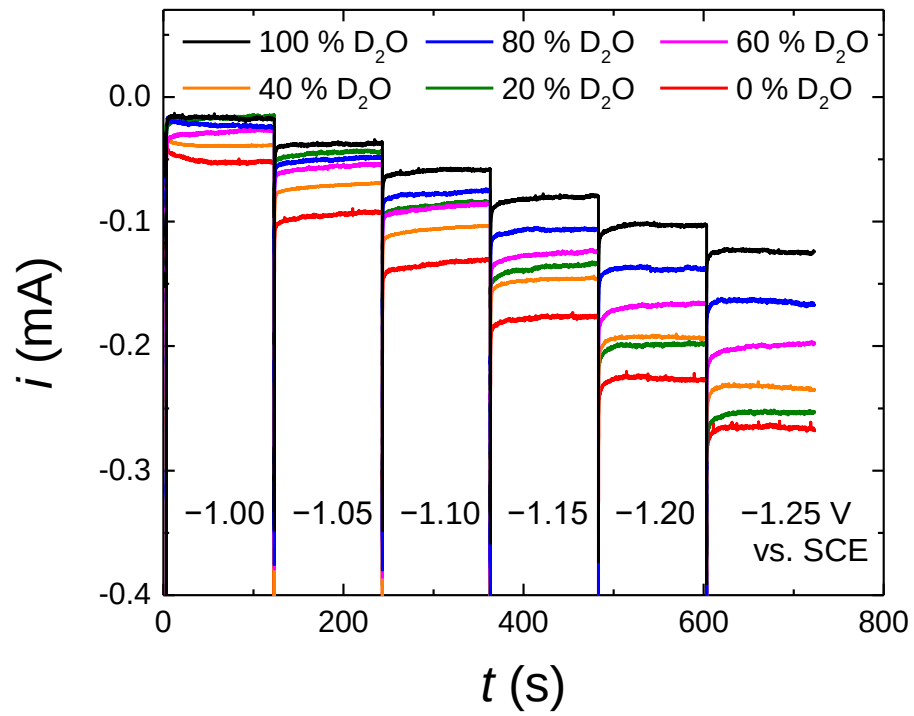

Figure A.25 Representative rotating disk chronoamperometric (CA) step measurements conducted at 1600 rpm with 2-min potential steps from -1.00 V to -1.25 V vs. SCE at 0.05 V increments for CoPc(py)-P2VP.

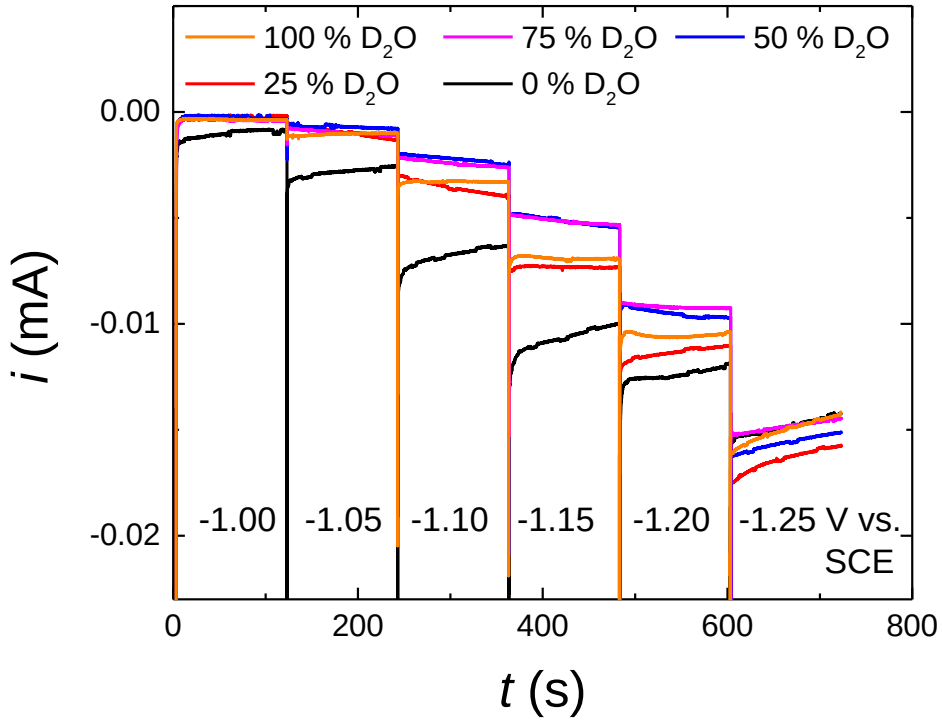

Figure A.26 Representative rotating disk chronoamperometric (CA) step measurements conducted at 1600 rpm with 2-min potential steps from -1.00 V to -1.25 V vs. SCE at 0.05 V increments for CoPc-PS.

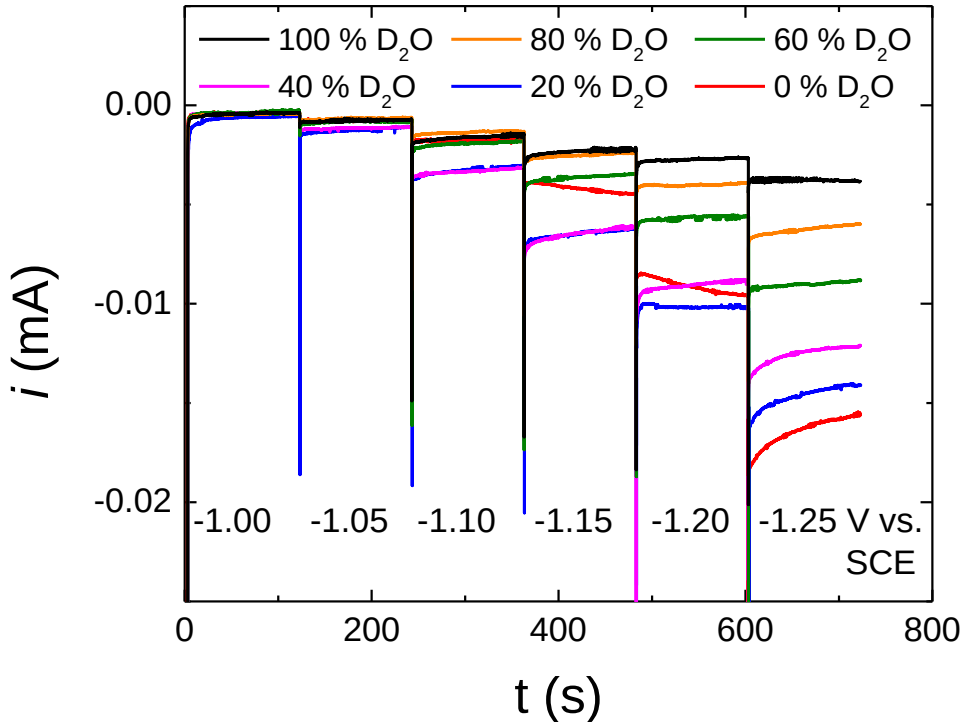

Figure A.27 Representative rotating disk chronoamperometric (CA) step measurements conducted at 1600 rpm with 2-min potential steps from -1.00 V to -1.25 V vs. SCE at 0.05 V increments for CoPc(py)-PS.

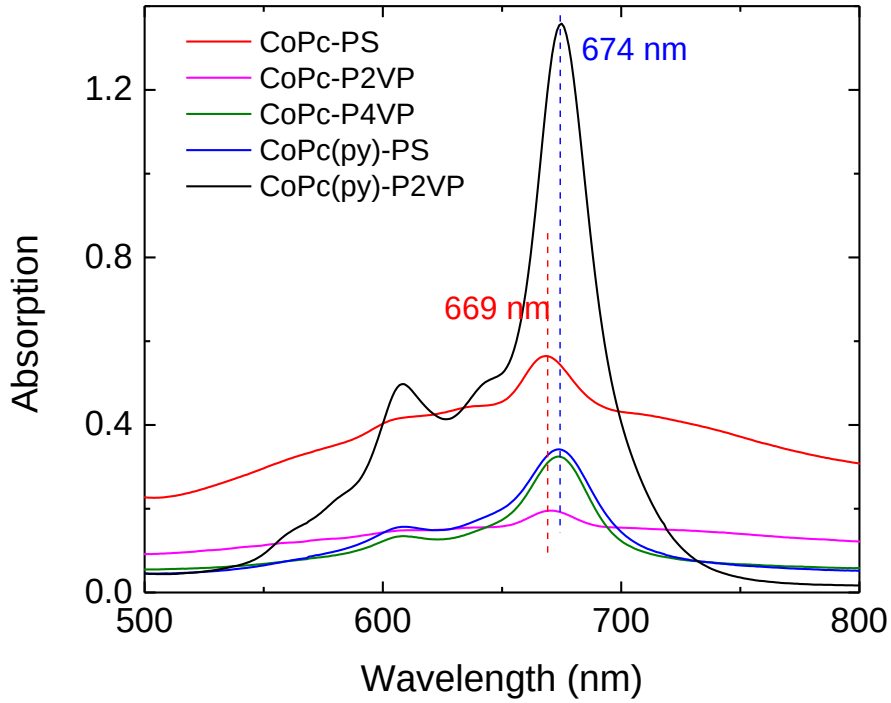

Figure A.28 UV-vis spectrum of CoPc-PS, CoPc-P2VP, CoPc-P4VP, CoPc(py)-PS, and CoPc(py)-P2VP films coated on glass slide. The Q band of CoPc in PS and P2VP near 669 nm is red shifted to 674 nm in UV-vis absorption spectrum of CoPc in P4VP, and CoPc(py) in PS and P2VP films, suggesting the formation of the axial coordination of CoPc in CoPc-P4VP, CoPc(py)-PS, CoPc(py)-P2VP samples.

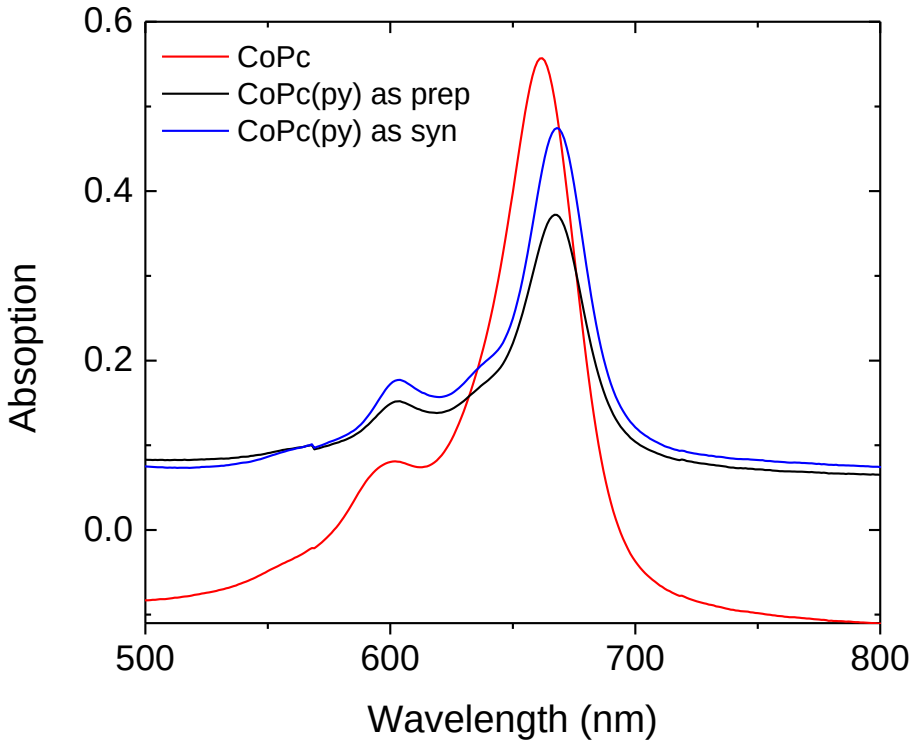

Figure A.29 UV-vis spectrum of 0.01 mM CoPc solution, 0.01 mM CoPc(py) solution as prepared, and 0.01 mM CoPc(py) solution as synthesized. Red shifted Q band is exhibited in the UV-vis spectrum of CoPc(py) as prepared and CoPc(py) as synthesized solutions by about 5 nm compared to that of CoPc, suggesting the formation of the axial coordination of CoPc in CoPc(py) solutions.

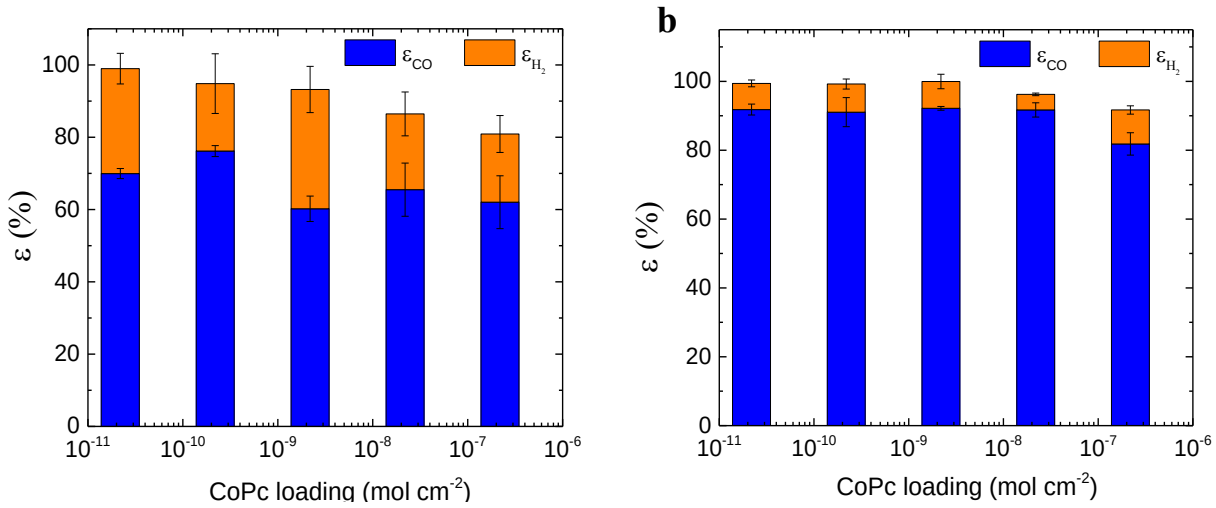

Figure A.30 Faradaic efficiencies (ε) obtained from 2-h controlled potential electrolyses (CPE) at -1.25 V vs. SCE for **a,** CoPc catalysts, and **b,** CoPc-P4VP catalysts at different CoPc loadings in CO_2 saturated pH 5 sodium phosphate electrolyte under CO_2 atmosphere. All reported values are averages from 3 independent measurements, and all errors are given as standard deviations.

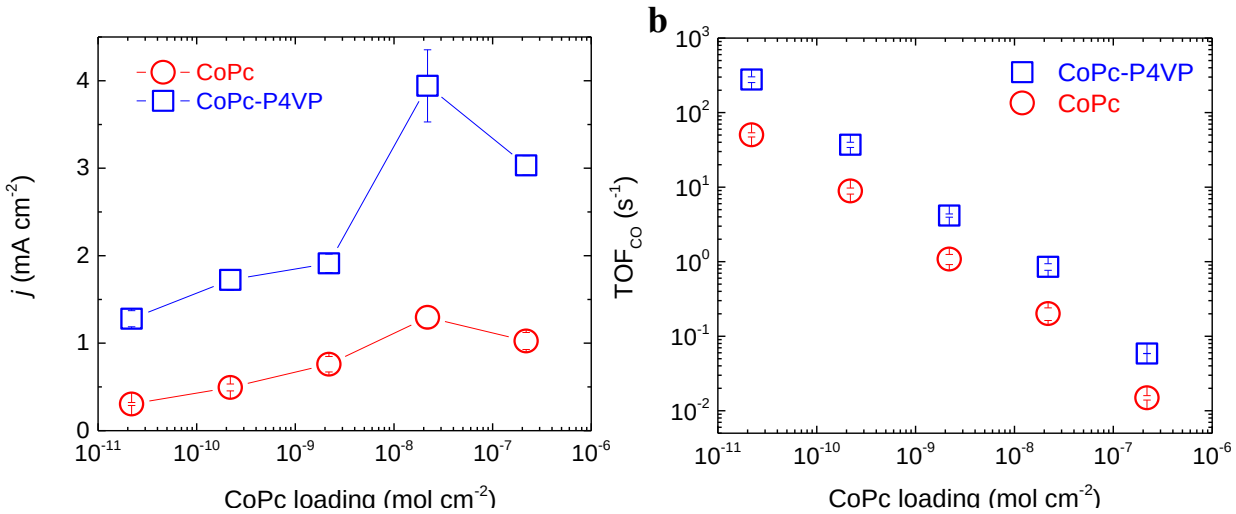

Figure A.31 CO_2 reduction results of 2-h controlled potential electrolyses (CPE) at different CoPc loadings a, Overall current densities (*j*), and **b,** Turnover frequencies for CO (TOF_{CO}) obtained from 2-h CPE at -1.25 V vs. SCE for CoPc and CoPc-P4VP catalysts at different CoPc loadings in CO_2 saturated pH 5 sodium phosphate electrolyte under CO_2 atmosphere. All reported values are averages from 3 independent measurements, and all errors are given as standard deviations.

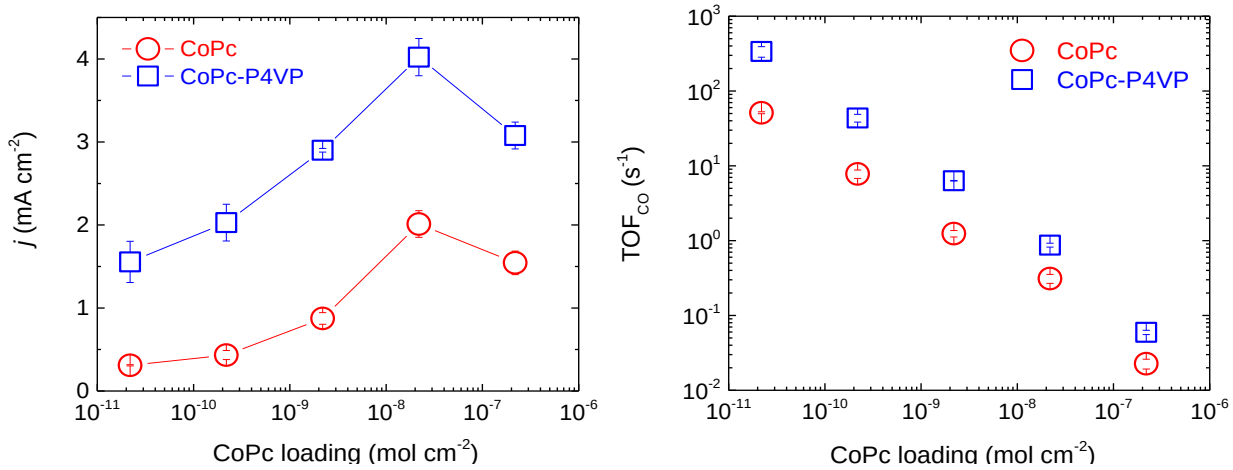

Figure A.32 CO_2 reduction results of rotating disk chronoamperometric (CA) step measurements at different CoPc loadings. a, Overall current densities (*j*), and b, Turnover frequencies for CO (TOF_{CO}) obtained from rotating disk CA step measurements at -1.25 V vs. SCE for CoPc and CoPc-P4VP catalysts at different CoPc loadings in CO_2 saturated pH 5 sodium phosphate electrolyte under CO_2 atmosphere (See Supplementary Methods for detailed TOF calculations). All reported values are averages from 3 independent measurements, and all errors are given as standard deviations.

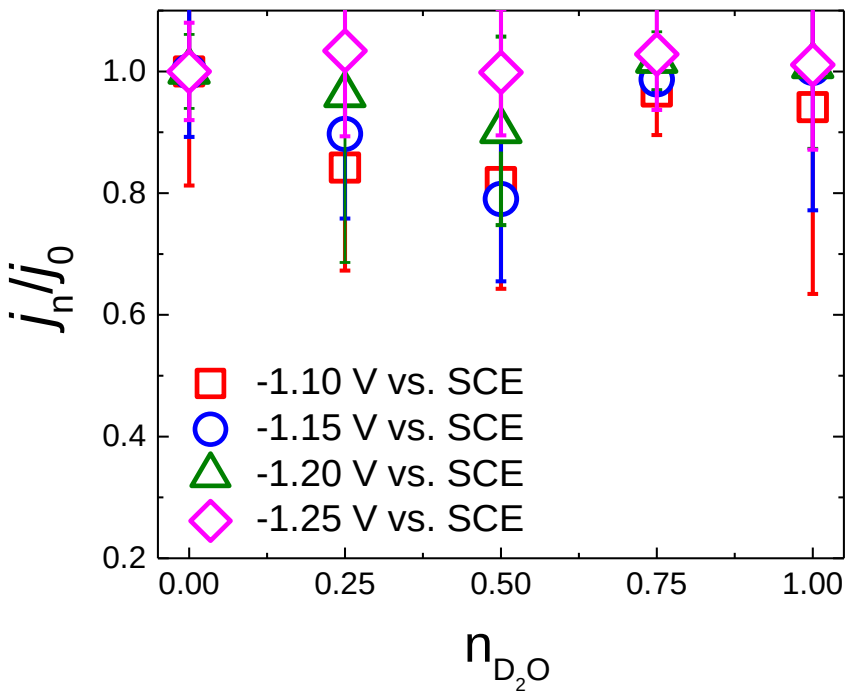

Figure A.33 Proton inventory measurements of CO_2 reduction by CoPc at different potentials based on chronoamperometric (CA) steps. Note: Data at −1.00 V and −1.05 V vs. SCE were not included because minimal catalytic current is observed at those potentials. All reported values are averages from 3 or more independent measurements, all errors are given as standard deviations, and the large standard deviations are due to the relative low measured currents. Note that each potential shows similar proton inventory behavior.

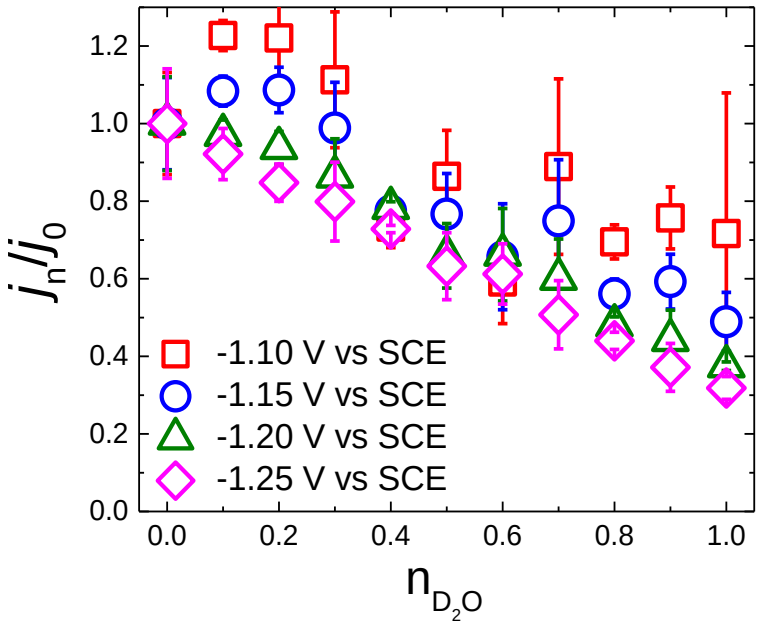

Figure A.34 Proton inventory measurements of CO_2 reduction by CoPc(py) at different potentials based on chronoamperometric (CA) steps. Note: Data at −1.00 V and −1.05 V vs. SCE were not included because minimal catalytic current is observed at those potentials. All reported values are averages from 3 or more independent measurements, all errors are given as standard deviations, and the large standard deviations are due to the relative low measured currents. Note that each potential shows similar proton inventory behavior.

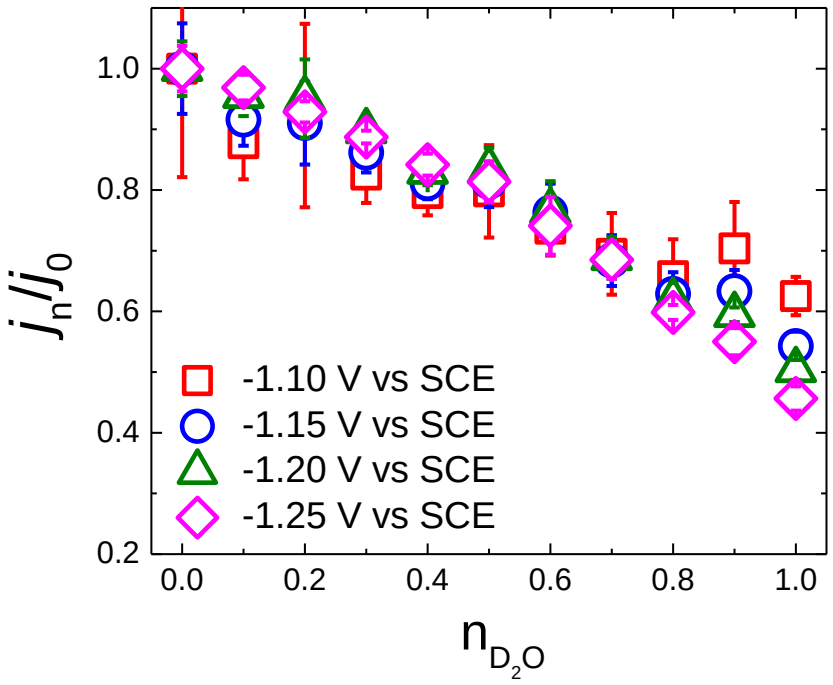

Figure A.35 Proton inventory measurements of CO_2 reduction by CoPc-0.5 %P4VP at different potentials based on chronoamperometric (CA) steps. Note: Data at −1.00 V and −1.05 V vs. SCE were not included because minimal catalytic current is observed at those potentials. All reported values are averages from 3 or more independent measurements, all errors are given as standard deviations, and the large standard deviations are due to the relative low measured currents. Note that each potential shows similar proton inventory behavior.

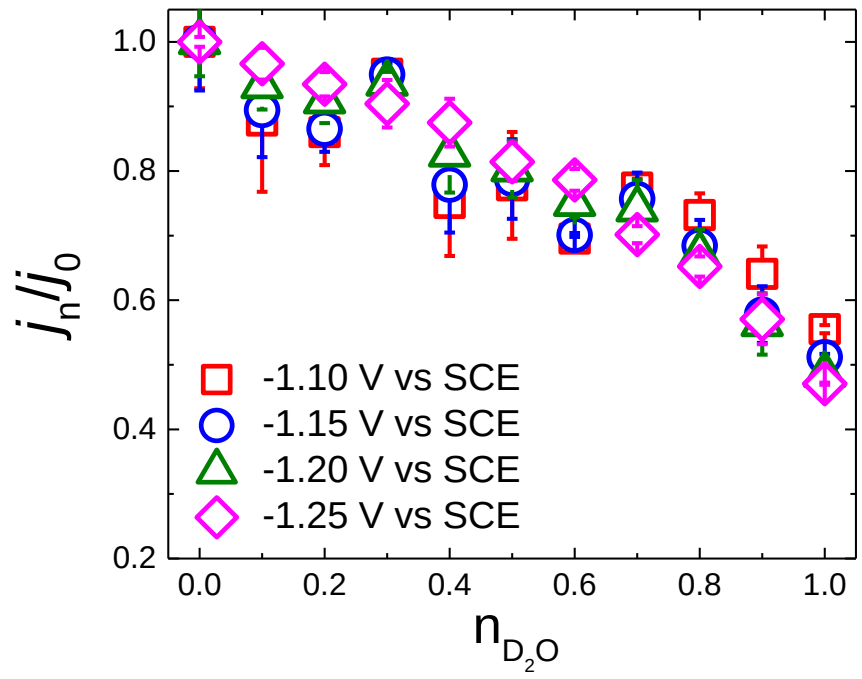

Figure A.36 Proton inventory measurements of CO_2 reduction by CoPc-1% P4VP at different potentials based on chronoamperometric (CA) steps. Note: Data at −1.00 V and −1.05 V vs. SCE were not included because minimal catalytic current is observed at those potentials. All reported values are averages from 3 or more independent measurements, all errors are given as standard deviations, and the large standard deviations are due to the relative low measured currents. Note that each potential shows similar proton inventory behavior.

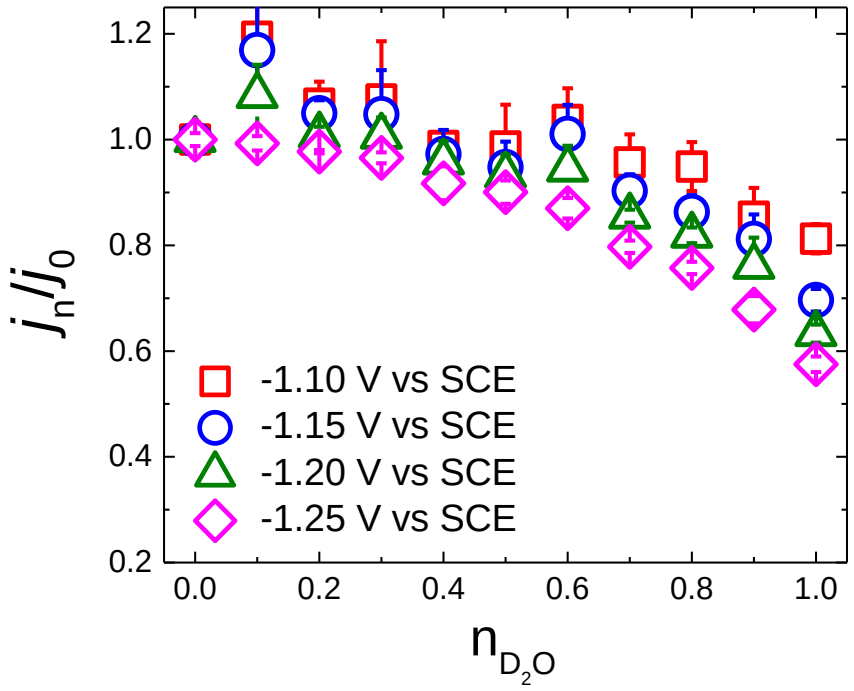

Figure A.37 Proton inventory measurements of CO_2 reduction by CoPc-3% P4VP at different potentials based on chronoamperometric (CA) steps. Note: Data at −1.00 V and −1.05 V vs. SCE were not included because minimal catalytic current is observed at those potentials. All reported values are averages from 3 or more independent measurements, all errors are given as standard deviations, and the large standard deviations are due to the relative low measured currents. Note that each potential shows similar proton inventory behavior.

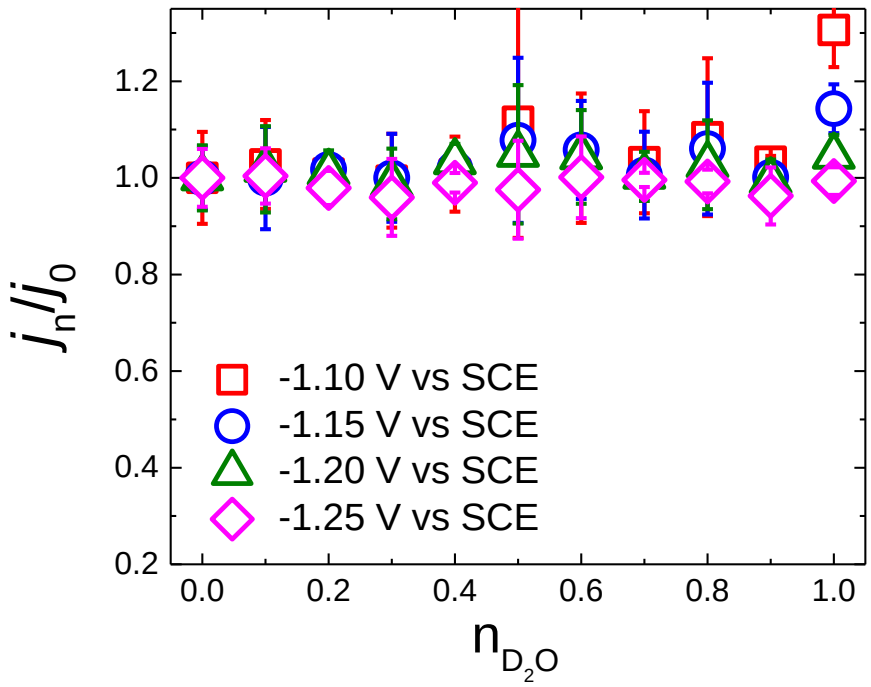

Figure A.38 Proton inventory measurements of CO_2 reduction by CoPc-P2VP at different potentials based on chronoamperometric (CA) steps. Note: Data at −1.00 V and −1.05 V vs. SCE were not included because minimal catalytic current is observed at those potentials. All reported values are averages from 3 or more independent measurements, all errors are given as standard deviations, and the large standard deviations are due to the relative low measured currents. Note that each potential shows similar proton inventory behavior.

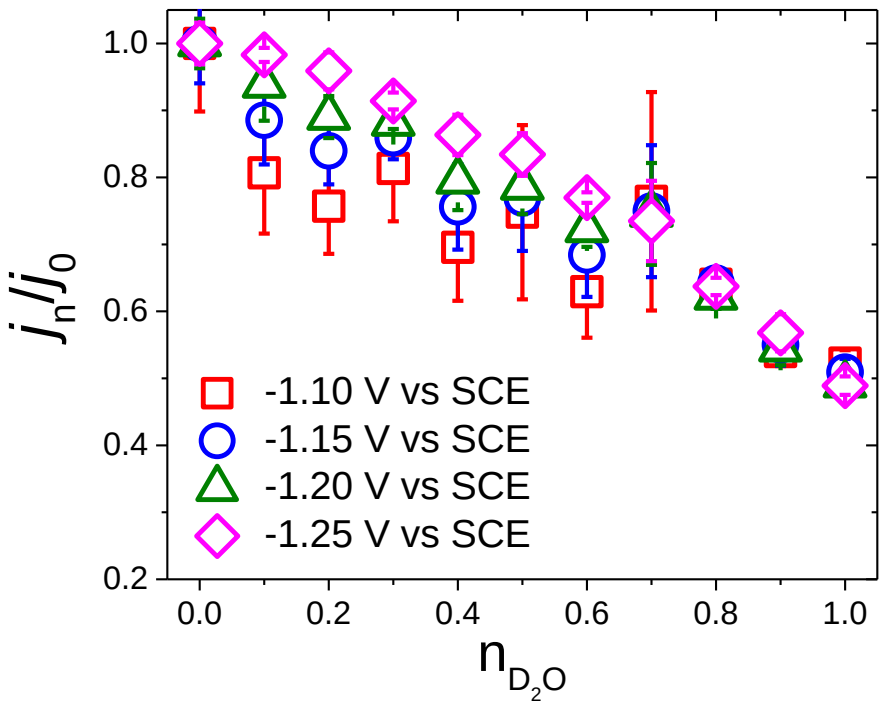

Figure A.39 Proton inventory measurements of CO_2 reduction by CoPc(py)-P2VP at different potentials based on chronoamperometric (CA) steps. Note: Data at −1.00 V and −1.05 V vs. SCE were not included because minimal catalytic current is observed at those potentials. All reported values are averages from 3 or more independent measurements, all errors are given as standard deviations, and the large standard deviations are due to the relative low measured currents. Note that each potential shows similar proton inventory behavior.

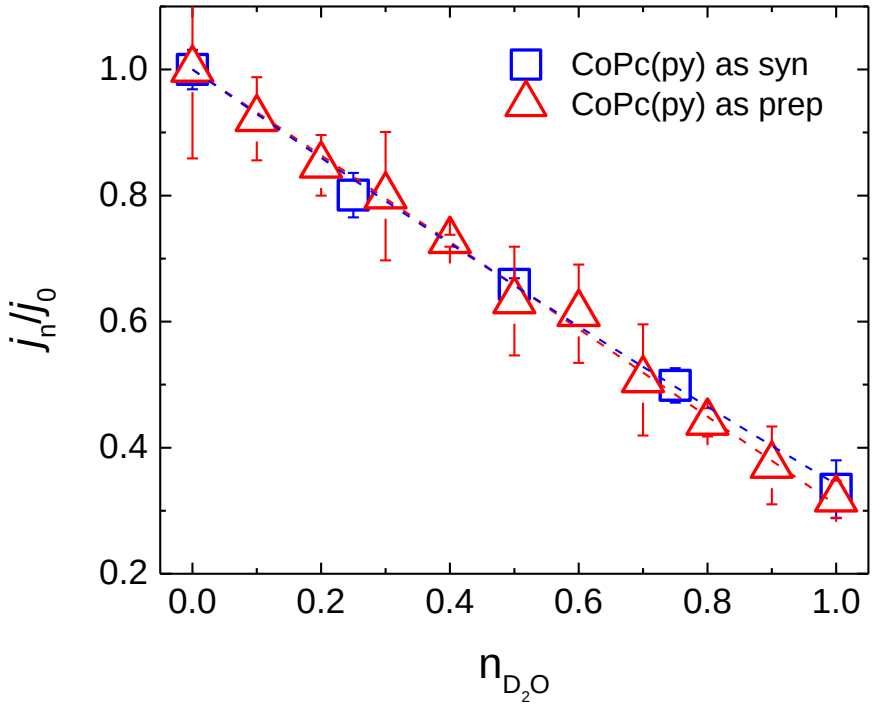

Figure A.40 Proton Inventory measurement of CO_2 reduction at -1.25 V vs SCE by CoPc(py) films prepared two different ways: by method 1 (CoPc and pyridine mixed in DMF and then dropcast) (red triangles) and method 2 (CoPc(py) synthesized independently and then dropcast from DMF) (blue squares). The red and blue dashed lines are fit to the data using equation (2). The resulting values for ϕ and Z are shown in Table A.8. Note that KIE $=j_H/j_D$. All reported values are averages from 3 or more independent measurements, and all errors are given as standard deviations.

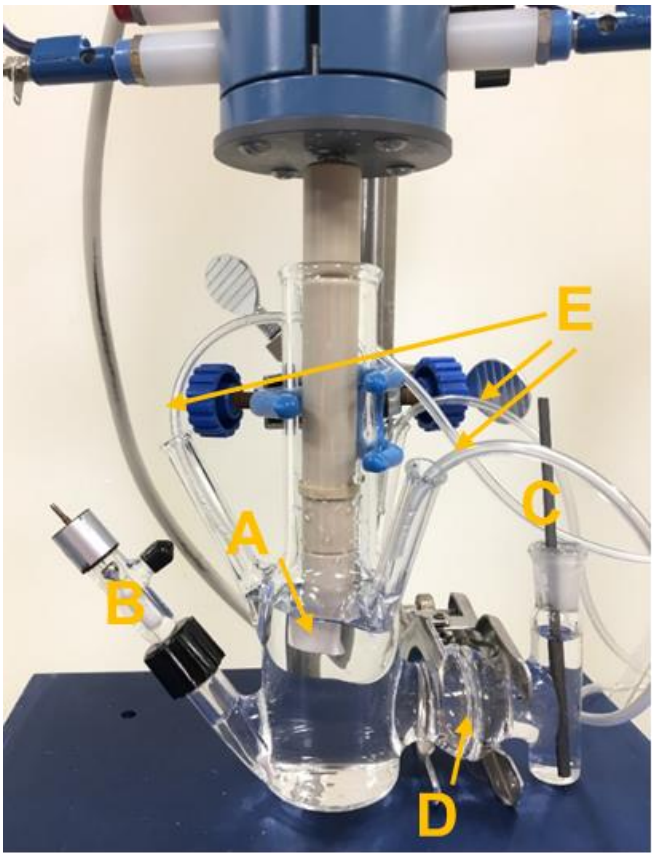

Figure A.41 Photograph of a custom two-compartment glass cell: (A) Modified working electrode held in a RDE assembly attached to an MSR rotator, (B) Sealed SCE reference electrode, (C) Carbon rod auxiliary electrode, (D) Nafion-117 membrane, (E) Tygon tubings for delivering CO_2 gas to blanket headspace of the cell. In general, gas-tight seals were made either by O-ring compression.

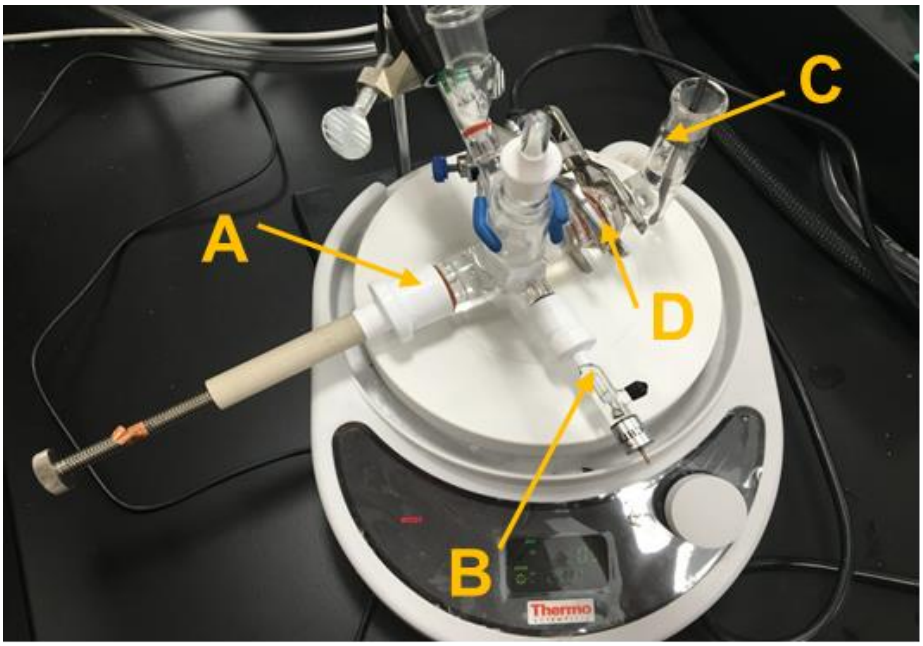

Figure A.42 Photograph of custom, gas-tight two-chamber U-cell: (A) Modified working electrode held in a RDE internal hardware kit and mounted into a custom PEEK sleeve, (B) Sealed SCE reference electrode, (C) Carbon rod auxiliary electrode, (D) Nafion-117 membrane. In general, gas-tight seals were made either by O-ring compression or with ground-glass joints.

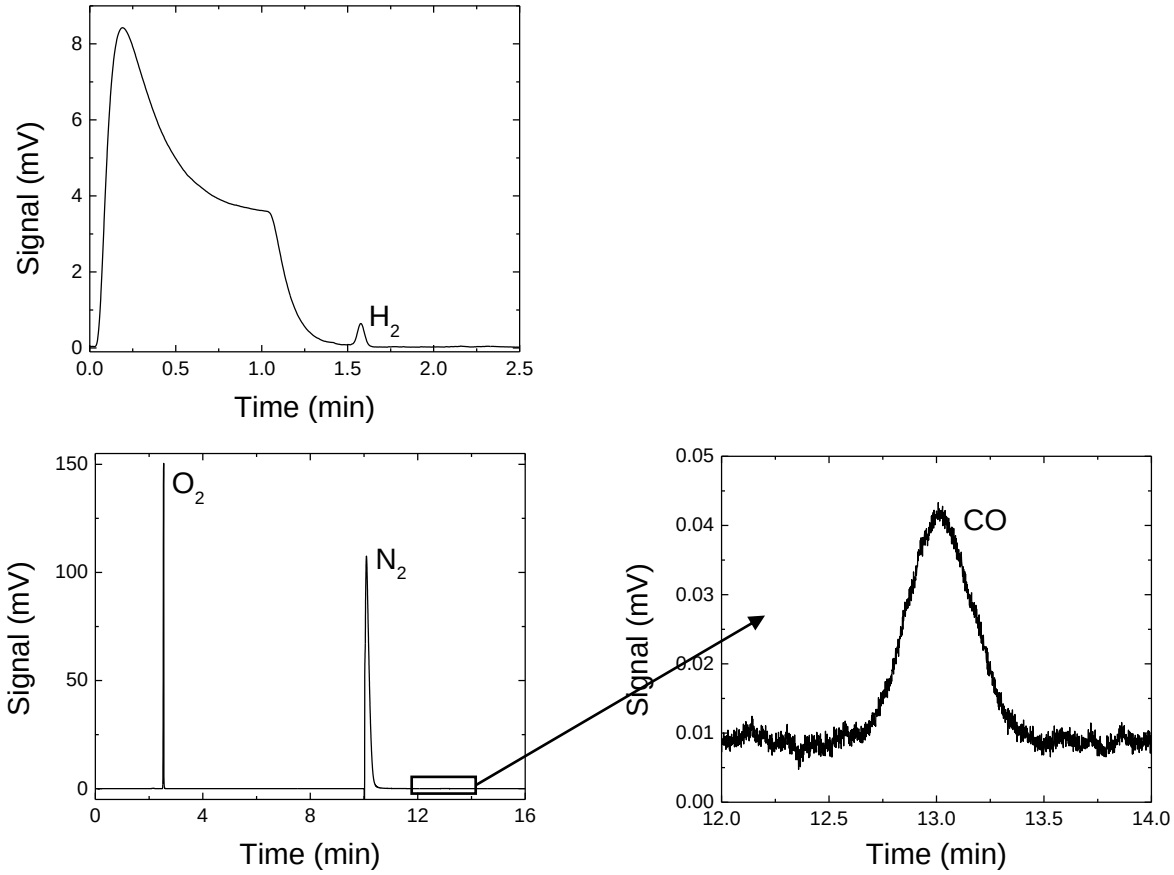

Figure A.43 Representative chromatograph of a calibration mixture containing 0.05 % H_2, 0.05 % CO, 99.9 % N_2. Note: the signal (retention time from 0 to 1 min) before H_2 peak in **a** is due to GC valve switching. **a,** Front TCD. **b,** Back TCD.

A.1.2 Supplementary Tables

Table A.1 Co loading of pre- and post-chronoamperometric (CA) measurement

Catalyst	Pre-CA measurement		Post-CA measurement	
	Co concentration (ppb)	Co loading ($\times 10^{-9}$ mol cm^{-2})	Co concentration (ppb)	Co loading ($\times 10^{-9}$ mol cm^{-2})
CoPc	2.74 ± 0.26	2.04 ± 0.19	2.89 ± 0.17	2.15 ± 0.13
CoPc(py)	2.44 ± 0.27	1.81 ± 0.20	2.60 ± 0.25	1.93 ± 0.18
CoPc-P2VP	2.40 ± 0.06	1.78 ± 0.05	2.85 ± 0.22	2.11 ± 0.17
CoPc-0.1 % P4VP	2.88 ± 0.47	2.14 ± 0.35	2.85 ± 0.34	2.12 ± 0.26
CoPc-0.5 % P4VP	2.74 ± 0.22	2.03 ± 0.16	2.71 ± 0.57	2.01 ± 0.42
CoPc-1 % P4VP	2.84 ± 0.28	2.11 ± 0.21	3.02 ± 1.28	2.25 ± 0.95
CoPc-2 % P4VP	2.88 ± 0.13	2.14 ± 0.09	2.80 ± 0.28	2.08 ± 0.21
CoPc-3 % P4VP	2.75 ± 0.35	2.04 ± 0.26	2.98 ± 0.15	2.21 ± 0.11
CoPc(py)-P2VP	2.80 ± 0.50	2.08 ± 0.37	2.82 ± 0.19	2.10 ± 0.14
CoPc-PS	2.79 ± 0.17	2.07 ± 0.13	2.82 ± 0.09	2.09 ± 0.07
CoPc(py)-PS	2.85 ± 0.11	2.12 ± 0.08	2.80 ± 0.41	2.08 ± 0.31

The catalyst films were dissolved from the electrode surface in 5 mL of 1 M nitric acid solution and then ICP-MS measurements were conducted. The catalyst loading was calculated based on the dissolution solution volume and the concentration. Because ICP-MS measurements require dissolution of the catalyst film from the electrode surface, it is not possible to confirm the loading of the same electrode Pre-CA and Post-CA. Instead, Co loadings were measured on identically-prepared electrodes pre-CA and post-CA (see Supplementary Methods). The errors are given as standard deviations on three identically prepared electrodes.

Table A.2 Results obtained from 2-h controlled potential electrolyses (CPE) experiments at -1.25 V vs SCE for CoPc modified electrodes in pH 5 protic phosphate solution and pD 5 deuterated phosphate solution for CO_2 reduction.

Catalyst	Solvent	Charge (C)	ε_{CO} (%)	TON_{CO} (2h)	TOF_{CO} (s^{-1})	ε_{H2} (%)	ε_{total} (%)
CoPc	H_2O	0.62 ± 0.07	60 ± 3	$7.8 \pm 1.2 \times 10^3$	1.08 ± 0.17	33 ± 6	93 ± 5
	D_2O	0.61 ± 0.05	58 ± 3	$7.5 \pm 0.7 \times 10^3$	1.04 ± 0.10	36 ± 1	95 ± 4
CoPc(py)	H_2O	1.09 ± 0.02	78 ± 4	$1.8 \pm 0.1 \times 10^4$	2.44 ± 0.13	11 ± 2	89 ± 2
	D_2O	0.32 ± 0.06	76 ± 2	$5.1 \pm 0.8 \times 10^3$	0.71 ± 0.12	11 ± 1	87 ± 3
CoPc-0.1 %P4VP	H_2O	1.07 ± 0.17	89 ± 2	$2.0 \pm 0.3 \times 10^4$	2.72 ± 0.40	7 ± 2	96 ± 1
	D_2O	0.47 ± 0.07	90 ± 2	$8.8 \pm 1.6 \times 10^3$	1.23 ± 0.22	8 ± 1	98 ± 2
CoPc-0.5 %P4VP	H_2O	1.31 ± 0.10	92 ± 3	$2.5 \pm 0.1 \times 10^4$	3.45 ± 0.17	8 ± 4	99 ± 4
	D_2O	0.62 ± 0.04	90 ± 5	$1.2 \pm 0.1 \times 10^4$	1.62 ± 0.15	7 ± 1	98 ± 5
CoPc-1 %P4VP	H_2O	1.57 ± 0.09	92 ± 1	$3.0 \pm 0.2 \times 10^4$	4.16 ± 0.21	8 ± 2	100 ± 2
	D_2O	0.78 ± 0.03	96 ± 5	$1.6 \pm 0.1 \times 10^4$	2.16 ± 0.14	5 ± 1	101 ± 4
CoPc-2 %P4VP	H_2O	1.97 ± 0.25	94 ± 3	$3.8 \pm 0.5 \times 10^4$	5.31 ± 0.65	5 ± 2	99 ± 3
	D_2O	1.10 ± 0.13	89 ± 3	$2.0 \pm 0.2 \times 10^4$	2.81 ± 0.30	9 ± 1	98 ± 4
CoPc-3 %P4VP	H_2O	2.28 ± 0.10	93 ± 2	$4.4 \pm 0.1 \times 10^4$	6.09 ± 0.16	6 ± 1	99 ± 2
	D_2O	1.27 ± 0.11	91 ± 2	$2.4 \pm 0.2 \times 10^4$	3.31 ± 0.28	10 ± 2	100 ± 2
CoPc-P2VP[a]	H_2O	0.40 ± 0.08	82 ± 2	$6.9 \pm 1.4 \times 10^3$	0.95 ± 0.20	14 ± 5	97 ± 3
	D_2O	0.41 ± 0.03	82 ± 1	$6.9 \pm 0.6 \times 10^3$	0.96 ± 0.08	12 ± 4	94 ± 4
CoPc(py)-P2VP[a]	H_2O	1.56 ± 0.04	91 ± 1	$2.9 \pm 0.1 \times 10^4$	4.08 ± 0.13	6 ± 1	97 ± 1
	D_2O	0.81 ± 0.11	90 ± 3	$1.5 \pm 0.2 \times 10^4$	2.08 ± 0.33	3 ± 1	93 ± 2
CoPc-PS[a]	H_2O	0.14 ± 0.06	86 ± 2	$2.5 \pm 1.4 \times 10^3$	0.35 ± 0.19	15 ± 2	100 ± 1
	D_2O	0.18 ± 0.06	81 ± 2	$3.0 \pm 1.0 \times 10^3$	0.41 ± 0.14	18 ± 4	100 ± 6
CoPc(py)-PS[a]	H_2O	0.20 ± 0.03	86 ± 4	$3.6 \pm 0.5 \times 10^3$	0.50 ± 0.07	7 ± 2	93 ± 2
	D_2O	0.07 ± 0.01	87 ± 3	$1.2 \pm 0.2 \times 10^3$	0.16 ± 0.03	14 ± 1	95 ± 3

All reported values are averages from 3 independent measurements, and all errors are given as standard deviations. a Polymer-catalyst composite films were drop-cast from deposition solutions containing 1 % w/v polymer.

Table A.3 Results obtained from 4-h controlled potential electrolyses (CPE) experiments at -1.25 V vs SCE for CoPc-P4VP catalyst in pH 5 phosphate solution under CO_2 atmosphere.

Catalyst	Charge(C)	ε_{CO} (%)	TON_{CO} (2h)	TOF_{CO} (s^{-1})	ε_{H2} (%)	ε_{total} (%)
CoPc-P4VP	3.77 ± 0.30	91 ± 3	7.1 ± 0.5 ×10^4	4.93 ± 0.34	10 ± 1	101 ± 4
CoPc-P4VP[a]	3.84	91	7.21 ×10^4	5.01	9	99

All reported values are averages from 3 or more independent measurements, and all errors are given as standard deviations. aContinue another 4-h CPE with the same catalyst after re-saturate the same electrolyte with CO_2.

Table A.4 Results of kinetic isotope effect (KIE) studies for CoPc, CoPc(py), CoPc-P2VP, CoPc-P4VP, and CoPc-PS catalyst for hydrogen evolution reaction (HER).

Catalyst	j_H (mA·cm^{-2})	j_D (mA·cm^{-2})	KIE
CoPc	-1.856 ± 0.158	-1.349 ± 0.241	1.38 ± 0.27
CoP(py)	-1.495 ± 0.155	-1.058 ± 0.228	1.41 ± 0.34
CoPc-P2VP	-1.397 ± 0.060	-1.066 ± 0.078	1.31 ± 0.11
CoPc-P4VP	-2.018 ± 0.195	-1.458 ± 0.021	1.38 ± 0.14
CoPc-PS	-0.277 ± 0.032	-0.209 ± 0.018	1.33 ± 0.19

All measurements conducted using rotating disk chronoamperometric (CA) measurements under N_2 in pH/pD = 4.7 (the same pH/pD of the electrolyte in CO_2 reduction measurements after saturated by CO_2) phosphate solutions at -1.25 V vs. SCE. All reported values are averages from 3 or more independent measurements, and all errors are given as standard deviations. Note that a weak KIE for HER has been observed for all the catalytic systems studied in this study, which suggests that the rate-determining step for HER may be the proton recombination step on the 2 H^+ protonated CoPc intermediate.[4]

Table A.5 Results of kinetic isotope effect (KIE) studies for CoPc and CoPc-P4VP at different CoPc loadings.

CoPc loading (mol cm^{-2})	Catalyst	j_H ($mA \cdot cm^{-2}$)	j_D ($mA \cdot cm^{-2}$)	$\varepsilon_{CO,H}$ (%)	$\varepsilon_{CO,D}$ (%)	KIE
2.19×10^{-11} [a]	CoPc	-0.31 ± 0.01	-0.32 ± 0.02	70 ± 1	66 ± 9	1.0 ± 0.1
	CoPc-P4VP	-1.56 ± 0.22	-0.88 ± 0.11	92 ± 2	91 ± 3	1.8 ± 0.3
2.19×10^{-9} [b]	CoPc	-0.87 ± 0.07	-0.88 ± 0.12	60 ± 3	58 ± 3	1.0 ± 0.2
	CoPc-P4VP	-2.90 ± 0.02	-1.37 ± 0.01	92 ± 1	96 ± 5	2.1 ± 0.1

Current density (j) measurements were conducted through rotating disk chronoamperometric (CA) step measurements, and Faradaic efficiency (ε) measurements were conducted through 2-h controlled potential electrolyses (CPE). All measurements were conducted at -1.25 V vs. SCE in pH/pD 5 phosphate solution under CO_2 atmosphere. All reported values are averages from 3 or more independent measurements, and all errors are given as standard deviations. [a] The lowest loading used in the loading dependence study. [b] Normal loading used in this work for comparison.

Table A.6 Results obtained from 2-h controlled potential electrolyses (CPE) experiments at -1.25 V vs SCE for bare EPG working electrodes in pH 5 phosphate solution under CO_2 atmosphere with 0.05 mM added pyridine (py). Results for CPE experiments with CoPc without added py and CoPc(py) are included for comparison.

Catalyst	Charge(C)	ε_{CO} (%)	TON_{CO} (2h)	TOF_{CO} (s^{-1})	ε_{H2} (%)	ε_{total} (%)
0.05 mM py	0.27 ± 0.03	4 ± 2	$5.2 \pm 2.8 \times10^{-2}$	$7.2 \pm 3.8 \times10^{-2}$	62 ± 11	66 ± 12
CoPc	0.62 ± 0.07	60 ± 3	$7.8 \pm 1.2 \times10^{3}$	1.08 ± 0.17	33 ± 6	93 ± 5
CoPc(py)	1.09 ± 0.02	78 ± 4	$1.8 \pm 0.1 \times10^{4}$	2.44 ± 0.13	11 ± 2	89 ± 2

Note that there's no liquid products detected in any of the above catalytic systems. All reported values are averages from 3 or more independent measurements, and all errors are given as standard deviations.

Table A.7 Elemental Analysis results for synthesized CoPc(py) complex

Element	Theory (%)	Found (%)
C	68.30	67.98
H	3.25	3.26
N	19.38	19.21

Table A.8 Results of kinetic isotope effect (KIE) studies and proton inventory measurements for CoPc(py) as synthesized, results of proton inventory measurements for CoPc(py) as prepared is included for comparison.

Catalyst	j_H (mA·cm^{-2})	j_D (mA·cm^{-2})	KIE	Proton Inventory Parameters	
				ϕ	Z
CoPc(py) as synthesized	-2.02 ± 0.06	-0.67 ± 0.09	3.0 ± 0.4	0.37 ± 0.04	0.92 ± 0.06
CoPc(py) as prepared	-1.92 ± 0.27	-0.61 ± 0.06	3.1 ± 0.5	0.30 ± 0.01	1.02 ± 0.02

All measurements conducted using rotating disk chronoamperometric (CA) measurements at -1.25 V vs. SCE in pH/pD 5 phosphate solution under CO_2 atmosphere. All reported values are averages from 3 or more independent measurements, and all errors are given as standard deviations.

A.1.3 Supplementary Methods

A.1.3.1 Materials and Chemicals

All purchased chemicals were used as received unless otherwise specified. Cobalt phthalocyanine (CoPc, 97%), poly-4-vinylpyridine (P4VP, average Mw ~ 160,000), poly-2-vinylpyridine (P2VP, average Mw ~ 159,000), N,N-Dimethylformamide (DMF, ACS grade), pyridine (ACS grade, ≥ 99%), Dimethyl sulfoxide (DMSO, ACS grade, ≥ 99.9 %), 2,2,2-trifluoroethanol (TFE, ReagentPlus grade, ≥ 99.0%), ferrocenecarboxylic acid (97%), sodium phosphate monobasic (BioXtra, > 99.0%), sodium deuteroxide solution (NaOD, 40 wt.% in D_2O, 99.5% D), phosphoric acid-D3 solution (85 wt.% in D_2O), and Nafion-117 cation exchange membrane (Nafion) were purchased from Sigma Aldrich. Deuterium oxide was purchased from both Sigma Aldrich (D, 99.9%, Mw = 20.03) and Cambridge Isotope Labs, Inc. (D, 99.9%, Mw = 20.03). Sulfuric acid (TraceMetal grade) and nitric acid (TraceMetal grade, 67-70 %) were purchased from Fisher Scientific. Tetrabutylammonium hexaflurophosphate (nBu_4NPF_6, > 98.0%) was purchased from TCI America and recrystallized from Methonal/H_2O (v/v = 8/1). Cobalt ICP standard (1000 ppm Co in 3 % HNO_3) was purchased from Ricca Chemical Company. Edge-plane graphite disk electrodes (5 mm diameter, effective electrode area: 0.114 cm^2) were purchased from Pine Research Instrumentation. Pt wire (99.99 %, 0.02” diameter) was purchased from Surepure Chemetals L.L.C. Compressed CO_2 gas (99.8 %) was purchased from Cryogenic Gases. All water used in this study was ultrapure water (18.2 MΩ·cm resistivity) purified with a Thermo Scientific GenPure UV-TOC/UF xCAD-plus water purification system. Plain glass microscope slides were purchased from Fisher Scientific.

A.1.3.2 Preparation of Deposition Solutions

CoPc. The CoPc/DMF deposition solution was prepared by dissolving 3 mg of CoPc in 100 mL DMF solvent. The resulting solution was sonicated for 30 min to fully disperse the CoPc. The concentration of CoPc in the resulting solution is 0.05 mM.

CoPc(py). The CoPc(py)/DMF deposition solution was prepared two ways:

Method 1: By dissolving 3 mg of CoPc in a mixture of 95 mL DMF and 5 mL of pyridine (19:1 DMF/pyridine). The resulting solution was sonicated for 30 min to fully disperse the CoPc. The concentration of CoPc(py) in the resulting solution is 0.05 mM.

Method 2: By first synthesizing CoPc(py) based on previously-reported procedures.[5] Synthesis of 5-coordinate CoPc(py) was confirmed by Elemental Analysis conducted by Midwest Microlab, Inc. (see Table A.7). Films were prepared by dissolving 3.3 mg CoPc(py) as synthesized in 100 mL DMF, then the solution was sonicated for 30 min, the concentration of CoPc(py) as synthesized in the resulting solution is 0.05 mM.

Drop-cast films prepared by both methods showed analogous KIE and proton inventory results (see Figure A.40 and Table A.8), suggesting the prepared films are identical. In addition, liquid-phase UV-Vis measurements of CoPc(py) deposition solutions prepared by both methods show an analogous red-shift in the UV-Vis spectra suggesting both are 5-coordinate species (see Figure A.29)

CoPc-P4VP. The CoPc-P4VP (CoPc-1% P4VP) deposition solution was prepared by dissolving 0.01 g of P4VP in 1 mL of CoPc/DMF solution. The resulting solution was sonicated for 20 mins to fully dissolve the P4VP and disperse the CoPc. The CoPc-0.1% P4VP and CoPc-0.5% P4VP solutions were prepared by diluting the CoPc-1% P4VP solution by a factor of 10 and a factor of 2, respectively. CoPc-2 % P4VP and CoPc-3 % P4VP deposition solutions were prepared by

dissolving 0.02 g P4VP and 0.03 g P4VP in 1 mL CoPc/DMF solution, respectively. The resulting solution was sonicated for 20 mins to fully dissolve the P4VP and disperse the CoPc.

CoPc-P2VP/DMF. The CoPc-P2VP deposition solution was prepared by dissolving 0.01 g P2VP in 1 mL of CoPc/DMF solution. The resulting solution was sonicated for 20 mins to fully dissolve the P2VP and disperse the CoPc.

CoPc(py)-P2VP. The CoPc(py)-P2VP deposition solution was prepared by dissolving 0.01 g P2VP in 1 mL of CoPc(py)/DMF solution. The resulting solution was sonicated for 20 mins to fully dissolve the P2VP and disperse the CoPc.

CoPc-PS. The CoPc-PS deposition solution was prepared by dissolving 0.01 g PS in 1 mL CoPc/DMF solution. The resulting solution was sonicated for 20 mins to fully dissolve the PS and disperse the CoPc.

CoPc(py)-PS. The CoPc(py)-PS deposition solution was prepared by dissolving 0.01 g PS in 1 mL CoPc(py)/DMF solution. The resulting solution was sonicated for 20 mins to fully dissolve the PS and disperse the CoPc.

A.1.3.3 Scan Rate Dependence Studies

Scan rate dependence studies were conducted in pH 5 phosphate solution using the same cell described in the main text (see Methods in the main text). The electrolyte solution was degassed with N_2 for ~ 30 min prior to the measurement, and the headspace was blanked with N_2 during the measurement. Rotating disk cyclic voltammetry measurement was conducted for all the catalyst systems investigated in this work at 1600 rpm with the potential range from 0.8 V to -0.8 V vs. SCE. The scan rate was varied from 0.2 V s^{-1} to 6.4 V s^{-1} (see Figure A.1−Figure A.14).

A.1.3.4 ICP-MS Measurement

To measure the Co loading on the film-modified electrodes, as-prepared electrodes and identically-prepared electrodes after the rotating disk chronoamperometric (CA) step measurements were submerged in individual scintillation vials containing 4.5 mL of 1 M nitric acid aqueous solution. The vials containing the electrodes and nitric acid solutions were placed onto a vortex mixer (Fisher Scientific) at 500 rpm for 3 h. The electrodes were then removed from the vials, and the resulting solutions were diluted with 0.5 mL ultrapure water to a final volume of 5 mL. The diluted samples were then analyzed for Co concentration using a Perkin-Elmer Nexion 2000 ICP-MS instrument. The instrument was calibrated using cobalt calibration standards at concentrations of 1 ppb, 3ppb, and 5 ppb which were prepared from dilution of a 1000 ppm standard (Ricca Chemical Company). The results of ICP-MS measurement are summarized in Table A.1.

A.1.3.5 CoPc Loading Dependence Study

CoPc catalyst deposition solution was prepared by dispersing ~ 3 mg of CoPc in 1 mL of DMF with 30 min of sonication. This solution was then serially diluted in DMF to obtain catalyst deposition solutions containing CoPc concentrations ranging from 3×10^{-4} mg mL^{-1} to 3 mg mL^{-1}. CoPc-1% P4VP catalyst deposition solutions was prepared by dissolving 0.01 g of P4VP in each of 1 mL of CoPc deposition solutions with 20 min of sonication. The modified EPG working electrode was then prepared by drop-casting 5 μL of the prepared deposition solution onto EPG. The electrode was then oven-dried in air at 70 ° for 15 min to allow solvent to evaporate. The resulting loading of CoPc on the electrode surface ranges from 2.19×10^{-11} to 2.19×10^{-7} mol cm^{-2}.

A.1.3.6 Sample Preparation for UV-vis Spectroscopy

Solid-state and liquid samples were analyzed using Varian Cary 100 Bio UV-Visble Spectrophotometer. Solid-state CoPc-PS, CoPc-P4VP, CoPc-P2VP, CoPc(py)-PS and CoPc(py)-P2VP films were prepared by drop-casting total volume of 1 mL of the corresponding deposition solution (see Preparation of Deposition Solutions in the Supplementary Methods) on a 0.9 cm by 3 cm glass slide cut from the plain microscope slide, the DMF solvent was evaporated at 70 °C in an oven. The glass slide was then put into a glass cuvette in the UV-vis spectrometer for measurement. 0.01 mM CoPc/DMF solution and 0.01 mM CoPc(py) solutions are prepared by diluting the corresponding deposition solution by 5 times (see Preparation of Deposition Solutions in the Supplementary Methods).

A.1.3.7 Cyclic Voltammetry

The working electrode was a 0.071 cm^2 glassy carbon disk electrode (CH instruments), and the counter electrode was Pt wire (99.99 %, Surepure Chemetals L.L.C.). The reference electrode was a $Ag/AgNO_3$ (1.0 mM)/DMSO nonaqueous reference electrode, separated from the solution by a Vycor frit (Bioanalytical Systems, Inc.) and externally referenced to ferrocene. The scan rate was 50 mV s^{-1}. Cyclic voltammograms were automatically corrected for IR drop at 85% through positive feedback using the Bio-Logic EC Lab software. DMSO solutions containing 0.1 M nBu_4NPF_6 were thoroughly degassed with N_2 or CO_2 for 20 min prior to measurements and a N_2 or CO_2 atmosphere was kept over the solutions during experiments.

A.1.3.8 Explanation of Equation 2.2:

Equation 2.2 in the main text , which was used to fit our proton inventory data, was derived from the Kresge-Gross-Butler equation (Equation A.1),[6, 7] which represents the isotope effect arises from a combination of pronounced isotope effect at a few sites (i.e., these sites have ∅ values that are quite different than unity), and from a *Z*-effect (i.e. these sites have ∅ values that are very close to unity individually but has an aggregate isotope effect as a whole):[6]

$$k_n = k_0 \left[\frac{\prod_{i=1}^{x}(1-n+n\emptyset_{Ti})}{\prod_{i=1}^{x}(1-n+n\emptyset_{Ri})}\right] Z^n \qquad \text{(A.1)}$$

where k_0 is the kinetic rate constant in protic solution, k_n is the kinetic rate constant in a solution containing a mole fraction of D_2O of *n*, x is the number of hydrogenic sites in the reactant or transition state, $\emptyset_{Ti}$ and $\emptyset_{Ri}$ are the isotopic fractionation factor for hydrogenic site in the transition- and reactant-state, respectively. And *Z* is given by Equation A.2:[8]

$$Z = \exp\left[-\gamma\left(1-\emptyset_{T,Z}\right)+\mu\left(1-\emptyset_{R,Z}\right)\right] \qquad \text{(A.2)}$$

Z^n reflects the *Z*-effect, or the solvent isotope effect that arises from small contributions at a large number of identical hydrogenic sites. These large number of hydrogenic sites can occur either only in the transition-state ($\emptyset_{R,Z} = 1, \emptyset_{T,Z} \neq 1$), the reactant-state ($\emptyset_{T,Z} = 1, \emptyset_{,R,Z} \neq 1$), or from a combination in the reactant- and transition-states).[6] μ and γ are the number of hydrogenic sites in the reactant- and transition-state from *Z*-sites, respectively.[8] Note that when $Z = 1$ then $\emptyset_{R,Z} = \emptyset_{T,Z} = 1$ and there are no *Z*-sites that contribute to the isotope effect. When $Z > 1$, then the Z-sites contribute an inverse isotope effect, and when $Z < 1$ then *Z*-sites contribute a normal isotope effect.[8]

In our case, the pronounced isotope effect occurs at a single hydrogenic site involved in step (iii) in Figure 2.3a, thus, Equation A.1 reduces to:

$$k_n = k_0 \left(\frac{1-n+n\emptyset_T}{1-n+n\emptyset_R}\right) Z^n \qquad \text{(A.3)}$$

If we assume that the reactant-state fractionation factor $\emptyset_R$ for the hydrogen attached to the oxygen of CO_2 molecule is unity,[9] then Equation A.3 becomes:

$$k_n = k_0 \, (1 - n + n\emptyset) Z^n \qquad \text{(A.4)}$$

Where $\emptyset$ is the isotopic fractionation factor for hydrogenic site involved in step (iii) in Figure 2.3a in the transition-state. Combining Equation A.4 and Equation KIE $= \frac{k_{\mathrm{H}}}{k_{\mathrm{D}}} = \frac{j_{\mathrm{H}}}{j_{\mathrm{D}}}$ produce equation:

$$j_n = j_0 \, (1 - n + n\emptyset) Z^n \qquad \text{(A.5)}$$

A.2 Supplementary Information for Chapter 3

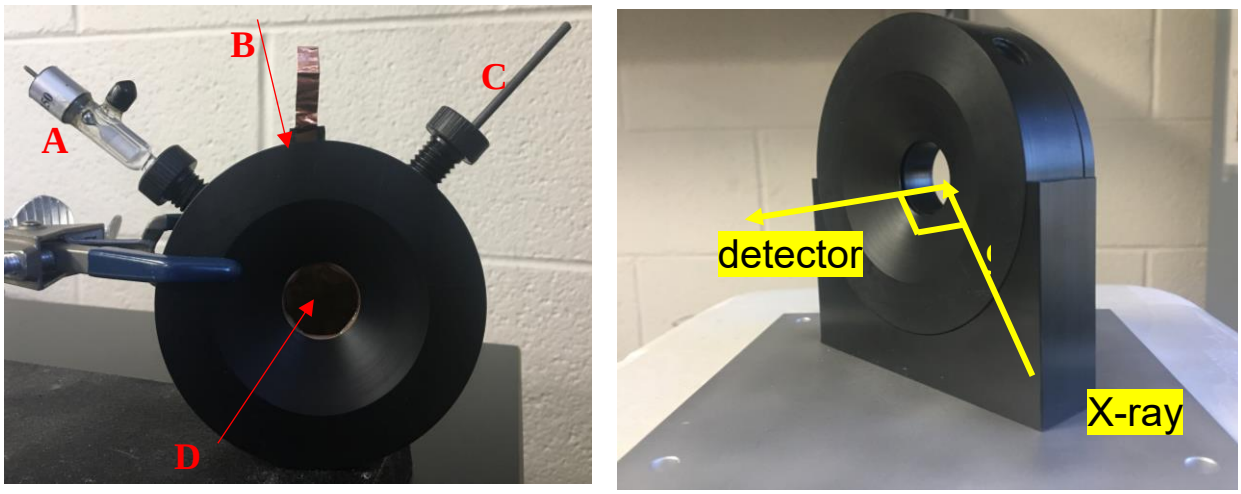

Figure A.44 Photograph of custom spectro-electrochemical reaction XAS cell: (A) SCE reference electrode, (B) catalyst modified carbon paper working electrode, (C) Carbon rod auxiliary electrode, (D) Kapton film.

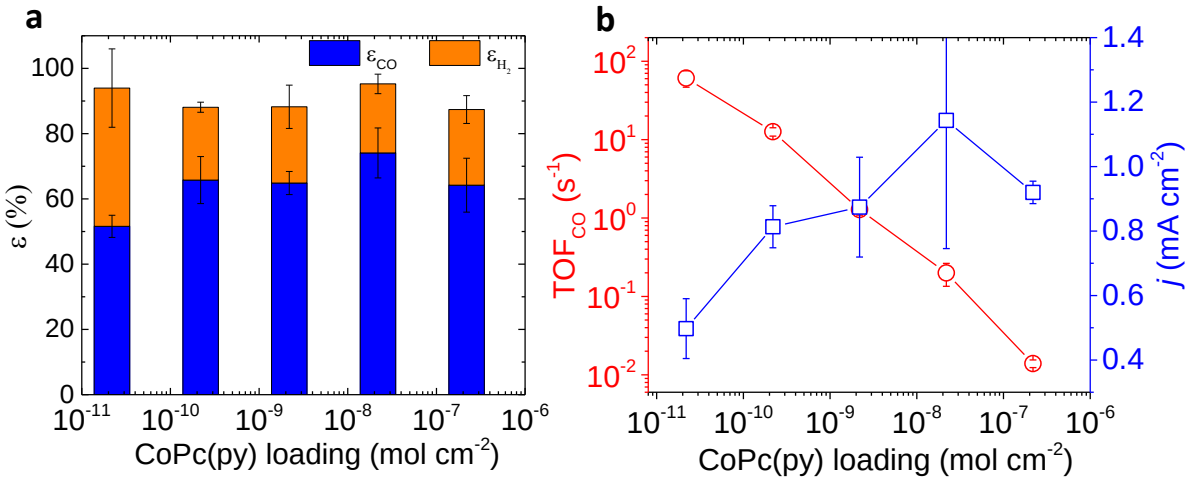

Figure A.45 CO_2RR results of 2-h CPE at different CoPc(py) loadings **(a)** Faradaic efficiencies for CO and H_2, **(b)** TOF_{CO} and overall current densitiies (*j*) obtained from 2-h CPE at -1.25 V vs. SCE at different CoPc(py) loadings in CO_2 saturated pH 5 phosphate electrolyte under CO_2 atmosphere. Errors are given as standard deviations. CoPc(py) was independently synthesized following the previously-reported procedures,[5] the decrease in TOF for CO_2RR with increasing CoPc(py) loading suggests the aggregation of CoPc(py), which shows relatively the same aggregation as CoPc and CoPc-P4VP.[10] We propose that even though all CoPc immobilized are likely redox active, but only those CoPc sites on the surface of the aggregates are electrocatalytically active.

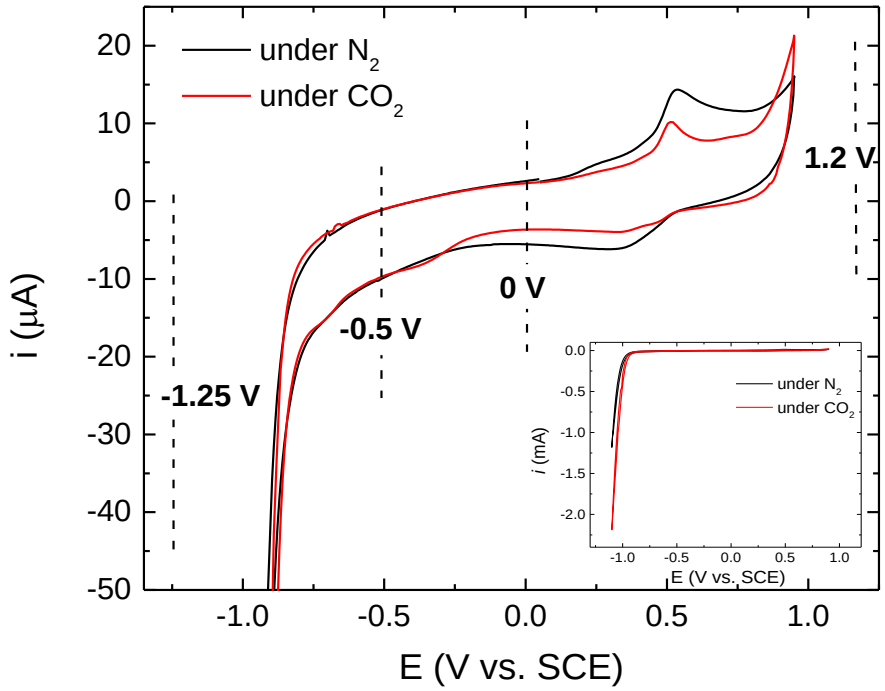

Figure A.46 Cyclic voltammogram (CV) of CoPc-P4VP modified edge plane graphite (EPG) electrode in pH 5 phosphate electrolyte solution under N_2 and CO_2 atmosphere. The main figure shows the main electrochemical features preceding catalysis, and the inset shows the catalytic features as well.

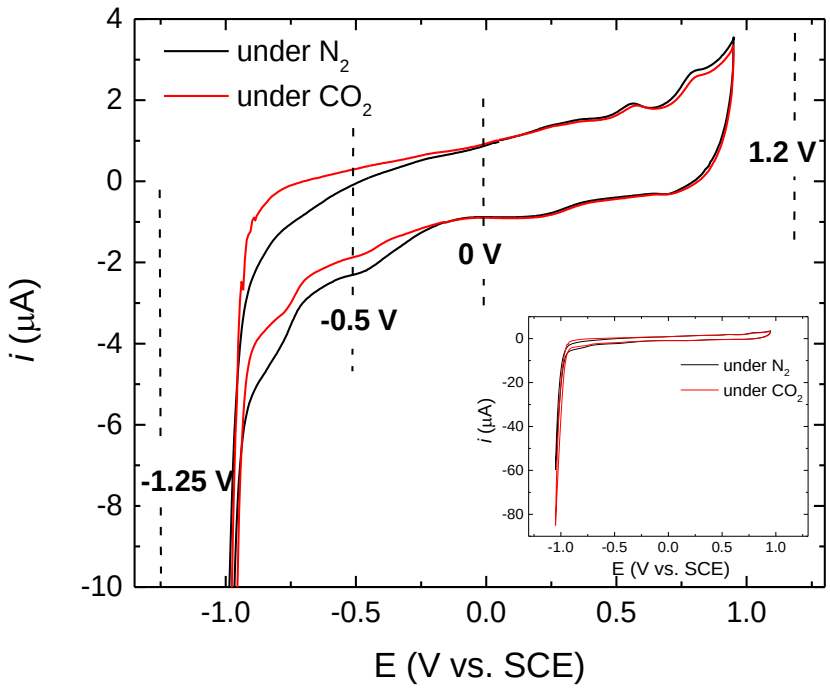

Figure A.47 Cyclic voltammogram (CV) of CoPc(py) modified edge plane graphite (EPG) electrode in pH 5 phosphate electrolyte solution under N_2 and CO_2 atmosphere. The main figure shows the main electrochemical features preceding catalysis, and the inset shows the catalytic features as well.

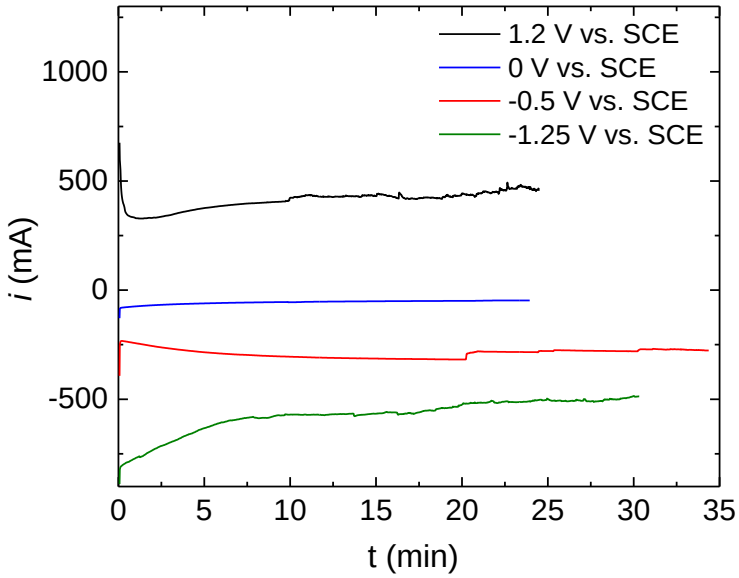

Figure A.48 Chronoamperometric (CA) measurements of CoPc modified carbon paper electrode in pH 5 phosphate electrolyte solution conducted at different potentials under N_2 atmosphere. The dissimilarity of CA curve shape at -1.25 V in 0-7 min time range compared to the one under CO_2 (Figure A.49) might be attributed to the higher electrochemical activity for HER compared to CO_2RR.

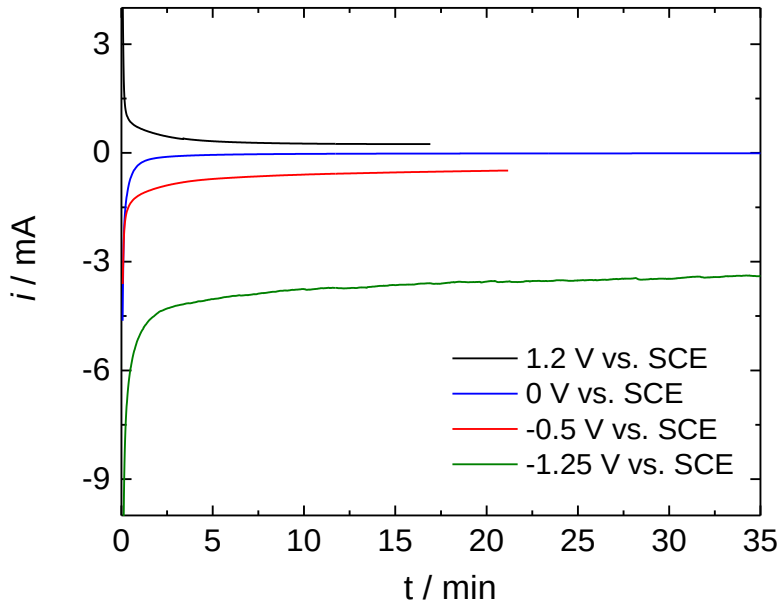

Figure A.49 Chronoamperometric (CA) measurements of CoPc modified carbon paper electrode in pH 5 phosphate electrolyte solution conducted at different potentials under CO_2 atmosphere.

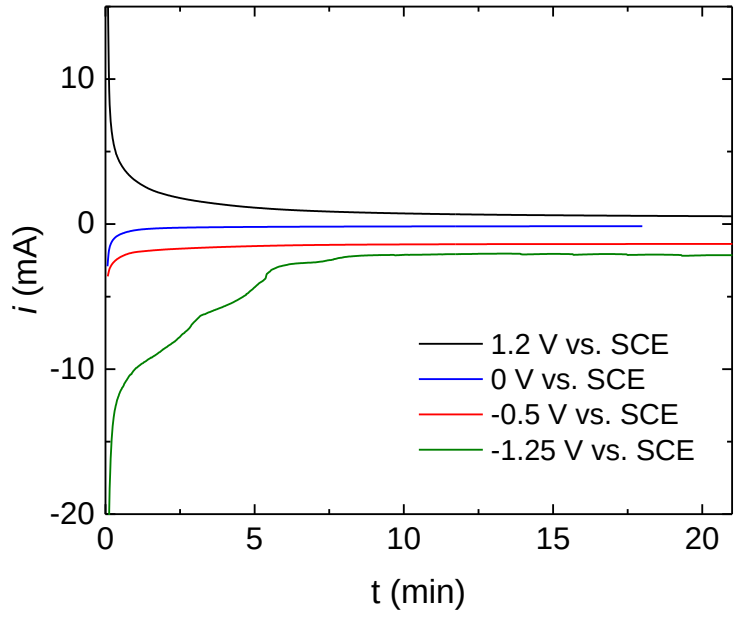

Figure A.50 Chronoamperometric (CA) measurements of CoPc(py) modified carbon paper electrode in pH 5 phosphate electrolyte solution conducted at different potentials under N_2 atmosphere. The dissimilarity of CA curve shape at -1.25 V in 0-7 min time range compared to the one under CO_2 (Figure A.51) might be attributed to the higher electrochemical activity for HER compared to CO_2RR.

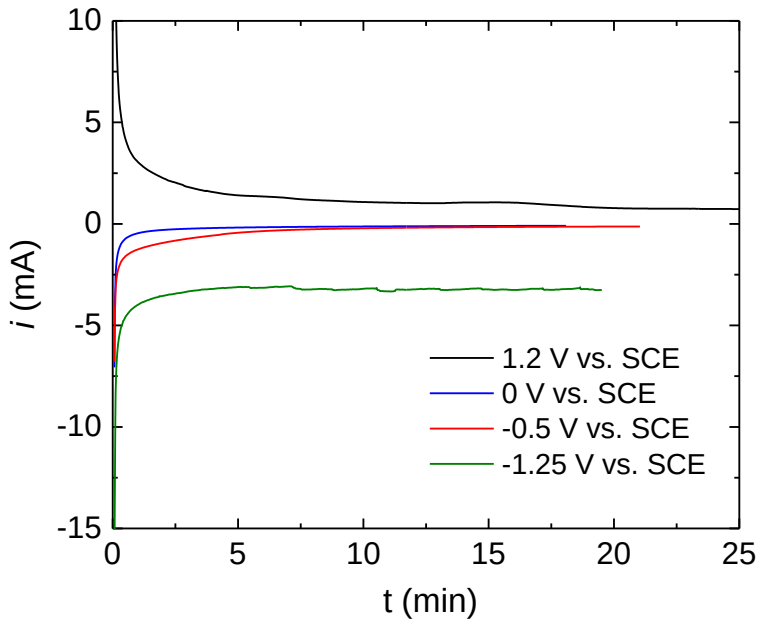

Figure A.51 Chronoamperometric (CA) measurements of CoPc(py) modified carbon paper electrode in pH 5 phosphate electrolyte solution conducted at different potentials under CO_2 atmosphere.

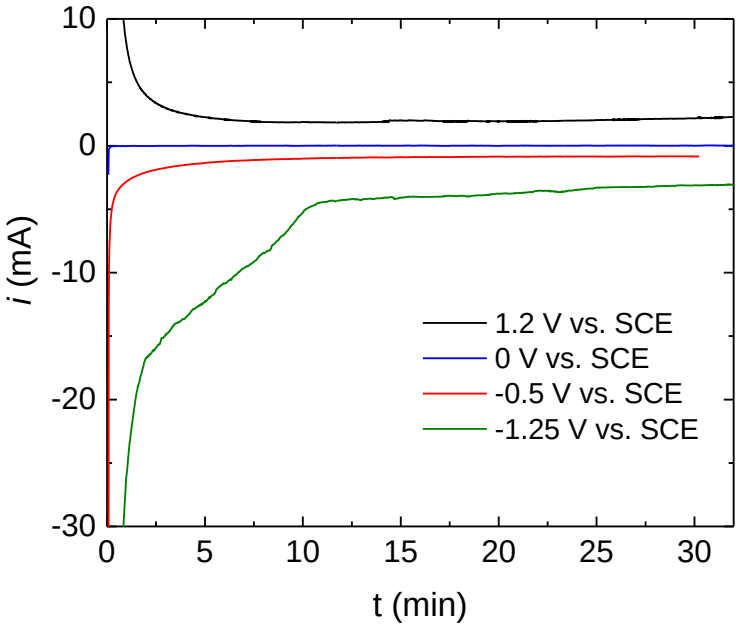

Figure A.52 Chronoamperometric (CA) measurements of CoPc-P4VP modified carbon paper electrode in pH 5 sodium phosphate solution conducted at different potentials under N_2 atmosphere. The dissimilarity of CA curve shape at -1.25 V in 0-10 min time range compared to the one under CO_2 (Figure A.53) might be attributed to the higher electrochemical activity for HER compared to CO_2RR.

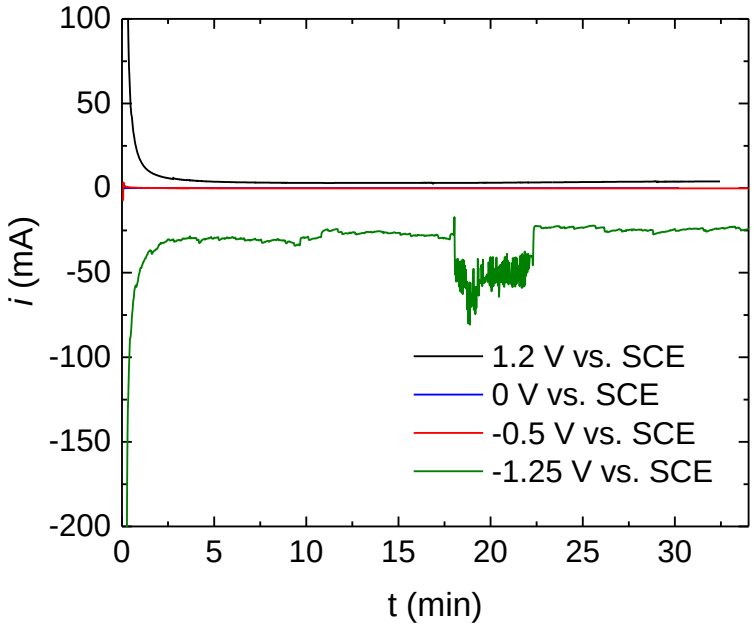

Figure A.53 Chronoamperometric measurements of CoPc-P4VP modified carbon paper electrode in pH 5 sodium phosphate solution conducted at different potentials under CO_2 atmosphere. Note that the noise at -1.25 V is due to gas product generation.

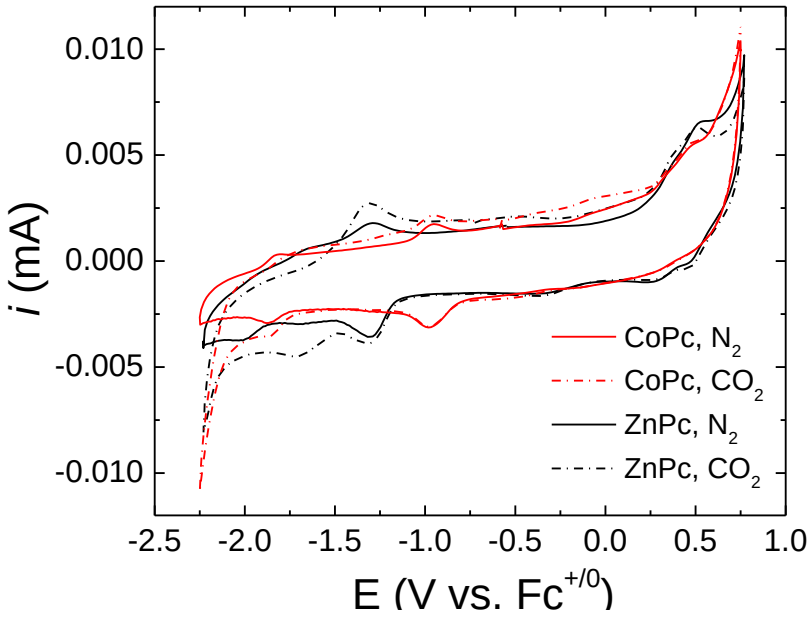

Figure A.54 Cyclic voltammogram (CV) of 0.1 mM CoPc and 0.1 mM ZnPc in DMSO with 0.1 M nBu_4NPF_6 under N_2 and CO_2. Conditions: scan rate: 100 mV/s; working electrode: glassy carbon working electrode; reference electrode: $Ag/AgNO_3$ (1 mM); auxiliary electrode: Pt wire. Note that all CVs have been *i*R compensated. Here we can observe similar CV redox peaks features for CoPc and ZnPc which suggests that Co center may be redox inactive as Zn. And the peak potentials shifted for CoPc compared to the redox innocent ZnPc. This may suggest that the Co center in CoPc play a role in influencing the energy of molecular orbitals of the metal phthalocyanine complex, thus shifting the potentials of redox couples in the CV, while the metal center does not necessarily needs to be redox active.

A.3 Supplementary Information for Chapter 4

A.3.1 Supplementary Figure

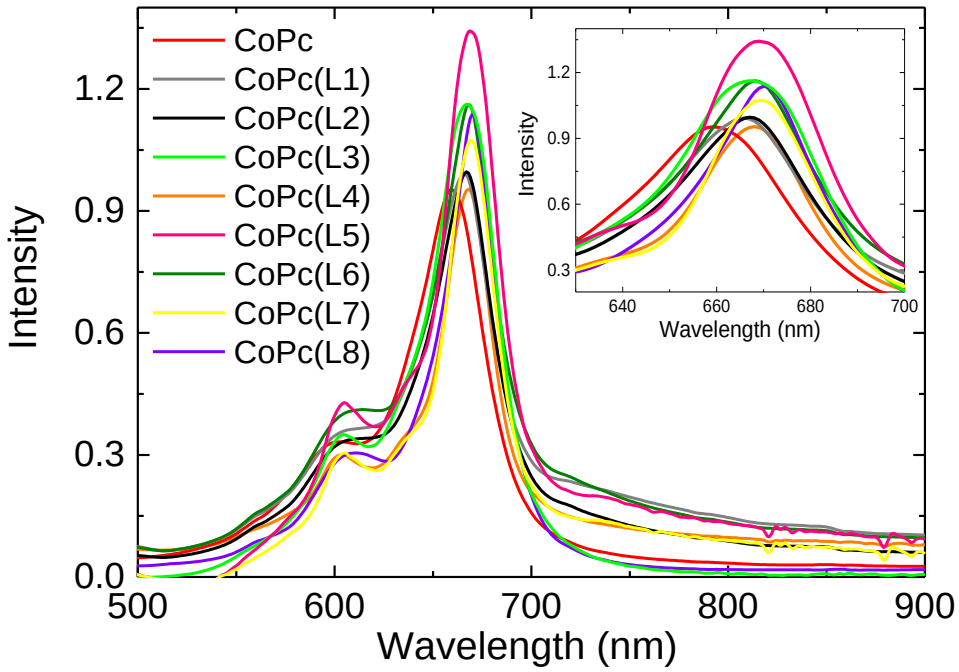

Figure A.55 UV-vis spectrum of 0.01 mM CoPc solution and 0.01 mM CoPc(L) solutions in DMF. Red shifted Q band is exhibited in the UV-vis spectrum of CoPc(L) solutions compared to that of CoPc, suggesting the formation of the axial coordination of CoPc in CoPc(L) solutions.

A.3.2 Supplementary Table

Table A.9 Results obtained from 2-h controlled potential electrolyses (CPE) experiments at -1.25 V vs SCE for modified electrodes in pH 5 phosphate solution for CO_2 reduction.

Catalyst	Charge/C	FE_{CO}/%	TON_{CO} (2h)	TOF_{CO} (s^{-1})	FE_{H2}/%	FE_{total}/%
CoPc	0.43 ± 0.07	57.5 ± 3.8	$5.13 \pm 1.10 \times 10^3$	0.71 ± 0.15	33.9 ± 2.3	91.4 ± 1.8
CoPc(L1)	0.65 ± 0.07	68.6 ± 7.6	$9.18 \pm 0.39 \times 10^3$	1.28 ± 0.05	25.6 ± 5.7	94.2 ± 5.7
CoPc(L2)	0.72 ± 0.05	64.8 ± 1.5	$9.65 \pm 0.78 \times 10^3$	1.34 ± 0.11	22.4 ± 4.4	87.3 ± 3.5
CoPc(L3)	0.74 ± 0.10	68.7 ± 3.5	$1.06 \pm 0.13 \times 10^4$	1.47 ± 0.17	23.7 ± 1.8	92.4 ± 4.7
CoPc(L4)	0.78 ± 0.16	65.0 ± 10.3	$1.04 \pm 0.18 \times 10^4$	1.45 ± 0.24	26.1 ± 8.4	91.2 ± 10.1
CoPc(L5)	0.92 ± 0.19	71.4 ± 9.6	$1.38 \pm 0.44 \times 10^4$	1.92 ± 0.61	22.0 ± 12.4	93.3 ± 11.2
CoPc(L6)	0.94 ± 0.32	72.3 ± 7.5	$1.42 \pm 0.61 \times 10^4$	1.98 ± 0.84	22.3 ± 4.1	94.7 ± 3.7
CoPc(L7)	1.09 ± 0.21	72.1 ± 1.3	$1.62 \pm 0.32 \times 10^4$	2.25 ± 0.45	22.6 ± 3.6	93.6 ± 4.0
CoPc(L8)	1.31 ± 0.31	70.9 ± 2.5	$1.93 \pm 0.50 \times 10^4$	2.69 ± 0.69	23.3 ± 2.8	94.2 ± 1.3
CoPc(L8)-P2VP/CB[a]	4.87 ± 0.72	86.8 ± 3.5	$8.74 \pm 1.09 \times 10^4$	12.14 ± 1.51	14.6 ± 3.5	101.4 ± 1.2

All reported values are averages from 3 independent measurements, and all errors are given as standard deviations. [a] Polymer-catalyst composite films were drop-cast from deposition solutions containing 3 % w/v P2VP and 1 % w/v CB.

A.3.3 Optimized Structures Information

Cartesian coordinates (Å) of optimized structures using DFT/BP86 method

CoPc (Charge = 0, Multiplicity =2)

N	-2.95661	-1.60399	0.00043
C	-1.84818	-2.31970	0.00038
C	-2.95234	-0.28465	0.00004
N	-1.85907	0.55133	-0.00085
C	-2.31966	1.84811	-0.00118
N	-1.60396	2.95657	-0.00157
C	-0.28461	2.95227	-0.00108
N	0.55137	1.85903	-0.00069
C	1.84822	2.31969	0.00006
N	2.95662	1.60400	0.00045
C	2.95230	0.28460	0.00059
N	1.85907	-0.55130	0.00085
C	2.31968	-1.84819	0.00074
N	1.60397	-2.95655	0.00074
C	0.28458	-2.95227	0.00054
N	-0.55139	-1.85906	0.00068
C	-4.17358	0.50674	0.00023
C	-3.77490	1.85073	-0.00065
C	0.50677	4.17355	-0.00057
C	1.85076	3.77490	0.00012
C	3.77491	-1.85075	0.00047
C	4.17355	-0.50675	0.00032
C	-0.50675	-4.17356	0.00011
C	-1.85076	-3.77490	0.00009
C	-0.15265	-5.52227	-0.00028
C	-1.18197	-6.45857	-0.00068
C	-2.53078	-6.05847	-0.00073
C	-2.88305	-4.71232	-0.00035

C	-5.52229	0.15267	0.00120
C	-6.45859	1.18198	0.00120
C	-6.05845	2.53079	0.00030
C	-4.71230	2.88302	-0.00061
C	0.15266	5.52225	-0.00057
C	1.18193	6.45858	0.00012
C	2.53077	6.05848	0.00082
C	2.88302	4.71234	0.00083
C	4.71231	-2.88305	0.00002
C	6.05846	-2.53084	-0.00054
C	6.45856	-1.18203	-0.00066
C	5.52228	-0.15269	-0.00027
Co	0.00003	0.00006	-0.00000
H	0.88799	-5.82243	-0.00020
H	-0.94441	-7.51641	-0.00097
H	-3.30673	-6.81566	-0.00110
H	-3.91907	-4.39655	-0.00042
H	-5.82247	-0.88797	0.00187
H	-7.51644	0.94447	0.00193
H	-6.81564	3.30675	0.00035
H	-4.39649	3.91903	-0.00130
H	-0.88800	5.82237	-0.00116
H	0.94441	7.51642	0.00010
H	3.30671	6.81569	0.00139
H	3.91905	4.39659	0.00142
H	4.39644	-3.91905	0.00008
H	6.81567	-3.30677	-0.00091
H	7.51639	-0.94446	-0.00109
H	5.82252	0.88793	-0.00031

CoPc(L1) (Charge = 0, Multiplicity =2)

N	-3.36584	0.00370	0.47910
C	-2.73196	1.16351	0.47254
C	-2.73451	-1.15745	0.47267
N	-1.37804	-1.37308	0.43428
C	-1.16290	-2.73007	0.45284
N	-0.00371	-3.36294	0.44827
C	1.15690	-2.73265	0.45280
N	1.37500	-1.37612	0.43432
C	2.73196	-1.16351	0.47254
N	3.36584	-0.00371	0.47910
C	2.73451	1.15744	0.47268
N	1.37804	1.37307	0.43429
C	1.16290	2.73006	0.45285
N	0.00371	3.36293	0.44828
C	-1.15690	2.73264	0.45281
N	-1.37500	1.37611	0.43433
C	-3.43293	-2.43555	0.50601
C	-2.44138	-3.42752	0.49225
C	2.43377	-3.43289	0.49199
C	3.42751	-2.44309	0.50566
C	2.44138	3.42751	0.49226
C	3.43293	2.43555	0.50602
C	-2.43377	3.43288	0.49200
C	-3.42752	2.44308	0.50567
C	-2.76299	4.78724	0.51994
C	-4.11343	5.12242	0.55719
C	-5.10980	4.12992	0.57072
C	-4.78023	2.77779	0.54692
C	-4.78638	-2.76726	0.54742
C	-5.11892	-4.11867	0.57127

C	-4.12474	-5.11335	0.55759
C	-2.77356	-4.78113	0.52018
C	2.76299	-4.78725	0.51992
C	4.11343	-5.12243	0.55717
C	5.10980	-4.12993	0.57070
C	4.78023	-2.77780	0.54691
C	2.77356	4.78113	0.52019
C	4.12474	5.11334	0.55761
C	5.11892	4.11866	0.57128
C	4.78638	2.76726	0.54743
Co	0.00000	-0.00000	0.32958
H	-1.99012	5.54601	0.51217
H	-4.40637	6.16609	0.57756
H	-6.15199	4.42717	0.60129
H	-5.54214	2.00806	0.56008
H	-5.54657	-1.99584	0.56066
H	-6.16176	-4.41362	0.60198
H	-4.41998	-6.15637	0.57797
H	-2.00236	-5.54161	0.51227
H	1.99012	-5.54602	0.51214
H	4.40637	-6.16610	0.57754
H	6.15199	-4.42717	0.60127
H	5.54214	-2.00807	0.56007
H	2.00236	5.54160	0.51229
H	4.41997	6.15636	0.57799
H	6.16176	4.41361	0.60199
H	5.54658	1.99583	0.56066
N	-0.00000	0.00000	-2.01258
C	1.12774	-0.00032	-2.73249
N	1.18690	-0.00032	-4.06199
C	-0.00000	0.00014	-4.67114

N	-1.18690	0.00037	-4.06199
C	-1.12774	0.00032	-2.73249
H	2.06611	-0.00061	-2.18854
H	-0.00000	-0.00007	-5.75710
H	-2.06611	0.00059	-2.18854

CoPc(L2) (Charge = 0, Multiplicity =2)

N	3.36576	0.00621	-0.48581
C	2.73066	1.16552	-0.47737
C	2.73494	-1.15541	-0.47758
N	1.37924	-1.37206	-0.43598
C	1.16487	-2.72883	-0.45197
N	0.00620	-3.36268	-0.44564
C	-1.15482	-2.73313	-0.45187
N	-1.37415	-1.37715	-0.43600
C	-2.73066	-1.16553	-0.47737
N	-3.36576	-0.00621	-0.48581
C	-2.73494	1.15541	-0.47758
N	-1.37924	1.37205	-0.43598
C	-1.16487	2.72882	-0.45198
N	-0.00620	3.36267	-0.44565
C	1.15482	2.73313	-0.45187
N	1.37415	1.37715	-0.43600
C	3.43463	-2.43308	-0.51061
C	2.44383	-3.42577	-0.49252
C	-2.43116	-3.43477	-0.49203
C	-3.42560	-2.44572	-0.51002
C	-2.44383	3.42576	-0.49253
C	-3.43463	2.43308	-0.51061
C	2.43116	3.43476	-0.49204

C	3.42560	2.44572	-0.51002
C	2.75939	4.78935	-0.51828
C	4.10951	5.12584	-0.55828
C	5.10657	4.13417	-0.57659
C	4.77790	2.78169	-0.55459
C	4.78815	-2.76408	-0.55549
C	5.12178	-4.11534	-0.57765
C	4.12835	-5.11067	-0.55918
C	2.77701	-4.77913	-0.51889
C	-2.75939	-4.78936	-0.51827
C	-4.10951	-5.12585	-0.55827
C	-5.10658	-4.13417	-0.57659
C	-4.77790	-2.78169	-0.55459
C	-2.77701	4.77912	-0.51889
C	-4.12835	5.11067	-0.55918
C	-5.12178	4.11534	-0.57765
C	-4.78815	2.76408	-0.55549
Co	-0.00000	-0.00000	-0.32370
H	1.98588	5.54747	-0.50729
H	4.40151	6.16982	-0.57755
H	6.14848	4.43224	-0.61007
H	5.54036	2.01253	-0.57247
H	5.54777	-1.99211	-0.57345
H	6.16476	-4.40959	-0.61136
H	4.42419	-6.15356	-0.57854
H	2.00630	-5.54007	-0.50777
H	-1.98589	-5.54747	-0.50728
H	-4.40151	-6.16982	-0.57754
H	-6.14848	-4.43224	-0.61006
H	-5.54036	-2.01253	-0.57247
H	-2.00630	5.54007	-0.50778

H	-4.42419	6.15356	-0.57855
H	-6.16476	4.40959	-0.61137
H	-5.54777	1.99211	-0.57345
N	-0.00000	0.00000	1.99195
C	-1.13790	-0.00012	2.69478
C	-1.13219	-0.00020	4.08810
N	-0.00000	0.00002	4.79386
C	1.13219	0.00022	4.08810
C	1.13790	0.00013	2.69478
H	-2.06793	-0.00019	2.13895
H	-2.06466	-0.00019	4.64340
H	2.06466	0.00022	4.64340
H	2.06793	0.00019	2.13895

CoPc(L3) (Charge = 0, Multiplicity =2)

N	3.36552	-0.00074	-0.49405
C	2.73258	1.15979	-0.48207
C	2.73203	-1.16098	-0.48219
N	1.37646	-1.37481	-0.43583
C	1.15912	-2.73067	-0.44847
N	-0.00081	-3.36235	-0.43993
C	-1.16046	-2.73012	-0.44842
N	-1.37713	-1.37416	-0.43574
C	-2.73259	-1.15966	-0.48211
N	-3.36553	0.00088	-0.49401
C	-2.73204	1.16111	-0.48209
N	-1.37647	1.37494	-0.43576
C	-1.15913	2.73080	-0.44834
N	0.00081	3.36249	-0.43977
C	1.16045	2.73025	-0.44830

N	1.37713	1.37429	-0.43573
C	3.42930	-2.44017	-0.51512
C	2.43654	-3.43074	-0.49128
C	-2.43821	-3.42958	-0.49119
C	-3.43049	-2.43852	-0.51504
C	-2.43655	3.43088	-0.49107
C	-3.42930	2.44031	-0.51494
C	2.43820	3.42971	-0.49100
C	3.43048	2.43866	-0.51490
C	2.76933	4.78358	-0.51553
C	4.12003	5.11756	-0.55975
C	5.11492	4.12386	-0.58401
C	4.78324	2.77200	-0.56384
C	4.78189	-2.77421	-0.56414
C	5.11289	-4.12623	-0.58446
C	4.11750	-5.11944	-0.56026
C	2.76697	-4.78478	-0.51596
C	-2.76933	-4.78345	-0.51582
C	-4.12004	-5.11743	-0.56010
C	-5.11493	-4.12372	-0.58431
C	-4.78324	-2.77186	-0.56403
C	-2.76698	4.78492	-0.51568
C	-4.11751	5.11958	-0.55995
C	-5.11289	4.12637	-0.58418
C	-4.78190	2.77435	-0.56392
Co	-0.00000	0.00007	-0.31599
H	1.99735	5.54322	-0.50016
H	4.41407	6.16104	-0.57793
H	6.15739	4.41974	-0.62092
H	5.54388	2.00113	-0.58637
H	5.54292	-2.00371	-0.58663

H	6.15520	-4.42262	-0.62144
H	4.41103	-6.16306	-0.57857
H	1.99460	-5.54402	-0.50064
H	-1.99736	-5.54309	-0.50050
H	-4.41407	-6.16090	-0.57837
H	-6.15739	-4.41959	-0.62126
H	-5.54388	-2.00099	-0.58652
H	-1.99460	5.54415	-0.50034
H	-4.41104	6.16320	-0.57820
H	-6.15521	4.42276	-0.62113
H	-5.54293	2.00385	-0.58643
N	0.00001	-0.00002	1.98751
C	-1.14753	-0.00008	2.67971
C	-1.19620	-0.00052	4.07009
C	0.00003	-0.00092	4.78101
C	1.19625	-0.00084	4.07008
C	1.14756	-0.00038	2.67970
H	-2.06116	0.00023	2.09706
H	-2.15376	-0.00055	4.57618
H	0.00003	-0.00127	5.86504
H	2.15382	-0.00113	4.57616
H	2.06118	-0.00029	2.09704

CoPc(L4) (Charge = 0, Multiplicity =2)

N	3.34595	-0.00166	-0.51346
C	2.71233	1.15650	-0.49534
C	2.71119	-1.15919	-0.49528
N	1.35754	-1.37457	-0.45642
C	1.14087	-2.73011	-0.46163
N	-0.01766	-3.36287	-0.44605

C	-1.17857	-2.73027	-0.44276
N	-1.39487	-1.37481	-0.42313
C	-2.75224	-1.15956	-0.44615
N	-3.38429	0.00165	-0.44438
C	-2.75109	1.16223	-0.44614
N	-1.39351	1.37616	-0.42317
C	-1.17589	2.73140	-0.44276
N	-0.01435	3.36285	-0.44612
C	1.14355	2.72894	-0.46174
N	1.35890	1.37319	-0.45649
C	3.41027	-2.43874	-0.52304
C	2.41943	-3.43034	-0.49980
C	-2.45616	-3.42908	-0.46885
C	-3.44948	-2.43789	-0.47206
C	-2.45280	3.43148	-0.46877
C	-3.44709	2.44125	-0.47201
C	2.42280	3.42791	-0.49996
C	3.41266	2.43535	-0.52313
C	2.75598	4.78090	-0.51974
C	4.10786	5.11267	-0.55883
C	5.10056	4.11730	-0.58166
C	4.76571	2.76570	-0.56560
C	4.76301	-2.77040	-0.56553
C	5.09656	-4.12231	-0.58150
C	4.10290	-5.11673	-0.55862
C	2.75134	-4.78365	-0.51953
C	-2.78780	-4.78335	-0.49426
C	-4.13850	-5.11784	-0.51835
C	-5.13438	-4.12414	-0.52198
C	-4.80307	-2.77259	-0.50074
C	-2.78315	4.78608	-0.49415

C	-4.13351	5.12187	-0.51823
C	-5.13036	4.12912	-0.52190
C	-4.80036	2.77726	-0.50074
Co	-0.01435	-0.00001	-0.32760
H	1.98539	5.54202	-0.50500
H	4.40385	6.15570	-0.57395
H	6.14382	4.41106	-0.61387
H	5.52439	1.99286	-0.58575
H	5.52241	-1.99827	-0.58572
H	6.13953	-4.41709	-0.61368
H	4.39787	-6.16004	-0.57369
H	1.98002	-5.54404	-0.50475
H	-2.01520	-5.54255	-0.49566
H	-4.43245	-6.16135	-0.53748
H	-6.17719	-4.42042	-0.54423
H	-5.56448	-2.00210	-0.50843
H	-2.00981	5.54453	-0.49552
H	-4.42646	6.16566	-0.53731
H	-6.17288	4.42643	-0.54414
H	-5.56249	2.00749	-0.50844
N	0.04468	0.00005	1.94069
C	-1.05447	-0.00016	2.69680
C	-1.00915	-0.00016	4.09097
C	0.23923	0.00006	4.68169
C	1.34559	0.00027	3.82872
N	1.24864	0.00027	2.50165
H	-1.99330	-0.00032	2.15693
H	-1.92414	-0.00033	4.67043
H	0.36862	0.00006	5.75723
H	2.36007	0.00045	4.21200

CoPc(L5) (Charge = 0, Multiplicity =2)

N	3.36164	0.00128	-0.39182
C	2.72776	1.16169	-0.39239
C	2.72865	-1.15969	-0.39234
N	1.37311	-1.37465	-0.36447
C	1.15632	-2.72976	-0.38142
N	-0.00370	-3.36246	-0.37599
C	-1.16334	-2.73064	-0.37547
N	-1.38077	-1.37524	-0.35622
C	-2.73578	-1.16110	-0.38113
N	-3.36994	-0.00124	-0.38113
C	-2.73665	1.15917	-0.38103
N	-1.38175	1.37424	-0.35628
C	-1.16538	2.72985	-0.37548
N	-0.00614	3.36250	-0.37593
C	1.15427	2.73063	-0.38131
N	1.37212	1.37572	-0.36435
C	3.42708	-2.43836	-0.42232
C	2.43418	-3.42949	-0.41487
C	-2.44147	-3.43111	-0.40583
C	-3.43419	-2.44044	-0.41018
C	-2.44392	3.42931	-0.40591
C	-3.43595	2.43786	-0.41018
C	2.43172	3.43136	-0.41468
C	3.42531	2.44100	-0.42225
C	2.76208	4.78546	-0.44213
C	4.11279	5.12088	-0.47317
C	5.10894	4.12806	-0.48119
C	4.77825	2.77599	-0.45773

C	4.78026	-2.77240	-0.45797
C	5.11194	-4.12420	-0.48167
C	4.11651	-5.11777	-0.47383
C	2.76558	-4.78335	-0.44270
C	-2.77241	-4.78477	-0.43332
C	-4.12364	-5.11923	-0.46088
C	-5.11896	-4.12592	-0.46525
C	-4.78722	-2.77394	-0.44170
C	-2.77591	4.78273	-0.43376
C	-4.12736	5.11618	-0.46142
C	-5.12196	4.12212	-0.46564
C	-4.78922	2.77041	-0.44189
Co	-0.00425	0.00001	-0.24014
H	1.98909	5.54425	-0.43968
H	4.40590	6.16459	-0.49418
H	6.15149	4.42479	-0.50877
H	5.53999	2.00588	-0.46886
H	5.54147	-2.00175	-0.46900
H	6.15471	-4.42016	-0.50932
H	4.41039	-6.16126	-0.49509
H	1.99312	-5.54269	-0.44041
H	-2.00003	-5.54417	-0.43303
H	-4.41750	-6.16275	-0.48132
H	-6.16180	-4.42189	-0.48916
H	-5.54824	-2.00313	-0.44868
H	-2.00407	5.54269	-0.43358
H	-4.42199	6.15947	-0.48207
H	-6.16502	4.41731	-0.48963
H	-5.54970	1.99907	-0.44879
N	0.00876	-0.00005	2.02313
N	0.72307	-0.00075	4.10614

C	1.07639	-0.00101	2.79399
H	2.10100	-0.00181	2.45825
C	-0.65537	0.00045	4.17074
C	-1.07891	0.00076	2.87057
H	1.35758	-0.00129	4.88919
H	-1.18954	0.00088	5.10529
H	-2.08900	0.00156	2.49549

CoPc(L6) (Charge = 0, Multiplicity =2)

N	-3.36537	-0.00409	-0.64744
C	-2.73067	-1.16367	-0.63522
C	-2.73349	1.15704	-0.63539
N	-1.37837	1.37287	-0.58857
C	-1.16295	2.72890	-0.60140
N	-0.00390	3.36233	-0.59275
C	1.15665	2.73170	-0.60098
N	1.37538	1.37622	-0.58775
C	2.73101	1.16365	-0.63427
N	3.36571	0.00408	-0.64627
C	2.73383	-1.15705	-0.63441
N	1.37871	-1.37289	-0.58778
C	1.16327	-2.72891	-0.60106
N	0.00421	-3.36235	-0.59270
C	-1.15634	-2.73172	-0.60124
N	-1.37505	-1.37623	-0.58849
C	-3.43272	2.43523	-0.66849
C	-2.44136	3.42727	-0.64458
C	2.43339	3.43316	-0.64415
C	3.42713	2.44355	-0.66761
C	2.44167	-3.42728	-0.64438

C	3.43304	-2.43524	-0.66788
C	-2.43308	-3.43318	-0.64427
C	-3.42681	-2.44358	-0.66816
C	-2.76226	-4.78752	-0.66883
C	-4.11248	-5.12353	-0.71307
C	-5.10882	-4.13129	-0.73730
C	-4.77905	-2.77894	-0.71710
C	-4.78577	2.76736	-0.71758
C	-5.11880	4.11889	-0.73788
C	-4.12486	5.11355	-0.71364
C	-2.77384	4.78079	-0.66928
C	2.76254	4.78749	-0.66938
C	4.11275	5.12351	-0.71388
C	5.10910	4.13127	-0.73770
C	4.77936	2.77893	-0.71682
C	2.77412	-4.78080	-0.66971
C	4.12512	-5.11356	-0.71435
C	5.11909	-4.11891	-0.73821
C	4.78608	-2.76738	-0.71725
Co	0.00015	-0.00000	-0.46657
H	-1.98913	-5.54599	-0.65355
H	-4.40499	-6.16745	-0.73134
H	-6.15087	-4.42867	-0.77422
H	-5.54079	-2.00914	-0.73965
H	-5.54564	1.99570	-0.74012
H	-6.16156	4.41376	-0.77490
H	-4.41989	6.15675	-0.73199
H	-2.00255	5.54113	-0.65397
H	1.98939	5.54595	-0.65449
H	4.40524	6.16743	-0.73274
H	6.15114	4.42865	-0.77492

H	5.54111	2.00913	-0.73912
H	2.00280	-5.54112	-0.65477
H	4.42013	-6.15676	-0.73327
H	6.16183	-4.41378	-0.77553
H	5.54596	-1.99573	-0.73958
N	-0.00155	0.00002	1.82831
C	1.14260	0.00003	2.52876
C	1.18666	0.00001	3.91597
C	-0.00476	-0.00002	4.64875
C	-1.19179	-0.00006	3.91477
C	-1.14477	-0.00003	2.52473
H	2.06004	0.00004	1.95191
H	2.14763	-0.00002	4.41850
C	0.00192	0.00026	6.15448
H	-2.15336	-0.00015	4.41531
H	-2.06182	-0.00009	1.94708
H	-1.01144	-0.00294	6.55869
H	0.52009	0.88283	6.54089
H	0.52595	-0.87862	6.54135

CoPc(L7) (Charge = 0, Multiplicity =2)

N	3.29714	-0.00882	-0.63182
C	2.66708	1.15357	-0.61105
C	2.66098	-1.16794	-0.61080
N	1.30666	-1.37894	-0.53729
C	1.08531	-2.73315	-0.54550
N	-0.07581	-3.36249	-0.50062
C	-1.23284	-2.72711	-0.46176
N	-1.44545	-1.37115	-0.43529
C	-2.79968	-1.15286	-0.41599

N	-3.43013	0.00885	-0.39557
C	-2.79356	1.16730	-0.41610
N	-1.43817	1.37843	-0.43562
C	-1.21853	2.73331	-0.46219
N	-0.05811	3.36254	-0.50114
C	1.09962	2.72706	-0.54591
N	1.31394	1.37174	-0.53736
C	3.35433	-2.44874	-0.66276
C	2.35924	-3.43688	-0.62101
C	-2.51349	-3.42380	-0.45049
C	-3.50278	-2.43010	-0.42265
C	-2.49543	3.43666	-0.45096
C	-3.48990	2.44809	-0.42291
C	2.37732	3.42411	-0.62167
C	3.36719	2.43079	-0.66331
C	2.71072	4.77724	-0.65835
C	4.06066	5.10886	-0.73354
C	5.05304	4.11312	-0.77604
C	4.71917	2.76201	-0.74360
C	4.70456	-2.78706	-0.74295
C	5.03137	-4.13990	-0.77519
C	4.03378	-5.13043	-0.73265
C	2.68561	-4.79176	-0.65757
C	-2.84934	-4.77637	-0.46849
C	-4.20183	-5.10671	-0.45366
C	-5.19368	-4.11037	-0.42568
C	-4.85711	-2.75941	-0.41144
C	-2.82433	4.79096	-0.46932
C	-4.17507	5.12829	-0.45455
C	-5.17208	4.13711	-0.42631
C	-4.84251	2.78444	-0.41179

Co	-0.06144	0.00002	-0.36396
H	1.94044	5.53826	-0.62952
H	4.35595	6.15177	-0.76294
H	6.09499	4.40680	-0.83811
H	5.47780	1.98964	-0.78154
H	5.46722	-2.01868	-0.78094
H	6.07177	-4.43904	-0.83714
H	4.32361	-6.17488	-0.76193
H	1.91136	-5.54875	-0.62870
H	-2.07966	-5.53813	-0.49323
H	-4.49942	-6.14931	-0.46569
H	-6.23769	-4.40308	-0.41678
H	-5.61556	-1.98623	-0.39357
H	-2.05072	5.54873	-0.49427
H	-4.46725	6.17242	-0.46684
H	-6.21456	4.43523	-0.41745
H	-5.60494	2.01520	-0.39373
N	0.03209	-0.00003	1.88917
N	0.84233	-0.00011	3.94875
C	1.12950	-0.00054	2.62104
H	2.14044	-0.00109	2.24428
C	-0.53350	0.00046	4.06139
C	-1.01625	0.00039	2.78043
C	1.80278	-0.00051	5.04357
H	-1.02914	0.00086	5.01779
H	-2.04237	0.00082	2.45074
H	2.81017	0.00002	4.62905
H	1.67686	-0.89181	5.66124
H	1.67638	0.89002	5.66226

CoPc(L8) (Charge = 0, Multiplicity =2)

N	3.36559	0.00016	-0.95288
C	2.73201	1.16045	-0.93956
C	2.73202	-1.16013	-0.93984
N	1.37715	-1.37439	-0.89221
C	1.15983	-2.72967	-0.90358
N	0.00003	-3.36188	-0.89443
C	-1.15977	-2.72967	-0.90364
N	-1.37710	-1.37439	-0.89228
C	-2.73196	-1.16014	-0.93998
N	-3.36554	0.00015	-0.95304
C	-2.73196	1.16044	-0.93970
N	-1.37710	1.37468	-0.89195
C	-1.15978	2.72997	-0.90298
N	0.00002	3.36218	-0.89362
C	1.15982	2.72997	-0.90292
N	1.37715	1.37469	-0.89188
C	3.43000	-2.43933	-0.97260
C	2.43744	-3.43008	-0.94701
C	-2.43738	-3.43009	-0.94712
C	-3.42994	-2.43934	-0.97277
C	-2.43739	3.43039	-0.94631
C	-3.42994	2.43965	-0.97219
C	2.43743	3.43040	-0.94618
C	3.42999	2.43966	-0.97202
C	2.76828	4.78428	-0.96985
C	4.11890	5.11901	-1.01532
C	5.11402	4.12567	-1.04163
C	4.78247	2.77362	-1.02226

C	4.78248	-2.77328	-1.02291
C	5.11404	-4.12532	-1.04260
C	4.11892	-5.11867	-1.01652
C	2.76829	-4.78396	-0.97099
C	-2.76823	-4.78397	-0.97112
C	-4.11885	-5.11868	-1.01672
C	-5.11397	-4.12534	-1.04284
C	-4.78242	-2.77329	-1.02314
C	-2.76824	4.78427	-0.96999
C	-4.11886	5.11900	-1.01553
C	-5.11398	4.12566	-1.04189
C	-4.78242	2.77361	-1.02250
H	1.99596	5.54360	-0.95311
H	4.41248	6.16268	-1.03314
H	6.15645	4.42177	-1.07975
H	5.54323	2.00286	-1.04652
H	5.54324	-2.00251	-1.04699
H	6.15646	-4.42141	-1.08077
H	4.41250	-6.16234	-1.03458
H	1.99598	-5.54328	-0.95444
H	-1.99591	-5.54329	-0.95453
H	-4.41242	-6.16236	-1.03479
H	-6.15639	-4.42143	-1.08106
H	-5.54318	-2.00253	-1.04725
H	-1.99592	5.54359	-0.95322
H	-4.41244	6.16267	-1.03336
H	-6.15640	4.42175	-1.08006
H	-5.54318	2.00285	-1.04680
N	-0.00003	-0.00017	1.50967
C	-1.13871	-0.00030	2.22043
C	-1.19742	-0.00059	3.60226

C	-0.00012	-0.00079	4.35467
C	1.19722	-0.00060	3.60233
C	1.13860	-0.00031	2.22049
H	-2.06063	-0.00015	1.65016
H	-2.16674	-0.00066	4.07971
H	2.16652	-0.00068	4.07985
H	2.06056	-0.00018	1.65029
Co	0.00002	0.00013	-0.76558
N	-0.00016	-0.00116	5.72238
C	-1.25948	-0.00104	6.45445
H	-1.05014	-0.00159	7.52241
H	-1.85917	0.88770	6.22741
H	-1.85971	-0.88920	6.22663
C	1.25912	-0.00102	6.45453
H	1.04971	-0.00152	7.52247
H	1.85935	-0.88920	6.22678
H	1.85883	0.88769	6.22747

A.4 References

1. H. A. Dinçer, A. Koca, A. Gül and M. B. Koçak, *Dyes and Pigments*, 2008, **76**, 825-831.
2. F. Bedioui, E. De Boysson, J. Devynck and K. J. Balkus, *J. Electroanal. Chem. Interfacial Electrochem.*, 1991, **315**, 313-318.
3. B. R. Kozub and R. G. Compton, *Sensors and Actuators B: Chemical*, 2010, **147**, 350-358.
4. F. Zhao, J. Zhang, T. Abe, D. Wöhrle and M. Kaneko, *J. Mol. Catal. A: Chem.*, 1999, **145**, 245-256.
5. F. Cariati, D. Galizzioli, F. Morazzoni and C. Busetto, *J. Chem. Soc., Dalton Trans.*, 1975, DOI: 10.1039/DT9750000556, 556-561.
6. A. Kohen and H. H. Limbach, *Isotope effects in chemistry and biology*, cRc Press, Boca Raton, 2005.
7. P. F. Fitzpatrick, *Biochim. Biophys. Acta, Proteins Proteomics*, 2015, **1854**, 1746-1755.
8. R. L. Schowen, *J. Labelled Compd. Radiopharm.*, 2007, **50**, 1052-1062.
9. K. Venkatasubban and R. L. Schowen, *Crit. Rev. Biochem.*, 1984, **17**, 1-44.
10. Y. Liu and C. C. L. McCrory, *Nat. Commun.*, 2019, **10**, 1683.